2012

On the synthesis, characterization, and magnetization of Ln-M-X (Ln = lanthanide; M = Ti-Cr, Cu, Mo, Pd; X = Al, Ga) intermetallics

Michael James Kangas
Louisiana State University and Agricultural and Mechanical College

ON THE SYNTHESIS, CHARACTERIZATION, AND MAGNETIZATION OF Ln-M-X (Ln = LANTHANIDE; M = Ti-Cr, Cu, Mo, Pd; X = Al, Ga) INTERMETALLICS

A Dissertation

Submitted to the Graduate Faculty of the
Louisiana State University and
Agricultural and Mechanical College
In partial fulfillment of the
Requirements for the degree of
Doctor of Philosophy

in

The Department of Chemistry

by
Michael J. Kangas
B.A., Carthage College, 2004
December 2012

To Angela and Helen

Acknowledgements

In the past four years at Louisiana State University, I've had the fortune of working on a number of enlightening projects with a greater number of helpful and equally enlightening colleagues and collaborators. Any achievements reported in this work are due in no small part to their efforts. In this section, I would like to briefly acknowledge a few of them.

I would like to thank my advisor Julia Chan for providing me with everything that I needed to be successful including advice, assistance writing and revising countless manuscripts, and the freedom to test my ideas.

I would like to thank my Ph.D. committee members Shane Stadler, George Stanley, and David Young for their constructive criticism of my general exam and dissertation. In addition, they have also provided a number of reference letters over the past four years, as well as a lot of great academic and life advice.

I would like to thank everyone that I have collaborated with for their time and expertise. David Young and Neel Haldolaarachchige provided physical property measurements and assistance interpreting them on the majority of the projects. Shane Stadler provided samples and introduced me to the magnetocaloric effect, which has been one of my favorite topics to study. Satoru Nakatsuji and Akito Sakai provided samples and physical property measurements for the LnM_2Al_{20} compounds. Emilia Morosan, Jackui Wang, and Liang Zhao provided heat capacity measurements and expertise for the $Ln(Cu,Al,Ga)_{13-x}$ project. Frank Fronczek provided a lot of assistance and advice about crystallography. Xiaoping Wang was invaluable for assistance with collecting and refining the neutron diffraction data. Moulay Sougrati provided the Mössbauer data and analysis for the $YbCr_2Fe_xAl_{20-x}$ project.

I would also like to thank my past and current colleagues in the Chan research group. We've shared a lot of memorable moments in and out of the lab. My colleagues have assisted my research through many insightful discussions and assistance preparing and proofreading manuscripts. In particular, I would acknowledge Brenton Drake, who taught me how to synthesize and characterized materials when I started in the Chan research group. In addition, I've had a number of successful collaborations with Brenton Drake, William Adam Phelan, and LaRico Treadwell. I was also fortunate to work with two excellent undergraduate researchers Jacob McAlpin and Marcus Toussaint who assisted in growing and characterizing of my samples.

I would like to thank my daughter Helen for teaching me something new each day, and last but not least, I would like to thank my lovely wife Angela. Without her support and many sacrifices I could not be writing this dissertation.

Table of Contents

Dedication ii

Acknowledgements iii

Abstract vii

Chapter 1. Introduction 1
1.1 References 10

Chapter 2. Pushing the Boundaries of Transition Metal Substitution: Synthesis, Structure, Magnetic and Electrical Properties of $LnCr_xGa_3$ (Ln = Ho, Er; x ~0.15) 15
2.1 Introduction 15
2.2 Experimental 16
2.3 Results and Discussion 20
2.4 Conclusions 28
2.5 References 29

Chapter 3. Structure and Physical Properties of Single Crystal $PrCr_2Al_{20}$ and CeM_2Al_{20} (M = V, Cr): A Comparison of Compounds Adopting the $CeCr_2Al_{20}$ Structure Type 32
3.1 Introduction 32
3.2 Experimental 35
3.3 Results and Discussion 36
3.4 Conclusions 51
3.5 References 51

Chapter 4. A ^{57}Fe Mössbauer Spectroscopy and Single Crystal X-ray Diffraction Study of Fe Disorder in Single Crystals of $YbCr_2Fe_xAl_{20-x}$ 55
4.1 Introduction 55
4.2 Experimental 56
4.3 Results and Discussion 61
4.4 Conclusions 67
4.5 References 68

Chapter 5. Magnetic and Electrical Properties of Flux Grown Single Crystals of $Ln_6M_4Al_{43}$ (Ln = Gd, Yb; M = Cr, Mo, W) 72
5.1 Introduction 72
5.2 Experimental 73
5.3 Results and Discussion 82
5.4 Conclusions 90
5.5 References 92

Chapter 6. Crystal Growth, Structure, and Physical Properties of Ln_2PdGa_{12} (Ln = La, Pr, Nd, and Sm) 96
6.1 Introduction 96

6.2 Experimental 97
6.3 Results and Discussion 102
6.4 Conclusions 112
6.5 References 112

Chapter 7. Synthesis and Physical Properties of $Yb_2Pd_3Ga_9$ 115
7.1 Introduction 115
7.2 Experimental 116
7.3 Results and Discussion 119
7.4 Conclusions 120
7.5 References 121

Chapter 8. Single Crystal Neutron Diffraction Studies of $Ln(Cu,Al,Ga)_{13-x}$ (Ln = La – Pr, Eu; x ~ 0.1) 123
8.1 Introduction 123
8.2 Experimental 124
8.3 Results and Discussion 127
8.4 Conclusions 132
8.5 References 133

Chapter 9. Conclusions and Future Work 135
9.1 Conclusions 135
9.2 Future Work 138
9.3 References 140

Appendices 143
A. Letters of Permission 143
B. $LnCr_xGa_3$ (Ln = Ho, Er) Crystallographic Information Files 146
C. $YbCr_2Fe_xAl_{20-x}$ Crystallographic Information Files 157
D. $YbCr_2Fe_xAl_{20-x}$ Fe Site Occupancy Data 174
E. Temperature Dependent Studies of $Ni_{50}Mn_{35}(In,Si)_{15}$ for Magnetocaloric Applications 175
F. Temperature Dependent X-ray Diffraction Studies of NiMn(Ge,Al) 181

Vita 186

Abstract

The focus of the research presented herein was to grow single crystals of Ln-M-X (Ln = lanthanide; M = Ti-Cr, Cu, Mo, Pd; X = Al, Ga) intermetallic compounds and to characterize their crystal structures and physical properties. Overall, the flux growth technique facilitated a detailed analysis of previously known structure-types (LnM_2Al_{20} (Ln = La, Ce, Pr, Yb; M = Ti, V, Cr), $Ln_6M_4Al_{43}$ (Ln = Gd, Yb; M = Cr, Mo), and $Yb_2Pd_3Ga_9$), as well as the synthesis and characterization of new compounds ($LnCr_xGa_3$ (Ln = Ho, Er; x ~ 0.13), $YbCr_2Al_{20-x}Fe_x$ (x ~ 0.2), $Ln(Cu,Al,Ga)_{13-x}$, and Ln_2PdGa_{12} (Ln = Pr, Nd, Sm)).

$LnCr_xGa_3$ (Ln = Ho, Er) adopt a stuffed variant of the $AuCu_3$ structure-type rather than the related Y_4PdGa_{12} structure-type which is adopted by the latter transition metals. Like the related Ln_4MGa_{12} compounds, both analogues exhibit positive magnetoresistance, with $ErCr_xGa_3$ reaching ~25% at H = 9 T.

After characterizing a number of LnM_2Al_{20} (Ln = La, Ce, Pr, Yb; M = Ti, V, Cr) compounds, Fe was introduced to determine if it would influence the physical properties and to better understand the stability of the $CeCr_2Al_{20}$ structure-type. Mössbauer spectroscopy results for $YbCr_2Fe_xAl_{20-x}$ indicate that Fe atoms occupy two crystallographic sites, and X-ray diffraction refinements suggest that the Fe atoms occupy the Al1 and Al2 sites rather than the Cr site. These results are consistent with LnM_2Al_{20} compounds only forming for early transition metals.

Single crystals of $Yb_6M_4Al_{43}$ are non-magnetic consistent with divalent Yb, which contrasts with previously reports. $Gd_6M_4Al_{43}$ (M = Ce, Mo, W) appear to order antiferromagnetically below 20 K with positive Weiss temperatures, suggesting that the magnetic structures of these materials are complex.

Single crystals of Ln_2PdGa_{12} order antiferromagnetically at 18, 7.5, and 7.5 K, respectively, and heat capacity measurements indicate that Pr_2PdGa_{12} may be a new Pr-containing heavy fermion compound.

Single crystal neutron diffraction experiments were successfully carried out on $NaZn_{13}$ type $Ln(Cu,Al,Ga)_{13-x}$, including $Eu(Cu,Al,Ga)_{13-x}$, to understand the site occupancies and disorder, and it was found that Cu partially occupies the 8*b* site while the 96*i* site is populated with Al, Cu, and Ga.

Chapter 1. Introduction

Scientists from a number of fields including chemistry, physics, materials science, and engineering are involved with research on solid-state materials. Traditionally chemists are interested in what will form and why, physicists are interested in discovering and understanding new phenomena and properties, and engineers utilize materials for applications. There is synergy between these separate fields, as the understanding of one aspect of a material deepens the understanding of other aspects [1-3]. However, neglecting the ever-expanding scope and power of theoretical methods [4-9], no progress can be made in any of these fields without materials. In addition, the discovery and understanding on new materials is essential for solving many issues facing mankind [10].

There are many synthetic methods capable of producing solid materials. Each method works best for certain classes of materials and has certain advantages and disadvantages associated with it. A selection of these methods is discussed in reference [11]. Likewise, solid materials can come in many forms including but not limited to aerogels, amorphous solids, thin-films, nanoparticles, single crystals, and bulk polycrystalline solids; which form is produced depends on the synthetic method.

Among the different forms, single crystals are often preferable over polycrystalline forms. The synthesis of single crystals facilitates the use of single crystal X-ray or neutron diffraction to determine the crystal structure of a material. An accurate structural determination is vital to the understanding of a material because the physical and chemical properties are due to both the composition and crystal structure. Another advantage of single crystals, provided they are large enough, is that anisotropic physical property measurements of can be performed. A number of physical properties including hardness, electrical and thermal conductivity, and magnetism are sensitive to direction. In addition to being able to measure a material's anisotropic physical properties, single crystals also allow for the determination of the material's intrinsic properties due to the high crystal quality [12]. Polycrystalline materials are composed of many small grains which can be oriented randomly. Between the individual grains are grain boundaries, which contribute to a number of effects, such as, the scattering of phonons or electrons. Impurities that can alter the materials properties can also be present at the grain boundaries. For example, in the ultra-hard material ReB_2 excess boron has been shown to accumulate at the grain boundaries and weaken the material [13]. On the other hand, some properties, including lowering the thermal conductivity of thermoelectrics, can be improved by introducing grain boundaries [14-16]. Despite that the high quality material should ideally be prepared to understand and optimize the properties.

In this section the mechanisms of crystal growth that are required to produce the desired single crystals are discussed. There are many modern methods that are still revealing new details on crystal growth. Crystal growth begins with a supersaturated solution which leads to the formation of a nucleus [17]. The nucleus has to be large and stable enough that it will not dissolve. This critical size is system and conditions dependent but typical estimates are in the range of ~5 nm in diameter [18-20]. After nucleation, the crystal grows outward as more material is added. A number of mechanisms are responsible for crystal growth including spiral growth, birth and spread, and adhesive growth depending on the degree of supersaturation (listed in order of lowest to most supersaturated) [18].

There are a number of techniques that can generate appropriate conditions for the growth of single crystals including the Bridgman, Czochralski, vapor transport, floating zone, and flux growth techniques [11]. In the research reported herein, the flux growth method was utilized. In the flux growth method, the solvent is a molten metal [17, 21-23] or salt [20, 24-27]. Ideal fluxes have low melting points and high boiling points to allow a range of working temperatures, some solubility for the reactants, a method for easy removal [28], and minimal reactivity towards the reaction vessel. The flux can be either inert or be incorporated into the products (self-flux). Generally, the reactants are dissolved in a large excess of flux by heating to a high temperature. Supersaturation is then achieved by lowering the temperature which lowers the solubility of the product. The ideal rate of cooling will result in a small number of nucleation sites and a few large well-formed crystals. Unfortunately, the ideal cooling rate is system dependent, and rates that are too fast will result in many nucleation sites and small aggregated crystals. Cooling rates that are too slow can result in a supercooled liquid which will also produce many small crystals [17]. At the end of the reaction, the excess flux can be removed by centrifugation, distillation, chemical etching, or mechanical separation.

A number of variables can be altered in the flux growth method to improve crystal quality, size, and yields or to produce different phases. These include the temperature ramp rates, the dwell temperature, end temperature, dwell times, and reaction stoichiometry. An example of a temperature profile is shown in Figure 1.1. As mentioned previously, the cooling rates affect the rates for nucleation and growth. The ramp up rate can be increased to avoid stable phases that form while heating or slowed to allow volatile elements to react. The maximum temperature is set high enough that the sample is fully melted and to allow homogenization. However, volatile and low-boiling elements limit the maximum temperatures attainable. The low temperature dwell (spin temperature) is typically chosen to be above the melting point of the flux to allow for easy removal. Raising the spin temperature can be a good method to avoid low temperature phases. One important point to note is that often relatively small changes in the temperature profile, such as a 50 K change, can have profound effects on the reaction products [29]. Additionally, changing the starting composition can also change which phases will be produced in the reaction [12].

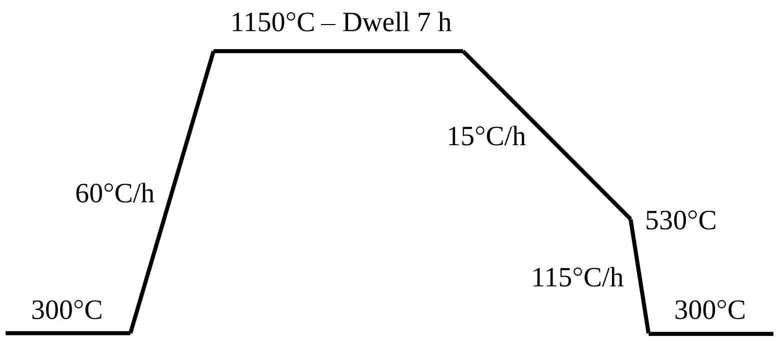

Figure 1.1. The temperature profile used to grow $HoCr_{0.15}Ga_3$ and $ErCr_{0.14}Ga_3$, as discussed in Chapter 2.

Often several aspects of a newly synthesized material must be characterized before the material and its properties can be understood. These aspects include, but are not limited to, the composition, the crystal structure, and various physical properties. Because solid state materials can contain voids or other atoms through substitution or as interstitial atoms the composition must be determined. The composition can be determined via energy dispersive X-ray spectroscopy (EDS) or inductively coupled plasma optical emission spectroscopy (ICP-OES). The crystal structure can be determined by diffraction with X-rays, neutrons, or electrons. Results and methods to measure the various physical properties such as electric resistivity, magnetism, and specific heat will be discussed in the following chapters, where appropriate. Additionally, the measurement of one property often improves the understanding of another property, such as the manner in which features in resistivity coincide with the magnetic ordering of a sample. A general description of various characterization methods can be found in Basic Solid State Chemistry by West [11] or in Materials Chemistry by Fahlman [30]. Mössbauer spectroscopy and the magnetocaloric effect are relatively less-common than the other techniques and properties featured herein, so they will be introduced in the following sections.

Mössbauer spectroscopy is a non-destructive, elemental specific technique that provides information on oxidation states, spin states, local structure, bonding, and magnetism. The technique is named for Rudolf Ludwig Mössbauer who demonstrated resonant absorption of γ-rays in 1958, and this discovery earned him the Nobel Prize in physics in 1961 [31]. The energy levels of the nucleus can be shifted or split by the atom's environment or a magnetic field (applied or internal), and these features can be measured to provide information on the sample. The >50,000 publications utilizing Mössbauer spectroscopy are a testament to its usefulness [32].

Traditionally, γ-rays are produced as a result of a nuclear decay, but recently synchrotron Mössbauer methods have become available and offer new capabilities [33-35]. One constraint of the traditional approach is that the emitting nucleus must be identical to the absorbing nucleus, and not all elements have suitable sources. Overall, 80 isotopes from ~40 elements are Mössbauer-active, and a few notable Mössbauer–active isotopes are ^{57}Fe, ^{40}K, ^{61}Ni, ^{119}Sn, ^{129}I and ^{155}Gd [32, 36, 37]. In the prominent Mössbauer-active ^{57}Fe, 14.41 keV γ-rays are produced by the decay of ^{57}Co, which is depicted in Figure 1.2.

Aside from the emission source, two important considerations remain. The first is that the recoil energies from the emission and absorption of the photons are a significant fraction of the and would alter the energy of the photon away from resonance. Encasing the active nuclei in a solid minimizes the recoil. The second consideration is that the energy must be accurately varied to observe all of the features of the spectrum. The energies of γ-rays used in Mössbauer spectroscopy are ~10^4 eV, while the energy shifts to be measured are ~12 orders of magnitude smaller [38]. These small shifts can be achieved by moving the source and utilizing the Doppler effect ($\Delta E = E_0 * v/c$), where v is the velocity, c is the speed of light, and E_0 is the photon energy. Typical source velocities are up to 10 mm/sec [32, 36].

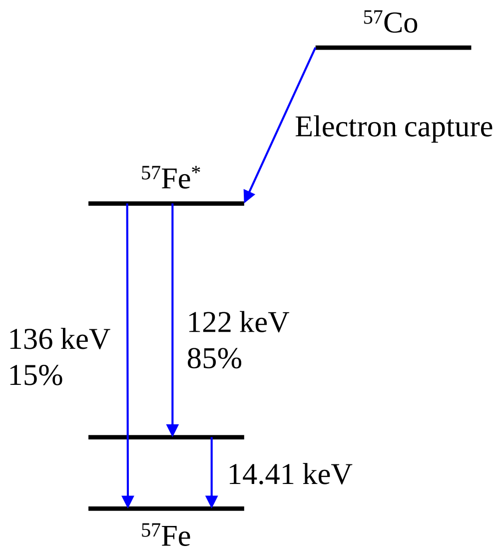

Figure 1.2. The transitions leading to the ^{57}Fe Mössbauer γ-ray emission are depicted as blue arrows. The 14.41 keV emission is spectroscopically useful and has a lifetime of ~220 ns.

A Mössbauer spectrum consists of a number of (partially resolved) peaks, and an example spectrum depicting the isomer shift and electric quadrupole splitting is shown in Figure 1.3. The spectrum is characterized by three important parameters (hyperfine interactions); the isomer shift, electric quadrupole splitting, and magnetic splitting. The isomer shift the offset from velocity = 0, and is caused by changes to the electron density at the nucleus. Phenomena that change the density of *s* electrons (oxidation state, spin state, and local environment) result in a chemical shift [38]. Quadrupole splitting is caused by interactions of a nucleus (with a spin) and a non-uniform electric field. This interaction results in a splitting of degenerate states yielding additional peaks in the spectrum. Both the ground and excited states can be split, and analysis of the quadrupole splitting provides similar information to the isomer shift. Magnetic splitting is due to Zeeman splitting of degenerate states in an applied or internal magnetic field. Like quadrupole splitting, magnetic splitting yields additional peaks in the spectrum. For example, for ^{57}Fe there can be 6 peaks. The magnetic splitting provides information on the type of magnetic orderings, as well as the direction and magnitude of the internal field [32]. Typically the parameters are used in an empirical manner, but Mössbauer parameters can also be obtained through computational methods with reasonable accuracy [39].

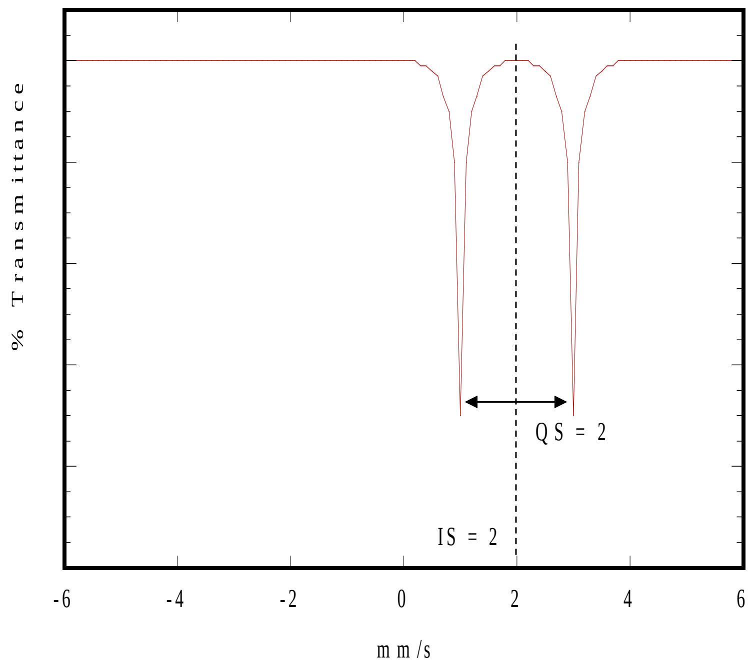

Figure 1.3. A hypothetical ^{57}Fe Mossbauer spectrum depicting the isomer shift and electric quadrupole splitting.

In addition to the three hyperfine interactions, the fraction of recoilless emission can be determined by measuring Mössbauer spectra as a function of temperature. Increased temperature results in increased lattice vibrations, decreased recoilless emission, and decreased absorbance. The recoilless emission fraction can be used to determine the Debye temperature (the temperature where phonons begin to saturate), which correlates with many physical properties [38].

The magnetocaloric effect (MCE) was originally discovered in 1881 by Warburg and is a promising technology for efficient, environmentally friendly refrigeration [40]. The magnetocaloric effect utilizes changes in entropy caused by magnetic spins aligning with an applied magnetic field [41]. Two important parameters for any functional magnetocaloric material are the changes in entropy (ΔS_m) and temperature (ΔT_{ad}) that occur when the field is applied, and these paramters can be determined with heat capacity or magnetic measurements [41].

Paramagnetic materials can exhibit the MCE at low temperatures, but at elevated temperatures a magnetic phase transition must occur. Low temperature MCE can be used for reaching cryo-temperatures or for gas liquefaction, and when a transition occurs near room temperature, MCE can be utilized for magnetic refrigeration or air conditioning. Several families of compounds have been explored for magnetocaloric applications, including the lanthanide systems such as EuS [42], ErGa [43], and $Gd_3Ga_{5-x}Fe_xO_{12}$ [44], and $(La,Na)MnO_3$ [45]. Although many of the rare earth phases show magnetic entropy change (ΔS_M) at low temperatures, the optimally prepared Gd_5Si_4-based system $Gd_5Si_2Ge_2$ can exhibit a MCE of 36 J/kg K between 270-300 K [46], which is enhanced due to the combination of the magnetic ordering and a structure change [47, 48]. The large (ΔS_M) makes $Gd_5Si_2Ge_2$ a potentially viable material for commercial applications, but opportunities remain to find improved magnetocaloric materials [49, 50].

Everything discussed thus far can apply equally well to a large number of intermetallic compounds, and in this section the motivation for the current research will be examined, with a brief summary of research in the Chan group. Previous members of the Chan group have had success growing single crystals of Ln-M-X (Ln = lanthanide; M = transition metal; X = group 13 or 14 element) intermetallics with latter transition metals such as Co-Cu, Rh-Ag, and Pt [51-60]. This work resulted in new structures such as $LaPdSb_3$ [52], β-$LnNiSb_3$ (Ln = La, Ce) [54], and

$CePdGa_6$ [51]. In addition to new and interesting structures, many compounds that exhibited novel physical properties including magnetism, magnetoresistance, and heavy fermion behavior were also reported. For example, two unusual ferromagnetic cerium compounds, $CeAg_{0.72}Al_{3.28}$ and $CeAg_{0.68}Ga_{3.32}$, were discovered. Both analogues order ferromagnetically near 3 K [56]. Large positive magnetoresistance up to ~900% was reported in the Ln_4MGa_{12} (Ln = Dy-Er; M = Pd, Pt) compounds [55]. A number of new heavy fermion compounds were also reported including $CePdGa_6$ (γ ~ 300 mJ/K^2-mol) [51] and $Pr(CuGa)_{13-x}$ (γ ~ 100 mJ/K^2-mol) [58]. Heavy fermion compounds are typically Ce- and U-based intermetallics where the conduction electrons interact strongly with and screen the magnetic moments of the rare earth atom. The interaction causes the electron's effective mass and the electronic contribution to specific heat to increase by at least 2 orders of magnitude [61-64].

In the research described herein the trend of investigating Ln-M-X phases (Ln = lanthanide, M = transition metal; X = group 13 or 14 element) will continue. The use of a ternary system adds complexity which can influence the structure and properties, and a ternary also aims to avoid binary phases, many of which are well known and characterized. The lanthanide atom possesses *f*-electrons which form the basis of the electrical and magnetic properties. The group 13 or 14 element influences the structure and bonding as well as provides a convenient flux for crystal growth.

Chapters 6-8 will continue the focus on latter transition metals, while in Chapters 2-5 the focus will be on Ln-M-X compounds containing early transition metals, Cr in particular. A change of the transition metal from the latter transition metals to Cr changes the number of valence electrons, atomic radius and electronegativity, all of which can have an impact on the crystal structure. In addition to the possibility of new structures and compounds, chromium containing intermetallics are also of interest because the Cr atoms can carry a magnetic moment. For example, Cr (T_N = 308 K) [11] and $AlCr_2$ (T_N = 472(8) K, μ = 0.92(2) μ_B / mol Cr) [65] are antiferromagnets and $CuAl_2$-type $CrSb_2$ (T_C = 170 K, μ_{eff} = 1.6 μ_B/mol Cr) [66] and $CrGa_2Sb_2$ (T_C = 345 K, μ_{eff} = 1.6 μ_B/mol Cr) [67] are ferromagnetic. In addition to magnetic ordering, the nature of the magnetism is also of interest. Magnetism is typically described by two opposing models, either localized magnetic ions or itinerant electrons, but a number of compounds show intermediate behavior including $LaCrSb_3$ [68, 69]. Herein, the synthesis, structure, and physical properties of $LnCr_xGa_3$ (Ln = Ho, Er), LnT_2Al_{20} (Ln = Ce, Pr, Yb; T = Ti-Cr), $YbCr_2Fe_xAl_{20-x}$, $Yb_2Pd_3Ga_9$, and Ln_2PdGa_{12} (Ln = Pr, Nd, Sm) are reported.

1.1 References

[1] J.N. Lalena, D.A. Cleary, E.E. Carpenter, N.F. Dean, Inorganic materials synthesis and fabrication, Wiley-Interscience, Hoboken, New Jersey, 2008.

[2] M.A. Serio, D.M. Gruen, R. Malhotra, Synthesis and characterization of advanced materials, in: ACS Symp. Ser., American Chemical Society, 1998, pp. 271.

[3] C.N.R. Rao, Chemistry of advanced materials, Blackwell Scientific Publications, London, 1993.

[4] G. Ceder, Predicting properties from scratch, Science, 280 (1998) 1099-1100.

[5] C.C. Fischer, K.J. Tibbetts, D. Morgan, G. Ceder, Predicting crystal structure by merging data mining with quantum mechanics, Nature Mater., 5 (2006) 641-646.

[6] S.M. Woodley, R. Catlow, Crystal structure prediction from first principles, Nature Mater., 7 (2008) 937-946.

[7] G. Ceder, Opprotunities and challenges for first-principles materials design and applications to Li battery materials, Mater. Res. Bull., 35 (2010) 693-701.

[8] A.R. Oganov, A.O. Lyakhov, M. Valle, How evolutionary crystal structure prediction works—and why, Acc. Chem. Res., 44 (2011) 227-237.

[9] A.O. Lyakhov, A.R. Oganov, Evolutionary search for superhard materials: Methodology and applications to forms of carbon and TiO_2, Phys. Rev. B, 84 (2011) 092103.

[10] Frontiers in crystalline matter: from discovery to technology, The National Academies Press, Washington, D.C., 2009.

[11] A.R. West, Basic Solid State Chemistry, Second ed., John Wiley & Sons, LTD, Chichester, England, 1999.

[12] I.R. Fisher, M.C. Shapiro, J.G. Analytis, Principles of crystal growth of intermetallic and oxide compounds from molten solutions, Philos. Mag., 92 (2012) 2401-2435.

[13] J.B. Levine, J.B. Betts, J.D. Garrett, S.Q. Guo, J.T. Eng, A. Migliori, R.B. Kaner, Full elastic tensor of a crystal of the superhard compound ReB_2, Acta Mater., 58 (2010) 1530-1535.

[14] D.M. Rowe, V.S. Shukla, N. Savvides, Phonon scattering at grain boundaries in heavily doped fine-grained silicon-germanium alloys, Nature, 290 (1981) 765-766.

[15] G.D. Mahan, Good thermoelectrics, in: E. Henry, S. Frans (Eds.) Solid State Physics, Academic Press, 1997, pp. 81-157.

[16] S.K. Bux, J.-P. Fleurial, R.B. Kaner, Nanostructured materials for thermoelectric applications, Chem. Commun., 46 (2010) 8311-8324.

[17] Z. Fisk, J.P. Remeika, Chapter 81 Growth of single crystals from molten metal fluxes, in: Karl A. Gschneidner, Jr., E. LeRoy (Eds.) Handbook on the Physics and Chemistry of Rare Earths, Elsevier, 1989, pp. 53-70.

[18] P. Cubillas, M.W. Anderson, Synthesis mechanism: crystal growth and nucleation, in: Zeolites and Catalysis, Wiley-VCH Verlag GmbH & Co. KGaA, 2010, pp. 1-55.

[19] E. Stavitski, M. Goesten, J. Juan-Alcañiz, A. Martinez-Joaristi, P. Serra-Crespo, A.V. Petukhov, J. Gascon, F. Kapteijn, Kinetic control of metal–organic framework crystallization investigated by time-resolved in situ X-ray scattering, Angew. Chem. Int. Ed., 50 (2011) 9624-9628.

[20] D.E. Bugaris, H.-C. zur Loye, Materials discovery by flux crystal growth: quaternary and higher order oxides, Angew. Chem. Int. Ed., 51 (2012) 3780-3811.

[21] P.C. Canfield, Z. Fisk, Growth of single crystals from metallic fluxes, Philos. Mag. B, 65 (1992) 1117 - 1123.

[22] M.G. Kanatzidis, R. Pöttgen, Wolfgang Jeitschko, The metal flux: A preparative tool for the exploration of intermetallic compounds, Angew. Chem. Int. Ed., 44 (2005) 6996-7023.

[23] W.A. Phelan, M.C. Menard, M.J. Kangas, G.T. McCandless, B.L. Drake, J.Y. Chan, Adventures in crystal growth: synthesis and characterization of single crystals of complex intermetallic compounds, Chem. Mater., 24 (2011) 409-420.

[24] A.R. Patel, H.L. Bhat, Growth of barite group crystals by the flux evaporation method, J. Cryst. Growth, 11 (1971) 166-170.

[25] C.M. Jones, Growth of α-Al_2O_3 crystals by Na_2O evaporation, J. Am. Ceram. Soc., 54 (1971) 347-349.

[26] S. Oishi, M. Mochizuki, Growth of emerald crystals by the evaporation of molybdenum trioxide flux, Br. Ceram. Trans., 92 (1993) 214-216.

[27] S. Oishi, K. Teshima, H. Kondo, Flux growth of hexagonal bipyramidal ruby crystals, J. Am. Chem. Soc., 126 (2004) 4768-4769.

[28] T. Wolf, Flux separation methods for flux-grown single crystals, Philos. Mag., 92 (2012) 2458-2465.

[29] Y. Janssen, M. Angst, K.W. Dennis, R.W. McCallum, P.C. Canfield, Differential thermal analysis and solution growth of intermetallic compounds, J. Cryst. Growth, 285 (2005) 670-680.

[30] B.D. Fahlman, Materials Chemistry, Second ed., Springer, New York, 2011.

[31] R.L. Mössbauer, Kernresonanzfluoreszenz von Gammastrahlung in Ir^{191}, Z. Phys. A, 151 (1958) 124-143.

[32] P. Gütlich, Fifty years of Mössbauer spectroscopy in solid state research – remarkable achievements, future perspectives, Z. Anorg. Allg. Chem., 638 (2012) 15-43.

[33] G.V. Smirnov, U. van Bürck, A.I. Chumakov, A.Q.R. Baron, R. Rüffer, Synchrotron Mössbauer source, Phys. Rev. B, 55 (1997) 5811-5815.

[34] E. Gerdau, R. Rüffer, H. Winkler, W. Tolksdorf, C.P. Klages, J.P. Hannon, Nuclear Bragg diffraction of synchrotron radiation in yttrium iron garnet, Phys. Rev. Lett., 54 (1985) 835-838.

[35] G. Smirnov, Nuclear resonant scattering of synchrotron radiation, Hyperfine Interact., 97-98 (1996) 551-588.

[36] H. Kuzmany, Solid-State Spectroscopy, Springer, Berlin, 1998.

[37] R. Pöttgen, K. Łątka, ^{155}Gd Mössbauer spectroscopy on intermetallics – an overview, Z. Anorg. Allg. Chem., 636 (2010) 2244-2255.

[38] B. Fultz, Mössbauer Spectrometry, in: E. Kaufmann (Ed.) Characterization of Materials, John Wiley, New York, 2011.

[39] P. Blaha, Calculations of Mössbauer parameters in solids by DFT bandstructure calculations, J. Phys. Conf. Ser., 217 (2010) 012009.

[40] E. Brück, Introduction to special issue on magnetocaloric materials, J. Magn. Magn. Mater., 321 (2009) 3533-3534.

[41] K.A. Gschneidner, Jr., V.K. Pecharsky, Magnetocaloric materials, Annu. Rev. Mater. Sci., 30 (2000) 387-429.

[42] P. Bredy, P. Seyfert, Measurement of magnetic field induced changes in the entropy of europium sulphide, Cryogenics, 28 (1988) 605-606.

[43] J. Chen, B.G. Shen, Q.Y. Dong, F.X. Hu, J.R. Sun, Large reversible magnetocaloric effect caused by two successive magnetic transitions in ErGa compound, Appl. Phys. Lett., 95 (2009) 132504.

[44] R.D. McMichael, J.J. Ritter, R.D. Shull, Enhanced magnetocaloric effect in $Gd_3Ga_{5-x}Fe_xO_{12}$, J. Appl. Phys., 73 (1993) 6946-6948.

[45] W. Zhong, W. Chen, W. Ding, N. Zhang, Y. Du, Q. Yan, Magnetocaloric properties of Na-substituted perovskite-type manganese oxides, Solid State Commun., 106 (1998) 55-58.

[46] A.O. Pecharsky, K.A. Gschneidner, V.K. Pecharsky, The giant magnetocaloric effect of optimally prepared $Gd_5Si_2Ge_2$, J. Appl. Phys., 93 (2003) 4722-4728.

[47] V.K. Pecharsky, K.A. Gschneidner Jr., Magnetocaloric effect and magnetic refrigeration, J. Mag. Magn. Mater., 200 (1999) 44-56.

[48] V.K. Pecharsky, K.A. Gschneidner, Jr., Advanced magnetocaloric materials: What does the future hold?, Int. J. Refrig., 29 (2006) 1239-1249.

[49] O. Gutfleisch, M.A. Willard, E. Brück, C.H. Chen, S.G. Sankar, J.P. Liu, Magnetic materials and devices for the 21st century: Stronger, lighter, and more energy efficient, Adv. Mater., 23 (2011) 821-842.

[50] L. Min, Y. Bing-feng, Development of magnetocaloric materials in room temperature magnetic refrigeration application in recent six years, J. Cent. South Univ. Technol., 16 (2009) 1-12.

[51] R.T. Macaluso, S. Nakatsuji, H. Lee, Z. Fisk, M. Moldovan, D.P. Young, J.Y. Chan, Synthesis, structure, and magnetism of a new heavy-fermion antiferromagnet, $CePdGa_6$, J. Solid State Chem., 174 (2003) 296-301.

[52] E.L. Thomas, D.P. Gautreaux, J.Y. Chan, The layered intermetallic compound $LaPdSb_3$, Acta Crystallogr. E, 62 (2006) i96-i98.

[53] W.M. Williams, L. Pham, S. MaQuilon, M. Moldovan, Z. Fisk, D.P. Young, J.Y. Chan, Crystal growth, structure, magnetic, and transport properties of $TbRhIn_5$, Inorg. Chem., 45 (2006) 4637-4641.

[54] E.L. Thomas, D.P. Gautreaux, H.-O. Lee, Z. Fisk, J.Y. Chan, Discovery of β-$LnNiSb_3$ (Ln = La, Ce); Crystal Growth, Structure, and Magnetic and Transport Behavior, Inorg. Chem., 46 (2007) 3010-3016.

[55] J.Y. Cho, et al., Crystal growth and magnetic properties of Ln_4MGa_{12} (Ln = Dy–Er; M = Pd, Pt), J. Phys.:Condens. Matter, 19 (2007) 266224.

[56] J.Y. Cho, M. Moldovan, D.P. Young, N.D. Lowhorn, J.Y. Chan, Physical properties of $LnAg_yX_{4-y}$ (Ln = La, Ce; X = Al, Ga; y ≈ 0.72), Physica B, 403 (2008) 795-796.

[57] E.K. Okudzeto, K. Kuga, S. Nakatsuji, J.Y. Chan, Crystal growth, transport, and magnetic properties of $YbCoGa_5$, Cryst. Growth Des., 9 (2009) 1956-1959.

[58] J.Y. Cho, E.L. Thomas, Y. Nambu, C. Capan, A.B. Karki, D.P. Young, K. Kuga, S. Nakatsuji, J.Y. Chan, Crystal growth, structure, and physical properties of $Ln(Cu,Ga)_{13-x}$ (Ln = La−Nd, Eu; x ≈ 0.2), Chem. Mater., 21 (2009) 3072-3078.

[59] B.L. Drake, C. Capan, J.Y. Cho, Y. Nambu, K. Kuga, Y.M. Xiong, A.B. Karki, S. Nakatsuji, P.W. Adams, D.P. Young, J.Y. Chan, Crystal growth, structure, and physical properties of $Ln(Cu,Al)_{12}$ (Ln = Y, Ce, Pr, Sm, and Yb) and $Ln(Cu,Ga)_{12}$ (Ln = Y, Gd–Er, and Yb), J. Phys.:Condens. Matter, 22 (2010) 066001.

[60] M.C. Menard, Y. Xiong, A.B. Karki, B.L. Drake, P.W. Adams, F.R. Fronczek, D.P. Young, J.Y. Chan, Crystal growth and properties of $Ln_2Ag_{1-x}Ga_{10-y}$ (Ln = La, Ce), a disordered variant of the Ce_2NiGa_{10}-structure type, J. Solid State Chem., 183 (2010) 1935-1942.

[61] Z. Fisk, J.L. Sarrao, J.L. Smith, J.D. Thompson, The physics and chemistry of heavy fermions, P. Natl. Acad. Sci. USA, 92 (1995) 6663-6667.

[62] Z. Fisk, J.L. Sarrao, J.D. Thompson, Heavy fermions, Curr. Opin. Solid State Mater. Sci., 1 (1996) 42-46.

[63] E.L. Thomas, J.N. Millican, E.K. Okudzeto, J.Y. Chan, Crystal growth and the search for highly correlated intermetallics, Comments Inorg. Chem., 27 (2006) 1 - 39.

[64] G.R. Stewart, Heavy-fermion systems, Rev. Mod. Phys., 56 (1984) 755-787.

[65] M. Atoji, Antiferromagnetic structure of $AlCr_2$, J. Chem. Phys., 43 (1965) 222-225.

[66] H. Takizawa, K. Uheda, T. Endo, A new ferromagnetic polymorph of $CrSb_2$ synthesized under high pressure, J. Alloys Comp., 287 (1999) 145-149.

[67] W. Sakakibara, Y. Hayashi, H. Takizawa, High-pressure synthesis of a new ferromagnetic compound, $CrGa_2Sb_2$, J. Alloys Comp., 496 (2010) L14-L17.

[68] T. Moriya, Y. Takahashi, Itinerant electron magnetism, Annu. Rev. Mater. Sci., 14 (1984) 1-25.

[69] E. Granado, H. Martinho, M.S. Sercheli, P.G. Pagliuso, D.D. Jackson, M. Torelli, J.W. Lynn, C. Rettori, Z. Fisk, S.B. Oseroff, Unconventional metallic magnetism in $LaCrSb_3$, Phys. Rev. Lett., 89 (2002) 107204.

Chapter 2. Pushing the Boundaries of Transition Metal Substitution: Synthesis, Structure, Magnetic and Electrical Properties of $LnCr_xGa_3$ (Ln = Ho, Er; x ~ 0.15)

2.1 Introduction

Many factors govern the stability of intermetallic phases including valence electron counts, atomic radii, electronegativity and oxidation states [70]. Determination of what phases will form in a given system is a complex task and can be attempted with exploratory synthesis, chemical intuition, and guidance from computation. A recent investigation of the Ho-Fe-Ga phase diagram shows 12 ternary/pseudobinary compounds adopting diverse structure-types such as $ScFe_6Ga_6$, $ThMn_{12}$, Th_2Ni_{17}, Th_2Zn_{17}, Ho_2CoGa_8, $NbBe_3$, $CeNi_3$, $U_4Fe_6Ga_7$, $MgCu_2$, $MgZn_2$, $CeCu_2$, and AlB_2 [71]. One finding in this work was that a phase previously identified as $AuCu_3$-type $HoFe_xGa_{3-x}$ actually adopts the Y_4PdGa_{12} structure type as Ho_4FeGa_{12} [71]. A similar $AuCu_3$-type YCr_xGa_{3-x} was previously reported [72], and it was of interest to see if early transition metals such as Cr, which is potentially magnetic, could be substituted for Pd in the Y_4PdGa_{12} structure-type. This structure type has previously been stabilized for Ln_4MGa_{12} (Ln = Y and Gd-Tm; M = Mn – Ni, Ag, Pd, Pt) [73-78] and U_4MGa_{12} (M = Fe, Co, Rh) [79, 80].

The Y_4PdGa_{12} structure-type can be described as a combination of 8 $LnGa_3$ ($AuCu_3$-type) unit cells. Transition metal atoms occupy the center of ¼ of the gallium octahedra and are ordered to form a body-centered unit cell [80]. A number of interesting physical properties have been reported for Y_4PdGa_{12} structure-type compounds including heavy fermion behavior, large magnetoresistance, and magnetic ordering due to the transition metal sublattice. U_4MGa_{12} (M = Fe, Co, Rh and Pd) show enhanced Sommerfeld coefficients of 100, 116, 140, and 83 mJ/K^2-mol, respectively [79, 80]. Ln_4MGa_{12} (Ln = Dy-Er; M = Pd, Pt) compounds display large positive magnetoresistance, with Ho_4PdG_{12} showing the largest magnetoresistance of the series with ~900% at 3 K and 9 T. With the exception of Ho_4PdGa_{12}, Ln_4MGa_{12} (Ln = Dy-Er; M = Pd, Pt) compounds show antiferromagnetic ordering between 3 and 10 K [81]. Ln_4FeGa_{12} (Ln = Tb-Er; M = Pd, Pt) also order antiferromagnetically at low temperatures, and Y_4FeGa_{12} exhibits itinerant ferromagnetism below 40 K [77]. Ferromagnetism was also reported in $Y_4Mn_{1-x}Ga_{12-y}Ge_y$ (x = 0 – 0.26, y = 0 – 4.0) with ordering temperatures up to 225 K for $Y_4Mn_{0.95(2)}Ga_{8.0(6)}Ge_{4.0(6)}$. The ferromagnetism was found to be induced by Mn vacancies as samples with a fully occupied Mn remained paramagnetic [78]. Herein, we report the report the flux growth, crystal structure, and physical properties of $LnCr_xGa_3$ (Ln = Ho, Er; x ~0.15), a compound adopting a stuffed $AuCu_3$ structure-type.

2.2 Experimental

2.2.1 Synthesis

The flux growth method was chosen as this technique has been proven to produce high quality single crystals suitable for X-ray diffraction and physical property measurements [82-84]. Er or Ho (99.9%), Cr (99.996%), and Ga (99.99999%) were weighed out in a molar ratio of 1:1:20 or 1:0.5:20, placed in an alumina crucible, covered with quartz wool, and sealed in an evacuated fused silica tube. The tubes were heated in a resistive furnace to 1423 K at 60 K/h and dwelled for 7 hours, cooled to 803 K at 15 K/h, and finally cooled to 573 K at 115 K/h. The samples were centrifuged to remove excess gallium, and residual flux from the crystal surface was removed by sonicating in hot water or etching in a solution of I_2 in *N*,*N*-dimethylformamide (DMF). The products were a mix of shiny silver cubes (~1 mm^3) of $LnCr_xGa_3$ shown in Figure 2.1, silver zig-zag rods of $CrGa_4$ ($PtHg_4$ structure-type) [85], and rough cubes of $LnGa_6$. The products were easily separated based on morphology. Synthesis of Tb and Dy analogues yielded small, low quality crystals of $TbCr_{0.20(2)}Ga_3$ (a = 4.286(1) Å) and $DyCr_{0.20(4)}Ga_{2.96(8)}$ that were identified with single crystal X-ray diffraction and EDS, respectively, and will not be discussed further in this manuscript. Additionally, attempts to synthesize Y, Gd, and Yb analogues yielded a combination of $CrGa_4$ and YGa_6, $GdGa_6$, and $YbGa_{3-x}$, respectively. Attempts to synthesize polycrystalline samples by melting stoichiometric samples with a radio frequency induction furnace produced a mix of $LnGa_6$, $CrGa_4$ and $LnCr_xGa_3$.

Figure 2.1. Three single crystals of $ErCr_{0.14}Ga_3$ with a mm scale.

2.2.2 Elemental Analysis

Elemental analysis was conducted via energy dispersive spectroscopy (EDS) on a FEI Quanta 200 scanning electron microscope with an accelerating voltage of 15 kV. Spectra were integrated for 60 seconds and results of at least 5 spots were averaged. The error listed is the standard deviation of the measurements, and the instrumental error is expected to be ~5-10 atomic percent. The compositions, normalized to the lanthanide, are $HoCr_{0.14(1)}Ga_{2.65(2)}$ and $ErCr_{0.13(1)}Ga_{2.60(3)}$. For clarity, the compounds will be referred to by the compositions $HoCr_{0.15}Ga_3$ and $ErCr_{0.14}Ga_3$, based on single crystal X-ray diffraction refinements, in the text.

2.2.3 Crystal Structure

The crystal structure was determined by single crystal X-ray diffraction using a Nonius Kappa CCD diffractometer with Mo Kα radiation (λ = 0.71073 Å). A suitably sized crystal for X-ray diffraction was cleaved from a single crystal and mounted on the end of a glass fiber using epoxy. Diffraction data out to 35° θ were collected at room temperature. The diffraction data were indexed to a primitive cubic cell with dimensions a ~ 4.25 Å. After integration a multi-scan absorption correction was applied. No systematic absences were observed, suggestive of the space groups $Pm\bar{3}m$, $P\bar{4}3m$, $P432$, $Pm\bar{3}$, and $P23$. Models were constructed in these potential space groups by solving with direct methods using SIR97 [86] and refined with SHELXL97 [87]. The program PLATON [88] was used to check the models for additional symmetry, and the suggested space group $Pm\bar{3}$m was selected as the best fit. The final models for each compound were corrected for extinction, and the atomic displacement parameters were modeled anisotropically. Anisotropic refinement revealed residual electron density, at the center the unit cell, of ~10 e Å^{-3}. This position was assigned as a chromium atom with a refined occupancy of ~14%, consistent with the EDS results. The refined atomic displacement parameter (ADP) of the Cr atom was approximately one third of the atomic displacement parameter of the lanthanide, so the Cr displacement parameter was constrained that of the lanthanide to avoid the unusually small value. Constraining the ADP values increased the Cr occupancy by ~1% which is still consistent with the elemental analysis data. However, attempts to refine the gallium occupancy to match that of EDS were unsuccessful, and the gallium site was modeled as fully occupied. Details of the data collection and refinement, atomic positions, and selected interatomic distances are provided in Tables 2.1-3, respectively.

2.2.4 Physical Properties

Single crystals selected for physical property measurements were first characterized by X-ray diffraction and EDS. Magnetic data were collected using a Quantum Design Physical Property Measurement System (PPMS). The temperature-dependent susceptibility data were measured under zero-field cooled (ZFC) conditions with an applied field of 0.1 T between 3 K to

275 K for $HoCr_{0.15}Ga_3$ and 2 K to 275 K for $ErCr_{0.14}Ga_3$. Field-dependent magnetization data were measured at 3 K with applied fields up to 9 T. The electrical resistivity measurements were measured on single crystals by the standard four-probe AC technique between 3 and 290 K. Magnetoresistance was collected at 3 K in applied magnetic fields up to 9 T.

Table 2.1. $LnCr_xGa_3$ (Ln = Ho, Er) Crystallographic Parameters

Compound	$HoCr_{0.15}Ga_3$	$ErCr_{0.14}Ga_3$
Refined Composition	$HoCr_{0.152(7)}Ga_3$	$HoCr_{0.136(9)}Ga_3$
Crystal System	cubic	cubic
Space Group	$Pm\bar{3}m$	$Pm\bar{3}m$
a (Å)	4.2508(10)	4.2383(10)
V ($Å^3$)	76.81(3)	76.13(3)
Z	1	1
Crystal size (mm)	0.05 x 0.05 x 0.05	0.08 x 0.08 x 0.08
θ range (°)	4.80-34.54	4.81-34.66
μ (mm^{-1})	51.67	56.671
Data Collection		
Measured Reflections	2183	2979
Independent Reflections	54	54
Reflections with I>2σ(I)	54	54
R_{int}	0.0074	0.0466
h	$-6 \leq h \leq 6$	$-6 \leq h \leq 6$
k	$-4 \leq k \leq 4$	$-4 \leq k \leq 4$
l	$-4 \leq l \leq 4$	$-6 \leq l \leq 6$
Refinement		
$R_1{}^a$	0.0113	0.0162
$wR_2{}^b$	0.0284	0.0366
Reflections	54	54
Parameters	6	6
$\Delta\rho_{max}$ (e $Å^{-3}$)	0.502	1.235
$\Delta\rho_{min}$ (e $Å^{-3}$)	-0.913	-0.85
Extinction coefficient	0.134(8)	0.131(10)
GOF	1.453	1.347

$^aR_1 = \Sigma||F_o| - |F_c||/\Sigma|F_o|$
$^bR_w = [\Sigma [w (F_o{}^2 - F_c{}^2)^2]/ \Sigma [w (F_o{}^2)^2]]^{1/2}$; $w = 1/[\sigma^2(F_o{}^2) + (0.0109\ P)^2 + 0.1558\ P]$ and $w = 1/[\sigma^2(F_o{}^2) + 0.3040\ P]$; $P = (F_o{}^2 + 2\ Fc^2)/3$ for $HoCr_{0.15}Ga_3$ and $ErCr_{0.14}Ga_3$, respectively.

Table 2.2. $LnCr_xGa_3$ (Ln = Ho, Er) Atomic Positions

Site	Wyckoff	Symmetry	x	y	z	occupancy	U_{eq} (Å^2)[a]
$HoCr_{0.15}Ga_3$							
Ho	1*a*	*m*3*m*	0	0	0	1	0.0084(2)
Cr	1*b*	*m*3*m*	0	1/2	1/2	0.152(7)	0.0084(2)[b]
Ga	3*c*	4/*mmm*	1/2	1/2	1/2	1	0.0215(3)
$ErCr_{0.14}Ga_3$							
Er	1*a*	*m*3*m*	0	0	0	1	0.0091(3)
Cr	1*b*	*m*3*m*	0	1/2	1/2	0.136(9)	0.0091(3)[b]
Ga	3*c*	4/*mmm*	1/2	1/2	1/2	1	0.0202(4)

[a]U_{eq} is defined as one-third of the trace of the orthogonalized U_{ij} tensor
[b]Cr atomic displacement parameters were constrained to the lanthanide values

Table 2.3. Selected Interatomic Distances (Å)

Compound	$HoCr_{0.15}Ga_3$	$ErCr_{0.14}Ga_3$
Ln-Ga (x12)	3.0058(7)	2.9969(7)
Ln-Cr (x8)	3.6813(10)	3.6702(10)
Ln-Ln (x6)	4.2508(10)	4.2383(10)
Cr-Ga (x6)	2.1254(5)	2.1191(5)
Ga-Ga (x8)	3.0058(7)	2.9969(7)

2.3 Results and Discussion

2.3.1 Crystal Structure

$HoCr_{0.15}Ga_3$ and $ErGa_{0.14}Ga_3$ adopt the space group $Pm\bar{3}m$ with a = 4.2508(10) Å and 4.2383(10) Å, respectively. Due to the structural similarities of the two analogues, the structural description will focus on the Ho analogue. The crystal structure of $HoCr_{0.15}Ga_3$ is shown in Figure 2.2a, and the crystal structures of ε-$HoGa_3$ ($AuCu_3$ structure-type) and Ho_4FeGa_{12} (Y_4PdGa_{12} structure-type) are shown in Figure 2.2b and Figure 2.2c for comparison. The crystal structure of $LnCr_xGa_3$ (Ln = Ho, Er) can be described as a stuffed variant of the well-known $AuCu_3$ structure-type. The lanthanide atoms occupy the corners of the unit cell and the gallium atoms occupy the centers of the faces. This portion of the structure is adopted by the binary phase $ErGa_3$ [89] and a high temperature polymorph (ε) of $HoGa_3$ [89]. In addition, Cr atoms partially occupy the center of the unit cell with refined occupancies of 15.2(7)% and 13.6(9)% for the Ho and Er analogues, respectively. This structure also shares the same atomic positions as the perovskite and inverse-perovskite structures [90].

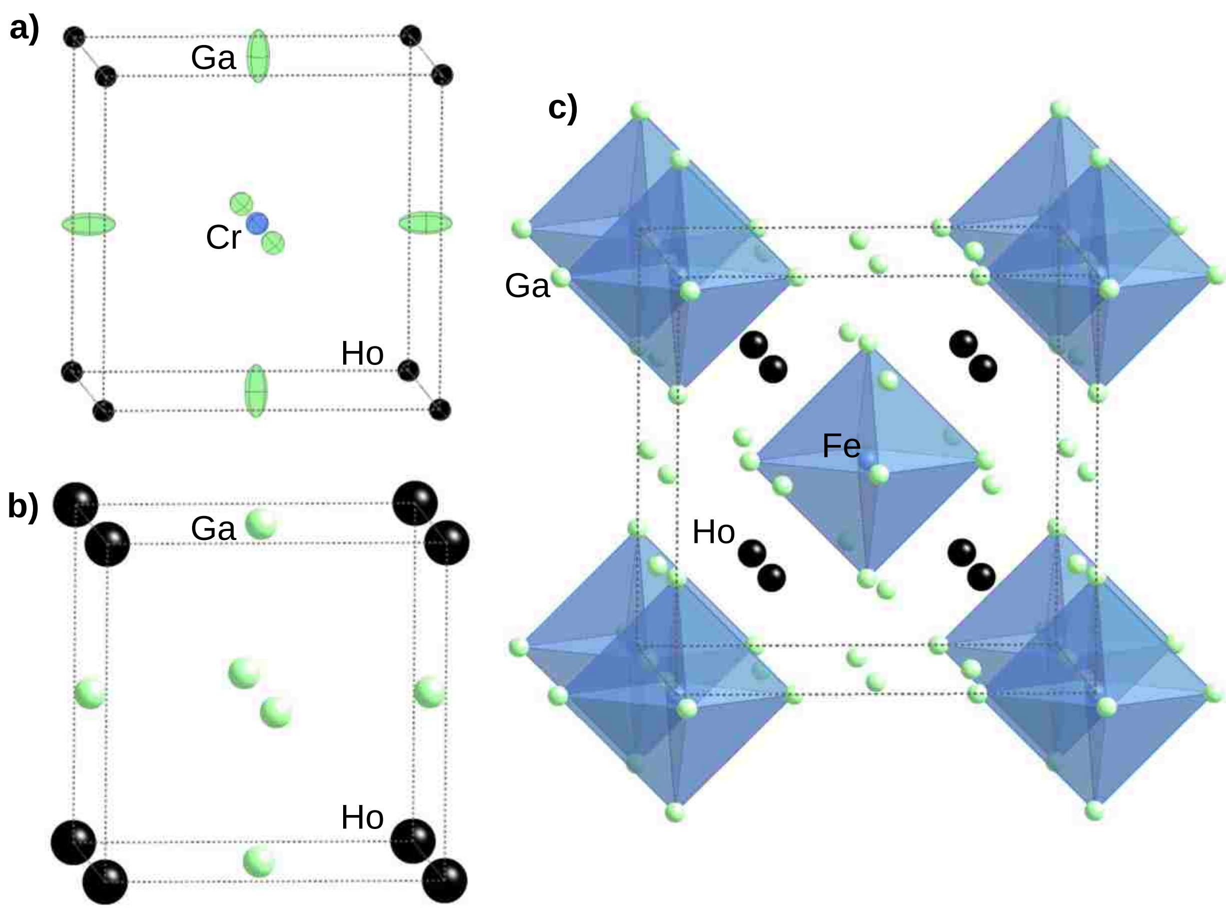

Figure 2.2. (a) The crystal structures of $HoCr_{0.15}Ga_3$ is depicted as thermal ellipsoids, where Ga is light green, Cr is blue, and Ho is black. $AuCu_3$-type $HoGa_3$ (b) and Ho_4FeGa_{12} (c) are shown for comparison. Crystallographic parameters for $HoGa_3$ and Ho_4FeGa_{12} were obtained from references [89] and [77], respectively.

As shown in Figure 2.2a, the Ga atoms have the largest ADPs of the three atoms due to elongated thermal ellipsoids, where the ratio of the long (U_{11} = 0.04776(6) Å^2) and short (U_{22} = U_{33} = 0.0084(2) Å^2) axes is ~ 5. During the refinement of the $LnCr_xGa_3$ (Ln = Ho, Er) compounds, residual electron density was observed near the position ½, ½, ~0.08 which is the expected distance for a Cr-Ga contact based on covalent radii [91]. However, attempts to refine the gallium atom as two partially occupied positions were unsuccessful, possibly due to the small electron density and the limited number of reflections. The enlongated ellipsoids can be described by the Ga atoms being pushed outward when the Cr atoms are present (~ 15%) because the Cr-Ga distances of 2.1254(5) are too short. A similar behavior was described in the Y_4PdGa_{12} structure type [80], and in $Er_4Fe_{0.67}Ga_{12}$, two gallium positions are observed; one on the face of the cube (12*e*; 0.249(4),0,0) and one at the extended position (12*e*; 0.280(4), 0,0) due to the Fe vacancies [77].

The Ho atoms are surrounded by 12 Ga atoms at 3.0058(7) Å and 8 partially occupied Cr sites at 3.6813(10) Å. Statistically, there should be approximately one Cr atom in the vicinity of each Ho atom. Ho-Ho distances are equal to the lattice parameter (4.2508(10) Å), and there are 6 nearest neighbors in an octahedral arrangement.

It is intriguing that $LnCr_xGa_3$ forms this stuffed variant of the $AuCu_3$ structure type rather than the Y_4PdGa_{12} structure type. A possible explanation is that the chromium concentration is not high enough to form the larger body centered cubic unit cell of the Y_4PdGa_{12} structure-type. This is supported by the disorder observed in $Er_4Fe_{0.67}Ga_{12}$ [77], where the Fe vacancies allow the Ga atoms to relax to where they would be found in the $ErGa_3$ subunits. The small site occupancies of Cr cannot easily be explained in terms of covalent [91] or metallic radii as the Y_4PdGa_{12} structure type can be formed for the smaller Ni [73] and the larger Ag [75]. It is possible that the ratio of the transition metal and lanthanide could play a role as an Ag analogue has only been reported for the larger Tb. A second possible explanation for the low Cr content could be based on different coordination preferences of the transition metals. This hypothesis also does not adequately explain the lower Cr occupancies because Cr atoms in Ga-rich binary phases have coordination numbers between 8 and 11, and similar coordination numbers are found in gallium-rich binary phases of Mn, Fe, Ni and Pd. One significant difference between Cr and the latter transition metals is that Cr does not form binary phases with the lanthanides [92, 93], but the latter transition metals, such as Fe, do form binary phases with the lanthanides [71]. This interaction may account for the observed differences.

2.3.2 Physical Properties

Temperature dependent magnetic susceptibility (H = 0.1 T) for $LnCr_xGa_3$ (Ln = Ho, Er) is shown in Figure 2.3, and the inset highlights the low temperature (< 30 K) susceptibility and inverse susceptibility. For $HoCr_{0.15}Ga_3$ there is a maximum and downturn in the susceptibility at 5.9 K which is indicative of antiferromagnetic ordering. As shown in the inset of Figure 3, there is a downturn in the inverse susceptibility of $HoCr_{0.15}Ga_3$ at ~7 K before the antiferromagnetic ordering at 5.9 K. This feature could potentially be ascribed to a Curie-tail due to magnetic moments on the Cr atoms or another magnetic state with a larger net magnetic moment, such as canted-antiferromagnetism, ferromagnetism, or a spin reorientation. A similar downturn in inverse susceptibility is also observed $ErCr_{0.14}Ga_3$ at ~3.5 K, but no subsequent antiferromagnetic ordering is observed down to the lowest measurement of 2 K. It is possible that the Er analogue does order antiferromagnetically below the lowest measured temperature of 2 K. $ErGa_3$ orders antiferromagnetically at 2.8 K with a number of spin reorientations as a function of temperature and field [94] but unlike $LnCr_xGa_3$, it does not have a downturn in inverse susceptibility before the ordering. The depression of T_N could be due to the expansion of the lattice, as the lattice parameter increases from 4.202 Å [94] to 4.2383(10) Å upon incorporation of Cr or possibly an electronic effect due to the additional electrons from Cr. In the structurally related Er_4MGa_{12} (M = Fe, Pd, Pt) compounds, antiferromagnetic order is observed below 6 K [77, 81]. Ho_4FeGa_{12} and Ho_4PtGa_{12} also order antiferromagnetically at 9 and 3.6 K, respectively, while Ho_4PdGa_{12} remains paramagnetic down to 2 K [77, 81].

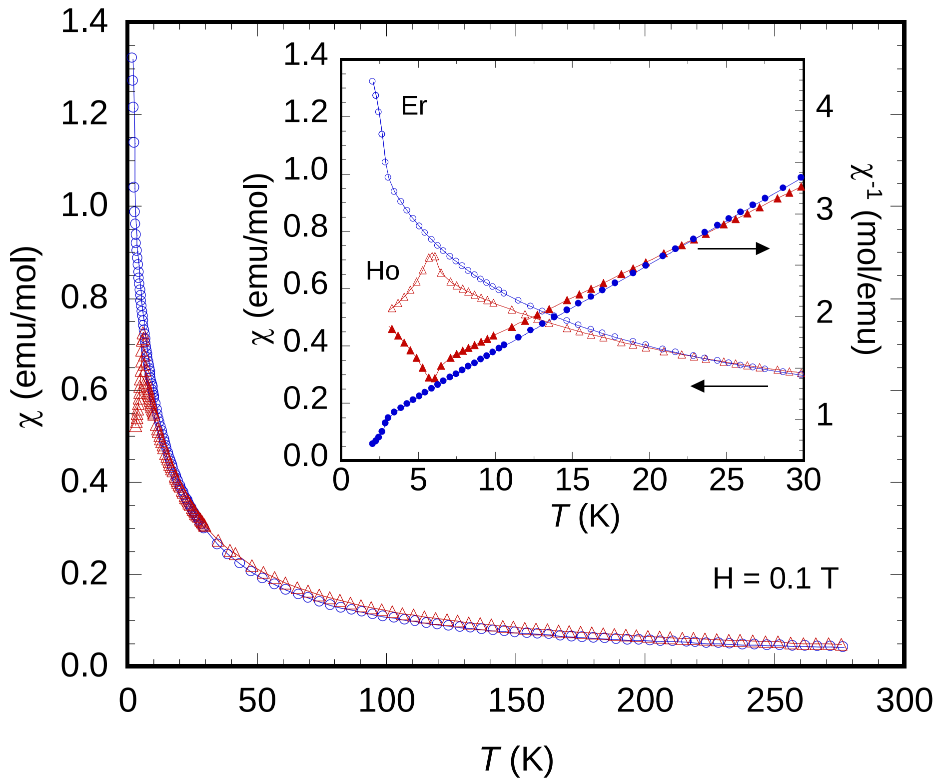

Figure 2.3. Temperature dependent magnetic susceptibility data for $HoCr_{0.15}Ga_3$ and $ErCr_{0.14}Ga_3$, are depicted as blue circles and red triangles, respectively. The inset shows the low temperature features of magnetic susceptibility (χ) and inverse magnetic susceptibility (χ^{-1}) for $HoCr_{0.15}Ga_3$ and $ErCr_{0.14}Ga_3$.

Both analogues show Curie-Weiss behavior above the low temperature anomalies. Magnetic susceptibility data were fit to a modified Curie-Weiss equation, $\chi = \chi_0 + (C/(T-\theta))$, where C is the Curie constant, χ_0 is a temperature independent contribution due to Pauli-paramagnetism/diamagnetism, and θ is the Weiss temperature. The parameters from the Curie-Weiss fits are provided in Table 2.4. Weiss constants for $HoCr_{0.15}Ga_3$ (-16.6(5) K) and $ErCr_{0.14}Ga_3$ (-8.6(2) K) are indicative of antiferromagnetic interactions. The magnetic moments

(μ_{eff}) from the fits are 10.61(8) and 9.63(4) μ_B/mol for $HoCr_{0.15}Ga_3$ and $ErCr_{0.14}Ga_3$, respectively, and are in excellent agreement with the expected moments for Ho^{3+} (10.61 μ_B/mol) and Er^{3+} (9.58 μ_B/mol). However, a magnetic moment due to Cr, on the order of the experimental error, cannot be fully ruled out. For comparison, in $YbCrSb_3$ the Cr atoms are magnetic and order ferromagnetically at ~280 K with magnetic moment of ~0.08 μ_B/mol [95], however $YbCr_4Al_{43}$ has been shown to be a temperature independent paramagnet consistent with a non-magnetic Yb and Cr. A Y analogue could aid in the determination if Cr is magnetic, however attempts to synthesize a Y analogue were unsuccessful.

Table 2.4. Magnetic Properties

Compound	Field (T)	Fit Range (K)	χ_0 (emu/mol)	μ_{calc} (μ_B/mol)	μ_{eff} (μ_B/mol)	θ (K)	T_N (K)
$HoCr_{0.15}Ga_3$	0.1	>50	0.0008(4)	10.61	10.61(8)	-16.6(5)	5.9
$ErCr_{0.14}Ga_3$	0.1	>50	0.0004(2)	9.58	9.63(4)	-8.6(2)	-

Field dependent magnetization data for $HoCr_{0.15}Ga_3$ and $ErCr_{0.14}Ga_3$ at 3 K and in applied fields up to 9 T are provided in Figure 2.4, and the derivative of magnetization with field is provided as the inset of Figure 2.4. The magnetization of $ErCr_{0.14}Ga_3$ increases with applied field as expected for a paramagnet and shows no hysteresis (decreasing field data not shown). At 9 T the magnetization is not fully saturated and is ~6.6 μ_B/mol, approximately 3/4 of the expected saturation magnetic moment for Er^{3+} (9 μ_B/mol). At 9 T the magnetization of $HoCr_{0.15}Ga_3$ (~7.1 μ_B/mol) is a similar fraction of the 10 μ_B/mol expected for Ho^{3+}. The magnetization of the Ho analogue also shows no hysteresis and at low fields is linear with applied field, as expected for an antiferromagnet. However, there are a number of anomalies at higher fields as shown in the inset of Figure 2.4. The magnetic phase diagram of the structurally related $AuCu_3$-type $ErGa_3$ indicates a number of spin reorientations below ~3 K and ~3 T [96], and similar phenomena could be exhibited in the present material. However, the anomalies seen in $HoCr_{0.14}Ga_3$ appear at fields up to ~6 T which larger than and the field dependent magnetization of $ErGa_3$ at 1.7 K appears to be linear up to 2 T where it begins to saturate [97]. More extensive measurements such as neutron diffraction would be required to determine the cause of the magnetic anomalies.

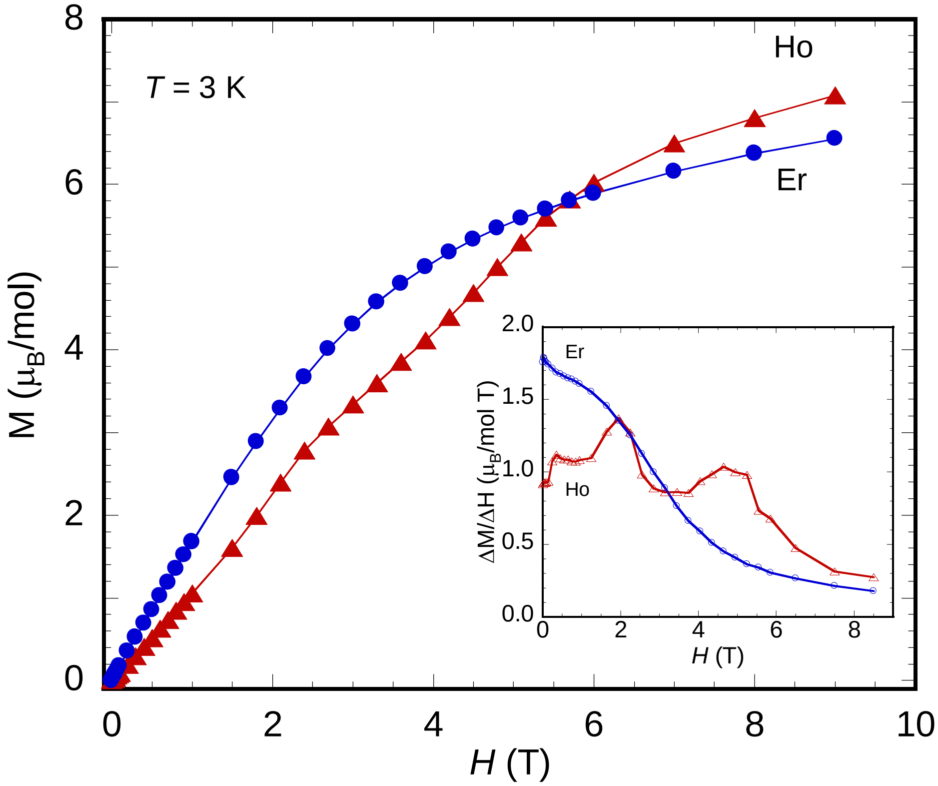

Figure 2.4. Field dependent magnetization data at 3 K for $HoCr_{0.15}Ga_3$ and $ErCr_{0.14}Ga_3$ are depicted as blue circles and red triangles, respectively. The inset shows the derivative of magnetization with applied field for $HoCr_{0.15}Ga_3$ and $ErCr_{0.14}Ga_3$.

2.3.3 Electrical Properties

Temperature dependent resistivity data for $ErCr_{0.14}Ga_3$ and $HoCr_{0.15}Ga_3$ are shown in Figure 2.5. For both analogues, the resistivity increases with temperature indicative of metallic behavior. $HoCr_{0.14}Ga_3$ shows a downturn at ~7 K which can be attributed to a decrease in spin disorder scattering due to magnetic ordering. However, this feature is lacking in $ErCr_{0.12}Ga_3$. Above the feature at ~7 K (10-40 K), the resistivity of $HoCr_{0.15}Ga_3$ follows a T^2 dependence indicative of Fermi liquid behavior. $ErCr_{0.14}Ga_3$, however, does not obey a T^2 dependence.

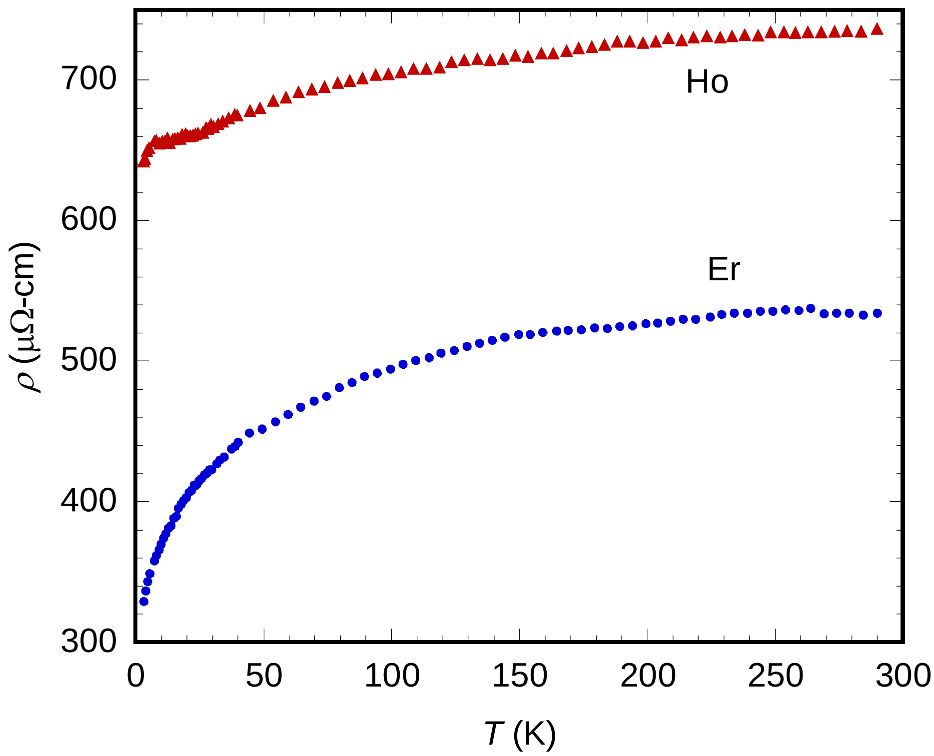

Figure 2.5. Temperature dependent resistivity data for single crystals of $HoCr_{0.15}Ga_3$ and $ErCr_{0.14}Ga_3$ are depicted as blue circles and red triangles, respectively.

Field dependent magnetoresistance (MR% = $(\rho_H-\rho_0)/\rho_0$ x 100) data measured at 3 K is shown in Figure 2.6. The magnetoresistance of $ErCr_{0.14}Ga_3$ reaches ~25% at 9 T while the magnetoresistance of $HoCr_{0.15}Ga_3$ saturates near 6%. Large positive magnetoresistance was also observed in the related Ln_4MGa_{12} (Ln = Dy-Er; M = Pd, Pt) compounds [81]. Dy_4PdGa_{12} had the highest MR of the palladium analogues at 45% (3 K, 9 T) while the other palladium analogues had MR values of ~10%. For the platinum analogues the MR values at 9 T were much larger at 50%, 220%, and 900% for Dy_4MGa_{12}, Er_4MGa_{12}, and Ho_4MGa_{12}, respectively. In the Ln_4MGa_{12} (Ln = Dy-Er; M = Pd, Pt) compounds the increase in magnetoresistance was attributed to spin fluctuations in the antiferromagnetic state or field dependent changes to the Fermi surface [81]. A similar explanation may be the cause of the large magnetoresistance in the present compounds.

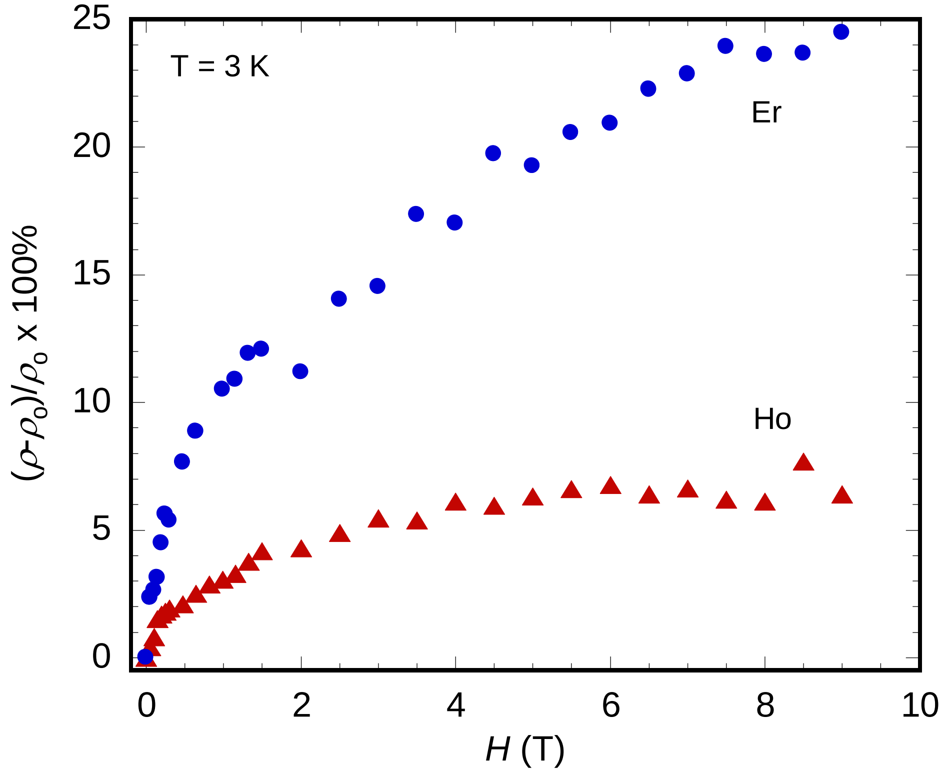

Figure 2.6. Field dependent magnetoresistance data for $ErCr_{0.12}Ga_3$ and $HoCr_{0.14}Ga_3$ at 3 K and in fields up to 9 T are depicted as blue circles and red triangles, respectively.

2.4 Conclusion

Single crystals of $LnCr_xGa_3$ (Ln = Ho, Er; x ~0.15) were grown with a molten gallium flux. The crystal structure of $LnCr_xGa_3$ (Ln = Ho, Er) consists of a stuffed variant of the $AuCu_3$ structure type, where the Cr atoms partially (~15%) occupy the center of the cell. Unlike the latter transition metals, the Y_4PdGa_{12} structure does not form for the chromium analogues. Both analogues exhibit metallic resistivity and positive magnetoresistance. The magnetic moments of both analogues fit well with the expected moments for the trivalent lanthanides suggesting that the Cr atoms are nonmagnetic. Weiss constants for both analogues are negative, indicative of antiferromagnetic correlations and $HoCr_{0.15}Ga_3$ exhibits antiferromagnetic order at ~ 5.9 K.

Further study could be required to understand the structural stability and magnetism of these compounds.

2.5 References

[70] F. Wang, G.J. Miller, Revisiting the Zintl–Klemm concept: alkali metal trielides, Inorg. Chem., 50 (2011) 7625-7636.

[71] F.S. Liu, Y.J. Yu, W.H. Zhang, J.Q. Li, W.Q. Ao, Isothermal section of the Ho-Fe-Ga ternary system at 773 K, J. Alloys Comp., 509 (2011) 1854-1860.

[72] V.Y. Markiv, T.I. Zhunkovskaya, N.N. Belyavina, A.A. Lysenko, Ternary phase diagrams of the systems Y - (Ti, Cr, Zr, Hf) - Ga, Dopov. Akad. Nauk. A, 45 (1983) 84-87.

[73] L.O. Vasilenko, A.S. Noga, Y.N. Grin, M.D. Koterlin, Y.P. Yarmolyuk, Crystal structure and some magnetic properties of R_4MGa_{12} compounds, Russ. Metall., (1988) 216-220.

[74] M.A. Zhuravleva, X. Wang, A.J. Schultz, T. Bakas, M.G. Kanatzidis, Isolation of the new cubic phases $RE_4FeGa_{12-x}Ge_x$ (RE = Sm, Tb; x = 2.5) from molten gallium: Single-crystal neutron diffraction study of the Ga/Ge distribution, Inorg. Chem., 41 (2002) 6056-6061.

[75] R.V. Gumeniuk, B.M. Stel'makhovych, Y.B. Kuz'ma, The Tb-Ag-Ga system, J. Alloys Comp., 352 (2003) 128-133.

[76] W.M. Williams, M. Moldovan, D.P. Young, J.Y. Chan, Synthesis, structure, and magnetism of Tb_4PdGa_{12} and Tb_4PtGa_{12}, J. Solid State Chem., 178 (2005) 52-57.

[77] B.L. Drake, F. Grandjean, M.J. Kangas, E.K. Okudzeto, A.B. Karki, M.T. Sougrati, D.P. Young, G.J. Long, J.Y. Chan, Crystal growth, transport, and the structural and magnetic properties of Ln_4FeGa_{12} with Ln = Y, Tb, Dy, Ho, and Er, Inorg. Chem., 49 (2009) 445-456.

[78] M.C. Francisco, C.D. Malliakas, P.M.B. Piccoli, M.J. Gutmann, A.J. Schultz, M.G. Kanatzidis, Development and loss of ferromagnetism controlled by the interplay of Ge concentration and Mn vacancies in structurally modulated $Y_4Mn_{1-x}Ga_{12-y}Ge_y$, J. Am. Chem. Soc., 132 (2010) 8998-9006.

[79] R. Jardin, E. Colineau, F. Wastin, J. Rebizant, J.P. Sanchez, New heavy-fermion compounds An_4PdGa_{12} (An=U, Np, Pu), Physica B, 378-380 (2006) 1031-1032.

[80] R. Jardin, E. Colineau, J.C. Griveau, P. Boulet, F. Wastin, J. Rebizant, A new family of heavy-fermion compounds: U_4TGa_{12} (T = Fe, Co, Rh and Pd), J. Alloys Comp., 432 (2007) 39-44.

[81] J.Y. Cho, et al., Crystal growth and magnetic properties of Ln_4MGa_{12} (Ln = Dy–Er; M = Pd, Pt), J. Phys.:Condens. Matter, 19 (2007) 266224.

[82] Z. Fisk, J.P. Remeika, Chapter 81 Growth of single crystals from molten metal fluxes, in: Karl A. Gschneidner, Jr., E. LeRoy (Eds.) Handbook on the Physics and Chemistry of Rare Earths, Elsevier, 1989, pp. 53-70.

[83] M.G. Kanatzidis, R. Pöttgen, Wolfgang Jeitschko, The metal flux: A preparative tool for the exploration of intermetallic compounds, Angew. Chem. Int. Ed., 44 (2005) 6996-7023.

[84] W.A. Phelan, M.C. Menard, M.J. Kangas, G.T. McCandless, B.L. Drake, J.Y. Chan, Adventures in crystal growth: synthesis and characterization of single crystals of complex intermetallic compounds, Chem. Mater., 24 (2012) 409-420.

[85] U. Häussermann, P. Viklund, M. Boström, R. Norrestam, S.I. Simak, Bonding and physical properties of Hume-Rothery compounds with the $PtHg_4$ structure, Phys. Rev. B, 63 (2001) 125118.

[86] A. Altomare, M.C. Burla, M. Camalli, G.L. Cascarano, C. Giacovazzo, A. Guagliardi, A.G.G. Moliterni, G. Polidori, R. Spagna, SIR97: a new tool for crystal structure determination and refinement, J. Appl. Crystallogr., 32 (1999) 115-119.

[87] G. Sheldrick, A short history of SHELX, Acta Crystallogr. A, 64 (2008) 112-122.

[88] A. Spek, Single-crystal structure validation with the program PLATON, J. Appl. Crystallogr., 36 (2003) 7-13.

[89] S. Cirafici, E. Franceschi, Stacking of close-packed AB_3 layers in RGa_3 compounds (R = heavy rare earth), J. Less-Common Met., 77 (1981) 269-280.

[90] M. Magnuson, M. Mattesini, C. Höglund, I.A. Abrikosov, J. Birch, L. Hultman, Electronic structure investigation of the cubic inverse perovskite Sc_3AlN, Phys. Rev. B, 78 (2008) 235102.

[91] B. Cordero, V. Gomez, A.E. Platero-Prats, M. Reves, J. Echeverria, E. Cremades, F. Barragan, S. Alvarez, Covalent radii revisited, Dalton Trans., (2008) 2832-2838.

[92] S. Ray, J.P. Neuman, Calculation of the binary chromium-lanthanide phase diagrams, J. Phase Equilib., 17 (1996) 179-185.

[93] M. Ling, Y. Liang, S. Wei, Y. Liu, M. Pang, Y. Zhan, Y. Du, Experimental investigation of the Al-Cr-Gd ternary system at 773 K, J. Phase Equilib. Diffus., 33 (2012) 203-209.

[94] P. Morin, M. Giraud, P.L. Regnault, E. Roudaut, A. Czopnik, Crystalline electric field and magnetic structure of RGa_3 compounds within the $AuCu_3$-type structure, J. Magn. Magn. Mater., 66 (1987) 345-350.

[95] S.J. Crerar, L. Deakin, A. Mar, Structure and physical properties of ternary antimonide $YbCrSb_3$, Chem. Mater., 17 (2005) 2780-2784.

[96] A. Murasik, A. Czopnik, L. Keller, P. Fischer, Spin rotation in $ErGa_3$, J. Magn. Magn. Mater., 213 (2000) 101-110.

[97] V.B. Pluzhnikov, A. Czopnik, O. Eriksson, G.E. Grechnev, Y.V. Fomenko, Effect of pressure on the Fermi surface and electronic structure of $ErGa_3$, Low Temperature Physics, 25 (1999) 670-676.

Chapter 3. Structure and Physical Properties of Single Crystal $PrCr_2Al_{20}$ and CeM_2Al_{20} (M = V, Cr): A Comparison of Compounds Adopting the $CeCr_2Al_{20}$ Structure Type*

3.1 Introduction

The study of rare earth intermetallics with competing interactions between electrons has led to the discovery of highly correlated states with interesting magnetic and electrical properties such as superconductivity, heavy fermion behavior [98-100], Kondo behavior [101, 102], valence instability [103], and quantum critical systems, such as β-$YbAlB_4$, which exhibits quantum critical behavior without doping or the application of pressure or a magnetic field [104, 105]. The Kondo effect, often seen in rare earth intermetallic compounds containing Ce and U, is caused by a coupling of localized electron moments with conduction electrons resulting in an enhancement of the electronic effective mass. The Kondo and long range Ruderman-Kittel-Kasuya-Yoshida (RKKY) effects are competing interactions present in materials with localized magnetic moments. Ce- and Yb-based intermetallics have attracted much interest in the last decade because of the interest in competition between magnetic interactions [106], such as the RKKY and Kondo competition in the structurally related $CePdGa_6$ and Ce_2PdGa_{12} systems [107]. Although the Kondo effect is due to coupling of magnetic ions with conduction electrons, the realization of a related effect, the quadrupolar Kondo effect, in the nonmagnetic ground state of $4f^2$ and $5f^2$ systems is a subject of interest in condensed matter. Based on the theoretical work of Cox [108], the electric quadrupole moment in the ground state can couple with conduction electrons in compounds with a cubic site symmetry. To reveal the quadrupolar Kondo effect, we have chosen to study compounds of the $CeCr_2Al_{20}$ structure-type to

* Originally appeared as M.J. Kangas, D.C. Schmitt, A. Sakai, S. Nakatsuji, J.Y. Chan, Structure and physical properties of single crystal $PrCr_2Al_{20}$ and CeM_2Al_{20} (M = V, Cr): A comparison of compounds adopting the $CeCr_2Al_{20}$ structure type, J. Solid State Chem. http://dx.doi.org/10.1016/j.jssc.2012.06.035.

systematically evaluate hybridization strength. It is expected that magnetic ordering temperatures in the RKKY systems and quadrupolar ordering are suppressed by increasing conduction–*f*-electron hybridization strength.

$CeCr_2Al_{20}$ is a robust structure-type that features interpenetrating networks of the lanthanide and transition metal [109]. The family of UM_2Zn_{20} and LnM_2Zn_{20} compounds (Ln = lanthanides, M = Fe, Ru, Os, Co, Ir, Rh, and Ni) has been recently been studied [110-117]. UIr_2Zn_{20} is a heavy fermion ferromagnet with T_c = 2.1 K and γ ~ 450 mJ/K^2-mol [111]. In addition, many Yb analogues (Fe, Ru, Rh, Os, and Ir) have been shown to be heavy fermion compounds with γ > 500 mJ/K^2-mol, while $YbCo_2Zn_{20}$ displays a higher Sommerfeld coefficient (γ ~ 7,400 mJ/K^2-mol) [112]. Recently, the effective mass of the electron of $YbCo_2Zn_{20}$ was determined to be 100-500 m_e by the de Haas-van Alphen effect [115]. The rare earth magnetic ordering temperature and ordering state in several GdM_2Zn_{20} analogues have been found to depend on the transition metal. GdM_2Zn_{20} orders ferromagnetically at 86, 20, and 4.2 K when the transition metal is Fe, Ru, and Os, respectively, while antiferromagnetic ordering near 8 K is observed in the Co triad [113]. The magnetic ordering of Tb compounds also depends heavily on the transition metal. $TbCo_2Zn_{20}$ orders antiferromagnetically at 2.5 K, while $TbFe_2Zn_{20}$ orders ferromagnetically at ~ 60 K and is very sensitive to disorder on the Fe site [114]. Additionally, doping Al onto the Zn2 site of $GdFe_2(Al_xZn_{1-x})_{20}$ decreases the Curie temperature from 86 K to 10 K (for x = 0.122) by decreasing the number of electrons at the Fermi level [116].

Aluminides of the $CeCr_2Al_{20}$ structure-type have previously been reported, including UCr_2Al_{20} [118], LnM_2Al_{20} (Ln = La-Nd, and Sm-Yb; M = Ti, V, Cr, Nb, Ta, Mo, and W) [119, 120]. However, the physical properties of these materials have been less extensively studied compared to the zinc analogues. CeM_2Al_{20} (M = Ti, V, Cr, Mo) display display weak temperature independent paramagnetism resulting from a tetravalent Ce, while Eu analogues are found to be nearly divalent. Lattice parameters of the Ce and Eu analogues have been shown to deviate from the expected lanthanide contraction trends, complementing the magnetic data [120, 121]. In addition $YbCr_2Al_{20}$ has been reported in a phase diagram but not characterized [122].

The Kondo effect has also been observed in a few Pr- and Sm-based intermetallic compounds, such as $Pr(Cu,Ga)_{13-x}$ [123] and $SmPt_4Ge_{12}$ [124] leading to heavy electron states with γ ~100 mJ/K^2-mol and γ ~450 mJ/K^2-mol, respectively. Although 4*f* electrons in Pr-based compounds are generally well localized, hybridization effects, especially between 4*f*-quadrupoles and conduction electrons, the nature of competing effects are still not well understood. Recently, the first example of a cubic Γ_3 nonmagnetic ground doublet system, demonstrated by resistivity and resonant photoemission spectroscopy measurements, has been shown to exhibit the Kondo effect [125, 126]. The crystal electric field ground state of $PrTi_2Al_{20}$ and PrV_2Al_{20} was determined as a non-magnetic Γ_3 doublet, which does not have a dipole degree of freedom. Therefore, the observed phase transitions at 2.0 K ($PrTi_2Al_{20}$) and 0.6 K (PrV_2Al_{20}) are attributed to quadrupolar orderings [125, 127-129]. An enhancement of the *f*-electron hybridization, manifested as the Kondo effect, is found in the vanadium analogue due to a combination of the compression of the unit cell volume and additional 3*d* electrons in the conduction band, leading to a possible quadrupolar Kondo effect in PrV_2Al_{20} [125]. SmM_2Al_{20} (M = Ti, V, Cr) exhibits Sm valence fluctuations concomitant with the Kondo effect, and the *f*-electron hybridization increases from Ti–Cr due the additional 3*d* conduction electrons and the smaller unit cell volume [130]. Herein we report resistivity, magnetic susceptibility, and heat capacity of flux grown single crystals of $CeTi_2Al_{20}$, CeV_2Al_{20}, $LnCr_2Al_{20}$ (Ln = Ce, Pr, and Yb), and compare to previously reported SmM_2Al_{20} (M = Ti, V, and Cr) [130] and PrM_2Al_{20} (M = Ti and V) [125, 126, 128, 129]. Additionally we present the full structural determination of $LnTi_2Al_{20}$ (Ln = La–Pr, Sm, and Yb), LnV_2Al_{20} (Ln = La–Pr, and Sm), and $LnCr_2Al_{20}$ (Ln = La–Pr, Sm, and Yb).

3.2 Experimental

3.2.1 Synthesis

Samples were prepared via the flux growth method [106, 131]. The elements Ln (99.99%), M (99.9%), and Al (99.999%) in the atomic ratio of 1:2:45 were placed in alumina crucibles, sealed in evacuated silica tubes, and slowly cooled from 1423 K to 1023 K over 80 hours. Excess Al was removed by centrifugation at the final temperature. $YbCr_2Al_{20}$ was grown under similar conditions except the dwell temperature was lowered to 1273 K to limit the vapor pressure of Yb. $LnTi_2Al_{20}$ series were also grown by the reaction ratio of 1:2:90 and cooled from 1423 K to 1173 K to reduce the $TiAl_3$ impurity phase. The modified conditions produce large crystals but the residual resistivity ratios (RRR) are lower, so both methods were used as the situation required.

3.2.2 Physical Properties

The electrical resistivity and specific heat above 0.4 K were measured by the standard four-probe dc method and a thermal relaxation method, respectively (PPMS, Quantum Design Co.). The dc magnetic susceptibility from 2 K to 350 K was measured by a commercial superconducting quantum interference device (SQUID) magnetometer (MPMS, Quantum Design Co.).

3.2.3 Structure Determination

Single crystal X-ray diffraction was used to determine crystal structure with a Nonius Kappa CCD X-ray diffractometer with graphite monochromatized Mo K_{α} radiation (λ = 0.71073 Å). Crystals were cut to suitable sizes (provided in Table 3.1) and mounted on glass fibers with epoxy for data collection. Data were collected at room temperature with a crystal to detector distance of 30 mm. Multi-scan absorption corrections were applied during the scaling process for all analogues. Direct methods were used to solve the crystal structures using SIR97 [132] or SIR2002 [133], and refinement was accomplished in SHELXL97 [134]. Details of the data collection and refinement, as well as atomic positions, are provided in Tables 3.1 and 3.2. All final models were corrected for extinction, and atomic displacement parameters were modeled anisotropically. Modeling partial or mixed occupancy of the Ln (8*a*), M (16*d*), and Al3 (16*c*) sites resulted in statistically insignificant deviations from fully occupied models with the exception of PrV_2Al_{20}. For PrV_2Al_{20}, the Pr 8*a* site occupancy was refined and found to be 89(1) %, in good agreement with EDXS elemental analysis data. The importance of these findings, as related to the crystal quality of the samples, is discussed in the physical properties section.

3.2.4 Elemental Analysis

Elemental analysis was performed via energy dispersive X-ray spectroscopy (EDS) using a JEOL JSM-5600 scanning electron microscope with an accelerating voltage of 15 kV. An average of at least four crystals per stoichiometric determination was used for our elemental analysis determination with a minimum of ten data points per crystal. The composition normalized to M = 2 for PrM_2Al_{20} (M = Ti and V) analogues are provided in Table 3.3.

3.3 Results and Discussion

3.3.1 Structure

Figure 3.1a shows the crystal structure of SmV_2Al_{20}. Compounds adopting the $CeCr_2Al_{20}$ structure-type [109] are of particular interest because of the interpenetrating rare earth and transition metal sublattices. The rare earth atom is 16-coordinate (depicted as orange in Figure 3.1a) and is surrounded by 12 Al1 and 4 Al3 atoms, and the transition metal is surrounded by 12

Table 3.1a. Crystallographic Parameters for $LnTi_2Al_{20}$ (Ln = La–Pr, Sm, and Yb)

Formula	$LaTi_2Al_{20}$	$CeTi_2Al_{20}$	$PrTi_2Al_{20}$	$SmTi_2Al_{20}$	$YbTi_2Al_{20}$
Crystal System	Cubic	Cubic	Cubic	Cubic	Cubic
Space Group	$Fd\bar{3}m$	$Fd\bar{3}m$	$Fd\bar{3}m$	$Fd\bar{3}m$	$Fd\bar{3}m$
a (Å)	14.7713(15)	14.710(2)	14.725(2)	14.705(3)	14.6890(18)
V (Å^3)	3223.0(6)	3183.0(8)	3192.8(8)	3179.8(11)	3169.4(7)
Z	8	8	8	8	8
Dimensions (mm^3)	0.05 x 0.05 x 0.08	0.08 x 0.08 x 0.08	0.05 x 0.05 x 0.05	0.05 x 0.08 x 0.08	0.08 x 0.08 x 0.08
Temperature (K)	298(2)	298(2)	298.0(5)	298(2)	298(2)
θ range (°)	2.39 – 30	3.92 - 29.52	3.91 - 29.95	3.92 - 30	3.92 - 29.1
μ (mm^{-1})	4.642	4.876	5.061	5.711	7.926
Data Collection					
Measured Reflections	779	742	792	706	688
Unique Reflections	264	249	260	261	241
Reflections (I>2σ)	238	229	240	224	222
R_{int}	0.0297	0.036	0.0282	0.0467	0.0477
h	$-20 \le h \le 20$	$-20 \le h \le 20$	$-20 \le h \le 20$	$-20 \le h \le 20$	$-19 \le h \le 20$
k	$-14 \le k \le 14$	$-14 \le k \le 14$	$-14 \le k \le 14$	$-14 \le k \le 14$	$-14 \le k \le 14$
l	$-13 \le l \le 13$	$-13 \le l \le 13$	$-13 \le l \le 13$	$-13 \le l \le 13$	$-13 \le l \le 13$
Refinement					
$\Delta_\rho$max / $\Delta_\rho$min (eÅ^{-3})	1.41 / -0.833	1.104 / -0.572	0.806 / -0.52	0.965 / -0.884	1.032 / -1.662
GoF	1.066	1.134	1.102	1.093	1.19
Extinction coefficient	0.00051(6)	0.00050(10)	0.00029(5)	0.00030(4)	0.0041(3)
Reflections/Parameters	264 / 17	249 / 17	260 / 17	261 / 17	241 / 17
R_1 ($F^2 > 2\sigma F^2$) [a]	0.0226	0.0285	0.0224	0.0278	0.028
wR_2 (F^2) [b]	0.0403	0.0702	0.0444	0.0436	0.0623

[a] $R_1\ \sum[|Fo| - |F_c|]/\sum|F_o|$.

[b] $wR_2 = [\sum[w(F - F^2_c)]/\sum[w(F^2_o)^2]]^{1/2}$.

Table 3.1b. Crystallographic Parameters for LnV_2Al_{20} (Ln = La–Pr, and Sm)

Formula	LaV_2Al_{20}	CeV_2Al_{20}	PrV_2Al_{20}	SmV_2Al_{20}
Crystal System	Cubic	Cubic	Cubic	Cubic
Space Group	$Fd\overline{3}m$	$Fd\overline{3}m$	$Fd\overline{3}m$	$Fd\overline{3}m$
a (Å)	14.623(5)	14.5580(18)	14.567(3)	14.5500(18)
V ($Å^3$)	3126.9(19)	3085.4(7)	3091.1(11)	3080.3(7)
Z	8	8	8	8
Dimensions (mm^3)	0.05 x 0.05 x 0.08	0.05 x 0.05 x 0.05	0.05 x 0.05 x 0.08	0.08 x 0.08 x 0.08
Temperature (K)	298(2)	298(2)	298(2)	298(2)
θ range (°)	2.41 - 29.87	2.42 - 30.02	2.42 - 30	3.96 - 30
μ (mm^{-1})	4.958	5.207	5.404	6.072
Data Collection				
Measured Reflections	654	779	743	766
Unique Reflections	252	256	257	254
Reflections (I>2σ)	234	242	237	243
R_{int}	0.0238	0.0189	0.0221	0.0192
h	$-20 \leq h \leq 20$	$-20 \leq h \leq 20$	$-20 \leq h \leq 20$	$-20 \leq h \leq 20$
k	$-14 \leq k \leq 14$	$-14 \leq k \leq 14$	$-14 \leq k \leq 14$	$-14 \leq k \leq 14$
l	$-13 \leq l \leq 13$	$-13 \leq l \leq 13$	$-13 \leq l \leq 13$	$-13 \leq l \leq 13$
Refinement				
$\Delta_\rho max / \Delta_\rho min$ ($eÅ^{-3}$)	0.311 / -0.325	0.474 / -0.574	0.402 / -0.473	0.516 / -0.832
GoF	0.98	1.173	1.132	1.179
Extinction coefficient	0.00033(5)	0.00042(5)	0.00019(4)	0.00061(5)
Reflections/Parameters	252 / 17	256 / 17	257 / 18	254 / 17
R_1 ($F^2 > 2\ \sigma F^2$) [a]	0.0174	0.0174	0.0164	0.0175
wR_2 (F^2) [b]	0.0358	0.035	0.0317	0.0399

[a] $R_1\ \sum[|Fo| - |F_c|]/\sum|F_o|$.
[b] $wR_2 = [\sum[w(F - F^2_c)]/\sum[w(F^2_o)^2]]^{1/2}$.

Table 3.1c. Crystallographic Parameters for $LnCr_2Al_{20}$ (Ln = La–Pr, Sm, and Yb)

Formula	$LaCr_2Al_{20}$	$CeCr_2Al_{20}$	$PrCr_2Al_{20}$	$SmCr_2Al_{20}$	$YbCr_2Al_{20}$
Crystal System	Cubic	Cubic	Cubic	Cubic	Cubic
Space Group	$Fd\bar{3}m$	$Fd\bar{3}m$	$Fd\bar{3}m$	$Fd\bar{3}m$	$Fd\bar{3}m$
a (Å)	14.550(2)	14.491(3)	14.512(3)	14.484(2)	14.473(13)
V (Å^3)	3080.3(7)	3043.0(9)	3056.2(11)	3038.5(7)	3032(5)
Z	8	8	8	8	8
Dimensions (mm^3)	0.05 x 0.08 x 0.08	0.08 x 0.08 x 0.08	0.05 x 0.08 x 0.1	0.05 x 0.05 x 0.05	0.03 x 0.03 x 0.03
Temperature (K)	298(2)	298(2)	298(2)	298(2)	298(2)
θ range (°)	2.42 – 30	2.43 - 30.01	2.43 - 27.48	2.44 - 30.03	2.44 - 29.85
μ (mm^{-1})	5.231	5.479	5.665	6.356	8.666
Data Collection					
Measured Reflections	728	716	542	685	701
Unique Reflections	255	250	200	250	248
Reflections (I>2σ)	242	236	188	236	224
R_{int}	0.0243	0.0206	0.0341	0.0237	0.0409
h	$-20 \leq h \leq 20$	$-20 \leq h \leq 20$	$-18 \leq h \leq 18$	$-20 \leq h \leq 20$	$-20 \leq h \leq 20$
k	$-14 \leq k \leq 14$	$-14 \leq k \leq 14$	$-13 \leq k \leq 13$	$-14 \leq k \leq 14$	$-14 \leq k \leq 14$
l	$-13 \leq l \leq 13$	$-13 \leq l \leq 13$	$-12 \leq l \leq 12$	$-13 \leq l \leq 13$	$-13 \leq l \leq 13$
Refinement					
$\Delta_\rho max / \Delta_\rho min$ (eÅ^{-3})	0.447 / -0.729	0.39 / -0.427	0.929 / -0.653	0.492 / -0.691	0.830 / -1.248
GoF	1.085	1.137	1.138	1.07	1.363
Extinction coefficient	0.00041(5)	0.00051(4)	0.00019(7)	0.00035(4)	0.00011(4)
Reflections/Parameters	255 / 17	250 / 17	200 / 17	250 / 17	248 / 17
R_1 ($F^2 > 2\sigma F^2$) [a]	0.0182	0.0162	0.0242	0.0175	0.0299
wR_2 (F^2) [b]	0.0376	0.0302	0.0542	0.0331	0.0501

[a] $R_1 \sum[|F_o| - |F_c|]/\sum|F_o|$.
[b] $wR_2 = [\sum[w(F - F^2_c)]/\sum[w(F^2_o)^2]]^{1/2}$.

Table 3.2a. Crystallographic Parameters for $LnTi_2Al_{20}$ (Ln = La–Pr, Sm, and Yb)

Atom	Site	x	y	z	U_{eq} (Å^2) [a]
$LaTi_2Al_{20}$					
La	8*a*	1/8	1/8	1/8	0.01076(18)
Ti	16*d*	1/2	1/2	1/2	0.0081(2)
Al1	96*g*	0.48707(7)	1/8	1/8	0.0116(3)
Al2	48*f*	0.05912(3)	0.05912(3)	0.32562(5)	0.0141(2)
Al3	16*c*	0	0	0	0.0246(5)
$CeTi_2Al_{20}$					
Ce	8*a*	1/8	1/8	1/8	0.0109(3)
Ti	16*d*	1/2	1/2	1/2	0.0080(4)
Al1	96*g*	0.48689(12)	1/8	1/8	0.0110(4)
Al2	48*f*	0.05938(5)	0.05938(5)	0.32475(8)	0.0134(3)
Al3	16*c*	0	0	0	0.0198(7)
$PrTi_2Al_{20}$					
Pr	8*a*	1/8	1/8	1/8	0.01088(18)
Ti	16*d*	1/2	1/2	1/2	0.0073(3)
Al1	96*g*	0.48668(8)	1/8	1/8	0.0105(3)
Al2	48*f*	0.05939(4)	0.05939(4)	0.32501(6)	0.0129(2)
Al3	16*c*	0	0	0	0.0207(5)
$SmTi_2Al_{20}$					
Sm	8*a*	1/8	1/8	1/8	0.0127(2)
Ti	16*d*	1/2	1/2	1/2	0.0081(3)
Al1	96*g*	0.48650(11)	1/8	1/8	0.0116(3)
Al2	48*f*	0.05958(5)	0.05958(5)	0.32453(7)	0.0138(3)
Al3	16*c*	0	0	0	0.0202(7)
$YbTi_2Al_{20}$					
Yb	8*a*	1/8	1/8	1/8	0.0134(3)
Ti	16*d*	1/2	1/2	1/2	0.0082(4)
Al1	96*g*	0.48613(14)	1/8	1/8	0.0118(5)
Al2	48*f*	0.05976(7)	0.05976(7)	0.32408(10)	0.0152(4)
Al3	16*c*	0	0	0	0.0211(8)

[a] U_{eq} is defined as 1/3 of the trace of the orthogonalized U_{ij} tensor.

Al (6 Al1 + 6 Al2) atoms, forming a distorted icosahedron, as represented as green in Figure 3.1a. It is worth noting that a diamond-like magnetic sublattice formed by the samarium polyhedra can lead to geometrical frustration [135]. The transition metal polyhedra form a tetrahedral network of vertex sharing distorted icosahedra similar to that of the pyrochlore lattice, which can also provide the framework for a geometrically frustrated magnetic sublattice [136].

The lanthanide and transition metal polyhedral units are both considered Frank-Kasper polyhedra [137], forming a series of triangular faces.

Table 3.2b. Crystallographic Parameters for LnV_2Al_{20} (Ln = La–Pr, and Sm)

Atom	Site	x	y	z	U_{eq} (Å^2) [a]
LaV_2Al_{20}					
La	8*a*	1/8	1/8	1/8	0.01001(16)
V	16*d*	1/2	1/2	1/2	0.0060(2)
Al1	96*g*	0.48712(6)	1/8	1/8	0.0089(2)
Al2	48*f*	0.05864(3)	0.05864(3)	0.32635(5)	0.01139(18)
Al3	16*c*	0	0	0	0.0223(4)
CeV_2Al_{20}					
Ce	8*a*	1/8	1/8	1/8	0.00956(15)
V	16*d*	1/2	1/2	1/2	0.0058(2)
Al1	96*g*	0.48719(6)	1/8	1/8	0.0083(2)
Al2	48*f*	0.05910(3)	0.05910(3)	0.32529(4)	0.01052(18)
Al3	16*c*	0	0	0	0.0175(4)
PrV_2Al_{20}					
Pr [b]	8*a*	1/8	1/8	1/8	0.01092(15)
V	16*d*	1/2	1/2	1/2	0.0068(3)
Al1	96*g*	0.48666(5)	1/8	1/8	0.0091(3)
Al2	48*f*	0.05907(3)	0.05907(3)	0.32529(4)	0.0118(2)
Al3	16*c*	0	0	0	0.0215(4)
SmV_2Al_{20}					
Sm	8*a*	1/8	1/8	1/8	0.00995(17)
V	16*d*	1/2	1/2	1/2	0.0043(2)
Al1	96*g*	0.48663(7)	1/8	1/8	0.0070(2)
Al2	48*f*	0.05911(3)	0.05911(3)	0.32519(5)	0.0092(2)
Al3	16*c*	0	0	0	0.0162(4)

[a] U_{eq} is defined as 1/3 of the trace of the orthogonalized U_{ij} tensor.
[b] 89(1) % occupied site.

In the $CeCr_2Al_{20}$ structure type, there are three aluminum positions. The Al1, Al2, and Al3 atoms are 12 (distorted bi-capped pentagonal prism), 12 (bi-capped pentagonal prism), and 14 (bi-capped hexagonal prism) coordinate, respectively. As shown in Table 3.2a-c, the atomic displacement parameter (ADP) of the Al3 atom is approximately twice the magnitude of the

Table 3.2c. Crystallographic Parameters for $LnCr_2Al_{20}$ (Ln = La–Pr, Sm, and Yb)

Atom	Site	x	y	z	U_{eq} ($Å^2$) [a]
$LaCr_2Al_{20}$					
La	8*a*	1/8	1/8	1/8	0.00946(16)
Cr	16*d*	1/2	1/2	1/2	0.0067(2)
Al1	96*g*	0.05817(3)	0.05817(3)	0.32697(5)	0.01036(19)
Al2	48*f*	0.48832(7)	1/8	1/8	0.0079(2)
Al3	16*c*	0	0	0	0.0230(4)
$CeCr_2Al_{20}$					
Ce	8*a*	1/8	1/8	1/8	0.00889(14)
Cr	16*d*	1/2	1/2	1/2	0.00739(18)
Al1	96*g*	0.05867(3)	0.05867(3)	0.32602(4)	0.01054(16)
Al2	48*f*	0.48830(5)	1/8	1/8	0.00810(19)
Al3	16*c*	0	0	0	0.0183(3)
$PrCr_2Al_{20}$					
Pr	8*a*	1/8	1/8	1/8	0.0116(3)
Cr	16*d*	1/2	1/2	1/2	0.0116(4)
Al1	96*g*	0.48827(11)	1/8	1/8	0.0111(4)
Al2	48*f*	0.05850(5)	0.05850(5)	0.32645(8)	0.0134(3)
Al3	16*c*	0	0	0	0.0223(7)
$SmCr_2Al_{20}$					
Sm	8*a*	1/8	1/8	1/8	0.00917(15)
Cr	16*d*	1/2	1/2	1/2	0.0069(2)
Al1	96*g*	0.48778(6)	1/8	1/8	0.0076(2)
Al2	48*f*	0.05868(3)	0.05868(3)	0.32600(4)	0.00973(18)
Al3	16*c*	0	0	0	0.0184(4)
$YbCr_2Al_{20}$					
Yb	8*a*	1/8	1/8	1/8	0.0137(3)
Cr	16*d*	1/2	1/2	1/2	0.0074(4)
Al1	96*g*	0.48692(13)	1/8	1/8	0.0087(4)
Al2	48*f*	0.05900(6)	0.05900(6)	0.32515(9)	0.0113(3)
Al3	16*c*	0	0	0	0.0182(8)

[a] U_{eq} is defined as 1/3 of the trace of the orthogonalized U_{ij} tensor.

Table 3.3 Composition and Typical RRR values for PrM_2Al_{20} (M = Ti, V)

Compound	Pr	M[a]	Al	Typical RRR
$PrTi_2Al_{20}$	0.96 (3)	2	19.6(10)	~50
PrV_2Al_{20}	0.90 (4)	2	19.1(10)	~2
PrV_2Al_{20}	0.98 (3)	2	19.4(6)	~10

[a] Normalized to M = 2

ADPs of the Al1 and Al2 atoms. A similar trend is observed in other compounds adopting the $CeCr_2Al_{20}$ structure type [119, 120]. The thermal ellipsoid of the Al3 atom is flattened in the equatorial-plane of the hexagonal prism. The anomalously large ADP of the Al3 atom can be explained by Al – X (X = Al or T) nearest neighbor interatomic distances. The Al1 atom is coordinated to two V atoms (2.579(1) Å) and two Al2 atoms (2.712(1) Å), and the Al2 atom is coordinated to four Al atoms (< 2.77 Å). The Al3 atom, however, is coordinated to 12 Al2 atoms at a much longer distance (3.107(1) Å). Therefore, the Al1 and Al2 sites are more spatially confined than the Al3 site concomitant with the enlarged ADP of Al3. Alternatively, the Al3 and Sm can be regarded as having similar spatial confinements. Since it is appropriate to compare the ADPs of atoms in similar environments, we compare the Sm and Al3 atom ADPs. Al3 ADP is enlarged approximately twofold over the Sm ADP, ruling out the possibility of a rattling-type event on the Sm atomic position.

Figure 3.2 shows unit cell volume as a function of lanthanide for $LnTi_2Al_{20}$, LnV_2Al_{20}, and $LnCr_2Al_{20}$. The unit cell volumes of the La, Pr, and Sm analogues follow the lanthanide contraction trend well. However, the Ce and Yb analogues, show a marked deviation from the systematic decrease as expected for lanthanide contraction, consistent with tetravalent and divalent (or intermediate) valence states, respectively. Previously reported magnetic susceptibility data indicates that CeM_2Al_{20} (M = Ti, V, and Cr) are, in fact, tetravalent [120, 121]. As expected, the volume of the LnM_2Al_{20} analogues contract as a function of transition metal, with the volume of similar rare earth analogues contracting by ~ 3% from Ti to V and ~1 % from V to Cr.

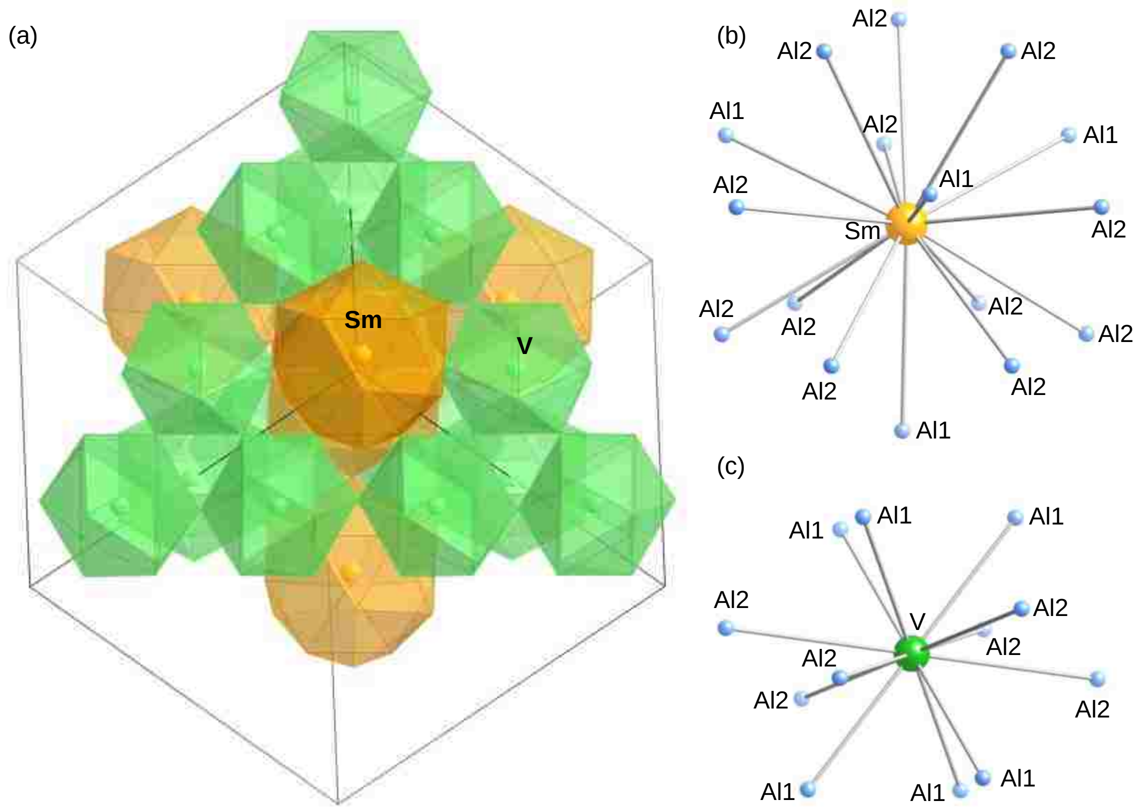

Figure 3.1.(a) The crystal structure of SmV_2Al_{20} showing interpenetrating networks of Sm and V. The diamond-like samarium sublattice (orange) is formed by corner sharing 16 coordinate polyhedra. The vanadium sublattice (green) is made up of corner sharing distorted icosahedra which form a pyrochlore network. Local environments of **(b)** Sm and **(c)** V with site symmetries of $\overline{4}3m$ and $\overline{3}m$, respectively.

3.3.2 Physical Properties

Figure 3.3 shows electrical resistivity as a function of temperature for CeV_2Al_{20} and $LnCr_2Al_{20}$ (Ln = Ce, Pr, and Yb). All analogues show metallic resistivity and no anomalies are observed in the Ce and Yb analogues. The upturn below ~36 K in $PrCr_2Al_{20}$ can be attributed to the Kondo effect and fits well to the expected logarithmic scaling. We attribute the decrease in resistivity below 5 K to Kondo interactions with quadrupolar ordering, similar to the behavior of the previously reported PrM_2Al_{20} (M = Ti and V) [125]. The anomaly in the temperature dependent resistivity of $PrCr_2Al_{20}$ corresponds well to that seen in temperature dependent heat capacity *vide infra*.

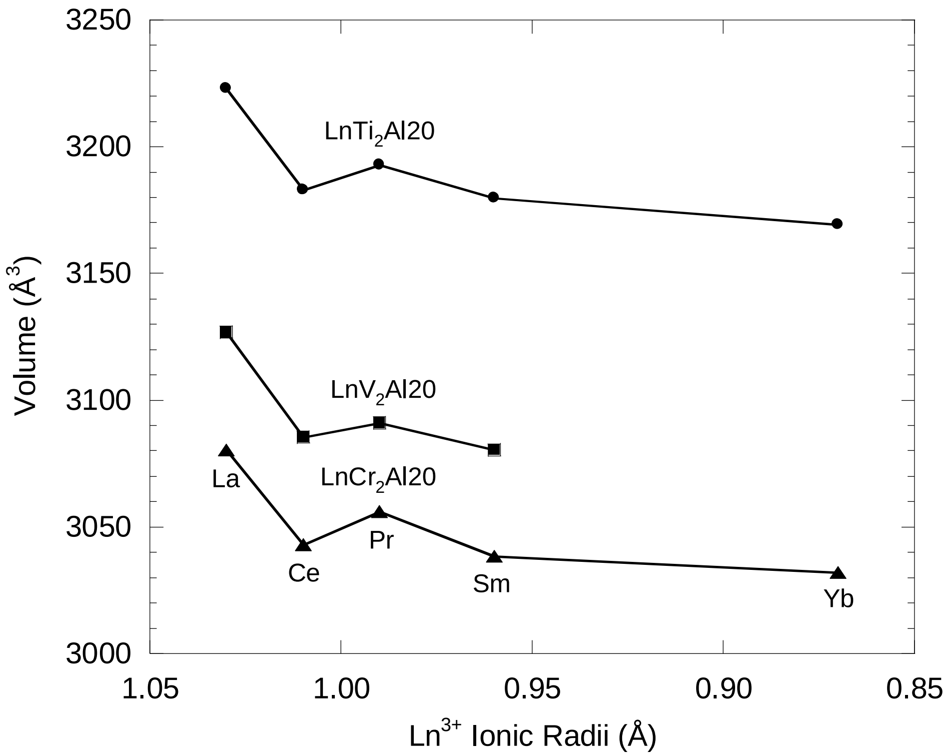

Figure 3.2. LnM_2Al_{20} unit cell volume as a function of lanthanide trivalent ionic radii. Circles, squares, and triangles represent Ti, V, and Cr analogues, respectively. Lines are given as a guide to the eye.

The substitution of the transition metal from titanium to chromium systematically increases the residual resistivity for all rare earth analogues and, thereby, decreases the residual resistivity ratios (RRR). One possible explanation is a decrease in the crystal quality by the substitution. A likely candidate, considering of the EDS results as shown in Table 3.3, is the vacancy at the lanthanide site. The $PrTi_2Al_{20}$ composition is stoichiometric within experimental error with no observable sample dependence in the stoichiometry even though RRR is different from sample to sample. However the composition of PrV_2Al_{20} shows sample dependence. The batch with a typical RRR of ~2 shows Pr deficiency, while full occupancy of the Pr site and stoichiometric composition were observed in the other batch with a typical RRR of ~10. As mentioned in the crystal structure section above, there was insufficient evidence supporting lanthanide deficiencies in all of the analogues except PrV_2Al_{20} with a refined occupancy of 89(1) %. Although the only sample that showed significant deviations was in site occupancy PrV_2Al_{20}, there may be fractional occupations out of the resolution of the analysis for other systems as well.

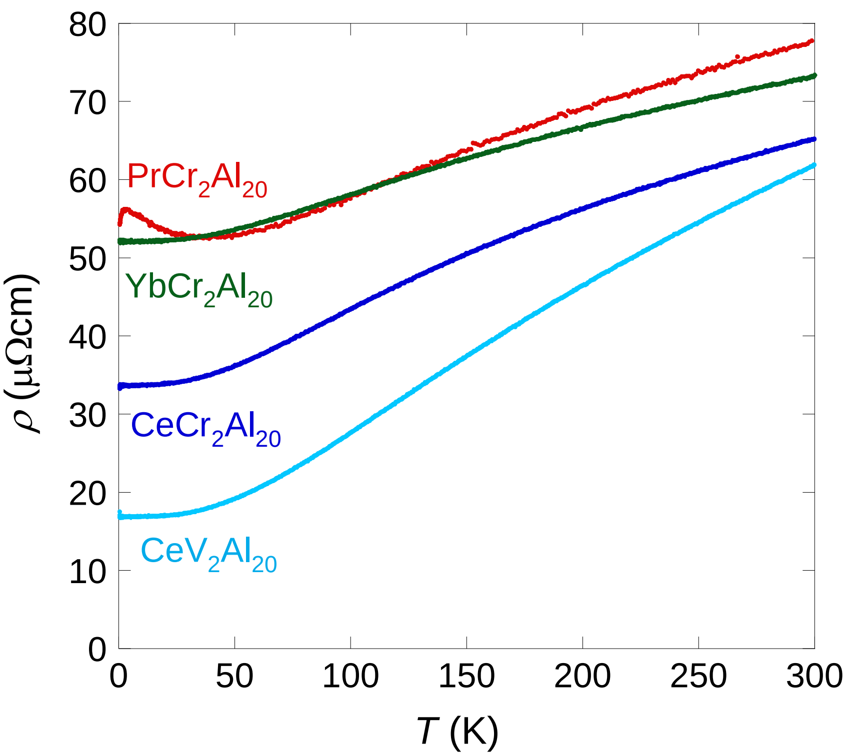

Figure 3.3. Resistivity as a function of temperature for single crystals of $LnCr_2Al_{20}$ (Ln = Pr and Yb) and CeM_2Al_{20} (M = Ti, V).

Figure 3.4 shows magnetic susceptibility as function of temperature for the $PrCr_2Al_{20}$. CeM_2Al_{20} (M = Ti, V, Cr) and $YbCr_2Al_{20}$ data, presented in the inset of Figure 3.4, shows temperature independent paramagnetism, indicating that the lanthanides are in tetravalent and divalent states for Ce and Yb, respectively. The feature at 6 K in $CeTi_2Al_{20}$ is consistent with a slight impurity of Ce_3Al_{11} [138]. The deviation from the lanthanide contraction for CeM_2Al_{20}

and $YbCr_2Al_{20}$, as shown in Figure 3.2, supports the observed non-magnetic states. $PrCr_2Al_{20}$ displays Curie-Weiss behavior with no indication of magnetic ordering. The data was fit to a modified Curie-Weiss law, $\chi = \chi_0 + C/(T - \theta)$, where χ_0 is the temperature independent contribution to the magnetic susceptibility, C is the Curie constant, and θ is the Weiss temperature. For comparison, the results of the fit for $PrCr_2Al_{20}$ and other previously reported PrM_2Al_{20} (M = Ti and V) analogues [125] are provided in Table 3.4. Susceptibility data fits of the PrM_2Al_{20} analogues in the high temperature paramagnetic region (250 – 350 K) give μ_{eff} between 3.43 – 3.57 μ_B/Pr, close to the theoretical value of 3.58 μ_B/Pr for trivalent Pr. Unlike the PrM_2Al_{20} analogues, the SmM_2Al_{20} (M = Ti, V, and Cr) analogues have been shown to deviate from Curie-Weiss behavior and display clear antiferromagnetic transitions at low temperature. The magnetic properties of SmM_2Al_{20} are shown in Table 3.4 for comparison to the PrM_2Al_{20} analogues. Previous reports have shown that increasing electron itinerancy enhances the Kondo interaction in SmM_2Al_{20} (M = Ti, V, Cr) analogues, which suppresses the RKKY magnetic ordering temperatures [130].

The low temperature heat capacity of $PrCr_2Al_{20}$ and $CeTi_2Al_{20}$, CeV_2Al_{20}, and $LnCr_2Al_{20}$ (Ln = Pr and Yb) are shown in Figure 3.5, and the inset of Figure 3.5 shows the low temperature heat capacity, as C_{4f}/T, for $PrTi_2Al_{20}$, PrV_2Al_{20}, and $PrCr_2Al_{20}$. The 4*f* electrons contribution (C_{4f}) to heat capacity was determined by subtracting the heat capacity of the La analogue from that of the Pr analogue. For the non-magnetic CeV_2Al_{20}, and $YbCr_2Al_{20}$ analogues, no phase transitions are present. A small anomaly at 6 K for $CeTi_2Al_{20}$ can be attributed to the ferromagnetic ordering of a slight impurity of Ce_3Al_{11}. $PrCr_2Al_{20}$ shows an upturn at 0.45 K and does not show any phase transition down to the lowest temperature of the resistivity

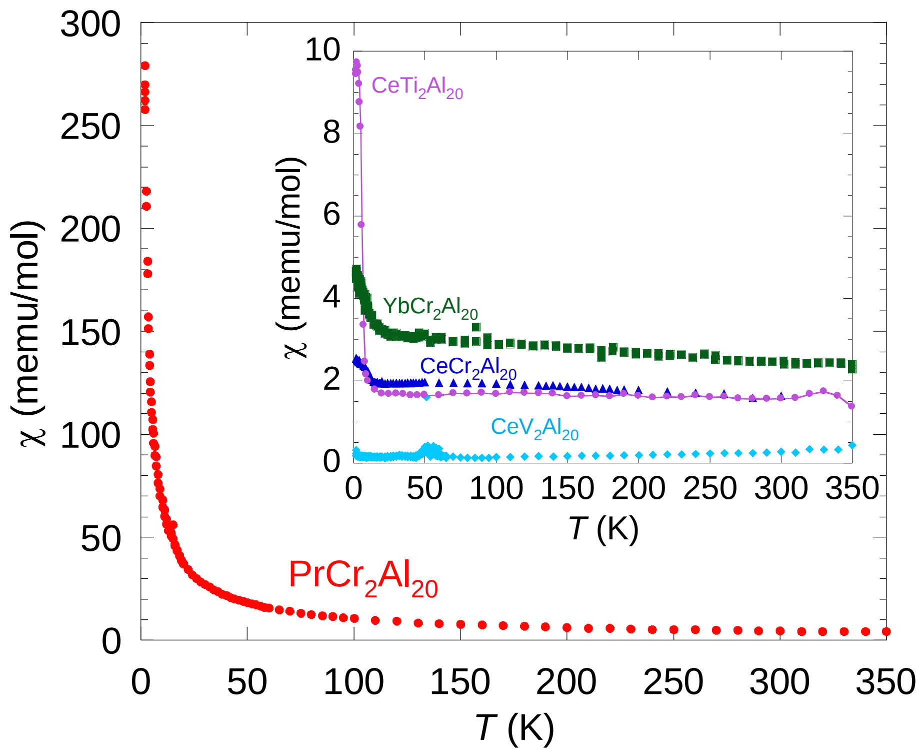

Figure 3.4. Magnetic susceptibility data as a function of temperature of single crystal $PrCr_2Al_{20}$. The inset shows the magnetic susceptibility of single crystal CeM_2Al_{20} (M = Ti, V, Cr) and $YbCr_2Al_{20}$.

measurements nor specific heat measurements down to 400 mK and attribute this feature to Kondo effect. Sharp transitions were previously observed for PrM_2Al_{20} (M = Ti and V) and SmM_2Al_{20} (M = Ti, V, and Cr) between 0.6 and 6 K. The peaks in heat capacity of the Sm analogues were attributed to antiferromagnetic ordering [130], while the anomalies in the Pr analogues are due to quadrupolar ordering [125, 127, 129].

Heat capacity data for CeM_2Al_{20} (M = Ti and V) and $YbCr_2Al_{20}$ was fit to $C_p = \gamma T + \beta T^3$, where γ is the Sommerfeld coefficient (electronic contribution) and β is the phonon contribution to the heat capacity. Sommerfeld coefficients for all LnM_2Al_{20} analogues reported in this paper and previously reported analogues are provided in Table 3.5. Although there could be errors in the magnitude of γ, as this approach neglects the low-temperature increase to heat capacity, the

Table 3.4. Magnetic Properties for LnM_2Al_{20} (Ln = Pr, Sm; M = Ti, V, Cr)

Compound	μ_{calc} (μ_B/mol)	μ_{eff} (μ_B/mol)	θ (K)	T_N/T_Q (K)	Reference
$PrTi_2Al_{20}$[a]	3.58	3.43	-40	2.0[c]	[28]
PrV_2Al_{20}[a]	3.58	3.57	-55	0.6[c]	[28]
$PrCr_2Al_{20}$[a]	3.58	3.56	-53	<0.4[c]	this work
$SmTi_2Al_{20}$[b]	0.85	0.55	-6.6	6.4[d]	[33]
SmV_2Al_{20}[b]	0.85	0.46	-5	2.9[d]	[33]
$SmCr_2Al_{20}$[b]	0.85	0.5	-0.76	1.8 [d]	[33]

[a] Fit region 250 K < T < 350 K
[b] Fit region T_N < T < 40 K
[c] T_Q = Quadrupolar ordering temperature
[d] T_N = Antiferromagnetic ordering temperature

Sommerfeld coefficient of PrM_2Al_{20} (M = Ti, V, and Cr) was estimated using the C_{4f}/T value from 5 K, which is the lowest temperature before the low-temperature upturns. The Sommerfeld coefficients of LaM_2Al_{20} and CeM_2Al_{20} analogues are less than 30 mJ/K^2-mol, indicating little enhancement to the electron's effective mass, as expected for non-magnetic lanthanides. The Sommerfeld coefficient of ~63 mJ/K^2-mol for $LaCr_2Al_{20}$, is similar to that of $YbCr_2Al_{20}$ (~74 mJ/K^2-mol) and UCr_2Al_{20} (80 mJ/K^2-mol) [118]. The Sommerfeld coefficients of PrM_2Al_{20} (Ti, V, Cr) increase across the transition metal analogues with γ of ~100 mJ/K^2-mol ~300 mJ/K^2-mol, and ~500 mJ/K^2-mol, respectively. Both the larger Sommerfeld coefficient and lower ordering temperatures observed in PrV_2Al_{20} and $PrCr_2Al_{20}$ are consistent with an increase in Kondo interactions [125]. The SmM_2Al_{20} analogues also show a dramatic increase in the Sommerfeld coefficient from Ti – V – Cr with values of ~100, ~1100, and ~1500 mJ/K^2-mol, respectively, consistent with an increase in hybridization between the *f* and conduction electrons with increasing electron itinerancy, and agrees well with the trend observed in the Praseodymium analogues [130].

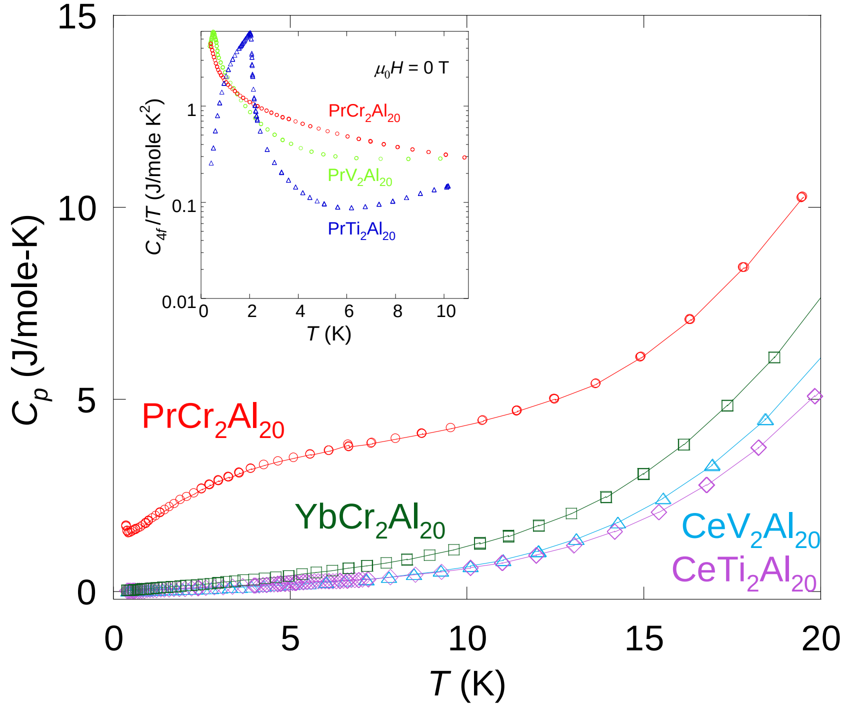

Figure 3.5. Specific heat as a function of temperature of single crystals of $LnCr_2Al_{20}$ (Ln = Pr and Yb) and CeM_2Al_{20} (M = Ti, V). The inset shows C_{4f}/T as a function of T for LnM_2Al_{20} (M = Ti, V, and Cr). Data for $PrTi_2Al_{20}$ and PrV_2Al_{20} were obtained from reference [28].

Table 3.5 Sommerfeld Coefficient (mJ/K^2-mol) of LnM_2Al_{20}

Lanthanide	Ti	V	Cr
La[a]	23[f]	22[f]	63[f]
Ce[a]	34[d]	30[d]	-
Pr[c]	100[e]	300[e]	500[d]
Sm[b]	100[f]	1100[f]	1500[f]
Yb[a]	-	-	74[d]

[a] Fit region T < 5 K
[b] Fit region T = 0.4 K
[c] Estimated from C/T at T = 5 K
[d] This work
[e] Reference [28]
[f] Reference [33]

3.4 Conclusions

We report the synthesis and structures of LnM_2Al_{20} (Ln = La–Pr, Sm and M = Ti, V, Cr), YbM_2Al_{20} (M = Ti, Cr). Temperature dependent magnetization data suggests non-magnetic tetravalent Ce and divalent Yb, consistent with lanthanide contraction trends. The resistivity data and enhanced Sommerfeld coefficient for $PrCr_2Al_{20}$ indicate significant Kondo interactions at low temperatures. $PrCr_2Al_{20}$ shows an upturn in heat capacity and an anomaly in resistivity, which can be ascribed to quadrupolar ordering similar to previously reported PrM_2Al_{20} (M = Ti and V) trends. The Sommerfeld coefficients are also increased as a function of transition metal in PrM_2Al_{20} and are consistent with a decrease in quadrupolar strength. The *f*-electron hybridization increases from Ti–Cr due the additional 3*d* conduction electrons and the smaller unit cell volume. Additionally, quadrupolar ordering is only present in high quality (high RRR) samples [125]; thus, the growth of high quality single crystals is of paramount importance in the study of these low temperature phenomena.

3.5 References

[98] G.R. Stewart, Heavy-fermion systems, Rev. Mod. Phys., 56 (1984) 755-787.

[99] Z. Fisk, J.L. Sarrao, J.D. Thompson, Heavy fermions, Curr. Opin. Solid State Mater. Sci., 1 (1996) 42-46.

[100] Z. Fisk, Searching for heavy fermion materials, Physica B, 378-380 (2006) 13-16.

[101] R. Egger, H. Schoeller, RKKY interaction and Kondo screening cloud for strongly correlated electrons, Phys. Rev. B, 54 (1996) 16337-16340.

[102] B. Coqblin, M.D. Nunez-Regueiro, A. Theumann, J.R. Iglesias, S.G. Magalhaes, Theory of the Kondo lattice: competition between Kondo effect and magnetic order, Philos. Mag., 86 (2006) 2567-2580.

[103] J.M. Lawrence, D.L. Mills, Recent progress in heavy fermion/valence fluctuation physics: introduction, Comments Cond. Mat. Phys., 15 (1991) 163-174.

[104] R.T. Macaluso, S. Nakatsuji, K. Kuga, E.L. Thomas, Y. Machida, Y. Maeno, Z. Fisk, J.Y. Chan, Crystal structure and physical properties of polymorphs of $LnAlB_4$ (Ln = Yb, Lu), Chem. Mater., 19 (2007) 1918-1922.

[105] Y. Matsumoto, S. Nakatsuji, K. Kuga, Y. Karaki, N. Horie, Y. Shimura, T. Sakakibara, A.H. Nevidomskyy, P. Coleman, Quantum criticality without tuning in the mixed valence compound β-$YbAlB_4$, Science, 331 (2011) 316-319.

[106] W.A. Phelan, M.C. Menard, M.J. Kangas, G.T. McCandless, B.L. Drake, J.Y. Chan, Adventures in crystal growth: synthesis and characterization of single crystals of complex intermetallic compounds, Chem. Mater., 24 (2012) 409-420.

[107] R.T. Macaluso, J.N. Millican, S. Nakatsuji, H.O. Lee, B. Carter, N.O. Moreno, Z. Fisk, J.Y. Chan, A comparison of the structure and localized magnetism in Ce_2PdGa_{12} with the heavy fermion $CePdGa_6$, J. Solid State Chem., 178 (2005) 3547-3553.

[108] D.L. Cox, Quadrupolar Kondo effect in uranium heavy-electron materials, Phys. Rev. Lett., 59 (1987) 1240-1243.

[109] P.I. Krypyakevich, O.S. Zarechnyuk, The RCr_2Al_{20} compounds in the systems of the rare earth metals and calcium and their crystal structures, Dopov. Akad. Nauk. Ukr., Ser A, 30 (1968) 364-366.

[110] A.P. Gonçalves, J.C. Waerenborgh, A. Amaro, M. Godinho, M. Almeida, UFe_2Zn_{20}: a new uranium intermetallic compound, J. Alloys Comp., 271-273 (1998) 456-458.

[111] E.D. Bauer, A.D. Christianson, J.S. Gardner, V.A. Sidorov, J.D. Thompson, J.L. Sarrao, M.F. Hundley, Physical properties of the ferromagnetic heavy-fermion compound UIr_2Zn_{20}, Phys. Rev. B, 74 (2006) 155118.

[112] M.S. Torikachvili, S. Jia, E.D. Mun, S.T. Hannahs, R.C. Black, W.K. Neils, D. Martien, S.L. Bud'ko, P.C. Canfield, Six closely related YbT_2Zn_{20} (T = Fe, Co, Ru, Rh, Os, Ir) heavy fermion compounds with large local moment degeneracy, P. Natl. Acad. Sci. USA, 104 (2007) 9960-9963.

[113] S. Jia, N. Ni, G.D. Samolyuk, A. Safa-Sefat, K. Dennis, H. Ko, G.J. Miller, S.L. Bud'ko, P.C. Canfield, Variation of the magnetic ordering in GdT_2Zn_{20} (T=Fe , Ru, Os, Co, Rh and Ir) and its correlation with the electronic structure of isostructural YT_2Zn_{20}, Phys. Rev. B, 77 (2008) 104408.

[114] W. Tian, A.D. Christianson, J.L. Zarestky, S. Jia, S.L. Bud'ko, P.C. Canfield, P.M.B. Piccoli, A.J. Schultz, Magnetic order in $TbCo_2Zn_{20}$ and $TbFe_2Zn_{20}$, Phys. Rev. B, 81 (2010) 144409.

[115] Y. Ōnuki, S. Yasui, M. Matsushita, S. Yoshiuchi, M. Ohya, Y. Hirose, N.D. Dung, F. Honda, T. Takeuchi, R. Settai, K. Sugiyama, E. Yamamoto, T.D. Matsuda, Y. Haga, T. Tanaka, Y. Kubo, H. Harima, Characteristic heavy fermion properties in $YbCu_2Si_2$ and YbT_2Zn_{20} (T: Co, Rh, Ir), J. Phys. Soc. Jpn., 80SA (2011) SA003.

[116] N. Ni, S. Jia, G.D. Samolyuk, A. Kracher, A.S. Sefat, S.L. Bud'ko, P.C. Canfield, Physical properties of $GdFe_2(Al_xZn_{1-x})_{20}$, Phys. Rev. B, 83 (2011) 054416.

[117] T. Nasch, W. Jeitschko, U.C. Rodewald, Ternary rare earth transition metal zinc compounds RT_2Zn_{20} with T=Fe, Ru, Co, Rh, and Ni, Z. Naturforsch., B 52 (1997) 1023-1030.

[118] K. Okuda, S. Noguchi, Y. Nakazawa, M. Ishikawa, Synthesis and characterization of new ternary uranium compound UCr_2Al_{20}, J. Phys. Soc. Jpn., 58 (1989) 4296-4299.

[119] S. Niemann, W. Jeitschko, Ternary aluminides AT_2Al_{20} (A = rare earth elements and eranium; T = Ti, Nb, Ta, Mo, and W) with $CeCr_2Al_{20}$-type structure, J. Solid State Chem., 114 (1995) 337-341.

[120] V.M.T. Thiede, W. Jeitschko, S. Niemann, T. Ebel, $EuTa_2Al_{20}$, $Ca_6W_4Al_{43}$ and other compounds with $CeCr_2Al_{20}$ and $Ho_6Mo_4Al_{43}$ type structures and some magnetic properties of these compounds, J. Alloys Comp., 267 (1998) 23-31.

[121] O. Moze, L.D. Tung, J.J.M. Franse, K.H.J. Buschow, Crystal structure and magnetic properties of CeV_2Al_{20} and $CeCr_2Al_{20}$, J. Alloys Comp., 268 (1998) 39-41.

[122] T.I. Yanson, N.B. Manyako, O.I. Bodak, R. Cerny, R.E. Gladyshevskii, K. Yvon, Peculiarities of the interaction of ytterbium with transition metals (Cr,Mn) and aluminium, J. Alloys Comp., 219 (1995) 219-221.

[123] J.Y. Cho, E.L. Thomas, Y. Nambu, C. Capan, A.B. Karki, D.P. Young, K. Kuga, S. Nakatsuji, J.Y. Chan, Crystal Growth, Structure, and Physical Properties of $Ln(Cu,Ga)_{13-x}$ (Ln = La-Nd, Eu; x ~ 0.2), Chem. Mater., 21 (2009) 3072-3078.

[124] R. Gumeniuk, M. Schöneich, A. Leithe-Jasper, W. Schnelle, M. Nicklas, H. Rosner, A. Ormeci, U. Burkhardt, M. Schmidt, U. Schwarz, M. Ruck, Y. Grin, High-pressure synthesis and exotic heavy-fermion behaviour of the filled skutterudite $SmPt_4Ge_{12}$, New J. Phys., 12 (2010) 103035.

[125] A. Sakai, S. Nakatsuji, Kondo effects and multipolar order in the cubic $PrTr_2Al_{20}$ (*Tr* = Ti, V), J. Phys. Soc. Jpn., 80 (2011) 063701.

[126] M. Matsunami, M. Taguchi, A. Chainani, R. Eguchi, M. Oura, A. Sakai, S. Nakatsuji, S. Shin, Kondo resonance in $PrTi_2Al_{20}$: Photoemission spectroscopy and single-impurity Anderson model calculations, Phys. Rev. B, 84 (2011) 193101.

[127] T.J. Sato, S. Ibuka, Y. Nambu, T. Yamazaki, A. Sakai, S. Nakatsuji, Ferro-quadrupolar ordering in $PrTi_2Al_{20}$, arXiv:1108.3705 v1 [cond-mat.str-el].

[128] T.U. Ito, W. Higemoto, K. Nimomiya, H. Luetkens, C. Baines, A. Sakai, S. Nakatsuji, μSR Evidence of nonmagnetic order and ^{141}Pr hyperfine enhanced nuclear magnetism in the cubic Γ_3 ground doublet system $PrTi_2Al_{20}$, J. Phys. Soc. Jpn., 80 (2011) 113703.

[129] M. Koseki, Y. Nakanishi, K. Deto, G. Koseki, R. Kashiwazaki, F. Shichinomiya, M. Nakamura, M. Yoshizawa, A. Sakai, S. Nakatsuji, Ultrasonic investigation on a cage structure compound $PrTi_2Al_{20}$, J. Phys. Soc. Jpn., 80SA (2011) SA049.

[130] A. Sakai, S. Nakatsuji, Strong valence fluctuation effects in $SmTr_2Al_{20}$ (Tr=Ti, V, Cr), Phys. Rev. B, 84 (2011) 201106(R).

[131] P.C. Canfield, Z. Fisk, Growth of single-crystals from metallic fluxes, Philos. Mag. B, 65 (1992) 1117-1123.

[132] A. Altomare, M.C. Burla, M. Camalli, G.L. Cascarano, C. Giacovazzo, A. Guagliardi, A.G.G. Moliterni, G. Polidori, R. Spagna, SIR97: a new tool for crystal structure determination and refinement, J. Appl. Crystallogr., 32 (1999) 115-119.

[133] M.C. Burla, B. Carrozzini, G.L. Cascarano, C. Giacovazzo, G. Polidori, More power for direct methods: SIR2002, Z. Kristallogr., 217 (2002) 629-635.

[134] G. Sheldrick, A short history of SHELX, Acta Crystallogr. A, 64 (2008) 112-122.

[135] N. Tristan, J. Hemberger, A. Krimmel, H.A.K. von Nidda, V. Tsurkan, A. Loidl, Geometric frustration in the cubic spinels MAl_2O_4 (M=Co, Fe, and Mn), Phys. Rev. B, 72 (2005) 9.

[136] R. Moessner, A.R. Ramirez, Geometrical frustration, Physics Today, 59 (2006) 24-29.

[137] F.C. Frank, J.S. Kasper, Complex alloy structures regarded as sphere packings. I. Definitions and basic principles, Acta Crystallogr., 11 (1958) 184-190.

[138] C.R. Wang, Y.Y. Chen, S. Neeleshwar, M.N. Ou, J.C. Ho, Size effect on magnetic ordering in Ce_3Al_{11}, Physica B, 329–333, Part 2 (2003) 620-621.

Chapter 4. A ^{57}Fe Mössbauer Spectroscopy and Single Crystal X-ray Diffraction Study of Fe Disorder in Single Crystals of $YbCr_2Fe_xAl_{20-x}$ (x ~0.2)

4.1 Introduction

Cerium containing intermetallic phases have recently garnered a lot of attention because of the valence instability between the Ce^{3+} (f^1) and Ce^{4+} (f^0) states and heavy fermion behavior. Heavy fermion compounds are materials where the conduction electrons interact strongly with the localized magnetic moment leading to an enhancement, by approximately two orders of magnitude, of the electron's effective mass. An enhancement of the electronic contribution to specific heat (Sommerfeld coefficient, γ) is a characteristic of these materials. Heavy fermion compounds such as $CeIrIn_5$ [139, 140], UNi_2Al_3 [141], and $CePt_3Si$ [142] have been shown to exhibit unconventional superconductivity. Ytterbium compounds can exhibit analogous valence instability between the Yb^{3+} (f^{13}) and Yb^{2+} (f^{14}) states and can show similar properties. Heavy fermion behavior has recently been observed in YbSi (ThAl structure-type) [143, 144], $YbCu_2Si_2$ ($ThCr_2Si_2$ structure-type) [145, 146], and YbT_2Zn_{20} (T = Fe, Co, Ru, Rh, Os, Ir; $CeCr_2Al_{20}$ structure-type) [147, 148]. In addition to the YbT_2Zn_{20} (T = Fe, Co, Ru, Rh, Os, Ir) compounds, the other members of the LnT_2Zn_{20} (Ln = lanthanides; T = Fe, Co, Ru, Rh, Os, Ir) series have also been investigated and it was shown that the magnetic properties greatly depend on the transition metal present and the valence electron count [148-151].

Isostructural LnT_2Al_{20} (Ln = lanthanides; T = Ti-Cr, Nb, Mo, Ta, W) compounds have also been reported [152, 153]. Recently, it was found that $PrTi_2Al_{20}$ and PrV_2Al_{20} exhibit quardupolar order at 2 and 0.6 K [154-157], respectively, while $PrCr_2Al_{20}$ shows Kondo behavior at low temperatures [158]. The SmT_2Al_{20} (T = Ti-Cr) analogues show valence fluctuations and order antiferromagnetically below 7 K [159], while GdV_2Al_{20} and $GdCr_2Al_{20}$ order antiferromagnetically at 2.35(5) and 3.90(5) K, respectively [160]. CeT_2Al_{20} (T = Ti-Cr) and

$YbCr_2Al_{20}$ are temperature independent paramagnets consistent with Ce^{4+} and Yb^{2+}, respectively [158, 161, 162].

LnT_2Al_{20} (Ln = lanthanides; T = early transition metals) compounds have been empirically determined to be stable with electron counts of 70-75 valence electrons [163], and a study on $LnMn_2X_yZn_{20-y}$ (Ln = lanthanides, X = Al, In; 2 < y < 7) compounds found that the both atomic size and electron counts are important for compound stabilization. Only by mixing zinc and a triel can the correct size and electron count be achieved to stabilize Mn analogues [164]. Doping iron into $YbCr_2Al_{20}$ would provide additional insight into the stability limits of the $CeCr_2Al_{20}$ structure type and possibly impact the physical properties. Herein the flux growth synthesis, structural characterization and physical properties of $YbCr_2Fe_xAl_{20-x}$ are reported.

4.2 Experimental

4.2.1 Synthesis

Single crystals of $YbCr_2Fe_xAl_{20-x}$ were prepared using the molten metal flux technique [165, 166]. $YbCr_2Al_{20}$ was prepared by weighing out Yb (99.9%), Cr (99.996 %) and Al (99.999%) in the molar ratio 1:2:50. The two iron containing samples were synthesized using Yb, Cr, Fe (99.998%), and Al in the ratios 1:1.5:0.5:50 and 1:1:1:50. The elements were placed in an alumina crucible which was capped with a second alumina crucible and placed in a fused silica tube. The tube was evacuated, sealed, and placed in a furnace. The samples were heated to 1273 K at 100 K/h, dwelled for 24 h, and slowly (2 K/h) cooled to 1073 K. At the end on the reaction, the samples were inverted and centrifuged to remove excess flux, and residual flux was etched using dilute (~ 1 M) NaOH. The undoped sample and the lower iron concentration (1:1.5:0.5:50) produced large octahedral single crystals, up to ~3 mm in length, and produced only crystals of the $CeCr_2Al_{20}$ structure-type (spacegroup $Fd\overline{3}m$, a ~ 14.5 Å) [153]. The larger iron concentration (1:1:1:50) produced smaller crystals ($\leq$ 1 mm^3) of the $CeCr_2Al_{20}$ structure-type and bar-shaped crystals of the $YbFe_2Al_{10}$ structure-type (spacegroup *Cmcm*, a ~ 8.966 Å, b ~ 10.153 Å, c ~ 9.003 Å) [167] which could be separated based on morphology. Higher concentrations of iron were not attempted due to the presence of $YbFe_2Al_{10}$.

4.2.2 Structural Characterization

An etched single crystal was cleaved to ~0.1 x 0.1 x 0.1 mm and was attached to a glass fiber with epoxy and mounted on the goniometer of a Nonius Kappa CCD diffractometer with Mo Kα radiation (λ = 0.71073 Å). The diffraction pattern was indexed to a face-centered cubic unit cell (a ~ 14.5 Å), consistent with the $CeCr_2Al_{20}$ structure type. After integration a multi-scan absorption correction was applied, and the crystal structure was solved using SIR97 [168] and refined with SHELXL97 [169]. The final models were corrected for extinction and atomic displacement parameters were modeled anisotropically. Details of the collection and refinement, atomic positions and displacement parameters, and interatomic distances are provided in Tables 4.1-4.3, respectively. Crystallographic data (in cif format) for both $YbCr_2Fe_xAl_{20-x}$ analogues is provided in Appendix C. Refinement of the iron occupancies is discussed in the results and discussion section below.

4.2.3 Elemental Analysis

Elemental analysis was performed via energy dispersive X-ray spectroscopy (EDS) using a JEOL JSM-5600 scanning electron microscope with an accelerating voltage of 15 kV. For each compound, two polished crystals were measured four times each and the results were averaged. The compositions, normalized to Yb, are $YbCr_{2.03(12)}Fe_{0.10(3)}Al_{25.01(18)}$ and $YbCr_{1.77(23)}Fe_{0.18(2)}Al_{20.11(33)}$ for the reaction ratios 1:1.5:0.5:50 and 1:1:1:50, respectively. For clarity both compounds will be referred to by the approximate Fe concentrations of 0.1 and 0.2, respectively, in the text.

Table 4.1 Collection and Refinement

Formula	$YbCr_2Al_{20}$[a]	$YbCr_2Fe_{0.1}Al_{19.9}$	$YbCr_2Fe_{0.2}Al_{19.8}$
Crystal System	Cubic	Cubic	Cubic
Space Group	$Fd\bar{3}m$	$Fd\bar{3}m$	$Fd\bar{3}m$
a (Å)	14.473(13)	14.450(4)	14.444(4)
V (Å^3)	3032(5)	3017.2(14)	3013.4(14)
Z	8	8	8
Crystal dimensions (mm)	0.03 x 0.03 x 0.03	0.05 x 0.08 x 0.1	0.05 x 0.08 x 0.1
Temperature (K)	293(2)	296(1)	296(1)
θ range (°)	2.44 - 29.85	3.99 - 29.91	3.99 - 29.92
μ (mm^{-1})	8.666	8.794	8.909
Data Collection			
Measured Reflections	701	1785	1552
Unique Reflections	248	247	247
Reflections with I>2σ(I)	224	223	230
R_{int}	0.0409	0.0384	0.0296
h	$-20 \leq h \leq 20$	$-20 \leq h \leq 20$	$-20 \leq h \leq 20$
k	$-14 \leq k \leq 14$	$-14 \leq k \leq 14$	$-14 \leq k \leq 14$
l	$-13 \leq l \leq 13$	$-13 \leq l \leq 13$	$-13 \leq l \leq 13$
Refinement			
$\Delta\rho_{max}$ (eÅ^{-3})/$\Delta\rho_{min}$ (eÅ^{-3})	0.816 / -1.24	0.862 / -0.744	0.694 / -0.769
GoF	1.167	1.062	1.185
Extinction coefficient	0.00011(5)	0.00035(5)	0.00023(3)
Reflections	248	247	247
Parameters/Restraints	17 / 0	21 / 3	21 / 3
R_1 ($F^2 > 2sF^2$) [b]	0.0295	0.0215	0.0198
wR_2 (F^2) [c]	0.0553	0.0456	0.0337

[a] Crystallographic data from reference [158].
[b] $R_1 = \Sigma||F_o| - |F_c||/\Sigma|F_o|$
[c] $R_w = [\Sigma [w (F_o^2 - F_c^2)^2]/ \Sigma [w (F_o^2)^2]]^{1/2}$; $w = 1/[\sigma^2(F_o^2) + (0.0137P)^2 + 20.00 P]$, $w = 1/[\sigma^2(F_o^2) + (0.0188P)^2 + 14.48P]$, $w = 1/[\sigma^2(F_o^2) + (0.0055P)^2]$; $P = (F_o^2 + 2 Fc^2)/3$ for $YbCr_2Al_{20}$, $YbCr_2Fe_{0.1}Al_{19.9}$, and $YbCr_2Fe_{0.2}Al_{19.8}$, respectively.

4.2.4 Physical Properties

Single crystals selected for physical property measurements were first characterized by X-ray diffraction and EDS. Magnetic data was collected using a Quantum Design Physical

Property Measurement System (PPMS). The temperature-dependent susceptibility data were measured under zero-field cooled (ZFC) conditions between 3 K and 300 K. Magnetic susceptibility was measured under an applied field of 0.1 T. Field-dependent magnetization data were measured at 3 K with applied fields up to 9 T. The electrical resistivity measurements were measured on single crystals by the standard four-probe AC technique.

Table 4.2 Atomic Positions

Atom	Site	Symmetry	x	y	z	Occ. [b]	U_{eq} (Å^2) [c]
$YbCr_2Al_{20}$ [a]							
Yb1	8*a*	$\bar{4}3m$	1/8	1/8	1/8	1	0.0139(3)
Cr1	16*d*	$\bar{3}m$	1/2	1/2	1/2	1	0.0078(4)
Al1	96*g*	*mm*	0.48698(14)	1/8	1/8	1	0.0091(4)
Al2	48*f*	2*mm*	0.05900(7)	0.05900(7)	0.32511(10)	1	0.0117(4)
Al3	16*c*	$\bar{3}m$	0	0	0	1	0.0182(8)
$YbCr_2Fe_{0.1}Al_{19.9}$							
Yb1	8*a*	$\bar{4}3m$	1/8	1/8	1/8	1	0.0113(2)
Cr1	16*d*	$\bar{3}m$	1/2	1/2	1/2	1	0.0091(3)
Al1	96*g*	*mm*	0.05899(5)	0.05899(5)	0.32525(8)	0.996(3)	0.0121(3)
Fe1	96*g*	*mm*	0.05899(5)	0.05899(5)	0.32525(8)	0.004(3)	0.0121(3)
Al2	48*f*	2*mm*	0.48670(11)	1/8	1/8	0.992(5)	0.0099(4)
Fe2	48*f*	2*mm*	0.48670(11)	1/8	1/8	0.008(5)	0.0099(4)
Al3	16*c*	$\bar{3}m$	0	0	0	1	0.0204(7)
$YbCr_2Fe_{0.2}Al_{19.8}$							
Yb1	8*a*	$\bar{4}3m$	1/8	1/8	1/8	1	0.01002(16)
Cr1	16*d*	$\bar{3}m$	1/2	1/2	1/2	1	0.0081(2)
Al1	96*g*	*mm*	0.05900(4)	0.05900(4)	0.32519(6)	0.988(2)	0.0119(3)
Fe1	96*g*	*mm*	0.05900(4)	0.05900(4)	0.32519(6)	0.012(2)	0.0119(3)
Al2	48*f*	2*mm*	0.48672(8)	1/8	1/8	0.988(4)	0.0093(4)
Fe2	48*f*	2*mm*	0.48672(8)	1/8	1/8	0.012(4)	0.0093(4)
Al3	16*c*	$\bar{3}m$	0	0	0	1	0.0194(5)

[a] Crystallographic data from reference [158].
[b] Site occupancy
[c] U_{eq} is defined as one-third of the trace of the orthogonalized U_{ij} tensor

Table 4.3 Selected Interatomic Distances (Å)

Compound	$YbCr_2Al_{20}$ [a]	$YbCr_2Fe_{0.1}Al_{19.9}$	$YbCr_2Fe_{0.2}Al_{19.8}$
Yb - 16 coordinate			
Yb-Al3 (x4)	3.133(3)	3.1285(9)	3.1269(9)
Ln-Al1 (x12)	3.196(3)	3.1929(15)	3.1912(13)
Cr - 12 coordinate			
Cr-Al2 (x6)	2.565(2)	2.5615(7)	2.5605(7)
Cr-Al1 (x6)	2.804(3)	2.7977(14)	2.7965(12)
Al1 - 12 coordinate			
Al1-Al2	2.702(2)	2.6945(19)	2.6941(16)
Al1-Al1	2.705(3)	2.699(2)	2.6972(19)
Al1-Al1 (x2)	2.745(3)	2.7434(19)	2.7418(16)
Al1-Cr	2.804(3)	2.7977(14)	2.7965(12)
Al1-Al2 (x2)	2.838(3)	2.8316(13)	2.8307(12)
Al1-Al1 (x2)	2.923(2)	2.9155(15)	2.9143(13)
Al1-Al3 (x2)	3.091(3)	3.0869(11)	3.0852(9)
Al1-Yb	3.196(3)	3.1930(13)	3.1913(11)
Al2 – 12 coordinate			
Al2-Cr (x2)	2.565(2)	2.5615(7)	2.5602(7)
Al2-Al1 (x2)	2.705(3)	2.5615(7)	2.6941(16)
Al2-Al2 (x4)	2.825(3)	2.826(2)	2.824(2)
Al2-Al1 (x4)	2.838(3)	2.8316(13)	2.8306(12)
Al3 – 14 coordinate			
Al3-Al1 (x12)	3.091(3)	3.0869(11)	3.0852(11)
Al3-Ln (x2)	3.133(3)	3.1287(9)	3.1269(9)

[a] Crystallographic data obtained from reference [158].

4.2.5 Mössbauer Spectroscopy

Single crystals used for physical property measurements were also used for Mössbauer spectroscopy. Powdered $YbCr_2Fe_xAl_{20-x}$ samples (x = 0.1 and 0.2) were analyzed at room temperature and at 77 K. The low amount of powder and the low iron content lead to spectra with low statistical quality even after more than 7 days per spectrum.

4.3 Results and Discussion

4.3.1 Crystal Structure

The $CeCr_2Al_{20}$ structure type (spacegroup $Fd\overline{3}m$, a ~ 14.5 Å) is a robust structure that is adopted by LnT_2Zn_{20} (Ln = lanthanides; T = Fe, Co, Ru, Rh, Os, Ir) [170], TT'_2Zn_{20} (T = Zr, Hf, Nb; T' = Mn-Ni, Ru, Rh) [163], and LnT_2Al_{20} (Ln = lanthanides; T = Ti-Cr, Nb, Mo, Ta, W) [152, 153] intermetallics, and variants of the $CeCr_2Al_{20}$ structure are adopted by $ReBe_{22}$ [171], $ZrZn_{22}$ [172], and $Mg_3Cr_2Al_{18}$ [173]. The crystal structure of $YbCr_2Al_{20}$ is shown in Figure 4.1, and consists of a diamond-like network of Yb polyhedra and a pyrochlore-like network of Cr polyhedra. The lattice parameter of $YbCr_2Al_{20}$ is 14.473(3) Å. With the incorporation of the smaller iron atoms the lattice parameter decreases to 14.450(4) Å and 14.444(4) Å for $YbCr_2Fe_{0.1}Al_{19.9}$ and $YbCr_2Fe_{0.2}Al_{19.8}$, respectively.

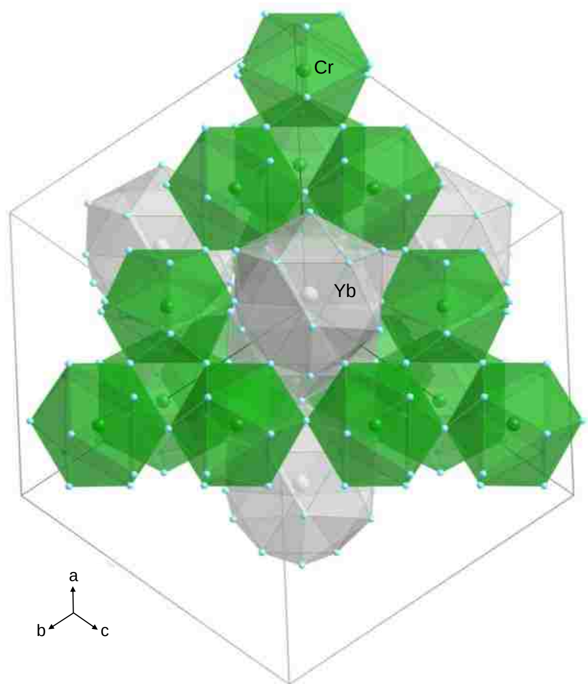

Figure 4.1. The crystal structure of $YbCr_2Al_{20}$ showing the interpenetrating networks of the Yb polyhedra and Cr polyhedra. Ytterbium polyhedra are shown as light grey and the Cr polyhedra are shown as green. All aluminum atoms are depicted as small light blue spheres. Crystallographic data for $YbCr_2Al_{20}$ was obtained from reference [158].

The $YbCr_2Al_{20}$ crystal structure has one Yb site (8*a*), one chromium site (16*d*) and three aluminum sites (96*g*, 48*f*, 16*c*), and the local environments of the five sites are depicted in Figure 4.2a-e. The Yb polyhedron is 16 coordinate and is made up of 4 Al3 and 12 Al1 atoms with Yb-Al bond distances of 3.133(3) and 3.196(3) Å, respectively. The Yb polyhedron corner shares with 4 other Yb polyhedra and the Yb-Yb distances are 6.267 Å. The Cr atoms are 12 coordinate and are surrounded by 6 Al1 and 6 Al2 atoms with Cr-Al distances of 3.133(3) and 3.196(3) Å, respectively. The three Al atoms are 12, 12, and 14 coordinate, respectively, and can be described as a distorted bi-capped pentagonal prism, a bi-capped pentagonal prism, and a bi-capped hexagonal prism. The Al-Al distances range from 2.702(2) to 3.091(3) Å, and are longer than the expected distance of 2.42 Å from covalent radii [174].

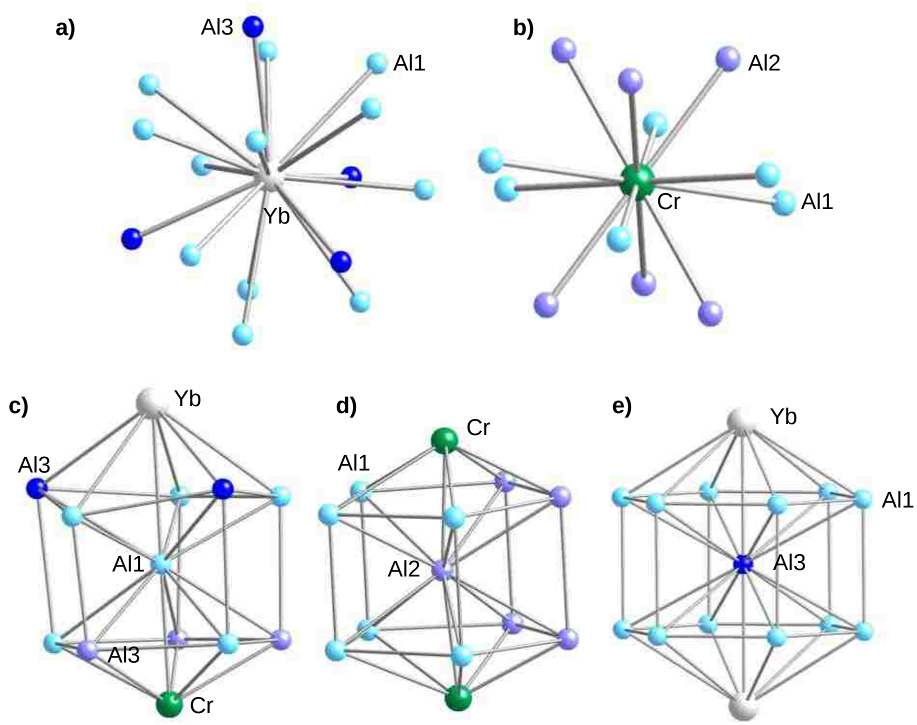

Figure 4.2. The local environments of Yb, Cr, Al1, Al2, and Al3 are shown as **a-e**, respectively. Yb atoms and Cr atoms are depicted as light grey spheres and green spheres, respectively, while the Al1, Al2, and Al3 atoms are depicted as light blue, blue, and royal blue respectively. Crystallographic data for $YbCr_2Al_{20}$ was obtained from reference [158].

4.3.2 Mössbauer Spectroscopy

Mössbauer spectra for $YbCr_2Fe_xAl_{20-x}$ (x = 0.1 and 0.2) are shown in Figure 4.3. The data can be modeled with either one (model 1) or two Fe sites (model 2). From the misfit, model 2 fits the data better than model 1. For both models, the isomer shifts and the quadrupole splittings (provided in Table 4.4) are in the range of iron atoms in an intermetallic environment rich in aluminum [175-180].

Table 4.4 Mössbauer Parameters

Sample	IS (mm/s)	QS (mm/s)	LW (mm/s)	%
Fe = 0.2	0.31(1)	0.14(5)	0.31(3)	40(7)
	0.27(1)	0.53(3)	-	60(7)
Fe = 0.1	0.35(2)	0.24(3)	0.27(4)	57(6)
	0.28(2)	0.60(5)	-	43(6)

Model 2 suggests the presence of two iron sites in both compositions (x =0.1 and 0.2). The site with the larger quadrupole splitting (blue in Figure 4.3) corresponds to the most distorted site. This model can only be explained if Fe atoms go simultaneously into two crystallographic sites. Finally, Mössbauer spectra were recorded at 77K and 300 K in a larger velocity range (Figure 4.4). The interest of recording spectra over this range (10 mm/s) was to check for the presence of iron oxides which would give absorption peaks at around 8-9 mm/s. From the lack of features in this range, we can conclude to there are no iron oxides present. In addition, the lack of magnetic splitting indicates there is no magnetic ordering between 77 K and 300 K.

4.3.3 Crystal Structure Refinements

The Mössbauer spectroscopy results indicated two crystallographic sites were occupied with Fe, so the X-ray diffraction models were examined to identify the two Fe sites.

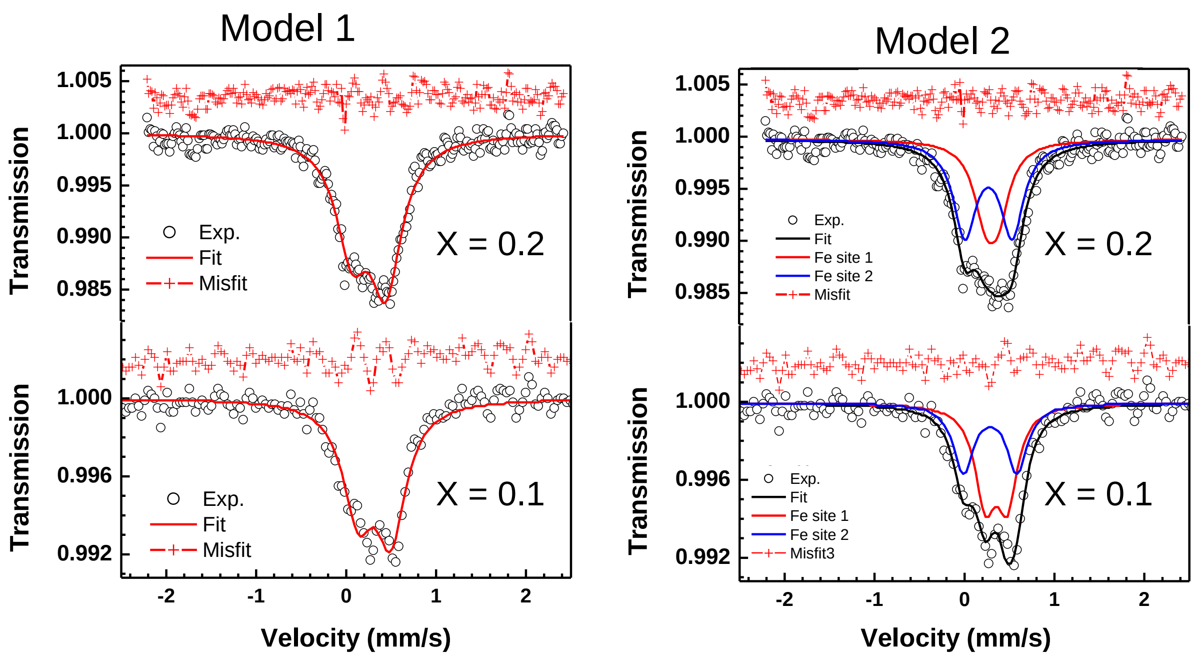

Figure 4.3. Mössbauer data for $YbCr_2Fe_xAl_{20-x}$ samples (with x = 0.1 and 0.2) fitted with two different models.

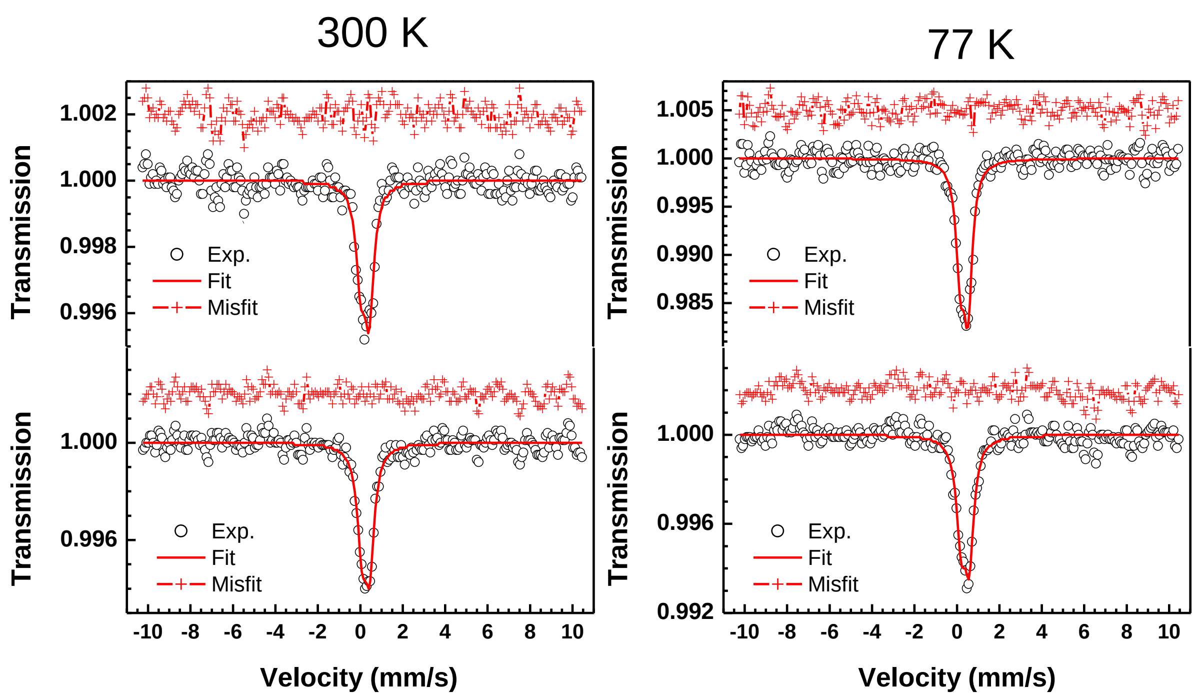

Figure 4.4. Mössbauer spectra at 300K and 77 K for $YbCr_2Fe_xAl_{20-x}$ samples (with x = 0.1 and 0.2)

Examining bond lengths, atomic displacement parameters (ADP), or site occupancies can be useful in determining partial or mixed occupancy in extended solids. As shown in Table 4.3, all bond lengths decrease as a function of Fe content. Therefore, the Fe sites could not be identified in this manner. Similarly, no ADP values were found to be anomalous, and refined site occupancies for all sites were within ~1% of fully occupied and were not helpful in determining the iron sites. Therefore to identify the iron occupied sites, refinements were conducted with iron occupying each pair of atomic positions. The total iron in the unit cell was restrained to the EDS values and the SUMP command in SHELXL97 was used to refine the iron occupancy of the two sites. Seven of the 10 possibilities were successfully refined and gave similar quality metrics (R factors, goodness of fit, and residual electron density). The remaining three refinements were unstable or resulted in negative site occupancies. Fe site occupancies for all models are provided in Appendix D. Sites were designated as more ordered or disordered based on the site symmetry to compare to the Mössbauer results. The assignments also agree with visual inspection of the coordination polyhedra shown in Figure 4.2. The model with iron occupying the Al1 and Al2 sites gave the best agreement with the site occupancies of the more ordered and disordered sites obtained from Mössbauer spectroscopy. This analysis assumes that the iron occupies the same two crystallographic sites in each of the two doping levels.

4.3.4 Physical Properties

Temperature dependent magnetic susceptibility data for $YbCr_2Al_{20}$, $YbCr_2Fe_{0.1}Al_{19.9}$, and $YbCr_2Fe_{0.2}Al_{19.8}$ are shown in Figure 4.5. The susceptibility for all three compounds is nearly temperature independent consistent with a non-magnetic Yb^{2+} and no moment due to Cr. This is similar to the previously reported CeT_2Al_{20} (T = Ti-Cr) compounds [158, 161, 162] which were also reported to be nearly temperature independent paramagnets.

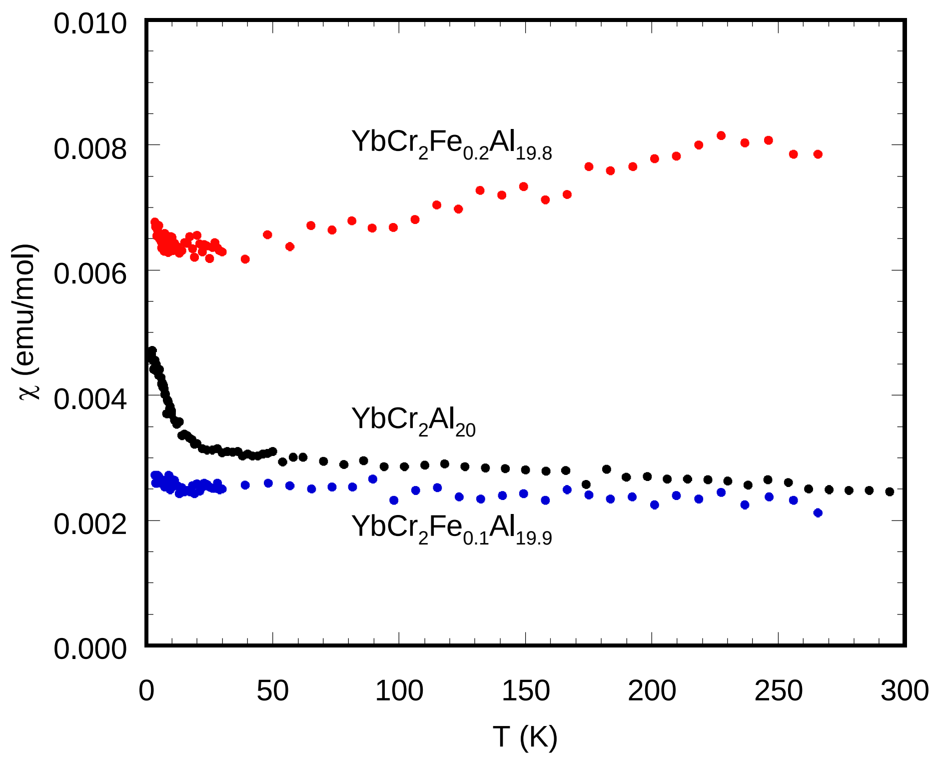

Figure 4.5. Temperature dependent magnetic susceptibility data for $YbCr_2Al_{20}$, $YbCr_2Fe_{0.1}Al_{19.9}$, $YbCr_2Fe_{0.2}Al_{19.8}$ are plotted as black, blue, and red circles, respectively. Data for $YbCr_2Al_{20}$ was obtained from reference [158].

Field dependent magnetization data at 3 K for $YbCr_2Fe_{0.1}Al_{19.9}$, and $YbCr_2Fe_{0.2}Al_{19.8}$ are shown in Figure 4.6. The magnetization of $YbCr_2Fe_{0.2}Al_{19.8}$ increases more rapidly with increasing field than $YbCr_2Fe_{0.1}Al_{19.9}$ and saturates at ~0.005 μ_B/mol. The magnetization of $YbCr_2Fe_{0.1}Al_{19.9}$ increases linearly with field after ~1 T and reaches ~ 0.007 μ_B/mol at 9 T. The magnetization of neither sample shows hysteresis.

Normalized resistivity (ρ_T / ρ_{290}) data for $YbCr_2Al_{20}$, $YbCr_2Fe_{0.1}Al_{19.9}$, and $YbCr_2Fe_{0.2}Al_{19.8}$ are shown in Figure 4.7. The resistivity of all three samples increases with temperature as expected for metals. The resistivity for $YbCr_2Al_{20}$ and $YbCr_2Fe_{0.1}Al_{19.9}$ are very similar while the low temperature resistivity for $YbCr_2Fe_{0.2}Al_{19.8}$ is higher. The increase in low temperature resistivity is consistent with the increased disorder. Magnetoresitance (MR% = (ρ_H-ρ_0)/ρ_0 x 100) for both compounds at 3 K reaches ~ 2% at 9 T which is typical for metals.

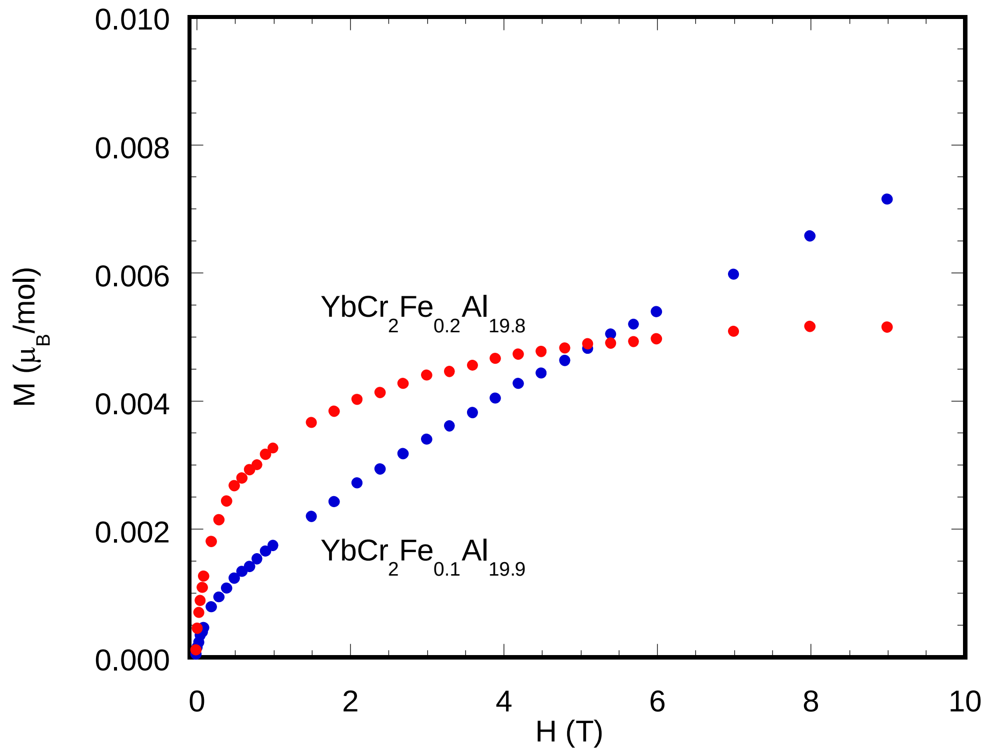

Figure 4.6. Field dependent magnetization data at 3 K is shown for $YbCr_2Fe_{0.1}Al_{19.9}$ and $YbCr_2Fe_{0.2}Al_{19.8}$.

4.4 Conclusions

Single crystals of $YbCr_2Fe_xAl_{20-x}$ (x ~ 0.1, 0.2) were grown in with molten aluminum flux. ^{57}Fe Mössbauer spectroscopy indicated that the iron atoms occupied two distinct crystallographic sites and was essential in determining which sites the iron atoms occupied. Crystallographic models were refined with Fe occupying each pair of crystallographic sites, and the best agreement with the Mössbauer spectroscopy was achieved when the Fe atoms partially occupied the Al1 (96*g*) and Al2 (48*f*) sites. The iron occupancy of the Al2 site remained fairly constant between the doping levels while the iron occupancy of the Al1 site increased from ~0.5% to ~1.3% for the larger doping level. The fact that the iron atoms do not occupy the transition metal site coincides with LnT_2Al_{20} compounds not being formed for the latter transition metals. Like $YbCr_2Al_{20}$, both $YbCr_2Fe_xAl_{20-x}$ compounds are nearly temperature independent paramagnets. All three samples exhibit metallic resistivity and the low temperature resistivity of $YbCr_2\ Fe_{0.2}Al_{18.8}$ is higher than that of the other two compounds consistent with increased disorder.

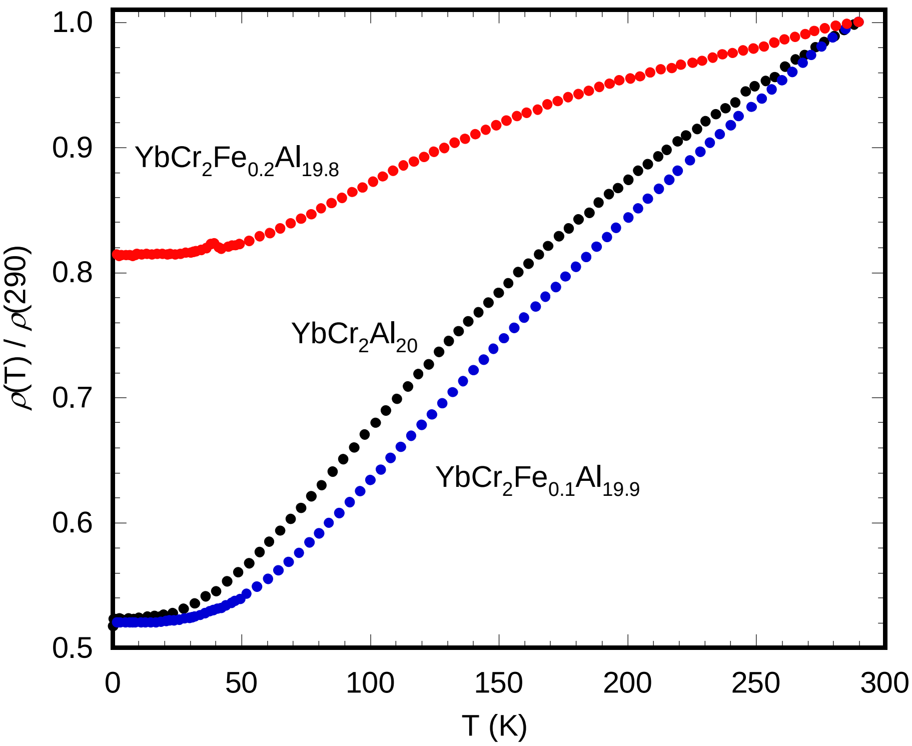

Figure 4.7. Temperature dependent normalized resistivity data for $YbCr_2Al_{20}$, $YbCr_2Fe_{0.1}Fe_{19.9}$, and $YbCr_2Fe_{0.2}Fe_{19.8}$, are shown as black, blue, and red circle, respectively. Data for $YbCr_2Al_{20}$ was obtained from reference [158].

4.5 References

[139] G. Knebel, D. Aoki, J.-P. Brison, L. Howald, G. Lapertot, J. Panarin, S. Raymond, J. Flouquet, Competition and/or coexistence of antiferromagnetism and superconductivity in $CeRhIn_5$ and $CeCoIn_5$, Phys. Status Solidi B, 247 (2010) 557-562.

[140] H. Hegger, C. Petrovic, E.G. Moshopoulou, M.F. Hundley, J.L. Sarrao, Z. Fisk, J.D. Thompson, Pressure-induced superconductivity in quasi-2D $CeRhIn_5$, Phys. Rev. Lett., 84 (2000) 4986.

[141] C. Geibel, S. Thies, D. Kaczorowski, A. Mehner, A. Grauel, B. Seidel, U. Ahlheim, R. Helfrich, K. Petersen, C.D. Bredl, F. Steglich, A new heavy-fermion superconductor: UNi_2Al_3, Z. Phys. B, 83 (1991) 305-306.

[142] E. Bauer, G. Hilscher, H. Michor, C. Paul, E.W. Scheidt, A. Gribanov, Y. Seropegin, H. Noël, M. Sigrist, P. Rogl, Heavy fermion superconductivity and magnetic order in noncentrosymmetric $CePt_3Si$, Phys. Rev. Lett., 92 (2004) 027003.

[143] C. Engkagul, R. Selim, T. Mihalisin, P. Schlottmann, YbSi: A nearly localized heavy-fermion antiferromagnet, Phys. Rev. B, 35 (1987) 3686-3689.

[144] P. Bonville, et al., Magnetic ordering in the heavy-electron compound YbSi, J. Phys.:Condens. Matter, 1 (1989) 8567.

[145] N. Tsujii, H. Kitazawa, T. Aoyagi, T. Kimura, G. Kido, Non-Fermi liquid behavior in $YbCu_2Si_2$, J. Magn. Magn. Mater., 310 (2007) 349-351.

[146] Y. Ōnuki, S. Yasui, M. Matsushita, S. Yoshiuchi, M. Ohya, Y. Hirose, N.D. Dung, F. Honda, T. Takeuchi, R. Settai, K. Sugiyama, E. Yamamoto, T.D. Matsuda, Y. Haga, T. Tanaka, Y. Kubo, H. Harima, Characteristic heavy fermion properties in $YbCu_2Si_2$ and YbT_2Zn_{20} (T: Co, Rh, Ir), J. Phys. Soc. Jpn., 80SA (2011) SA003.

[147] M.S. Torikachvili, S. Jia, E.D. Mun, S.T. Hannahs, R.C. Black, W.K. Neils, D. Martien, S.L. Bud'ko, P.C. Canfield, Six closely related YbT_2Zn_{20} (T = Fe, Co, Ru, Rh, Os, Ir) heavy fermion compounds with large local moment degeneracy, P. Natl. Acad. Sci. USA, 104 (2007) 9960-9963.

[148] P.C. Canfield, S. Jia, E.D. Mun, S.L. Bud'ko, G.D. Samolyuk, M.S. Torikachvili, Myriad of correlated electron effects found in the RT_2Zn_{20} family, Physica B, 403 (2008) 844-846.

[149] S. Jia, N. Ni, G.D. Samolyuk, A. Safa-Sefat, K. Dennis, H. Ko, G.J. Miller, S.L. Bud’ko, P.C. Canfield, Variation of the magnetic ordering in GdT_2Zn_{20} (T=Fe , Ru, Os, Co, Rh and Ir) and its correlation with the electronic structure of isostructural YT_2Zn_{20}, Phys. Rev. B, 77 (2008) 104408.

[150] W. Tian, A.D. Christianson, J.L. Zarestky, S. Jia, S.L. Bud’ko, P.C. Canfield, P.M.B. Piccoli, A.J. Schultz, Magnetic order in $TbCo_2Zn_{20}$ and $TbFe_2Zn_{20}$, Phys. Rev. B, 81 (2010) 144409.

[151] N. Ni, S. Jia, G.D. Samolyuk, A. Kracher, A.S. Sefat, S.L. Bud’ko, P.C. Canfield, Physical properties of $GdFe_2(Al_xZn_{1-x})_{20}$, Phys. Rev. B, 83 (2011) 054416.

[152] S. Niemann, W. Jeitschko, Ternary aluminides AT_2Al_{20} (A = rare earth elements and uranium; T = Ti, Nb, Ta, Mo, and W) with $CeCr_2Al_{20}$-type structure, J. Solid State Chem., 114 (1995) 337-341.

[153] P.I. Krypyakevich, O.S. Zarechnyuk, The RCr_2Al_{20} compounds in the systems of the rare earth metals and calcium and their crystal structures, Dopov. Akad. Nauk. Ukr., Ser A, 30 (1968) 364-366.

[154] T.J. Sato, S. Ibuka, Y. Nambu, T. Yamazaki, A. Sakai, S. Nakatsuji, Ferro-quadrupolar ordering in $PrTi_2Al_{20}$, arXiv:1108.3705 v1 [cond-mat.str-el].

[155] M. Koseki, Y. Nakanishi, K. Deto, G. Koseki, R. Kashiwazaki, F. Shichinomiya, M. Nakamura, M. Yoshizawa, A. Sakai, S. Nakatsuji, Ultrasonic investigation on a cage structure compound $PrTi_2Al_{20}$, J. Phys. Soc. Jpn., 80SA (2011) SA049.

[156] T.U. Ito, W. Higemoto, K. Nimomiya, H. Luetkens, C. Baines, A. Sakai, S. Nakatsuji, μSR Evidence of nonmagnetic order and ^{141}Pr hyperfine enhanced nuclear magnetism in the cubic Γ_3 ground doublet system $PrTi_2Al_{20}$, J. Phys. Soc. Jpn., 80 (2011) 113703.

[157] A. Sakai, S. Nakatsuji, Kondo effects and multipolar order in the cubic $PrTr_2Al_{20}$ (*Tr* = Ti, V), J. Phys. Soc. Jpn., 80 (2011) 063701.

[158] M.J. Kangas, D.C. Schmitt, A. Sakai, S. Nakatsuji, J.Y. Chan, Structure and physical properties of single crystal $PrCr_2Al_{20}$ and CeM_2Al_{20} (M = V, Cr): A comparison of compounds adopting the $CeCr_2Al_{20}$ structure type, J. Solid State Chem., in press (2012).

[159] A. Sakai, S. Nakatsuji, Strong valence fluctuation effects in $SmTr_2Al_{20}$ (Tr=Ti, V, Cr), Phys. Rev. B, 84 (2011) 201106(R).

[160] Y. Verbovytsky, K. Latka, K. Tomala, The crystal structure and magnetic properties of the GdV_2Al_{20} and $GdCr_2Al_{20}$ ternary compounds, J. Alloys Comp., 442 (2007) 334-336.

[161] O. Moze, L.D. Tung, J.J.M. Franse, K.H.J. Buschow, Crystal structure and magnetic properties of CeV_2Al_{20} and $CeCr_2Al_{20}$, J. Alloys Comp., 268 (1998) 39-41.

[162] V.M.T. Thiede, W. Jeitschko, S. Niemann, T. Ebel, $EuTa_2Al_{20}$, $Ca_6W_4Al_{43}$ and other compounds with $CeCr_2Al_{20}$ and $Ho_6Mo_4Al_{43}$ type structures and some magnetic properties of these compounds, J. Alloys Comp., 267 (1998) 23-31.

[163] N. Gross, T. Nasch, W. Jeitschko, Ternary intermetallics with high zinc content: TT'_2Zn_{20} (T=Zr, Hf, Nb; T'=Mn, Fe, Ru, Co, Rh, Ni) with $CeCr_2Al_{20}$-type structure, J. Solid State Chem., 161 (2001) 288-293.

[164] E.M. Benbow, S.E. Latturner, Mixed-metal flux synthesis of quaternary $RMn_2Tr_xZn_{20-x}$ compounds with Tr = Al, In, J. Solid State Chem., 179 (2006) 3989-3996.

[165] Z. Fisk, J.P. Remeika, Chapter 81 Growth of single crystals from molten metal fluxes, in: Karl A. Gschneidner, Jr., E. LeRoy (Eds.) Handbook on the Physics and Chemistry of Rare Earths, Elsevier, 1989, pp. 53-70.

[166] W.A. Phelan, M.C. Menard, M.J. Kangas, G.T. McCandless, B.L. Drake, J.Y. Chan, Adventures in crystal growth: synthesis and characterization of single crystals of complex intermetallic compounds, Chem. Mater., 24 (2012) 409-420.

[167] S. Niemann, W. Jeitschko, The crystal structure of $YbFe_2Al_{10}$, a combined substitution and stacking variant of the $ThMn_{12}$ and $CeMn_4Al_8$ type structures, Z. Kristallogr., 210 (1995) 338-341.

[168] A. Altomare, M.C. Burla, M. Camalli, G.L. Cascarano, C. Giacovazzo, A. Guagliardi, A.G.G. Moliterni, G. Polidori, R. Spagna, SIR97: a new tool for crystal structure determination and refinement, J. Appl. Crystallogr., 32 (1999) 115-119.

[169] G. Sheldrick, A short history of SHELX, Acta Crystallogr. A, 64 (2008) 112-122.

[170] T. Nasch, W. Jeitschko, U.C. Rodewald, Ternary rare earth transition metal zinc compounds RT_2Zn_{20} with T=Fe, Ru, Co, Rh, and Ni, Z. Naturforsch., B 52 (1997) 1023-1030.

[171] D.E. Sands, Q.C. Johnson, A. Zalkin, O.H. Krikorian, K.L. Kromholtz, The crystal structure of $ReBe_{22}$, Acta Crystallogr., 15 (1962) 832-834.

[172] S. Samson, The crystal structure of the intermetallic compound $ZrZn_{22}$, Acta Crystallogr., 14 (1961) 1229-1236.

[173] S. Samson, The crystal structure of the intermetallic compound $Mg_3Cr_2Al_{18}$, Acta Crystallogr., 11 (1958) 851-857.

[174] B. Cordero, V. Gomez, A.E. Platero-Prats, M. Reves, J. Echeverria, E. Cremades, F. Barragan, S. Alvarez, Covalent radii revisited, Dalton Trans., (2008) 2832-2838.

[175] E. Fazakas, S. Kane, K. Lazar, L. Varga, Mössbauer study of rapidly solidified Al-Fe based amorphous alloys, Hyperfine Interact., 189 (2009) 119-123.

[176] R. Preston, Mössbauer study of the surface barrier to the diffusion of iron into aluminum, Metall. Mater. Trans. B, 3 (1972) 1831-1835.

[177] S. Sério, J.C. Waerenborgh, M. Almeida, M. Godinho, ^{57}Fe Mössbauer spectroscopy and magnetization study of YFe_xAl_{12-x} ($4.4 < x < 5$), J. Magn. Magn. Mater., 265 (2003) 33-43.

[178] V.A. Shabashov, I.G. Brodova, A.G. Mukoseev, V.V. Sagaradze, A.V. Litvinov, Deformation-induced phase transformations in the Al-Fe system under intensive plastic deformation, J. Phys.:Condens. Matter, 19 (2007) 386222.

[179] J.C. Waerenborgh, P. Salamakha, O. Sologub, S. Sério, M. Godinho, A.P. Gonçalves, M. Almeida, Y-Fe-Al ternary system: partial isothermal section at 1070 K: Powder X-ray diffraction and Mössbauer spectroscopy study, J. Alloys Comp., 323-324 (2001) 78-82.

[180] A. Zaleskia, J. Fedotovaa, A. Ilyuschenkob, T. Talakob, A. Belyaevb, L. A., J. Stanekc, Mössbauer, XRD, and SEM Study of FeAl-based powder alloys with nanoinclusions, Acta Phys Pol, A, 109 (2006) 441-444.

Chapter 5. Magnetic and Electrical Properties of Flux Grown Single Crystals of $Ln_6M_4Al_{43}$ (Ln = Gd, Yb; M = Cr, Mo, W)

5.1 Introduction

Cerium containing intermetallics have garnered tremendous interest due to the discovery of magnetically mediated superconductivity and heavy fermion behavior [181-184]. Heavy electron systems are unusual materials where the electronic contribution to the specific heat (γ) is at least two orders of magnitude larger than that of typical metals, such as copper which has $\gamma \sim 1$ mJ/mol-K^2 [185]. Like the cerium-containing compounds, ytterbium intermetallics display unusual physical properties, such as, heavy fermion behavior, often resulting from valence instability. However, there are relatively few Yb analogues that have been extensively characterized due to the challenge of growing larger single crystals with Yb. A small number of ytterbium-based heavy fermion compounds have been reported including, YbSi [186], YbT_2Zn_{20} (T = Fe, Co, Ru, Rh, Os, Ir) [187], and $YbCu_2Si_2$ [188]. Quantum criticality has also been observed in a number of Yb compounds including, β-$YbAlB_4$[189], YbAgGe [190], and Yb_2Pd_2Sn [191]. A number of ytterbium superconductors have been reported including, Pd_2YbSn (T_C = 2.46 K) [192], $YbSb_2$ (T_C = 1.3 K) [193], β-$YbAlB_4$ (T_C = 80 mK) [194], and $YbGa_xSi_{2-x}$ (T_C = 2.5 K for x = 1) [195]. Synthesis and characterization of other ytterbium compounds could lead to a better understanding of other types of strongly correlated systems [196].

Structures containing magnetic ions in triangular networks often exhibit magnetic frustration [197-199]. Recently [200], we have synthesized and characterized single crystals of the $CeCr_2Al_{20}$ structure type [201], which can be stabilized for many AM_2Al_{20} analogues (A = La-Yb, and U; M = Ti, V, Cr, Nb, Mo, Ta, and W) [201-206]. Here, we have selected to work with compounds adopting the $Ho_6Mo_4Al_{43}$ structure type [207, 208] which is quite robust and can be stabilized for $A_6M_4Al_{43}$ (A = Ca, Y, Nd, Sm, Gd-Lu, U, and Th; M = Ti, V, Cr, Mn, Nb, Mo, Ta and W) [207-212]. Both structure types consist of similar coordination polyhedra, but differ in the interpenetrating networks of the lanthanides and transition metals. The $CeCr_2Al_{20}$ structure type consists of a diamond-like lanthanide network and a pyrochlore-like network of the transition metals. In the $Ho_6Mo_4Al_{43}$ structure type, the rare earth atoms form distorted kagome networks that stack along the *c*-axis, and the two transition metal polyhedra form columns through the six-member rings of the kagome network.

Magnetic properties were previously measured on polycrystalline samples of $Ln_6M_4Al_{43}$ (Ln = Nd, Gd-Tm; M = Ti, V, Cr, Nb, Mo, Ta and W), and the materials were reported to be ferromagnetic or metamagnetic with ordering temperatures below 20 K [213]. Polycrystalline $Gd_6Cr_4Al_{43}$ was found to have two antiferromagnetic transitions at 19.0(1) and 6.8(1) K and a linear field-dependent magnetization with no sign of saturation up to 5 T [213]. In addition, polycrystalline $Yb_6M_4Al_{43}$ (M = V, Cr, Nb, Ta, and W) showed non-Curie-Weiss behavior, indicating mixed or intermediate valence of the Yb ions [211]. However, there is still much to learn about these compounds. Herein, the synthetic details, flux growth synthesis, and the electrical and magnetic properties of single crystals of $Ln_6M_4Al_{43}$ (Ln = Gd and Yb; M = Cr, Mo, and W) are reported.

5.2 Experimental

5.2.1 Synthesis

The self-flux growth method was used to produce single crystals suitable for X-ray diffraction and physical property measurements. For all analogues, elements of at least 99.9% purity were weighed out and placed into an alumina crucible. The samples were then sealed in an evacuated fused silica tube, heat treated, and pulled from the furnace above the melting point of aluminum and centrifuged to remove excess flux. After centrifugation, residual flux was removed by etching with dilute (~ 1 M) NaOH solution.

The ternary phase diagrams for the Yb-Cr-Al system [210] and Gd-Cr-Al system [214] show a number of binary and ternary phases in the aluminum-rich region, so suitable reaction conditions had to be optimized to avoid both $LnAl_3$ and $LnCr_2Al_{20}$ ($CeCr_2Al_{20}$ type) [201]. A number of reaction ratios were evaluated, and it was found that when Yb and Cr were used in a molar ratio of 6:4, the concentration of aluminum flux governs the phases formed. Growths with molar ratios 6:4:43 and 6:4:60 yielded $Yb_6Cr_4Al_{43}$ and $YbAl_3$, while more flux-rich growths (6:4:100) yielded $Yb_6Cr_4Al_{43}$ and $YbCr_2Al_{20}$. Thus, the ratio 6:4:80 was found to be optimal at producing the desired $Yb_6Cr_4Al_{43}$ phase with minimal impurities and was also used to successfully synthesize $Gd_6Cr_4Al_{43}$.

Numerous temperature profiles were also explored to determine the optimal conditions for growth of $Yb_6Cr_4Al_{43}$. In all heat treatments, the samples were ramped to 1273 K and dwelled for 24 hours to ensure homogeneity. The samples were then cooled to 1073 K, with the ramp rates ranging from 1 K/h to 100 K/h. Although millimeter-sized crystals appeared to be well-formed by visual inspection for reactions cooled at 100 K/h, subsequent SEM-EDS and single crystal X-ray diffraction revealed the crystals were of poor crystal quality and contained aluminum-rich inclusions. Slow cooling (1-5 K/h) produced high-quality crystals with 1 K/h producing the largest crystals (1-5 mm on an edge) with hexagonal prismatic morphology, as shown in Figure 5.1.

For the growth of $Ln_6W_4Al_{43}$ (Ln = Yb, and Gd), a different set of conditions was found to be effective. Ln, W, and Al were weighed out in the ratio 1:2:50 and heated at a rate 160 K/h to 1273 K. The sample was dwelled for 5.2 h and then cooled to 973 K at 5.5 K/h. After this temperature was reached, the silica tube was centrifuged to try to separate crystals from the aluminum flux, and residual flux was removed by etching with a ~1 M NaOH solution. The resulting crystals were hexagonal prisms that were ~3 mm in length and ~2 mm in width.

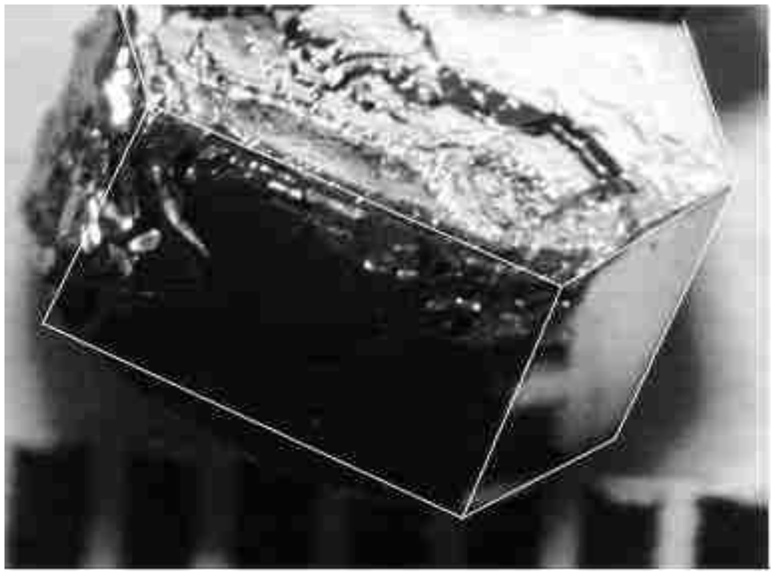

Figure 5.1. A single crystal of $Yb_6Cr_4Al_{43}$ shown on a mm scale. The white lines are drawn as guides to the eye.

Initial attempts to synthesize $Ln_6Mo_4Al_{43}$ (Ln = Gd, Yb) were conducted with the same reaction ratio (1:2:50) and heating profile (ramp to 1273 K, cool at 5.5 K/h to 973 K) as the tungsten growths. The gadolinium growth yielded hexagonal crystals (~2 mm in length and width), but the ytterbium growths yielded polycrystalline products. The synthesis of $Yb_6Mo_4Al_{43}$ using the same temperature profile to prepare the Cr analogue was successful; however, the reaction ratio of 6:4:120 was found to be optimal. Attempts with smaller concentration of Al produced polycrystalline ingots composed of $Yb_6Mo_4Al_{43}$, $YbAl_3$, and Al. More flux-rich growths produced smaller crystals of $Yb_6Mo_4Al_{43}$ and $MoAl_5$.

5.2.2 Structural Characterization

Structural characterization was conducted via single crystal X-ray diffraction and powder X-ray diffraction. Etched single crystals were selected, cut to an appropriate size, and mounted with epoxy on glass fibers. Data were collected on an Enraf Nonius Kappa CCD single crystal X-ray diffractometer with Mo Kα radiation (λ = 0.72073 Å) at room temperature. Crystal structures were solved by direct methods using SIR97 [215] and refined with SHELXL97 [216]. The final models were corrected for extinction, and the atomic displacement parameters were modeled anisotropically. Details of the data collection and refinement are provided in Tables 5.1 and 5.2 for the Gd and Yb analogues, respectively. Atomic positions and displacement parameters for the Gd and Yb analogues are provided in Tables 5.3 and 5.4, respectively, and selected interatomic distances are provided in Table 5.5. X-ray powder diffraction was used to confirm the crystal structure and phase purity. Samples for powder diffraction were manually ground and dispersed on a no-background holder. Data were collected on a Bruker D8 Advance powder diffractometer with Cu Kα radiation (λ = 1.540562 Å) over the range 5-80º in 2θ.

5.2.3 Elemental Analysis

Elemental analysis was conducted via energy dispersive spectroscopy (EDS) on a FEI Quanta 200 scanning electron microscope with an EDAX detector. The accelerating voltage was 20 kV. Spectra were integrated for 50 seconds and results from 5-10 spots were averaged. The approximate compositions obtained with EDS are provided in Table 5.6. The accuracy is estimated to be within 5-10 atomic percent of the values reported. For clarity, all compounds discussed will be referred to as $Ln_6M_4Al_{43}$ in the text.

5.2.4 Physical Properties

Single crystals selected for physical property measurements were first characterized by X-ray diffraction and energy dispersive spectroscopy. Magnetic data were collected using ACMS with a Quantum Design Physical Property Measurement System (PPMS). The temperature-dependent susceptibility data were measured under zero-field cooled (ZFC) conditions between 3 K and 300 K with an applied magnetic field of 0.1 T. Field-dependent magnetization data were measured at 3 K for all analogues and 13 K for $Gd_6Mo_4Al_{43}$ and $Gd_6W_4Al_{43}$ with applied fields up to 9 T. The additional measurements were conducted to investigate a low temperature feature in the magnetic susceptibility.

Table 5.1. $Gd_6M_4Al_{43}$ (M = Cr, Mo, and W) Crystallographic Parameters

Compound	$Gd_6Cr_4Al_{43}$	$Gd_6Mo_4Al_{43}$	$Gd_6W_4Al_{43}$
Refined Composition	$Gd_6Cr_{4.44}Al_{42.56}$	$Gd_6Mo_{4.17}Al_{42.83}$	$Gd_6W_{4.24}Al_{42.76}$
Crystal System	Hexagonal	Hexagonal	Hexagonal
Space Group	$P6_3/mcm$	$P6_3/mcm$	$P6_3/mcm$
a (Å)	10.9252(8)	11.0189(10)	11.0243(10)
c (Å)	17.7563(16)	17.7799(15)	17.7563(19)
c/*a*	1.625	1.614	1.611
V ($Å^3$)	1835.4(3)	1869.5(3)	1871.2(3)
Z	2	2	2
Crystal dimensions (mm)	0.05 x 0.05 x 0.05	0.05 x 0.05 x 0.05	0.08 x 0.08 x 0.08
θ range (°)	2.29 - 30.03	2.13 - 30.97	2.13 - 30.01
μ (mm^{-1})	12.967	12.844	24.461
Data Collection			
Measured Reflections	5798	7378	6054
Independent Reflections	1011	1104	1026
Reflections with I>2σ(I)	954	1050	955
R_{int}	0.0301	0.0296	0.0349
h	$-15 \leq h \leq 15$	$-15 \leq h \leq 15$	$-15 \leq h \leq 15$
k	$-12 \leq k \leq 12$	$-13 \leq k \leq 13$	$-12 \leq k \leq 12$
l	$-19 \leq l \leq 24$	$-25 \leq l \leq 25$	$-18 \leq l \leq 24$
Refinement			
R_1 (F)[a]	0.0165	0.0176	0.0221
wR_2[b]	0.0372	0.0398	0.0522
Reflections	1011	1104	1026
Parameters	54	54	54
$\Delta\rho_{max}$ (e $Å^{-3}$)	1.240	1.198	1.477
$\Delta\rho_{min}$ (e $Å^{-3}$)	-0.973	-1.137	-1.776
Extinction coefficient	0.00082(5)	0.00081(4)	0.00056(5)
GOF	1.174	1.114	1.215

[a] $R_1 = \Sigma||F_o| - |F_c||/\Sigma|F_o|$
[b] $R_w = [\Sigma [w(F_o^2 - F_c^2)^2]/\Sigma [w(F_o^2)^2]]^{1/2}$; $w = 1/[\sigma^2(F_o^2) + (0.012 P)^2 + 4.62 P]$, $w = 1/[\sigma^2(F_o^2) + (0.0131 P)^2 + 8.674 P]$, $w = 1/[\sigma^2(F_o^2) + (0.0226 P)^2 + 25.5395 P]$, for $Gd_6Cr_4Al_{43}$, $Gd_6Mo_4Al_{43}$, and $Gd_6W_4Al_{43}$, respectively.

Table 5.2. $Yb_6M_4Al_{43}$ (M = Cr, Mo, and W) Crystallographic Parameters

Compound	$Yb_6Cr_4Al_{43}$	$Yb_6Mo_4Al_{43}$	$Yb_6W_4Al_{43}$
Refined Composition	$Yb_6Cr_{5.23}Al_{41.77}$	$Yb_6Mo_{4.15}Al_{42.85}$	$Yb_6W_4Al_{43}$
Crystal System	Hexagonal	Hexagonal	Hexagonal
Space Group	$P6_3/mcm$	$P6_3/mcm$	$P6_3/mcm$
a (Å)	10.8819(5)	11.0034(10)	11.0079(10)
c (Å)	17.5876(12)	17.6903(15)	17.6878(15)
c/*a*	1.616	1.608	1.607
V (Å^3)	1803.62(19)	1854.9(3)	1856.2(3)
Z	2	2	2
Crystal dimensions (mm)	0.05 x 0.08 x 0.08	0.05 x 0.08 x 0.10	0.08 x 0.08 x 0.08
θ range (°)	3.17 - 30.03	2.3 – 30.99	2.14 – 28.69
μ (mm^{-1})	17.927	17.345	28.322
Data Collection			
Measured Reflections	6219	7302	2972
Independent Reflections	993	1098	903
Reflections with I>2σ(I)	937	1034	824
R_{int}	0.0266	0.0483	0.0297
h	$-15 \le h \le 15$	$-15 \le h \le 15$	$0 \le h \le 14$
k	$-12 \le k \le 12$	$-13 \le k \le 13$	$-12 \le k \le 0$
l	$-24 \le l \le 21$	$-25 \le l \le 25$	$-23 \le l \le 23$
Refinement			
R_1 (F)[a]	0.0182	0.0238	0.0262
wR_2[b]	0.0415	0.0573	0.0658
Reflections	993	1098	903
Parameters	54	54	53
$\Delta\rho_{max}$ (e Å^{-3})	1.003	1.784	2.227
$\Delta\rho_{min}$ (e Å^{-3})	-0.0835	-2.626	-2.019
Extinction coefficient	0.00111(5)	0.00589(19)	0.00046(6)
GOF	1.238	1.141	1.100

[a] $R_1 = \Sigma||F_o| - |F_c||/\Sigma|F_o|$

[b] $R_w = [\Sigma [w(F_o^2 - F_c^2)^2]/\Sigma [w(F_o^2)^2]]^{1/2}$; $w = 1/[\sigma^2(F_o^2) + (0.0099\ P)^2 + 11.31\ P]$, $w = 1/[\sigma^2(F_o^2) + (0.0269\ P)^2 + 9.49\ P]$, and $w = 1/[\sigma^2(F_o^2) + (0.0393\ P)^2 + 22.1100\ P]$ for $Yb_6Cr_4Al_{43}$, $Yb_6Mo_4Al_{43}$, and $Yb_6W_4Al_{43}$, respectively.

Preliminary measurements on $Gd_6Cr_4Al_{43}$ indicated minimal anisotropy in T_N, θ, and μ_{eff}, so only measurements with the magnetic field applied parallel to the *c*-axis are presented herein. The electrical resistivity measurements were performed on single crystals by the standard four-probe AC technique.

Table 5.3. $Ln_6M_4Al_{43}$ (Ln = Gd and Yb; M = Cr, Mo, and W) Atomic Positions

Element	Position	symmetry	x	y	z	U_{eq} (Å^2)[a]
Gd1	12k	*m*	0.468807(16)	0	0.095407(10)	0.00794(7)
Cr1	6g	*mm*	0.26560(7)	0	1/4	0.00666(16)
Cr2	2b	$\bar{3}m$	0	0	0	0.0069(3)
Al1	24l	1	0.23329(8)	0.39203(8)	0.16536(5)	0.01040(16)
Al2	12k	*m*	0.15654(10)	0	0.11526(7)	0.0096(2)
Al3	12k	*m*	0.25119(10)	0	0.52991(7)	0.0103(2)
Al4	12j	*m*	0.14580(12)	0.54713(11)	1/4	0.0098(2)
Al5	12i	2	0.24758(6)	0.49515(12)	0	0.0152(3)
Al6[b]	8h	3	1/3	2/3	0.12848(8)	0.0110(4)
Al7	6g	*m*2*m*	0.85392(12)	0	1/4	0.0089(3)
Gd1	12k	*m*	0.469694(17)	0	0.095044(7)	0.00917(7)
Mo1	6g	*mm*	0.26856(4)	0	1/4	0.00545(10)
Mo2	2b	$\bar{3}m$	0	0	0	0.00571(14)
Al1	24l	1	0.23573(9)	0.39396(9)	0.16413(5)	0.01010(17)
Al2	12k	*m*	0.15959(11)	0	0.11451(7)	0.0099(2)
Al3	12k	*m*	0.25364(11)	0	0.53028(7)	0.0095(2)
Al4	12j	*m*	0.14687(13)	0.55042(12)	1/4	0.0099(2)
Al5	12i	2	0.24706(6)	0.49413(13)	0	0.0113(2)
Al6[c]	8h	3	1/3	2/3	0.12699(8)	0.0096(4)
Al7	6g	*m*2*m*	0.85233(16)	0	1/4	0.0091(3)
Gd1	12k	*m*	0.53199(6)	0	0.09572(3)	0.01237(16)
W1	6g	*mm*	0.73173(4)	0	1/4	0.00620(12)
W2	2b	$\bar{3}m$	0	0	0	0.00648(16)
Al1	24l	1	0.15864(19)	0.39462(18)	0.16372(10)	0.0111(3)
Al2	12k	*m*	0.1605(2)	0	0.61382(14)	0.0101(5)
Al3	12k	*m*	0.2537(2)	0	0.03015(15)	0.0100(5)
Al4	12j	*m*	0.1469(3)	0.5962(3)	1/4	0.0107(5)
Al5	12i	2	0.24714(13)	0.4943(3)	0	0.0118(5)
Al6[d]	8h	3	1/3	2/3	0.12831(13)	0.0123(7)
Al7	6g	*m*2*m*	0.1486(3)	0	1/4	0.0096(9)

[a] U_{eq} is defined as one-third of the trace of the orthogonalized U_{ij} tensor.
[b] Al6 site mixed occupancy with 11.0(7) % Cr.
[c] Al6 site mixed occupancy with 4.1(3) % Mo.
[d] Al6 site mixed occupancy with 6.1(2) % W.

Table 5.4. $Ln_6M_4Al_{43}$ (Ln = Gd and Yb; M = Cr, Mo, and W) Atomic Positions

Element	Position	symmetry	x	y	z	U_{eq} (Å^2)[a]
Yb1	12k	*m*	0.467340(19)	0	0.095353(12)	0.00923(8)
Cr1	6g	*mm*	0.26318(9)	0	1/4	0.0063(2)
Cr2	2b	$\bar{3}m$	0	0	0	0.0065(3)
Al1	24l	1	0.23420(11)	0.39397(11)	0.16381(7)	0.0105(2)
Al2	12k	*m*	0.15624(14)	0	0.11513(9)	0.0092(3)
Al3	12k	*m*	0.25258(14)	0	0.52973(9)	0.0108(3)
Al4	12j	*m*	0.14704(16)	0.54639(15)	1/4	0.0100(3)
Al5	12i	2	0.24847(8)	0.49694(17)	0	0.0224(4)
Al6[b]	8h	3	1/3	2/3	0.13014(10)	0.0123(4)
Al7	6g	*m*2*m*	0.85152(19)	0	1/4	0.0087(4)
Yb1	12k	*m*	0.46918(2)	0	0.094516(13)	0.00941(10)
Mo1	6g	*mm*	0.26852(5)	0	1/4	0.00559(14)
Mo2	2b	$\bar{3}m$	0	0	0	0.00574(19)
Al1	24l	1	0.23644(13)	0.39415(12)	0.16359(7)	0.0106(2)
Al2	12k	*m*	0.15968(15)	0	0.11431(9)	0.0098(3)
Al3	12k	*m*	0.25457(14)	0	0.53080(10)	0.0097(3)
Al4	12j	*m*	0.14642(18)	0.54960(17)	1/4	0.0107(3)
Al5	12i	2	0.24694(9)	0.49388(17)	0	0.0111(3)
Al6[c]	8h	3	1/3	2/3	0.12667(10)	0.0098(6)
Al7	6g	*m*2*m*	0.8520(2)	0	1/4	0.0093(4)
Yb1	12k	*m*	0.46893(4)	0	0.09475(2)	0.01041(15)
W1	6g	*mm*	0.26884(4)	0	1/4	0.00655(16)
W2	2b	$\bar{3}m$	0	0	0	0.0069(2)
Al1	24l	1	0.2369(2)	0.3944(2)	0.16349(12)	0.0110(4)
Al2	12k	*m*	0.1610(3)	0	0.11401(16)	0.0113(6)
Al3	12k	*m*	0.2544(3)	0	0.53107(17)	0.0110(6)
Al4	12j	*m*	0.1464(3)	0.5502(3)	1/4	0.0107(6)
Al5	12i	2	0.24704(15)	0.4941(3)	0	0.0117(6)
Al6[d]	8h	3	1/3	2/3	0.12613(19)	0.0088(6)
Al7	6g	*m*2*m*	0.8520(4)	0	1/4	0.0103(8)

[a] U_{eq} is defined as one-third of the trace of the orthogonalized U_{ij} tensor.
[b] Al6 site mixed occupancy with 30.8(10) % Cr.
[c] Al6 site mixed occupancy with 3.7(5) % Mo.
[d] Al6 site is fully occupied with Al.

Table 5.5. Selected Interatomic Distances (Å)

	$Gd_6Cr_4Al_{43}$	$Yb_6Cr_4Al_{43}$	$Gd_6Mo_4Al_{43}$	$Yb_6Mo_4Al_{43}$	$Gd_6W_4Al_{43}$	$Yb_6W_4Al_{43}$
Ln(17 coordinate)						
Ln - Al4 (x2)	3.0727(6)	3.0531(7)	3.0921(6)	3.0852(8)	3.0877(13)	3.0816(14)
Ln - Al5 (x2)	3.0806(2)	3.0588(2)	3.0994(3)	3.0845(8)	3.1018(4)	3.0867(4)
Ln - Al1 (x2)	3.0820(8)	3.0617(11)	3.0700(9)	3.0620(12)	3.0681(18)	3.059(2)
Ln - Al3	3.2564(12)	3.2095(16)	3.2588(12)	3.2390(16)	3.260(3)	3.249(3)
Ln - Al6 (x2)	3.2261(3)	3.2200(4)	3.2484(4)	3.2447(4)	3.2536(5)	3.2435(6)
Ln - Al1 (x2)	3.2985(10)	3.2584(11)	3.3346(12)	3.3303(16)	3.3260(16)	3.304(2)
Ln - Al3	3.2727(11)	3.2590(16)	3.2608(12)	3.2419(16)	3.267(2)	3.2472(11)
Ln - Al5 (x2)	3.3773(12)	3.3653(17)	3.3929(16)	3.3835(17)	3.3992(14)	3.3878(14)
Ln - Al2	3.4297(11)	3.4032(15)	3.4345(13)	3.4235(17)	3.419(2)	3.4067(5)
Ln - Ln1	3.4560(4)	3.4286(4)	3.4451(4)	3.4121(4)	3.4575(6)	3.4209(7)
Ln - M1	3.5304(6)	3.5119(7)	3.5359(4)	3.5271(5)	3.5310(5)	3.5203(5)
M1 (12coordinate)						
M1 - Al7 (x2)	2.5171(7)	2.4870(9)	2.5670(4)	2.5633(5)	2.5662(5)	2.5672(10)
M1 - Al4 (x2)	2.6643(13)	2.6696(17)	2.6905(13)	2.6792(17)	2.697(2)	2.683(3)
M1 - Al2 (x2)	2.6728(8)	2.6422(16)	2.6917(12)	2.6826(16)	2.697(3)	2.682(3)
M1 - Al1 (x4)	2.6725(8)	2.6817(11)	2.7200(9)	2.7239(12)	2.7272(18)	2.729(2)
M1 - Ln1 (x2)	3.5304(6)	3.5119(7)	3.5359(4)	3.5271(5)	3.5309(5)	3.5203(5)
M2 (12 coordinate)						
M2 - Al2 (x6)	2.6671(12)	2.6440(15)	2.6903(12)	2.6789(16)	2.688(2)	2.685(3)
M2 - Al3 (x6)	2.7952(11)	2.7979(15)	2.8462(12)	2.8537(16)	2.847(2)	2.853(3)
Ln-Ln Network						
Ln-Ln NN // *c* [a]	3.5304(6)	3.4286(4)	3.4451(4)	3.4121(4)	3.4575(6)	3.409(7)
Ln-Ln NNN // *c* [b]	5.4900(6)	5.4397(6)	5.5102(5)	5.5011(6)	5.4988(8)	5.4921(7)
Ln-Ln // *ab*	5.4944(4)	5.4757(3)	5.5397(5)	5.5330(5)	5.5434(6)	5.5357(6)

[a] Nearest neighbors
[b] Next nearest neighbors

Table 5.6. Elemental Analysis

Compound	% Ln [a]	% T [a]	% Al [a]	Composition [b]
$Gd_6Cr_4Al_{43}$	13(2)	10(1)	76(4)	$Gd_6Cr_{4.6(7)}Al_{34.0(16)}$
$Yb_6Cr_4Al_{43}$	10(1)	9(1)	81(1)	$Yb_6Cr_{5.6(2)}Al_{50.3(5)}$
$Gd_6Mo_4Al_{43}$	10(1)	9(1)	81(1)	$Gd_6Mo_{5.1(6)}Al_{47.1(7)}$
$Yb_6Mo_4A_{43}$	16(1)	12(1)	71(1)	$Yb_6Mo_{4.6(3)}A_{26.2(1)}$
$Gd_6W_4Al_{43}$	12(1)	7(1)	81(1)	$Gd_6W_{3.5(1)}Al_{40.2(6)}$
$Yb_6W_4Al_{43}$	11(1)	7(1)	82(1)	$Yb_6W_{4.2(2)}Al_{46.5(2)}$

[a] Percentages given as atomic percent
[b] Formula normalized to Ln = 6

5.3 Results and Discussion

5.3.1 Crystal Structure

Since all six $Ln_6M_4Al_{43}$ (Ln = Gd, Yb; M = Cr, Mo, W) analogues adopt the $Ho_6Mo_4Al_{43}$ structure type (space group *$P6_3/mcm$*, *a* ~ 11 Å and *c* ~17.8 Å), we will limit the description of the structure to $Yb_6Cr_4Al_{43.}$ As expected from covalent radii [217], the Cr analogues are smallest while the larger Mo and W analogues are similar. Comparing the lattice parameters of $Yb_6Cr_4Al_{43}$ (*a* = 10.8819(5) Å, *c* = 17.5576(12) Å, *c*/*a* = 1.616) and $Yb_6Mo_4Al_{43}$ (*a* = 11.0034(10) Å, *c* = 17.6903(15) Å, *c*/*a* = 1.608), it is evident that the lattice expands in both directions upon incorporation of the larger transition metal. The *c*/*a* ratio of $Yb_6Mo_4Al_{43}$ (1.608) is smaller than that of $Yb_6Mo_4Al_{43}$ (1.616), indicating the expansion is most significant in the *ab*-plane. For all three transition metals, the ytterbium analogues are slightly smaller than the corresponding gadolinium analogue. Comparing the lattice parameters and *c*/*a* ratio of $Yb_6Cr_4Al_{43}$ (*c*/*a* = 1.616) and $Gd_6Cr_4Al_{43}$ (*a* = 10.9252(8) Å, *c* = 17.7563(16) Å, *c*/*a* = 1.625), it is evident that the lattice expands in all directions, but most significantly along the *c*-direction with the incorporation of the larger lanthanide. The same trend can also be observed in the other transition metal analogues. Unit cell volumes of all analogues reported here are in good agreement with previously reported values, with the present volumes larger by less than 1% [207, 213].

The crystal structure of $Yb_6Cr_4Al_{43}$, as shown in Figures 5.2 and 5.3, consists of one lanthanide site, two Cr sites, and seven Al sites, and can be visualized as two interpenetrating networks of Yb atoms and Cr polyhedra. The Yb site, shown in Figure 5.4, is coordinated by 1 Yb atom, 1 Cr atom, and 15 Al atoms. Yb-Al distances range from 3.0531(7) Å to 3.4032 (15) Å, and the coordinated Yb atom is at 3.4286(4) Å. The Yb polyhedra form a kagome network in the *ab* plane with the in-plane Yb atoms separated by 5.4757(3) Å. The angles of the hexagonal rings of the kagome lattice are distorted from the 120° of a regular hexagon to ~107° and ~133°, while the triangles remain equilateral triangles. A second kagome layer is separated from the first by ~ 3.4 Å and slightly offset from the first. A second pair of kagome layers is stacked along the *c*-direction with a larger Yb-Yb interatomic distance of 5.4397(6) Å.

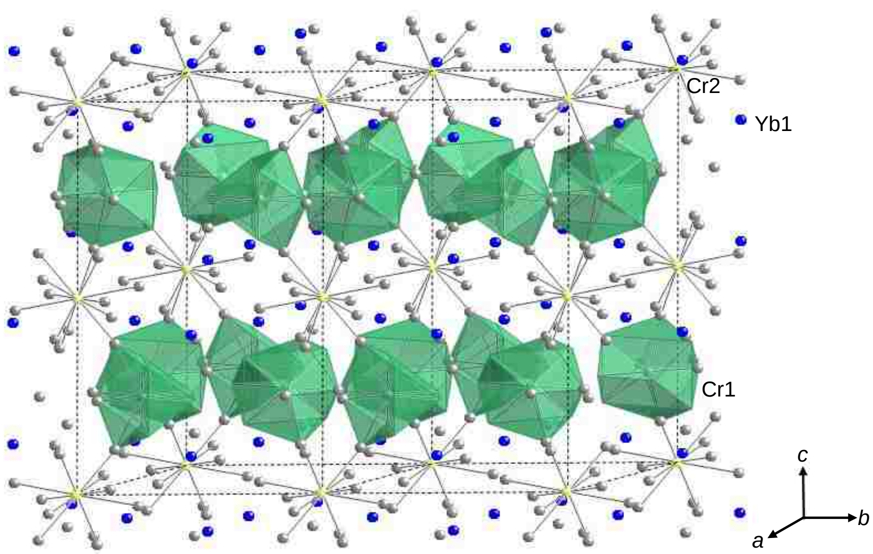

Figure 5.2. Transition metal sublattices in $Yb_6Cr_4Al_{43}$ crystal structure viewed along the ***bc*** plane. Cr1 polyhedra are shown as green translucent solids and Cr2 polyhedra are shown as light green spheres with bonds. The Cr2 polyhedron occupies the center of a trigonal anti-prism formed by 6 Cr1 polyhedra. Aluminum atoms are grey spheres and Yb atoms are blue spheres.

The center of the two 6-membered rings of the kagome lattices is occupied by a Cr2 icosahedron, and Cr1 slabs lie above and below the ytterbium kagome layers, as shown in Figure 2. The Cr1 slabs are composed of groups of three Cr1 icosahedra which are corner-sharing with each other by Al7 atoms. Another group of three Cr1 icosahedra is colligated perpendicular to the hexagonal plane. The two sets of three icosahedral combinations of Cr1 atoms form columns in the *c*-direction, which is depicted in Figure 3. The Cr2 icosahedra are corner-sharing via Al2 atoms with six Cr1 polyhedra forming trigonal antiprisms. Cr1 atoms are surrounded by 10 Al atoms and 2 Yb atoms, with Cr-Al bond distances ranging from 2.4870(9) to 2.6817(11) Å and a Cr-Yb bond distance of 3.5119(7) Å. Cr2 atoms are surrounded by six Al2 and six Al3 atoms with bond distances of 2.6440(15) Å and 2.7979(15) Å, respectively.

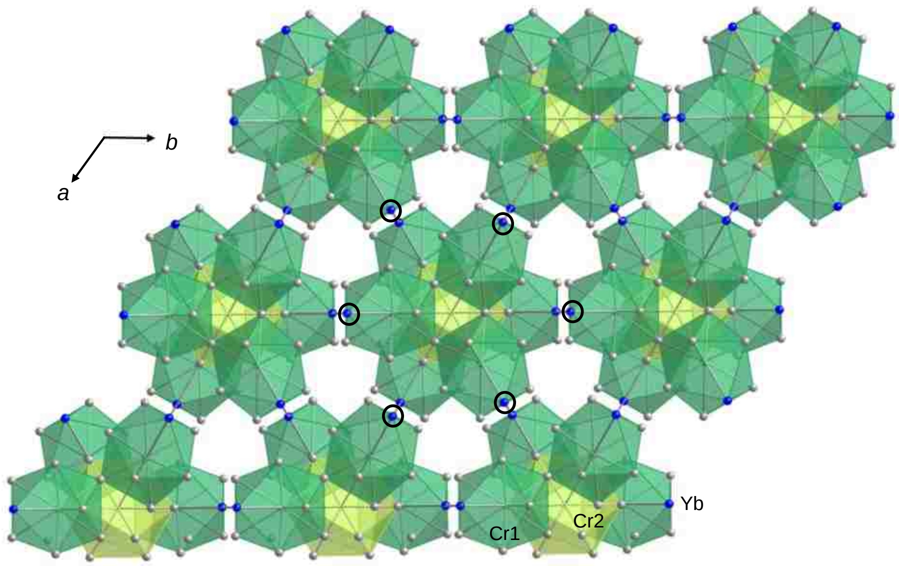

Figure 5.3. Transition metal sublattices in $Yb_6Cr_4Al_{43}$ structure type as viewed perpendicular to the ***ab*** plane. Cr2 polyhedra are shown as light green translucent polyhedra which are surrounded by a trigonal anti-prism of Cr1 polyhedra (green translucent solids). Aluminum atoms are grey spheres and Yb atoms are blue spheres. The black circles are a guide to the eye to highlight Yb atoms that make up the six-membered ring of one of the kagome layers.

During refinement, it was noticed that the atomic displacement parameter of the Al6 site was smaller than the other aluminum sites coupled with some unaccounted electron density at this position. The Al6 site of several compounds with the $Ho_6Mo_4Al_{43}$ structure type have been previously modeled with a mixed-occupancy of aluminum and the transition metal, and the transition metal occupancy has been reported to be as high as 44(2)% in $Y_6Cr_{6.57}Al_{40.43}$ [218]. Consistent with the previous reports, the Al6 position was modeled with mixing of Al and Cr, Mo, or W. The transition metal occupancies of the Al6 site in the present study range from 30.8(10)% ($Yb_6Cr_4Al_{43}$) to 0% ($Yb_6W_4Al_{43}$), but the remaining four analogues are all between 3 and 11%. The larger mixed-occupancies on the Al6 site for the Cr analogues is likely due to the similar size of Cr and Al compared to the heavier Mo and W analogues.

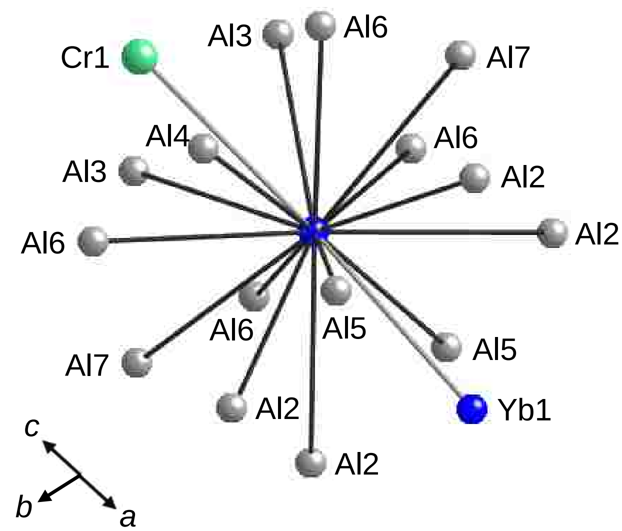

Figure 5.4. The Yb local environment. Aluminum, chromium, and ytterbium atoms are depicted as gray, green, and blue spheres, respectively.

5.3.2 Magnetic Properties

Figure 5.5 shows the temperature dependent magnetic susceptibility data for $Gd_6Cr_4Al_{43}$, $Gd_6Mo_4Al_{43}$, and $Gd_6W_4Al_{43}$ with the inset highlighting the low temperature (< 50 K) features. In $Gd_6Cr_4Al_{43}$ and $Gd_6W_4Al_{43}$, a drop in susceptibility is present at 19 K and 15 K, respectively, consistent with antiferromagnetic ordering. In both analogues there is a slight upturn below 10 K. $Gd_6Mo_4Al_{43}$ shows different behavior with slope changes at ~10 and ~15 K, but for all temperatures the susceptibility increases with decreasing temperature. The magnetic ordering temperature of $Gd_6Cr_4Al_{43}$ is in excellent agreement with a previous report on a polycrystalline sample that showed two successive antiferromagnetic orderings at 19.0(1) K and 6.8(1) K [213]. However, in the present study a second ordering at a lower temperature was not observed. A previous study on polycrystalline $Gd_6Mo_4Al_{43}$ and $Gd_6W_4Al_{43}$ indicated that the type of ordering could not be determined with certainty and that the magnetic orderings occurred below 10 K [211]. All three analogues show Curie-Weiss behavior at high temperatures and were fit to a modified Curie-Weiss equation, $\chi = \chi_0 + (C/(T-\theta))$, where C is the Curie constant, χ_0 is temperature independent paramagnetism/diamagnetism, and θ is the Weiss temperature. The parameters from the Curie-Weiss fits are provided in Table 5.7. All three analogues show positive Weiss temperatures of 14.9(4) K, 18.6(2), and 16.4(3) K for $Gd_6Cr_4Al_{43}$, $Gd_6Mo_4Al_{43}$, and $Gd_6W_4Al_{43}$, respectively, suggesting ferromagnetic exchange interactions. Although there are differences in the magnitudes, the positive θ agree with previously reported data on polycrystalline samples of $Gd_6Cr_4Al_{43}$ (7.9(1) K) [213], $Gd_6Mo_4Al_{43}$ (12(5) K) [211], and $Gd_6W_4Al_{43}$ (8(5) K) [211]. The trend of θ for the three analogues can be rationalized by the Ruderman-Kittel-Kasuya-Yosida (RKKY) exchange mechanism and Gd-Gd nearest neighbor distances, which are 3.5304(6) Å, 3.4451(4) Å, and 3.4575 (6) Å for $Gd_6Cr_4Al_{43}$, $Gd_6Mo_4Al_{43}$, and $Gd_6W_4Al_{43}$, respectively. It is worth noting that neither the Gd-Gd next nearest distance nor the Gd-Gd distance in the *ab*-plane display the same trend. The effective moments (μ_{eff}) from the Curie-Weiss fits are 7.94(5), 8.01(3), and 7.90(4) μ_B/mol Gd, for $Gd_6Cr_4Al_{43}$, $Gd_6Mo_4Al_{43}$, and $Gd_6W_4Al_{43}$, respectively, and are in excellent agreement with the magnetic moment expected for a free Gd^{3+} ion (7.94 μ_B).

Table 5.7. Magnetic Properties

Compound	Fit range	Field (T)	μ_{calc} ($\mu_{B/mol}$)	μ_{eff} ($\mu_{B/mol}$)	θ (K)	T (K)	χ_0 (emu/mol)
$Gd_6Cr_4Al_{43}$	>80	0.1	7.94	7.94(5)	14.9(4)	19	0.0001(2)
$Gd_6Mo_4Al_{43}$	>90	0.1	7.94	8.01(3)	18.6(2)	15?	-0.0002(1)
$Gd_6W_4A_{l43}$	>80	0.1	7.94	7.90(4)	16.4(3)	15	0.0004(1)

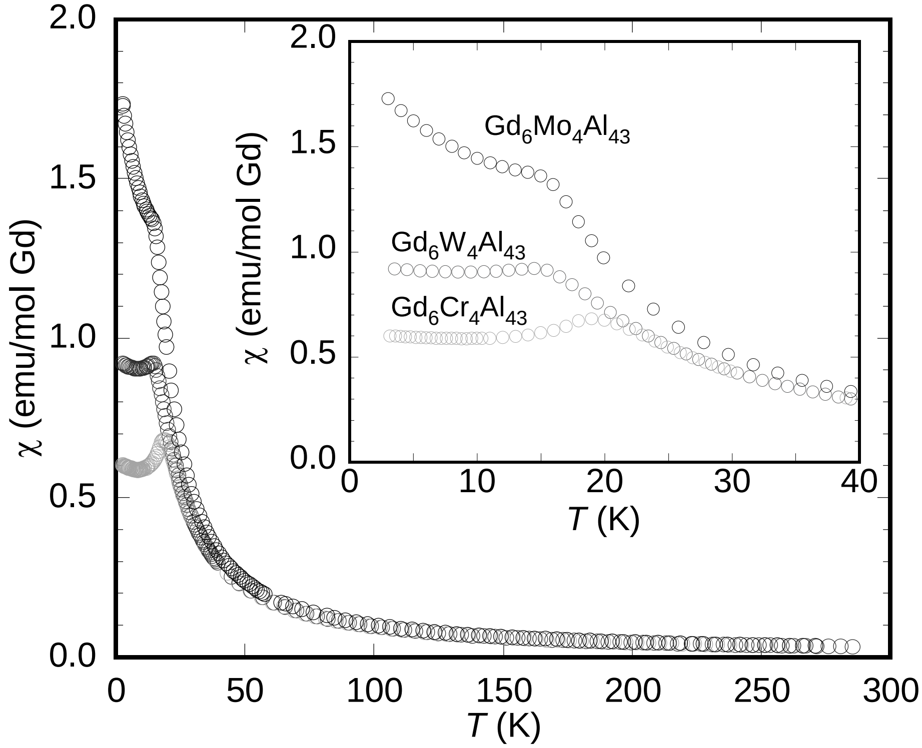

Figure 5.5. Temperature dependent magnetic susceptibility for $Gd_6Cr_4Al_{43}$, $Gd_6Cr_4Al_{43}$, and $Gd_6Cr_4Al_{43}$. The inset shows the low temperature region.

Field dependent magnetism for $Gd_6Cr_4Al_{43}$, $Gd_6Mo_4Al_{43}$, and $Gd_6W_4Al_{43}$ at 3 K and in applied fields up to 9 T is shown in Figure 5.6, and the inset of Figure 5.6 shows the field dependent magnetization at 13 K for $Gd_6Mo_4Al_{43}$, and $Gd_6W_4Al_{43}$. At 3 K, all samples show approximately linear behavior until they show saturation near 5 T. The magnetic moments at saturation are approximately 6.3, 6.6, and 6.5 μ_B/mol Gd for $Gd_6Cr_4Al_{43}$, $Gd_6Mo_4Al_{43}$, and $Gd_6W_4Al_{43}$, respectively, and are less than the expected 7 μ_B/mol Gd expected for a spin-only Gd^{3+} ion. Magnetization data at 13 K was collected to compare the magnetic behavior of $Gd_6W_4Al_{43}$ which shows a clear maximum in susceptibility at 15 K and $Gd_6Mo_4Al_{43}$ which only shows a slope change near 15 K. In both analogues, the magnetization at 13 K shows a similar trend as the 3 K data, but the magnetization at 9 T is only 5.9 and 5.3 μ_B/mol Gd for $Gd_6Mo_4Al_{43}$

and $Gd_6W_4Al_{43}$, respectively. The field-dependent behavior and saturated moment are consistent with the previously reported results for polycrystalline samples [211, 213].

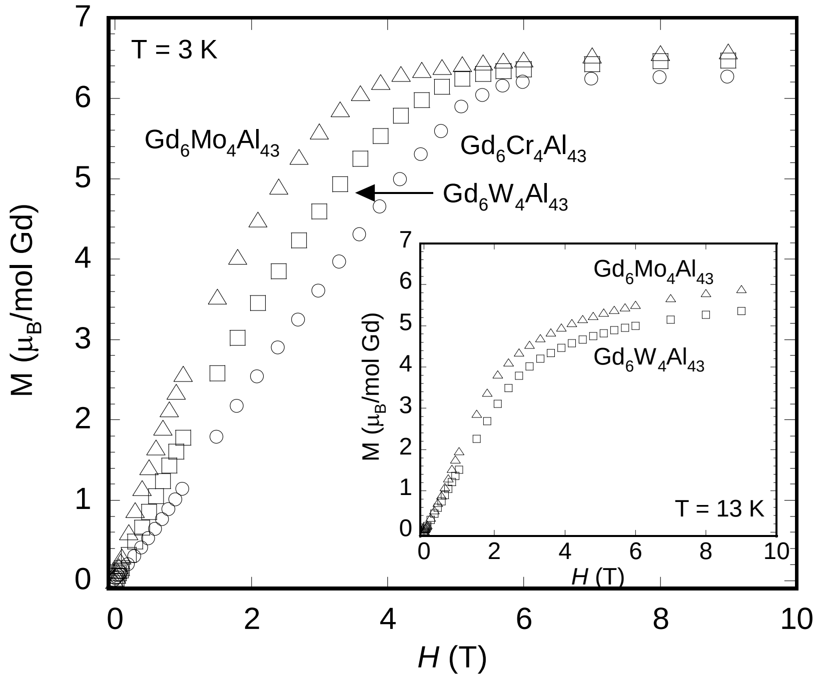

Figure 5.6. Field dependent magnetism at 3 K. $Gd_6Cr_4Al_{43}$, $Gd_6Mo_4Al_{43}$, and $Gd_6W_4Al_{43}$ are depicted as circles, triangles, and squares, respectively. The inset shows field dependent magnetization at 13 K for $Gd_6Mo_4Al_{43}$ and $Gd_6W_4Al_{43}$.

Unlike $GdCr_2Al_{20}$ which behaves like a typical antiferromagnet (T_N = 3.90(5) K, θ = -2.4(1) K) [206], $Gd_6M_4Al_{43}$ (M = Cr, Mo, W) is likely more complex as a positive θ suggests ferromagnetic interactions, while there is a decrease in the low temperature susceptibility below ~20 K. A maximum in susceptibility followed by a decrease is often a sign of antiferromagnetic order, and previously reported antiferromagnets with positive θ include $NaNiO_2$ [219] and EuSnP [220]. The crystal structures of both of these compounds feature slabs of magnetic ions, and the combination of ferromagnetism and antiferromagnetism is the result of one type of ferromagnetic interactions within the slab and antiferromagnetic between the slabs. For example, in $NaNiO_2$ (T_N = 20 K, θ = 36 K), there are ferromagnetic sheets of Ni ions which are coupled antiferromagnetically. Below the ordering temperature (3 K), $NaNiO_2$ shows magnetization that is approximately linear with applied field between a spin-flop at 1.8 T and saturation at 10 T [219]. The crystal structure of EuSnP (spacegroup *P*4/*nmm*) is composed of two EuP slabs and a Sn-only slab stacked along the *c*-axis. The magnetic structure has been described as ferromagnetically coupled slabs with antiferromagnetic interactions between the slabs. However, due to the stacking pattern, the antiferromagnetic interactions could be between adjacent Eu-P slabs or pairs Eu-P slabs that are separated by the tin layers [220]. The $Yb_6Cr_4Al_{43}$ structure can also be described as a stacking of pairs of rare earth kagome slabs, so a similar magnetic structure could potentially exist in the present compounds.

Magnetic susceptibility, not shown, for $Yb_6Cr_4Al_{43}$, $Yb_6Mo_4Al_{43}$, and $Yb_6W_4Al_{43}$ is consistent with nearly temperature independent paramagnets with susceptibilities of ~10^{-2} emu/mol Yb and is consistent with non-magnetic divalent ytterbium. The valence assignment is supported by the similarity between the lattice parameters of the Gd and Yb analogues as expected for divalent Yb. The nonmagnetic behavior of $Yb_6Cr_4Al_{43}$, $Yb_6Mo_4Al_{43}$, and $Yb_6W_4Al_{43}$ is similar to that of $YbCr_2Al_{20}$ which showed nearly temperature independent susceptibility [200], but contrasts with previous reports on $Yb_6Cr_4Al_{43}$ and $Yb_6W_4Al_{43}$ that showed non-Curie-Weiss behavior which was attributed to mixed or intermediate valence [211]. Magnetic properties have not previously been reported for $Yb_6Mo_4Al_{43}$. Differences in the physical properties between single crystals and polycrystalline samples are common and can be caused by slight changes in disorder, composition, or impurities. For example, $EuCu_2Si_2$ single crystals grown from an indium flux shows antiferromagnetic order at 10 K, and the magnetic moment is consistent with a divalent Eu (μ_{eff} = 7.8(1) μ_B) [221]. This behavior contrasts with polycrystalline samples and single crystals grown via the floating zone technique which show intermediate valence and lack magnetic ordering [221, 222].

5.3.3 Resistivity

Figure 5.7 shows temperature dependent resistivity for single crystals of $Ln_6M_4Al_{43}$ (Ln = Yb, Gd; M = Cr, Mo, W). All six analogues show metallic behavior for the entire temperature range investigated (3-300 K) with room temperature resistivities of a few hundred μΩ-cm and residual resistivity ratio values of 1.1, 1.9, 1.3, 1.2, 2.7, and 1.9 for $Gd_6Cr_4Al_{43}$, $Yb_6Cr_4Al_{43}$, $Gd_6Mo_4Al_{43}$, $Yb_6Mo_4Al_{43}$, $Gd_6W_4Al_{43}$, and $Yb_6W_4Al_{43}$, respectively. The similar residual resistivity ratios of all six analogues indicate the samples are all of comparable crystal quality.

The $Gd_6M_4Al_{43}$ (M = Cr, Mo) compounds are more metallic than the comparable ytterbium analogues. However, the resistivity of $Yb_6W_4Al_{43}$ is larger than that of $Gd_6W_4Al_{43}$. One possible explanation for this anomaly is that unlike the other analogues, the Al6 site in $Yb_6W_4Al_{43}$ is not partially occupied by the transition metal leading to changes in the number of conduction electrons. No decrease in spin disorder scattering below ~20 K is observed in the resistivity of $Gd_6M_4Al_{43}$ (M = Cr, Mo, and W) which would be expected for a magnetic ordering. Therefore, the downturn in susceptibility could be attributed to a spin reorientation.

5.4 Conclusions

One of the challenges of using flux growth is to find the optimal conditions to promote the growth of the target phase and to avoid competing phases, and the variables include the choice of flux, the reaction stoichiometry, and the heat treatment [184]. The synthesis of Yb compounds, in particular, can be difficult due to the high vapor pressure of Yb. For the $Ln_6M_4Al_{43}$ compounds it was found the ratio of aluminum flux was critical in determining the product. Likewise adjusting the cooling rate was effectual in producing millimeter-sized well-formed single crystals. Unlike other systems, such as, $CePdGa_6$, Ce_2PdGa_{12}, and Ce_2PdGa_{12}, the cooling rate had minimal effects on the phases produced [184].

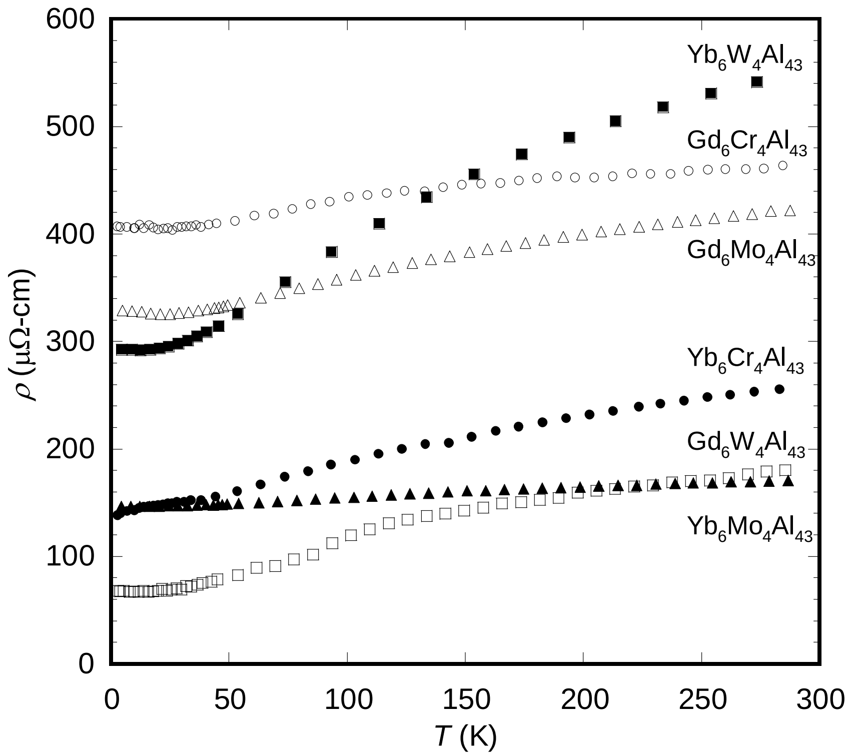

Figure 5.7. Temperature dependent resistivity. Chromium, molybdenum, and tungsten analogues are depicted as circles, triangles, and squares, respectively. Ytterbium analogues are depicted as filled symbols and gadolinium analogues are depicted as open symbols.

Physical properties were collected on millimeter-sized single crystals of $Ln_6M_4Al_{43}$ (Ln = Gd, Yb; M = Cr, Mo, W). Resistivity measurements show that all six analogues reported herein show metallic behavior. Unlike the previous reports on polycrystalline samples magnetic measurements indicate that the ytterbium analogues are divalent rather than of mixed or intermediate valence. The magnetic moments (μ_{eff}) for $Gd_6Cr_4Al_{43}$ (7.94(5) μ_B/mol), $Gd_6Mo_4Al_{43}$ (8.01(3) μ_B/mol), and $Gd_6W_4Al_{43}$ (7.90(4) μ_B/mol) are consistent with that expected for a Gd^{3+} ion (7.94 μ_B/mol). The magnetic structure is likely complex as Weiss temperatures suggest ferromagnetic interactions and there is a maximum in the low temperature magnetic susceptibility. The lack of a decrease in the resistivity due to spin disorder scattering is consistent with a spin reorientation rather than magnetic order. Unfortunately the high neutron absorption cross-section of gadolinium limits the possibility to use neutron diffraction to accurately determine the magnetic structure.

5.5 References

[181] N.D. Mathur, F.M. Grosche, S.R. Julian, I.R. Walker, D.M. Freye, R.K.W. Haselwimmer, G.G. Lonzarich, Magnetically mediated superconductivity in heavy fermion compounds, Nature, 394 (1998) 39-43.

[182] Z. Fisk, H.R. Ott, T.M. Rice, J.L. Smith, Heavy-electron metals, Nature, 320 (1986) 124-129.

[183] E.L. Thomas, J.N. Millican, E.K. Okudzeto, J.Y. Chan, Crystal growth and the search for highly correlated intermetallics, Comments Inorg. Chem., 27 (2006) 1 - 39.

[184] W.A. Phelan, M.C. Menard, M.J. Kangas, G.T. McCandless, B.L. Drake, J.Y. Chan, Adventures in crystal growth: synthesis and characterization of single crystals of complex intermetallic compounds, Chem. Mater., 24 (2012) 409-420.

[185] Z. Fisk, J.L. Sarrao, J.L. Smith, J.D. Thompson, The physics and chemistry of heavy fermions, P. Natl. Acad. Sci. USA, 92 (1995) 6663-6667.

[186] C. Engkagul, R. Selim, T. Mihalisin, P. Schlottmann, YbSi: A nearly localized heavy-fermion antiferromagnet, Phys. Rev. B, 35 (1987) 3686-3689.

[187] M.S. Torikachvili, S. Jia, E.D. Mun, S.T. Hannahs, R.C. Black, W.K. Neils, D. Martien, S.L. Bud'ko, P.C. Canfield, Six closely related YbT_2Zn_{20} (T = Fe, Co, Ru, Rh, Os, Ir) heavy fermion compounds with large local moment degeneracy, P. Natl. Acad. Sci. USA, 104 (2007) 9960-9963.

[188] N. Tsujii, H. Kitazawa, T. Aoyagi, T. Kimura, G. Kido, Non-Fermi liquid behavior in $YbCu_2Si_2$, J. Magn. Magn. Mater., 310 (2007) 349-351.

[189] Y. Matsumoto, S. Nakatsuji, K. Kuga, Y. Karaki, N. Horie, Y. Shimura, T. Sakakibara, A.H. Nevidomskyy, P. Coleman, Quantum criticality without tuning in the mixed valence compound β-$YbAlB_4$, Science, 331 (2011) 316-319.

[190] G.M. Schmiedeshoff, E.D. Mun, A.W. Lounsbury, S.J. Tracy, E.C. Palm, S.T. Hannahs, J.H. Park, T.P. Murphy, S.L. Bud'ko, P.C. Canfield, Multiple regions of quantum criticality in YbAgGe, Phys. Rev. B, 83 (2011) 180408.

[191] T. Muramatsu, T. Kanemasa, T. Kagayama, K. Shimizu, Y. Aoki, H. Sato, M. Giovannini, P. Bonville, V. Zlatic, I. Aviani, R. Khasanov, C. Rusu, A. Amato, K. Mydeen, M. Nicklas, H. Michor, E. Bauer, Reentrant quantum criticality in Yb_2Pd_2Sn, Phys. Rev. B, 83 (2011) 180404.

[192] H.A. Kierstead, B.D. Dunlap, S.K. Malik, A.M. Umarji, Shenoy, K. G, Coexistence of ordered magnetism and superconductivity in Pd_2YbSn, Phys. Rev. B, 32 (1985) 135-138.

[193] Y. Yamaguchi, S. Waki, K. Mitsugi, Superconductivity of $YbSb_2$, J. Phys. Soc. Jpn., 56 (1987) 419-420.

[194] S. Nakatsuji, K. Kuga, Y. Machida, T. Tayama, T. Sakakibara, Y. Karaki, H. Ishimoto, S. Yonezawa, Y. Maeno, E. Pearson, G.G. Lonzarich, L. Balicas, H. Lee, Z. Fisk, Superconductivity and quantum criticality in the heavy-fermion system β-$YbAlB_4$, Nat Phys, 4 (2008) 603-607.

[195] N. Tsujii, M. Imai, H. Yamaoka, I. Jarrige, H. Oohashi, T. Tochio, K. Handa, J. Ide, H. Atsuta, Y. Ito, H. Yoshikawa, H. Kitazawa, Phase stability and superconducting properties of AlB_2-type $YbGa_xSi_{2-x}$ ($1.12 \leq x \leq 1.49$), Chem. Mater., 22 (2010) 4690-4699.

[196] Z. Fisk, A whiff of chemistry in heavy electron physics, Science, 318 (2007) 1559-1560.

[197] A.P. Ramirez, Strongly geometrically frustrated magnets, Annu. Rev. Mater. Sci., 24 (1994) 453-480.

[198] J.E. Greedan, Geometrically frustrated magnetic materials, J. Mater. Sci., 11 (2001) 37-53.

[199] C. Lacroix, Magnetic properties of strongly frustrated and correlated systems, Physica B, 404 (2009) 3038-3041.

[200] M.J. Kangas, D.C. Schmitt, A. Sakai, S. Nakatsuji, J.Y. Chan, Structure and physical properties of single crystal $PrCr_2Al_{20}$ and CeM_2Al_{20} (M = V, Cr): A comparison of compounds adopting the $CeCr_2Al_{20}$ structure type, J. Solid State Chem., in press (2012).

[201] P.I. Krypyakevich, O.S. Zarechnyuk, The RCr_2Al_{20} compounds in the systems of the rare earth metals and calcium and their crystal structures, Dopov. Akad. Nauk. Ukr., Ser A, 30 (1968) 364-366.

[202] K. Okuda, S. Noguchi, Y. Nakazawa, M. Ishikawa, Synthesis and characterization of new ternary uranium compound UCr_2Al_{20}, J. Phys. Soc. Jpn., 58 (1989) 4296-4299.

[203] S. Niemann, W. Jeitschko, Ternary aluminides AT_2Al_{20} (A = rare earth elements and uranium; T = Ti, Nb, Ta, Mo, and W) with $CeCr_2Al_{20}$-type structure, J. Solid State Chem., 114 (1995) 337-341.

[204] V.M.T. Thiede, W. Jeitschko, S. Niemann, T. Ebel, $EuTa_2Al_{20}$, $Ca_6W_4Al_{43}$ and other compounds with $CeCr_2Al_{20}$ and $Ho_6Mo_4Al_{43}$ type structures and some magnetic properties of these compounds, J. Alloys Comp., 267 (1998) 23-31.

[205] I. Halevy, E. Sterer, M. Aizenshtein, G. Kimmel, D. Regev, E. Yahel, L.C.J. Pereira, A.P. Goncalves, High pressure studies of a new ternary actinide compound, UV_2Al_{20}, J. Alloys Comp., 319 (2001) 19-21.

[206] Y. Verbovytsky, K. Latka, K. Tomala, The crystal structure and magnetic properties of the GdV_2Al_{20} and $GdCr_2Al_{20}$ ternary compounds, J. Alloys Comp., 442 (2007) 334-336.

[207] S. Niemann, W. Jeitschko, Ternary aluminides $A_6T_4Al_{43}$ with A=Y, Nd, Sm, Gd-Lu, Th, U and T = Cr, Mo, W, Z. Metallkd., 85 (1994) 345-349.

[208] T.I. Yanson, M.B. Manyako, O.I. Bodak, O.S. Zarechnyuk, R.E. Gladyshevskii, R. Cerny, K. Yvon, Hexagonal $Yb_6Cr_{4+x}Al_{43-x}$ (x = 1.76) with a new structure type, Acta Crystallogr. C, 50 (1994) 1529-1531.

[209] T.I. Yanson, M.B. Manyako, O.I. Bodak, R. Cerny, J.V. Pacheco, K. Yvon, Crystal structure of terbium chromium aluminum, $Tb_6Cr_{4+x}Al_{43-x}$ (x=1.6), erbium chromium aluminum $Er_6Cr_{4+x}Al_{43-x}$ (x=1.96), homium chromium aluminum $Ho_6Cr_{4+x}Al_{43-x}$ (x=1.6), and lutecium chromium aluminum $Lu_6Cr_{4+x}Al_{43-x}$ (x=2.76), Z. Kristallogr., 209 (1994) 922-923.

[210] T.I. Yanson, N.B. Manyako, O.I. Bodak, R. Cerny, R.E. Gladyshevskii, K. Yvon, Peculiarities of the interaction of ytterbium with transition metals (Cr,Mn) and aluminium, J. Alloys Comp., 219 (1995) 219-221.

[211] M.W. Wolff, S. Niemann, T. Ebel, W. Jeitschko, Magnetic properties of rare-earth transition metal aluminides $R_6T_4Al_{43}$ with $Ho_6Mo_4Al_{43}$-type structure, J. Magn. Magn. Mater., 223 (2001) 1-15.

[212] C.L. Condron, J.D. Strand, P.C. Canfield, G.J. Miller, The intermetallic compound $Gd_6Ta_4Al_{43}$, Acta Crystallogr. E, 59 (2003) i147-i148.

[213] Y. Verbovytsky, K. Latka, K. Tomala, The crystal structure and magnetic properties of the $Gd_6Cr_4Al_{43}$ compound, J. Alloys Comp., 450 (2008) 114-117.

[214] M. Ling, Y. Liang, S. Wei, Y. Liu, M. Pang, Y. Zhan, Y. Du, Experimental investigation of the Al-Cr-Gd ternary system at 773 K, J. Phase Equilib. Diffus., 33 (2012) 203-209.

[215] A. Altomare, M.C. Burla, M. Camalli, G.L. Cascarano, C. Giacovazzo, A. Guagliardi, A.G.G. Moliterni, G. Polidori, R. Spagna, SIR97: a new tool for crystal structure determination and refinement, J. Appl. Crystallogr., 32 (1999) 115-119.

[216] G. Sheldrick, A short history of SHELX, Acta Crystallogr. A, 64 (2008) 112-122.

[217] B. Cordero, V. Gomez, A.E. Platero-Prats, M. Reves, J. Echeverria, E. Cremades, F. Barragan, S. Alvarez, Covalent radii revisited, Dalton Trans., (2008) 2832-2838.

[218] R. Cerny, K. Yvon, T.I. Yanson, M.B. Manyako, O.I. Bodak, Rietveld refinement of the crystal structures of hexagonal $Y_6Cr_{4+x}Al_{43-x}$ (x=2.57) and tetragonal $YCr_{4-x}Al_{8+x}$ (x=1.22), Powder Diffr., 10 (1995) 86-90.

[219] E. Chappel, M.D. Núñez-Regueiro, F. Dupont, G. Chouteau, C. Darie, A. Sulpice, Antiferromagnetic resonance and high magnetic field properties of $NaNiO_2$, Eur. Phys. J. B, 17 (2000) 609-614.

[220] A.C. Payne, A.E. Sprauve, A.P. Holm, M.M. Olmstead, S.M. Kauzlarich, EuSnP: a novel antiferromagnet with two-dimensional, corrugated Sn sheets, J. Magn. Magn. Mater., 338 (2002) 229-234.

[221] P.G. Pagliuso, J.L. Sarrao, J.D. Thompson, M.F. Hundley, M.S. Sercheli, R.R. Urbano, C. Rettori, Z. Fisk, S.B. Oseroff, Antiferromagnetic ordering of divalent Eu in $EuCu_2Si_2$ single crystals, Phys. Rev. B, 63 (2001) 092406.

[222] C. Cao, W. Löser, G. Behr, R. Klingeler, N. Leps, H. Vinzelberg, B. Büchner, Self-flux growth of large $EuCu_2Si_2$ single crystals, J. Cryst. Growth, 318 (2011) 1043-1047.

Chapter 6. Crystal Growth, Structure, and Physical Properties of Ln_2PdGa_{12} (Ln = La, Pr, Nd, and Sm)*

6.1 Introduction

The competition of interactions in highly correlated systems can lead to new and interesting phenomena. These interactions can be tuned by changing temperature, field, pressure, or chemical doping. Compounds adopting the $HoCoGa_5$ structure type [223] provide a number of remarkable examples. These include the heavy fermion superconductors $CeCoIn_5$ [224] and $CeIrIn_5$, and the antiferromagnetic superconductor $CeRhIn_5$ [225]. The discovery of these phases led our group to investigate whether similar phases could be found in the Ce-Pd-Ga phase space. Three new phases were discovered: $CePdGa_6$ [226], Ce_2PdGa_{12} [227], and Ce_2PdGa_{10} [228]. All three structure types are tetragonal and can be described as layers of cerium and gallium resembling those found in the $HoCoGa_5$ structure type compounds [223]. $CePdGa_6$ and Ce_2PdGa_{12} are heavy fermion antiferromagnets with γ ~300 mJ/K^2-mol (T_N = 10 K) and γ ~72 mJ/K^2-mol (T_N = 11 K), respectively. Heavy fermions are compounds where conduction electrons interact strongly with local magnetic moments and thus behave as if they have increased electron mass. A large (γ >100 mJ/K^2-mol) Sommerfeld parameter is a characteristic of these materials and is determined by fitting low-temperature heat capacity to $C = \gamma T + \beta T^3$, where βT^3 is the phonon contribution to the specific heat. Ce_2PdGa_{10} does not show any magnetic ordering down to 2K; however, it shows a positive 200% change in magnetoresistance in a 9-T field.

Further studies were conducted on Ce_2NiGa_{12} and Ce_2CuGa_{12} to determine the role the transition metal plays in the physical properties. The nickel analogue is a moderate heavy

---

* Originally appeared as M.J. Kangas, B.L. Drake, N. Haldolaarachchige, D.P. Young, J.Y. Chan, Crystal growth, structure, and physical properties of Ln_2PdGa_{12} (Ln = La, Pr, Nd, and Sm), J. Alloys Comp., 514 (2012) 64-70. Reprinted by permission of Journal of Alloys and Compounds.

fermion ($\gamma \sim 191$ mJ/K^2-mol) and also displays antiferromagnetic ordering, while the copper analogue does not show magnetic ordering down to 2 K, and the electron mass is less enhanced ($\gamma \sim 69$ mJ/K^2-mol) [229]. Investigation of the phases Ln_2MGa_{12} (Ln= Pr, Nd, Sm and M = Cu, Ni) show antiferromagnetic order between 3 and 18 K, with Nd_2NiGa_{12} showing the highest ordering of the nickel series, and Nd_2CuGa_{12} having the lowest ordering of the copper series. However, we note that in the copper analogues, occupancies on the transition metal sites decrease going from Ce to Sm [230].

Many Ce-, Yb-, and U-containing heavy fermion compounds have been discovered. However, relatively few heavy fermion compounds have been discovered for the lanthanides Pr, Nd, and Sm [231]. Notable Pr heavy fermions include $Pr(Cu,Ga)_{13-x}$ ($\gamma \sim 100$ mJ/mol K^2) [232], $PrOs_4Sb_{12}$ ($\gamma \sim 500$ mJ/K^2-mol) [233], $Pr_2Rh_3Ge_5$ ($\gamma \sim 80$ mJ/K^2-mol) [234], and $PrInAg_2$ ($\gamma \sim 6{,}500$ mJ/K^2-mol) [235]. Unlike Ce and U compounds, where valence instability correlates with heavy fermion behavior, the trivalent Pr materials are stable, and the enhanced electron mass has been attributed to quadrupolar-Kondo interactions or the interaction of a low-lying excited state [234-236]. Herein we report the synthesis, structure, and the physical properties of Pr_2PdGa_{12}, Nd_2PdGa_{12}, and Sm_2PdGa_{12}.

6.2 Experimental

6.2.1 Synthesis

Single crystals of La_2PdGa_{12}, Pr_2PdGa_{12}, Nd_2PdGa_{12}, and Sm_2PdGa_{12} were grown in the presence of excess Ga flux [237]. Ln (99.9%, chunks, Alfa Aesar), Pd (99.995%, powder, Alfa Aesar) and Ga (99.99999%, pellets, Alfa Aesar) were used as received and were placed in alumina crucibles with a reaction ratio of 1.5:1:15 for Ln:Pd:Ga. Each crucible was loaded into a fused silica tube and the contents evacuated (0.05 – 0.07 mmHg) and sealed. The samples were placed into a furnace and heated to a dwell temperature of 1423 K for 7 hours at 170 K/h. The samples were then rapidly cooled (150 K/h) to 773 K followed by slow cooling to 673 K at a rate of 8 K/h. The samples were then inverted and centrifuged to separate the single crystals from excess Ga flux. Residual flux on the surface of the crystals was removed by sonicating in hot water or etching with a solution of iodine in dimethylformamide (3 M). Etched crystals were thin silver plates of ~1-2 mm^2. Single crystals were mechanically separated based on morphology and were ground and characterized by powder X-ray diffraction and the data show that the sample is indeed homogeneous and single phase. Attempts to extend the series to Gd with the same reaction conditions were unsuccessful and resulted in the formation of the Gd_4PdGa_{12} which crystallizes in the Y_4PdGa_{12} structure type [238].

6.2.2 X-ray Diffraction and Elemental Analysis

For each compound, a suitable crystal of approximately 0.05 × 0.05 × 0.05 mm^3 were cut and mounted to the tip of a glass fiber using epoxy. They were then positioned onto the goniometer of a Nonius Kappa diffractometer. Diffraction data were collected at 298 K with Mo K_α radiation (λ = 0.71073 Å). Further crystallographic parameters for Ln_2PdGa_{12} (Ln = La, Pr, Nd, and Sm) are provided in Table 6.1. The crystal structure was solved with direct methods using SIR97 to give a starting model and refined with SHELXL97 [239, 240]. Structural refinement included extinction and anisotropic atomic displacement parameters. The extinction coefficient for the La analogue was subsequently removed as it was not statistically significant. Attempts to refine the occupancy of each atomic position individually resulted in nearly 100% occupancy of each site, and all sites were treated as fully-occupied in the final model. In addition, an attempt to split the Ga4 site into two partially-occupied sites, as observed in La_2CuGa_{12} [229], resulted in minimal occupancy (~5%) of the minority site and was not considered in the final model. Atomic positions and displacement parameters are presented in Table 6.2, and selected interatomic distances are provided in Table 6.3. The *001* reflection was found to be obstructed by the X-ray beam stop in the Pr, Nd, and Sm analogues and was omitted from the final model.

Table 6.1 Crystallographic Parameters

Compound	La_2PdGa_{12}	Pr_2PdGa_{12}	Nd_2PdGa_{12}	Sm_2PdGa_{12}
Crystal System	tetragonal	tetragonal	tetragonal	tetragonal
Space Group	*P*4/*nbm*	*P*4/*nbm*	*P*4/*nbm*	*P*4/*nbm*
a (Å)	6.1550(9)	6.0870(6)	6.0680(12)	6.0480(12)
c (Å)	15.594(2)	15.547(2)	15.531(2)	15.5100(16)
V (Å^3)	590.76(15)	576.04(11)	571.86(18)	567.33(17)
Z	2	2	2	2
Crystal dimensions (mm)	0.03x0.05x0.05	0.08x0.08x 0.08	0.08x0.08x0.08	0.05x0.08x0.08
θ range (^{o})	2.61 - 30.01	2.62 - 29.96	2.62 - 30.04	2.63 - 30.04
μ (mm^{-1})	35.331	37.275	38.107	39.61
Data Collection				
Measured Reflections	1572	1454	1283	1327
Independent Reflections	497	477	479	478
Reflections with I>2σ(I)	409	453	325	389
R_{int}	0.0333	0.0265	0.1052	0.0647
h	$-8 \leq h \leq 8$	$-8 \leq h \leq 8$	$-8 \leq h \leq 8$	$-8 \leq h \leq 8$
k	$-8 \leq k \leq 8$	$-6 \leq k \leq 6$	$-6 \leq k \leq 6$	$-6 \leq k \leq 6$
l	$-21 \leq l \leq 21$	$-21 \leq l \leq 19$	$-21 \leq l \leq 16$	$-21 \leq l \leq 16$
Refinement				
R_1[a]	0.0354	0.0349	0.043	0.0309
wR_2[b]	0.0848	0.1096	0.0937	0.0795
Reflections	497	477	479	478
Parameters	25	26	26	26
$\Delta\rho_{max}$(e^-/Å^3)	5.163	4.21	2.432	2.631
$\Delta\rho_{min}$(e^-/Å^3)	-2.12	-2.308	-2.126	-1.546
Extinction coefficient	-	0.0022(4)	0.0034(4)	0.0045(4)
GoF	1.078	1.355	1.016	1.078

[a] $R_1 = \Sigma||F_o| - |F_c||/\Sigma|F_o|$
[b] $R_w = [\Sigma [w (F_o^2 - F_c^2)^2]/ \Sigma [w (F_o^2)^2]]^{1/2}$; $w = 1/[\sigma^2(F_o^2) + (0.0410P)^2 + 7.0512P]$, $w = 1/[\sigma^2(F_o^2) + (0.00561P)^2 + 5.0173P]$, $w = 1/[\sigma^2(F_o^2) + (0.0404)^2]$, and $w = 1/[\sigma^2(F_o^2) + (0.0354P)^2 + 2.7132P]$, respectively, for La_2PdGa_{12}, Pr_2PdGa_{12}, Nd_2PdGa_{12}, and Sm_2PdGa_{12}.

The composition was confirmed using energy dispersive spectroscopy (EDS) on a Hitachi S-3600 N variable-pressure scanning electron microscope equipped with an energy-dispersive spectrometer. The accelerating voltage was 15 kV with a beam-to-sample distance of 15 mm. An average of 15-20 scans was performed on each single crystal. The compositions determined by EDS and normalized to the lanthanide were $La_{2.00}Pd_{1.13(7)}Ga_{11.71(11)}$, $Pr_{2.00}Pd_{1.04(4)}Ga_{11.59(5)}$, $Nd_{2.00}Pd_{0.94(7)}Ga_{11.44(12)}$, and $Sm_{2.00(4)}Pd_{0.96(7)}Ga_{11.42(8)}$, and are in excellent agreement with the models from the single crystal X-ray diffraction refinement.

Table 6.2 Atomic Positions and Atomic Displacement Parameters

Site	Wyckoff	Symmetry	x	y	z	U_{eq}[a]
La_2PdGa_{12}						
La1	4*h*	*mm*	3/4	1/4	0.24638(4)	0.0089(2)
Pd1	2*c*	$\bar{4}2m$	3/4	1/4	0	0.0095(3)
Ga1	4g	4	3/4	3/4	0.18229(9)	0.0107(3)
Ga2	4*g*	4	3/4	3/4	0.34073(9)	0.0139(3)
Ga3	8*m*	*m*	0.50009(11)	0.00009(11)	-0.08677(6)	0.0107(3)
Ga4	8*m*	*m*	0.5649(2)	0.0649(2)	0.42782(8)	0.0325(4)
Pr_2PdGa_{12}						
Pr1	4*h*	*mm*	3/4	1/4	0.24665(4)	0.0069(3)
Pd1	2*c*	$\bar{4}2m$	3/4	1/4	0	0.0069(3)
Ga1	4*g*	4	3/4	3/4	0.18459(9)	0.0082(4)
Ga2	4*g*	4	3/4	3/4	0.34209(9)	0.0111(4)
Ga3	8*m*	*m*	0.50027(10)	0.00027(10)	-0.08816(6)	0.0082(3)
Ga4	8*m*	*m*	0.57215(14)	0.07215(14)	0.42893(7)	0.0191(4)
Nd_2PdGa_{12}						
Nd1	4*h*	*mm*	3/4	1/4	0.24688(7)	0.0104(3)
Pd1	2*c*	$\bar{4}2m$	3/4	1/4	0	0.0103(5)
Ga1	4*g*	4	3/4	3/4	0.18521(15)	0.0109(5)
Ga2	4*g*	4	3/4	3/4	0.34224(15)	0.0143(5)
Ga3	8*m*	*m*	0.50024(17)	0.00024(17)	-0.08854(10)	0.0117(4)
Ga4	8*m*	*m*	0.5740(2)	0.0740(2)	0.42911(13)	0.0231(5)
Sm_2PdGa_{12}						
Sm1	4*h*	*mm*	3/4	1/4	0.24678(5)	0.0066(2)
Pd1	2*c*	$\bar{4}2m$	3/4	1/4	0	0.0067(3)
Ga1	4*g*	4	3/4	3/4	0.18634(11)	0.0073(3)
Ga2	4*g*	4	3/4	3/4	0.34273(11)	0.0106(3)
Ga3	8*m*	*m*	0.50019(11)	0.00019(11)	-0.08909(7)	0.0079(3)
Ga4	8*m*	*m*	0.57592(13)	0.07592(13)	0.42918(8)	0.0168(3)

[a] U_{eq} is defined as one-third of the trace of the orthogonalized U_{ij} tensor.

Table 6.3 Selected Interatomic Distances (Å)

Compound	La_2PdGa_{12}	Ce_2PdGa_{12} [a]	Pr_2PdGa_{12}	Nd_2PdGa_{12}	Sm_2PdGa_{12}
Ln Layer					
Ln-Ga1 (x4)	3.2357(7)	3.2033(5)	3.1928(6)	3.1816(10)	3.1660(8)
Ln-Ga4 (x2)	3.2561(14)	3.2286(13)	3.2210(12)	3.208(2)	3.1969(14)
Ln-Ga3 (x2)	3.3056(11)	3.2772(11)	3.2701(10)	3.2621(18)	3.2476(12)
Ln-Ga3 (x2)	3.3066(11)	3.2808(11)	3.2731(10)	3.2649(18)	3.2498(12)
Ln-Ga2 (x4)	3.4112(8)	3.3914(11)	3.3859(7)	3.3762(12)	3.3703(10)
$PdGa_6$ Segment					
Ga1-Ga3 (x4)	2.6371(10)	2.6257(10)	2.6228(9)	2.6185(16)	2.6168(12)
Pd-Ga3 (x4)	2.5618(10)	2.5512(10)	2.5495(9)	2.5465(15)	2.5445(11)
Pd-Ga3 (x4)	2.5631(10)	2.5558(10)	2.5534(9)	2.5500(15)	2.543(11)
Ga-only Segment					
Ga2-Ga4 (x4)	2.6265(11)	2.6173(10)	2.6153(10)	2.6126(16)	2.6061(12)
Ga4-Ga4 (x1)	2.519(2)	2.5290(2)	2.535(2)	2.542(4)	2.552(2)

[a] Data from reference [227].

6.2.3 Physical Properties

Single crystals were selected for physical property measurements were first characterized by X-ray diffraction and energy dispersive spectroscopy. Magnetic data were collected using a Quantum Design Physical Property Measurement System (PPMS). The temperature-dependent susceptibility data were measured under zero-field cooled (ZFC) conditions between 3 K to 300 K for Ln_2PdGa_{12} (Ln= Pr - Sm). Pr and Nd were each measured under an applied field of 0.1 T, and $Sm_2PdGa_{12}$was measured under an applied field of 4 T. Field-dependent magnetization data were measured at 3 K with applied fields up to 9 T. The electrical resistivity measurements were measured on single crystals by the standard four-probe AC technique. The heat capacity was measured by the standard adiabatic heat-pulse relaxation technique down to 0.4 K.

6.3 Results and Discussion

6.3.1 Crystal Structure

Ln_2PdGa_{12} (Ln = Pr, Nd, or Sm) are isostructural to Sm_2NiGa_{12} [241] and adopt the space group *P*4/*nbm* with a ~ 6.1 Å and c ~ 15.5 Å. The lanthanide contraction can be observed in the decrease in unit cell volume as well as the a and c lattice parameters with c/a ratios of 2.534(1), 2.554(1), 2.559(1), 2.564(1) for La, Pr, Nd, and Sm, respectively. The crystal structure has been previously described as a Ga-Pd network with lanthanide atoms occupying cavities in the network [241] (Figure 6.1). The Ln atoms reside in a cavity formed by 14 Ga atoms with Pr-Ga distances of ~3.2 – 3.3 Å. The Pd-Ga segment is comprised of edge-sharing rectangular prisms formed from 4 Ga3 atoms at 2.5495(9) Å and another 4 Ga3 atoms at 2.5534(9) Å in Pr_2PdGa_{12}.

6.3.2 Physical Properties

Figures 6.2a and 6.2b show the temperature dependent molar magnetic susceptibility (χ_m) of single crystals Ln_2PdGa_{12} (Ln = Pr, Nd, and Sm) with magnetic field parallel and perpendicular to the direction of the plate. Anisotropic field-dependent magnetization data at T = 3 K for all analogues are shown in Figures 6.3a and 6.3b. All analogues were fit with a modified Curie-Weiss equation in the form of $\chi(T) = \chi_0 + C/(T - \theta_w)$, where C is the Curie constant, θ_W is the Weiss temperature, and χ_0 is a constant representing the background contribution to the magnetic susceptibility. In all cases, the modified Curie-Weiss equation was fit over the linear region of $1/[\chi(T) - \chi_o]$ and Table 6.4 provides the fit range, θ_w, μ_{calc}, and μ_{eff}.

6.3.2.1 Magnetic Susceptibility and Magnetization of Ln_2PdGa_{12} (Ln = Pr, Nd, and Sm)

Figure 6.2a shows the molar magnetic susceptibility of Pr_2PdGa_{12} down to 3 K with H parallel to the c-axis of the plate. Pr_2PdGa_{12} undergoes a very sharp antiferromagnetic transition

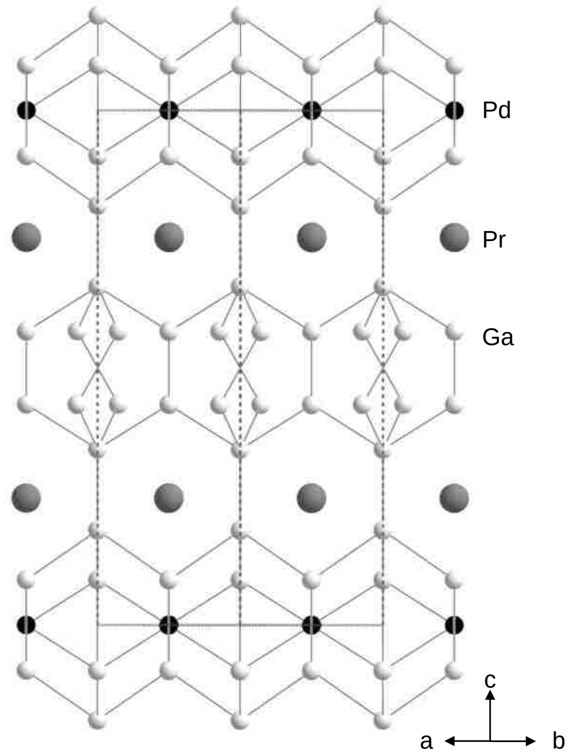

Figure 6.1. The crystal structure of Pr_2PdGa_{12} is shown. Pr, Pd, and Ga atoms are represented as large gray, black, and small gray spheres, respectively.

Table 6.4 Magnetic Properties

Compound	direction	θ_w (K)	T_N (K)	μ_{calc} (μ_B/Pr)	μ_{eff} (μ_B/Pr)	Fit range (K)
Ce_2PdGa_{12}[a]	$H \parallel c$	18.2	11	2.54	2.59	> 100
Ce_2PdGa_{12}[a]	$H \parallel ab$	-14.8	-	2.54	2.54	> 100
Pr_2PdGa_{12}	$H \parallel c$	10.1(1)	18.0	3.58	3.64(1)	> 30
Pr_2PdGa_{12}	$H \parallel ab$	-21.5(1)	-	3.58	3.61(3)	> 35
Nd_2PdGa_{12}	$H \parallel c$	-7.3(4)	7.5	3.62	3.51(3)	> 30
Nd_2PdGa_{12}	$H \parallel ab$	-13.3(7)	-	3.62	3.32(1)	> 40
Sm_2PdGa_{12}	$H \parallel c$	-21(1)	7.5	0.85	0.58(2)	> 30
Sm_2PdGa_{12}	$H \parallel ab$	-16(1)	7	0.85	0.67(1)	> 30

[a] Data obtained from ref. [227].

at 18 K for H = 0.1 T. At low temperature the value of the magnetic susceptibility is less than the room-temperature value,   indicating that the parallel component of the spins is exactly aligned with the crystal c-axis (and thus the applied field). Figure 6.2b shows the molar magnetic susceptibility of Pr_2PdGa_{12} down to 3 K with H parallel to the ab-plane of the crystal. A modest decease in χ as T decreases, is present at 18 K, and could be caused by imperfect alignment of the crystal resulting in some contribution from the c-direction. Inverse molar magnetic susceptibility (not shown), in each direction, is consistent with Curie-Weiss like behavior at temperatures greater than 30 K. Fitting above this temperature with a modified Curie-Weiss equation, θ_W and μ_{eff} were found to be 10.1(2) K and 3.64(1)μ_B/mol Pr for the field parallel to the c-axis and -21.5(5) K and 3.61(3)μ_B/mol Pr for the field parallel to the ab-plane. The magnetic moment from the high temperature Curie-Weiss fits is in good agreement with the calculated moment of a Pr^{3+} ion (3.58 μ_B/Pr). The positive Weiss temperature, along the c-direction, is indicative of ferromagnetic coupling between spins. Previous reports on Ce_2PdGa_{12} indicate that the spins are ferromagnetically coupled in the ab-plane and antiferromagnetic between planes along the c-axis [227]. A similar structure could be present here; however, additional measurements would have to be performed to verify the magnetic structure.

The field-dependent magnetization for H along the c-axis is shown in Figure 6.3a. At low fields (< ~1 T) the magnetization increases linearly with field, consistent with a slight spin canting along the c-axis. However, near H ~ 3 T, we observe a sudden change in slope associated with a metamagnetic transition that is slightly hysteretic. The metamagnetic transition

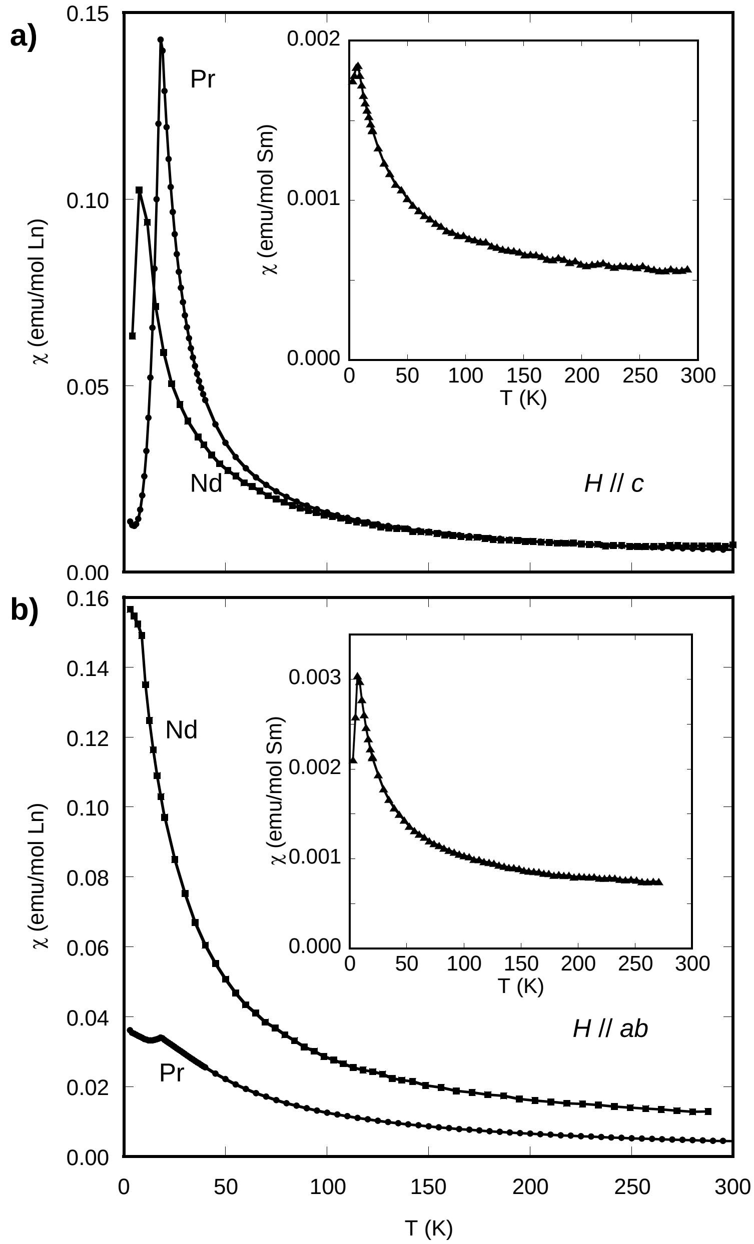

Figure 6.2a and 6.2b. a) Molar magnetic susceptibility for Pr_2PdGa_{12} (circles) and Nd_2PdGa_{12} (squares) as a function of temperature measured under an applied field of 0.1 T ($H \| c$). The inset shows molar magnetic susceptibility of Sm_2PdGa_{12} ($H \| c$) (triangles) as a function of temperature measured under an applied field of 4 T. **b)** Temperature dependent molar magnetic susceptibility for crystals oriented $H \| ab$ for Pr_2PdGa_{12} (circles) and Nd_2PdGa_{12} (squares). The inset shows magnetic susceptibility for Sm_2PdGa_{12} (triangles) as a function of temperature.

is consistent with those observed for Ln_2MGa_{12} (Ln = Ce – Nd, *M* = Pd, Ni, and Cu) and is reminiscent of a spin-flip transition from an antiferromagnetic state at low fields to a spin re-orientation at higher applied fields [227, 229, 242], i.e. in this case, an abrupt aligning of all the spins along the *c*-axis. The saturated magnetic moment (M ~ 1.7 μ_B/Pr) is well below that expected for free Pr^{3+} ions, μ_{sat} = 3.20 μ_B/Pr, indicative of a strong crystal electric field. The field-dependent magnetization for *H* along the *ab*-plane is shown in Figure 6.3b. In this direction, the magnetization increases linearly with field and no metamagnetic transition is present.

Figure 6.2a and 6.2b show the temperature dependent molar magnetic susceptibility of Nd_2PdGa_{12} down to 3 K with the magnetic field applied along *c*-axis and *ab*-plane, respectively. With the field parallel to the *c*-axis, Nd_2PdGa_{12} undergoes an antiferromagnetic transition at 7.5 K with H = 0.1 T. However, in the *ab*-direction, no transition is observed. The inverse molar magnetic susceptibility (not shown) is consistent with Curie-Weiss like behavior at temperatures greater than 30 K, and fitting above this temperature with a modified Curie Weiss equation resulted in θ_W = -7.3(4) K along the *c*-axis and θ_W = -13.3(7) K along the *ab*-plane, as would be expected for antiferromagnetic coupling. The magnetic moment of 3.51(3) μ_B/Nd (along *c*) is in close agreement with the calculated moment of 3.62 μ_B for a free Nd^{3+} ion, while in the *ab*-direction the magnetic is slightly smaller at 3.32(1) μ_B/Nd. The field dependent magnetization of Nd_2PdGa_{12} with the field along the *c*-axis is shown in Figure 6.3a. A sudden change in slope associated with a metamagnetic transition is observed at H ~ 3 T with a saturating magnetization of ~ 1.6 μ_B/Nd. The observed tendency toward saturation at 1.6μ_B/Nd is well below the expected calculated saturation moment of 3.27 μ_B/Nd, indicative of strong crystal electric field effects. In the *ab*-direction (Figure 6.3b) the magnetization increases linearly with *H*, and no metamagnetic transition is observed.

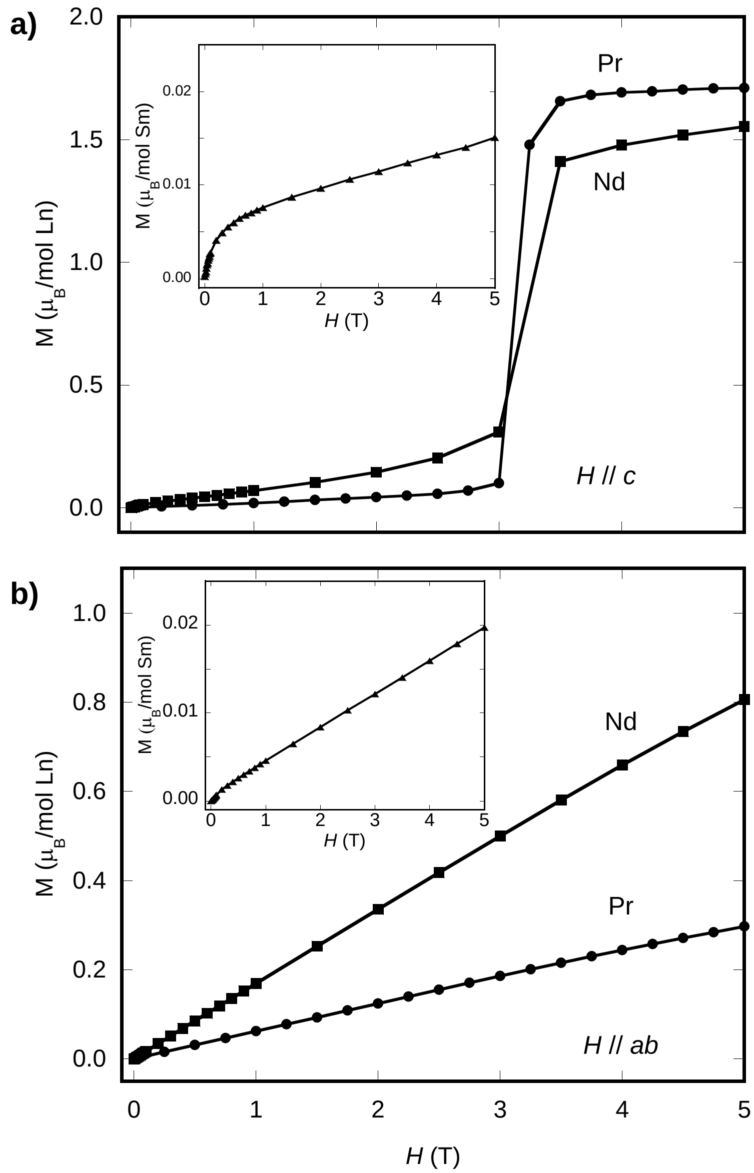

Figure 6.3a and 6.3b. a) Magnetization of Ln_2PdGa_{12} as a function of applied field (parallel to the *c*-axis) at 3 K. **b)** Magnetization of Ln_2PdGa_{12} as a function of applied field (parallel to *ab*-plane) at 3 K.

The inset of Figure 6.2a shows the temperature dependent molar magnetic susceptibility of Sm_2PdGa_{12} with *H* parallel to the *c*-axis of the single crystal, and shows an antiferromagnetic transition at T_N ~ 7.5 K at *H* = 4 T. A broad curvature can be observed from the inverse molar magnetic susceptibility (not shown) most likely from van Vleck paramagnetism. Fitting above 30 K with a modified Curie-Weiss equation resulted in a θ_W = -21(1) K as would be expected for an antiferromagnetic material, and the effective magnetic moment of 0.58(2) μ_B/Sm is less than the calculated moment of 0.85 μ_B for a free Sm^{3+} ion. Unlike the Pr and Nd analogues, for Sm_2PdGa_{12} the temperature dependent molar magnetic susceptibility along the *ab*-plane (inset of Figure 6.2b) shows an antiferromagnetic transition at 7 K. In this direction, the inverse molar magnetic susceptibility also shows curvature possibly due to van Vleck paramagnetism. Fitting the susceptibility above 30 K with a modified Curie-Weiss equation resulted in a θ_W = -16(1) K as would be expected for an antiferromagnetic material, and the effective magnetic moment of 0.67(1) μ_B/Sm again less than the expected for a free Sm^{3+} ion.

Field-dependent magnetization of Sm_2PdGa_{12} along the *c*-axis is shown in the inset of Figure 6.3a and is linear at low fields then a change in slope occurs near 1 T before increasing linearly up to 9 T. With the field applied field in the *ab*-direction (Figure 6.3b), the magnetization increases linearly with field. In both directions, the gradual linear increase in magnetization is consistent with the canting of antiferromagnetic spins. These results differ from Ce_2PdGa_{12}, Pr_2PdGa_{12}, and Nd_2PdGa_{12}, as these three analogues undergo metamagnetic transitions at H ~ 3 T. This behavior, coupled with the trend in θ_W, suggests that the lanthanide contraction is suppressing the magnetic anisotropy in these layered compounds.

6.3.2.2 Transport Properties of Ln_2PdGa_{12} (Ln = Pr, Nd, and Sm)

Figures 6.4a and 6.4b show the heat capacity and entropy for Pr_2PdGa_{12} as a function of temperature, respectively. Two transitions are observed, T_1 and T_2, at 3.0 and 14.9 K, respectively. The second transition (T_2) at 14.9 K corresponds with the antiferromagnetic transition observed at 18 K in the molar magnetic susceptibility. The molar magnetic susceptibility was measured down to 3 K with only a slight upturn below 5 K. The T_1 transition could be magnetic in nature but lies just beyond the range of the collected magnetic susceptibility data. The sudden and dramatic upturn observed in the heat capacity data as $T \rightarrow 0$ is consistent with the hyperfine interaction. This interaction can result in a splitting of the six-fold degenerate nuclear states and give rise to a nuclear Schottky anomaly in $C(T)$ at 0.1 K of ~ 7 J/mol K. Phonon subtraction was achieved by the subtracting the nonmagnetic La_2PdGa_{12} analogue from the heat capacity data for Pr_2PdGa_{12}. Fitting this data over the range of 15.6 < T < 21.0 K, the Sommerfeld parameter, γ, is 250 mJ/K^2-mol f.u.. This indicates Pr_2PdGa_{12} may be a heavy fermion material. As can be seen in Figure 6.4b, the recovered entropy is ~ 0.87Rln3 at 15 K, and the expected full entropy of Rln3 is not recovered up to 20 K. We see no evidence for short-range order above T_c, and the effective moments obtained from susceptibility fits agree well with a Pr^{3+} ion. The saturation of the magnetization well below what is expected for a Pr^{3+} ion (μ_{sat} = 3.20 μ_B/Pr), as shown in Figure 6.3a, is indicative of strong crystalline electric field effects, which may account for the lower than expected magnetic entropy associated with Rln(2S+1). It is unclear if Pr_2PdGa_{12} is a heavy fermion, but the Kadowaki-Woods ratio, discussed below, is in agreement with previously published Pr-containing heavy fermions [233].

Resistivity data (Figure 6.5) show metallic behavior for all three compounds for the entire temperature range investigated. The plot of resistivity vs. temperature for Pr_2PdGa_{12} shows some curvature near 100 K. Resistivity scales with T^2 for Pr_2PdGa_{12}, while Nd_2PdGa_{12} and Sm_2PdGa_{12} do not. Linear dependence of resistivity with T^2, shown as the inset of Figure 6.5, is indicative of Fermi-liquid behavior and is common to many heavy fermion compounds, including the Pr-containing heavy fermion compounds $Pr_2Pd_3Ge_5$[234]and $PrFe_4Sb_{12}$ (above its superconducting transition) [233]. However, the Pr heavy fermion $PrAg_2In$ does not show T^2

behavior [235]. Fitting the resistivity between 0 and 40 K to the equation $\rho = \rho_0 + A T^2$, yields an A-value of 0.0032(1) μΩ-cm/K^2. The Kadowaki-Woods ratio, A/γ^2, where A is the coefficient of the quadratic term of the low temperature resistivity, and γ is the electronic term from heat capacity can be used to characterize heavy fermion compounds.

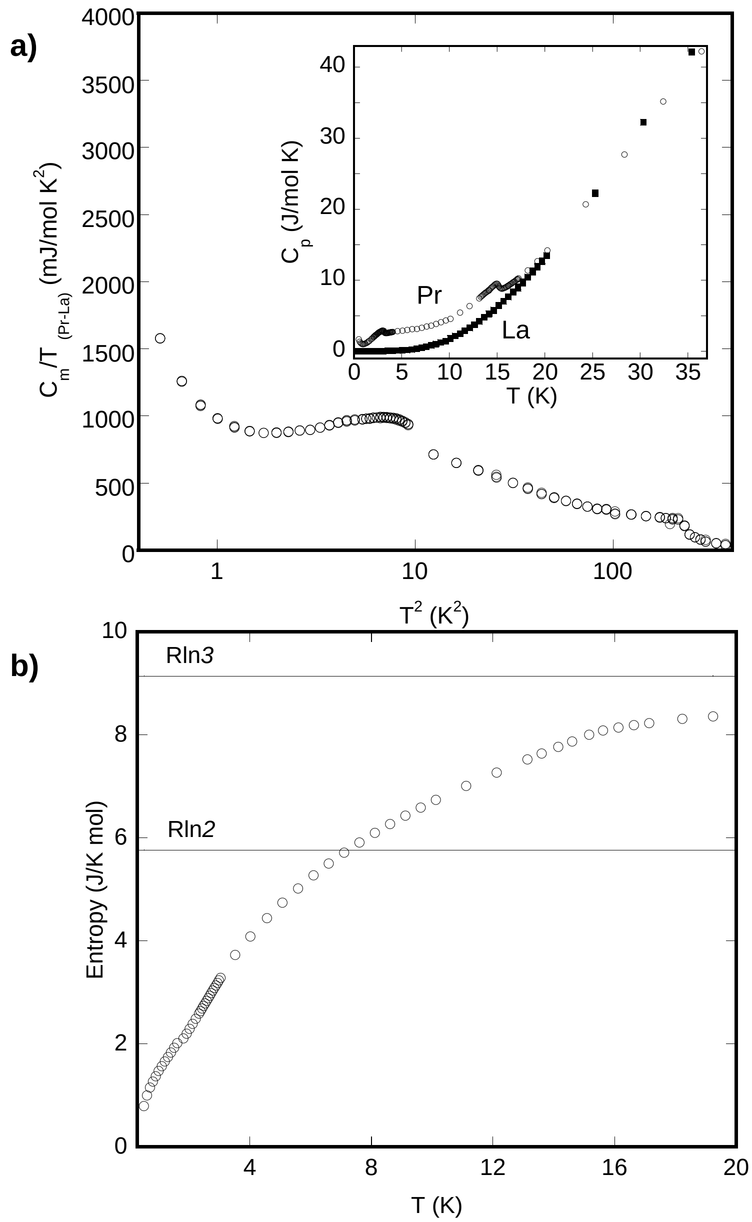

Figure 6.4a and 6.4b. **a)** C_m/T vs. T^2 as obtained by subtraction of La_2PdGa_{12} from Pr_2PdGa_{12}. Inset shows C_p vs. T for both the La and Pr analogues. **b)** Entropy vs. T as obtained from data shown in 7a. Rln2 and Rln3 shown to guide expected S_{mag} contribution.

Using $\gamma \sim 250$ mJ/mol-K^2 gives a Kadowaki-Woods ratio of ~5x10^{-8} μΩ-cm mol^{2}K^{2}mJ^{-2}, which is approximately two orders of magnitude smaller than that expected for a heavy fermion compound, and more like that of a transition metal [243, 244]. However, this is in excellent agreement with the praseodymium heavy system $PrOs_4Sb_{12}$ which gives a Kadowaki-Woods ratio of ~4x10^{-8}μΩ cm mol^2-K^2/mJ^2 [233]. This contrasts with praseodymium heavy systems $Pr_2Rh_3Ge_5$ and $Pr(CuGa)_{13-x}$ which have KW ratios of ~4x10^{-5}and ~0.7x10^{-5}μΩ cm mol^{2}K^2/mJ^2, respectively [232, 234].

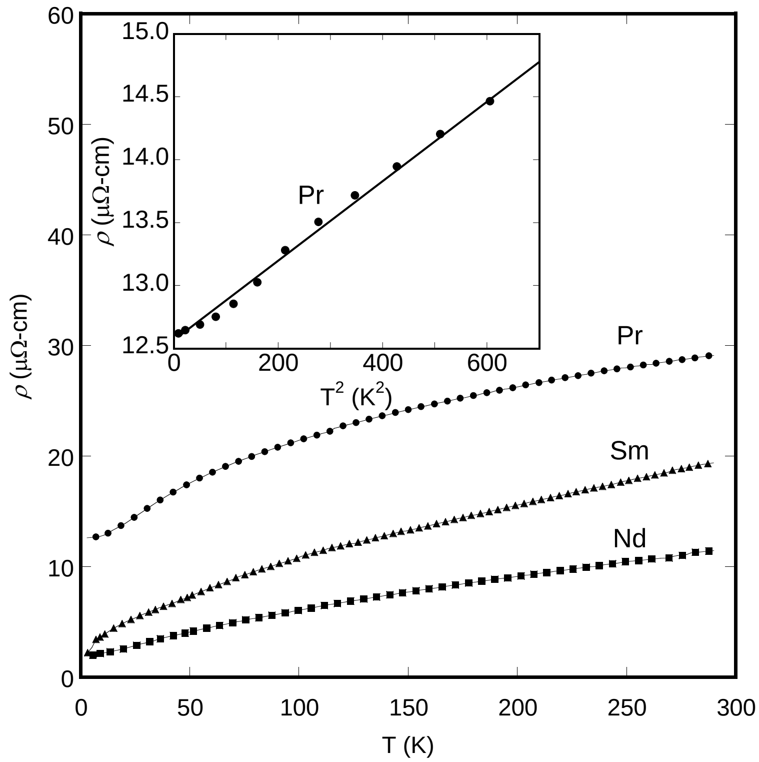

Figure 6.5. Electrical resistivity data for Pr_2PdGa_{12} (circles), Nd_2PdGa_{12} (squares), and Sm_2PdGa_{12} (triangles). Inset show T^2 dependence of resistivity for Pr_2PdGa_{12} fit over the range of $3 < T < 25$ K.

6.4 Conclusions

We have reported the single crystal growth of Pr_2PdGa_{12}, Nd_2PdGa_{12}, and Sm_2PdGa_{12} via the flux growth technique. Single crystals of all three phases were characterized by single crystal X-ray diffraction and their composition determined by SEM/EDS analysis. Pr_2PdGa_{12}, Nd_2PdGa_{12}, and Sm_2PdGa_{12} order antiferromagnetically at 18, 7.5, and 7.5 K, respectively. Comparing all analogues of Ln_2PdGa_{12} (Ln = Ce, Pr, Nd, and Sm), θ_w becomes increasingly more negative as nearest neighbor distances decrease. This contrasts with the Ni and Cu analogues, where no clear trend can be observed in θ_w [242]. Both Pr_2PdGa_{12} and Nd_2PdGa_{12} undergo metamagnetic transitions with applied fields larger than 3 T, while Sm_2PdGa_{12} remains linear up to H = 9 T, consistent with related phases. Pr_2PdGa_{12} shows two transitions, T_1 and T_2, in the heat capacity at 3 and 15 K, respectively. The Sommerfeld parameter, γ, was determined to be ~ 250 mJ/K^2-mol (16 < T < 21 K), and the Kadowaki-Woods ratio was consistent with that of $PrOs_4Sb_{12}$ [233]. Preliminary results support that Pr_2PdGa_{12} is a new Pr-containing heavy fermion, but experiments are warranted to elucidate the nature of the heavy electron state and the role of the crystal electric field in this system.

6.5 References

[223] Y.N. Grin, Y.P. Yarmolyuk, E.I. Gladyshevskii, Crystal structures of R_2CoGa_8 compounds (R = Sm, Gd, Tb, Dy, Er, Tm, Lu, Y) and $RCoGa_5$ compounds (R = Sm, Gd, Tb, Dy, Er, Tm, Lu, or Y), Sov. Phys. Crystallogr., 24 (1979) 137-139.

[224] C. Petrovic, et al., Heavy-fermion superconductivity in $CeCoIn_5$ at 2.3 K, J. Phys.:Condens. Matter, 13 (2001) L337.

[225] H. Hegger, C. Petrovic, E.G. Moshopoulou, M.F. Hundley, J.L. Sarrao, Z. Fisk, J.D. Thompson, Pressure-induced superconductivity in quasi-2D $CeRhIn_5$, Phys. Rev. Lett., 84 (2000) 4986.

[226] R.T. Macaluso, S. Nakatsuji, H. Lee, Z. Fisk, M. Moldovan, D.P. Young, J.Y. Chan, Synthesis, structure, and magnetism of a new heavy-fermion antiferromagnet, $CePdGa_6$, J. Solid State Chem., 174 (2003) 296-301.

[227] R.T. Macaluso, J.N. Millican, S. Nakatsuji, H.-O. Lee, B. Carter, N.O. Moreno, Z. Fisk, J.Y. Chan, A comparison of the structure and localized magnetism in Ce_2PdGa_{12} with the heavy fermion $CePdGa_6$, J. Solid State Chem., 178 (2005) 3547-3553.

[228] J.N. Millican, R.T. Macaluso, D.P. Young, M. Moldovan, J.Y. Chan, Synthesis, structure, and physical properties of Ce_2PdGa_{10}, J. Solid State Chem., 177 (2004) 4695-4700.

[229] J.Y. Cho, J.N. Millican, C. Capan, D.A. Sokolov, M. Moldovan, A.B. Karki, D.P. Young, M.C. Aronson, J.Y. Chan, Crystal growth, structure, and physical properties of Ln_2MGa_{12} (Ln = La, Ce; M = Ni, Cu), Chem. Mater., 20 (2008) 6116-6123.

[230] K.R. Thomas, J.Y. Cho, J.N. Millican, R.D. Hembree, M. Moldovan, A. Karki, D.P. Young, J.Y. Chan, Crystal growth and physical properties of Ln_2MGa_{12} (*Ln* = Pr, Nd, and Sm; *M* = Ni, Cu), J. Cryst. Growth, 312 (2010) 1098-1103.

[231] E.L. Thomas, J.N. Millican, E.K. Okudzeto, J.Y. Chan, Crystal growth and the search for highly correlated intermetallics, Comments Inorg. Chem., 27 (2006) 1 - 39.

[232] J.Y. Cho, E.L. Thomas, Y. Nambu, C. Capan, A.B. Karki, D.P. Young, K. Kuga, S. Nakatsuji, J.Y. Chan, Crystal growth, structure, and physical properties of $Ln(Cu,Ga)_{13-x}$ (Ln = La−Nd, Eu; $x \approx 0.2$), Chem. Mater., 21 (2009) 3072-3078.

[233] E.D. Bauer, N.A. Frederick, P.C. Ho, V.S. Zapf, M.B. Maple, Superconductivity and heavy fermion behavior in $PrOs_4Sb_{12}$, Phys. Rev. B, 65 (2002) 100506.

[234] V.K. Anand, Z. Hossain, C. Geibel, Magnetic order in $Pr_2Pd_3Ge_5$ and possible heavy-fermion behavior in $Pr_2Rh_3Ge_5$, Phys. Rev. B, 77 (2008) 184407.

[235] A. Yatskar, W.P. Beyermann, R. Movshovich, P.C. Canfield, Possible correlated-electron behavior from quadrupolar fluctuations in $PrInAg_2$, Phys. Rev. Lett., 77 (1996) 3637.

[236] E.A. Goremychkin, R. Osborn, E.D. Bauer, M.B. Maple, N.A. Frederick, W.M. Yuhasz, F.M. Woodward, J.W. Lynn, Crystal field potential of $PrOs_4Sb_{12}$: consequences for superconductivity, Phys. Rev. Lett., 93 (2004) 157003.

[237] P.C. Canfield, Z. Fisk, Growth of single crystals from metallic fluxes, Philos. Mag. B, 65 (1992) 1117-1123.

[238] L.O. Vasilenko, A.S. Noga, Y.N. Grin, M.D. Koterlin, Y.P. Yarmolyuk, Crystal structure and some magnetic properties of R_4MGa_{12} compounds, Russ. Metall., (1988) 216-220.

[239] A. Altomare, M.C. Burla, M. Camalli, G.L. Luca, C. Gaicovazzo, A. Guagliardi, A.G.G. Moliterni, G. Polidori, R. Spagna, SIR97: a new tool for crystal structure determination and refinement, J. Appl. Cryst., 32 (1999) 115.

[240] G.M. Sheldrick, A short history of SHELX., Acta Crystallogr. A, 64 (2008) 112-122.

[241] X.Z. Chen, P. Small, S. Sportouch, M. Zhuravleva, P. Brazis, C.R. Kannewurf, M.G. Kanatzidis, Molten Ga as a solvent for exploratory synthesis: the new ternary polygallide Sm_2NiGa_{12}, Chem. Mater., 12 (2000) 2520-2522.

[242] K.R. Thomas, J.Y. Cho, J.N. Millican, R.D. Hembree, M. Moldovan, A. Karki, D.P. Young, J.Y. Chan, Crystal growth and physical properties of Ln_2MGa_{12} (Ln=Pr, Nd, and Sm; M=Ni, Cu), J. Cryst. Growth, 312 (2010) 1098-1103.

[243] K. Kadowaki, S.B. Woods, Universal relationship of the resistivity and specific heat in heavy-Fermion compounds, Solid State Commun., 58 (1986) 507-509.

[244] A.C. Jacko, J.O. Fjaerestad, B.J. Powell, A unified explanation of the Kadowaki-Woods ratio in strongly correlated metals, Nature Phys., 5 (2009) 422-425.

Chapter 7. Synthesis and Physical Properties of $Yb_2Pd_3Ga_9$

7.1 Introduction

Ytterbium compounds are of great interest partly because they are analogous to the more commonly studied Ce compounds. One similarity is that they both can exhibit valence instability. Cerium can adopt the oxidation states Ce^{3+} (f^1) and Ce^{4+} (f^0), and Yb can adopt the oxidation states Yb^{2+} (f^{14}) and Yb^{3+} (f^{13}). In addition to these oxidation states, mixed valence (combination of both oxidation states in sample) and intermediate valence (non-integral valence) are also possible. Changes in valence can have a number of effects on the magnetic and electrical properties. One major change is that both Ce^{4+} and Yb^{2+} are nonmagnetic but both of the trivalent ions have magnetic moments of 2.54 μ_B/mol and 4.54 μ_B/mol, respectively. Valence instability correlates with heavy fermion behavior, particularly in Ce, Yb, and U compounds. A number of Yb containing heavy fermions have been recently reported including YbM_2Zn_{20} (M = Fe, Ru, Rh, Os, Ir), $YbCo_2Zn_{20}$ [244], YbSi [245], and $YbCu_2Si_2$ [246], with Sommerfeld coefficients (γ) of 520-740 mJ/ K^2-mol, 7900 mJ/ K^2-mol, 900 mJ/ K^2-mol, and 150 mJ/ K^2-mol, respectively. The intermediate valence of Yb in $YbAl_3$ [247] gives rise to the largest reported Seebeck coefficient of -90 μV/K, and makes it an attractive material for thermoelectric applications if the thermal conductivity can be effectively lowered without disturbing the electrical properties [248]. Quantum criticality has also been observed in a number of Yb compounds including β-$YbAlB_4$ [249], YbAgGe [250], and Yb_2Pd_2Sn [251]. In addition, a number of Yb based superconductors have been discovered including AlB_2 type $YbGa_xSi_{2-x}$ (T_C = 2.5 K for x = 1) [252].

While exploring the Ln-Pd-Ga system, single crystals of Ln_2PdGa_{12} (Ln = Pr, Nd, and Sm) were grown from a molten gallium flux and characterized [253]. It was found that

Ln_2PdGa_{12} (Ln = Pr, Nd, and Sm) order antiferromagnetically at 18, 7.5, and 7.5 K, respectively, and Pr_2PdGa_{12} is a heavy fermion compound with a Sommerfeld coefficient of ~250 mJ/K^2-mol f.u. [253]. Due to the potentially interesting properties of Yb-containing intermetallics, described above, it was also of interest to see what Yb compounds could be synthesized under identical reaction conditions. Previously reported compounds in this phase space include $YbPd_xGa_{4-x}$ (x ~ 0.25, $BaAl_4$-type) [254], $YbPdGa_2$ ($MgCuAl_2$-type) [255], $YbPd_xGa_{11-x}$ (x ~ 3, $BaHg_{11}$-type) [256], and $Yb_2Pd_3Ga_9$ [257]. $YbPd_xGa_{4-x}$, has been shown to be nearly divalent [254], $YbPdGa_2$ is trivalent [255], and for $YbPd_xGa_{11-x}$ the Yb valence and magnetic properties depend on the Pd concentration. For x < 3, the Yb is nonmagnetic and for x>3 the magnetic susceptibility follows Curie-Weiss behavior (μ_{eff} = 1.9 μ_B) [256]. Based on the magnetic data one could conclude that there is a valence change from Yb^{2+} for x < 3 a value between +2 and +3 for x > 3. However, X-ray absorption measurements show that the valence for all palladium concentrations of $YbPd_xGa_{11-x}$, both magnetic and not, is approximately +2.2 and does not vary with temperature [256]. $Yb_2Pd_3Ga_9$ was also reported to be predominately divalent based on magnetic measurements [257].

7.2 Experimental

7.2.1 Synthesis

Single crystals were synthesized with the molten metal flux technique [258, 259]. Yb (99.9%), Pd (99.995%), and Ga (99.99999%) were weighed out in the ratio 1:1.5:15 and placed in an alumina crucible. The crucible was placed in a quartz tube and topped with quartz wool for filtration, evacuated, and sealed. The sample was then placed a furnace and heated at 150 K/h to 1423 K and dwelled for 7 h. The sample was then cooled to 773K at 150 K/h and slowly cooled to 670 °C at 8 K/h. The sample was then removed from the furnace, inverted, and centrifuged to remove excess gallium. Residual gallium was removed by sonication in hot water or chemically etched with ~1 M iodine in dimethylformamide. Cleaned crystals were silver in color and ~2 x 2 x 3 mm^3, as shown in Figure 7.1 [260]. Crystals appeared stable in air and after a few months showed no obvious discoloration or changes.

Ca^{2+} has nearly the same ionic radius as Yb^{2+} [261], so many Ca and Yb compounds share the same structure types. Attempts to prepare an isostructural analogue with Ca (99.9%) under identical conditions were unsuccessful. These syntheses yielded a new compound $CaPd_xGa_{11-x}$ (x ~ 3.75, $BaHg_{11}$ type, $Pm\overline{3}m$, a ~ 8.499(1) Å). $CaPd_{3-x}Ga_{11-x}$ is isostructural to the previously reported $YbPd_xGa_{11-x}$ [256].

Figure 7.1. A single crystal of $Yb_2Pd_3Ga_9$ on a mm scale.

7.2.2 Single Crystal X-ray Diffraction

A cleaned single crystal was cleaved and a suitable fragment was mounted to a glass fiber with epoxy and mounted on the goniometer of an Enraf-Nonius Kappa CCD diffractometer (λ = 0.71073 Å). The diffraction data was initially indexed to a hexagonal cell a ~ 7.60 Å and c ~ 28.50 Å. However, the crystal structure solution was far from trivial. A colleague, Greg

McCandless, was able to the structure in four different but related space groups (*Cmcm*, $P6_122$, $P6_522$, $C2/c$) based on related structures. Each space group had its own intricacies and finally the *Cmcm* (a ~ 13.2, b ~ 7.6, c ~ 10.5, β ~ 114.9°) structure was selected as the most reasonable model, and a full discussion of the crystallographic study was reported in reference [260].

7.2.3 Elemental Analysis

The composition was confirmed using energy dispersive X-ray spectroscopy (EDS) on a Hitachi S-3600 N variable-pressure scanning electron microscope equipped with an energy-dispersive spectrometer. The accelerating voltage was 15 kV with a beam-to-sample distance of 15 mm. Two crystals were analyzed and 4 scans were performed on each single crystal. The composition determined by EDS and normalized to the lanthanide was $Yb_2Pd_{2.5(3)}Ga_{8.1(3)}$, in reasonable agreement with the previously reported $Yb_2Pd_3Ga_9$.

7.2.4 Physical Properties

Single crystals were selected for physical property measurements were first characterized by X-ray diffraction and energy dispersive spectroscopy. As shown in Figure 7.1, the crystals typically has one long axis and two shorter but approximately equal axes, and magnetic properties were measured both along and perpendicular to the long axis. Transport properties were measured parallel to the long axis. Magnetic data were collected using a Quantum Design Physical Property Measurement System (PPMS). The temperature-dependent susceptibility data were measured under zero-field cooled (ZFC) conditions between 3 K and 300 K under an applied field of 0.1 T. Field-dependent magnetization data were measured at 3 K with applied fields up to 9 T. The electrical resistivity measurements were measured on single crystals by the standard four-probe AC technique. Magnetoresistance was measured at 3 K, in fields up to 9 T.

The heat capacity was measured by the standard adiabatic heat-pulse relaxation technique down to 0.4 K.

7.3 Results and Discussion

Normalized resistivity data as a function of temperature is shown in Figure 7.2. The resistivity increases with increasing temperature indicating metallic behavior, and no anomalies are observed. Magnetoresistance (($\rho - \rho_0$)/ρ_0 x 100%) at 3 K is nearly linear with applied field reaching +4% at 9 T.

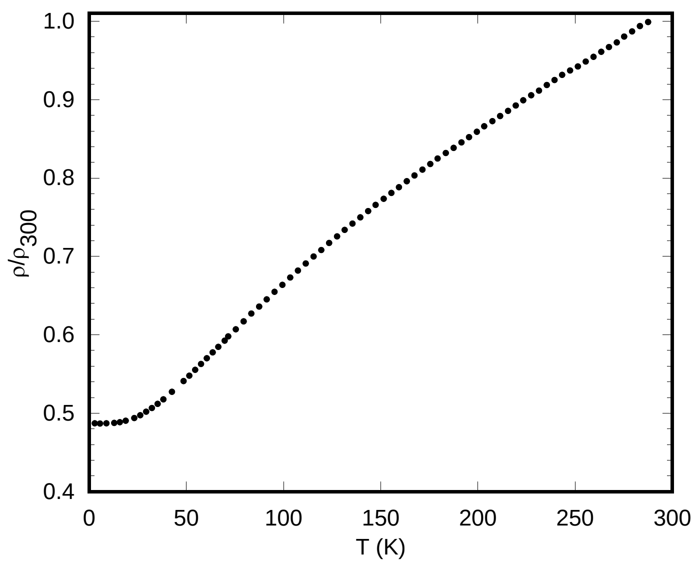

Figure 7.2. Normalized resistivity for a single crystal of $Yb_2Pd_3Ga_9$.

Magnetic properties were collected both parallel and perpendicular to the long axis of the crystal. In both directions, the magnetic susceptibility was nearly temperature independent with a magnitude of ~$3x10^{-3}$ emu/mol Yb. This is consistent with Pauli paramagnetism and a non-magnetic Yb^{2+}. This is in agreement with previous reports of $Yb_2Pd_3Ga_9$ [257] and with $YbPd_xGa_{11-x}$ (x < 3) [256] and $YbPd_xGa_{4-x}$ [254] which are nearly divalent and non-magnetic.

Heat capacity data as a function of temperature is shown in Figure 7.3. No anomalies are observed consistent with the lack of transitions observed in the resistivity and magnetic data.

The inset of Figure 7.3 shows a plot C/T as a function of T^2. At low temperatures and omitting phase transitions, heat capacity (C) typically follows the function $C = \gamma T + \beta T^3$, where γ is the electronic contribution (Sommerfeld coefficient) and β is the phonon contribution. Fitting the C/T data as a function of T^2 gives a Sommerfeld coefficient of ~4 mJ/ K^2-mol Yb which is similar to that of copper (0.5 mJ/ K^2 mol) [262] indicating that there is no enhancement to the effective mass.

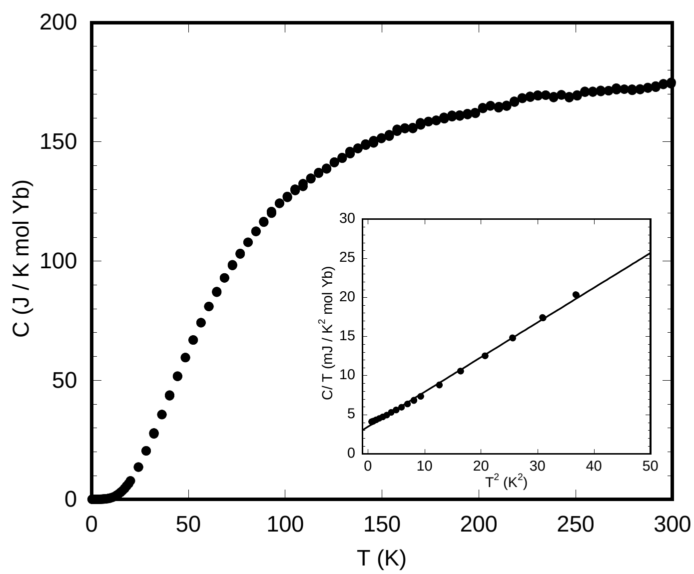

Figure 7.3. Heat capacity of $Yb_2Pd_3Ga_9$. The inset shows C/T as a function of T^2 for $Yb_2Pd_3Ga_9$. The Sommerfeld coefficient is ~4 mJ/K^2 mol Yb.

7.4 Conclusions

Large single crystals of $Yb_2Pd_3Ga_9$ were successfully grown form excess gallium flux. The crystals show metallic resistivity. Magnetic measurements indicate that it is non-magnetic, consistent with a divalent ytterbium ion. Heat capacity measurements show no enhanced electron mass. Overall, $Yb_2Pd_3Ga_9$ is a reminder that even if you know where to look for compounds with interesting physical properties, it does not always lead to success [263]. However, it did provide an interesting and unexpected question on what the best structural model is. There are still some unresolved questions about this structure including why it forms for Yb and not for the similarly sized Ca and Gd [253] which adopt the $BaHg_{11}$ and Y_4PdGa_{12} structure types, respectively. Calculations or experimental methods such as XPS, XANES, or ^{170}Yb Mössbauer may shed light on these subjects but are outside the scope of this investigation.

7.5 References

[244] M.S. Torikachvili, S. Jia, E.D. Mun, S.T. Hannahs, R.C. Black, W.K. Neils, D. Martien, S.L. Bud'ko, P.C. Canfield, Six closely related YbT_2Zn_{20} (T = Fe, Co, Ru, Rh, Os, Ir) heavy fermion compounds with large local moment degeneracy, P. Natl. Acad. Sci. USA, 104 (2007) 9960-9963.

[245] C. Engkagul, R. Selim, T. Mihalisin, P. Schlottmann, YbSi: A nearly localized heavy-fermion antiferromagnet, Phys. Rev. B, 35 (1987) 3686-3689.

[246] N. Tsujii, H. Kitazawa, T. Aoyagi, T. Kimura, G. Kido, Non-Fermi liquid behavior in $YbCu_2Si_2$, J. Magn. Magn. Mater., 310 (2007) 349-351.

[247] E.E. Havinga, K.H.J. Buschow, H.J. van Daal, The ambivalence of Yb in $YbAl_2$ and $YbAl_3$, Solid State Commun., 13 (1973) 621-627.

[248] G.D. Mahan, Good thermoelectrics, in: E. Henry, S. Frans (Eds.) Solid State Physics, Academic Press, 1997, pp. 81-157.

[249] Y. Matsumoto, S. Nakatsuji, K. Kuga, Y. Karaki, N. Horie, Y. Shimura, T. Sakakibara, A.H. Nevidomskyy, P. Coleman, Quantum criticality without tuning in the mixed valence compound β-$YbAlB_4$, Science, 331 (2011) 316-319.

[250] G.M. Schmiedeshoff, E.D. Mun, A.W. Lounsbury, S.J. Tracy, E.C. Palm, S.T. Hannahs, J.H. Park, T.P. Murphy, S.L. Bud'ko, P.C. Canfield, Multiple regions of quantum criticality in YbAgGe, Phys. Rev. B, 83 (2011) 180408.

[251] T. Muramatsu, T. Kanemasa, T. Kagayama, K. Shimizu, Y. Aoki, H. Sato, M. Giovannini, P. Bonville, V. Zlatic, I. Aviani, R. Khasanov, C. Rusu, A. Amato, K. Mydeen, M. Nicklas, H. Michor, E. Bauer, Reentrant quantum criticality in Yb_2Pd_2Sn, Phys. Rev. B, 83 (2011) 180404.

[252] N. Tsujii, M. Imai, H. Yamaoka, I. Jarrige, H. Oohashi, T. Tochio, K. Handa, J. Ide, H. Atsuta, Y. Ito, H. Yoshikawa, H. Kitazawa, Phase stability and superconducting properties of AlB_2-type $YbGa_xSi_{2-x}$ ($1.12 \leq x \leq 1.49$), Chem. Mater., 22 (2010) 4690-4699.

[253] M.J. Kangas, B.L. Drake, N. Haldolaarachchige, D.P. Young, J.Y. Chan, Crystal growth, structure, and physical properties of Ln_2PdGa_{12} (Ln = La, Pr, Nd, and Sm), J. Alloys Comp., 514 (2012) 64-70.

[254] Y.N. Grin, M. Ellner, K. Hiebl, P. Rogl, New ytterbium compounds with the $BaAl_4$ type of structure: crystal chemistry and magnetic properties of $Yb(Cu,Ag,Au,Pd,Pt)_xGa_{4-x}$, J. Alloys Comp., 196 (1993) 207-212.

[255] Y. Grin, K. Hiebl, P. Rogl, C. Godart, Crystal structure and magnetic behaviour of ternary $YbTGa_2$ compounds (T = Ni, Pd, Pt) and quaternary solid solutions $YbPd_{1-x}Ag_xGa_2$, J. Alloys Comp., 239 (1996) 127-130.

[256] Y.N. Grin, K. Hiebl, P. Rogl, C. Godart, E. Alleno, Crystal structure and valence behavior of $YbPd_xGa_{11-x}$, J. Alloys Comp., 252 (1997) 88-92.

[257] R. Giedigkeit, W. Schnelle, Y. Grin, R. Kniep, $Yb_2Pd_3Ga_9$: Synthesis, structure and properties, in: 7th European conference on solid state chemistry, 1999, pp. 136.

[258] Z. Fisk, J.P. Remeika, Chapter 81 Growth of single crystals from molten metal fluxes, in: Karl A. Gschneidner, Jr., E. LeRoy (Eds.) Handbook on the Physics and Chemistry of Rare Earths, Elsevier, 1989, pp. 53-70.

[259] M.G. Kanatzidis, R. Pöttgen, Wolfgang Jeitschko, The metal flux: A preparative tool for the exploration of intermetallic compounds, Angew. Chem. Int. Ed., 44 (2005) 6996-7023.

[260] W.A. Phelan, M.C. Menard, M.J. Kangas, G.T. McCandless, B.L. Drake, J.Y. Chan, Adventures in crystal growth: synthesis and characterization of single crystals of complex intermetallic compounds, Chem. Mater., 24 (2012) 409-420.

[261] R.D. Shannon, Revised effective ionic radii and systematic studies of interatomic distances in halides and chalcogenides, Acta Crystallogr. A, 32 (1976) 751-766.

[262] N.W. Ashcroft, N.D. Mermin, Solid State Physics, Brooks/Cole CENGAGE Learning, Australia, 1976.

[263] P.C. Canfield, Fishing the Fermi sea, Nature Phys., 4 (2008) 167-169.

Chapter 8. Single Crystal Neutron Diffraction Studies of Ln(Cu,Al,Ga)$_{13-x}$ (Ln = La – Pr, Eu; x ~ 0.1)

8.1 Introduction

The $NaZn_{13}$ structure type (space group $Fm\overline{3}c$ a ~ 12 Å) [264] is adopted by a range of intermetallics. A few notable compounds that adopt the $NaZn_{13}$ structure type are the room temperature magnetocaloric material La(Fe,Si)$_{13}$ [265, 266], the intermediate valence $CeBe_{13}$ [267], the heavy fermion superconductor UBe_{13} [268], and the Pr-containing heavy fermion Pr(Cu,Ga)$_{12.85}$ [269, 270]. Motivated the discovery of the heavy fermion Pr(Cu,Ga)$_{12.85}$ synthesis of aluminum analogues was attempted. Although Ln(Cu,Al)$_{13}$ compounds have been synthesized by arc melting [271], the flux growth synthesis was unsuccessful and instead produced crystals of the $ThMn_{12}$ structure type (spacegroup *I*4/*mmm*) [272].

Using a flux comprised of Al and Ga, large (up to 5x5x5 mm^3) single crystals of Ln(Cu,Al,Ga)$_{13-x}$ were synthesized. The compositions determined by energy dispersive spectroscopy (EDS) were found to be $La_{1.0}Cu_{6.3(6)}Al_{4.2(8)}Ga_{2.1(1)}$, $Ce_{1.0}Cu_{6.6(2)}Al_{4.4(5)}Ga_{1.9(1)}$, $Pr_{1.0}Cu_{6.0(3)}Al_{4.3(4)}Ga_{2.0(1)}$, and $Eu_{1.0}Cu_{5.9(3)}Al_{5.2(5)}Ga_{1.7(1)}$. The crystals were characterized with single crystal X-ray diffraction and found to be consistent with the $NaZn_{13}$ structure type. However, due to the similar X-ray scattering of the Cu and Ga, the Al-Cu-Ga disorder could not be accurately determined, prompting the need for neutron diffraction experiments. Subsequent physical property measurements revealed an enhanced Sommerfeld coefficient (γ ~350 mJ/K^2-mol) for Pr(Cu,Al,Ga)$_{13-x}$ and that Eu(Cu,Al,Ga)$_{13-x}$ orders ferromagnetically at ~6 K with a modest magnetocaloric effect of ~11 J/kg-K [273]. Herein, elemental analysis and single crystal neutron diffraction for Ln(Cu,Al,Ga)$_{13-x}$ (Ln = La, Ce, Pr, Eu) are discussed.

8.2 Experimental

Single crystal neutron diffraction experiments were performed using the TOPAZ beamline at the Spallation Neutron Source at Oak Ridge National Laboratory [274, 275]. Single crystals with dimensions of ~ 4 mm^3 were mounted onto a vanadium post with glue and positioned onto the goniometer. Data collections were conducted at room temperature in wavelength-resolved time-of-flight (TOF) Laue mode using neutrons with wavelengths in the range of 0.6 to 3.5 Å. To ensure good coverage and redundancy for each data collection, data were collected with 14 detectors and using 10 – 16 crystals orientations, which were selected by evaluation with CrystalPlan software [276], with collection times of approximately two hours per orientation. Data were corrected for background and detector efficiency. Data reduction including neutron TOF spectrum and absorption corrections for all analogues were carried out with the ANVRED2 program of the ISAW program suite [277]. The reduced data were saved in SHELX HKLF2 format in which the wavelength is recorded separately for each individual reflection, and the reduced data were not merged as consequence of this saved format. Initial models were based on the single crystal X-ray diffraction refinement results, and the neutron models were refined using SHELXL97 [278]. Restraints based on elemental analysis results were applied and extinction correction was refined in the model. During the final stages of refinement, all atoms were modeled anisotropically and weighting schemes were applied. Details regarding data collections and refinements are given Table 8.1, atomic positions are provided in Table 8.2, and bond lengths are provided in Table 8.3. Due to the systematic similarites of analogues presented in this manuscript, only the structural models for $La(Cu,Al,Ga)_{13-x}$ will be described in detail.

Table 8.1. Crystallographic Parameters

Formula	$La(CuAlGa)_{13-x}$	$Ce(CuAlGa)_{13-x}$	$Pr(CuAlGa)_{13-x}$	$Eu(CuAlGa)_{13-x}$
Refined Composition	$LaCu_{6.33}Al_{4.53}Ga_{1.97}$	$CeCu_{6.62}Al_{3.95}Ga_{2.28}$	$PrCu_{6.04}Al_{3.02}Ga_{3.84}$	$EuCu_{5.87}Al_{4.42}Ga_{2.48}$
Crystal System	Cubic	Cubic	Cubic	Cubic
Space Group	$Fd\bar{3}c$	$Fd\bar{3}c$	$Fd\bar{3}c$	$Fd\bar{3}c$
a (Å)	11.897(4)	11.863(3)	11.858(4)	11.921(3)
V (Å3)	1683.7(10)	1669.3(8)	1667.4(9)	1694.2(8)
Z	8	8	8	8
MW	800.51	826.18	873.81	816.95
Temperature (K)	296(2)	296(2)	296(2)	296(2)
θ range (º)	9.03 - 77.14	7.71 - 77.54	8.85 - 78.06	8.24 - 76.95
μ (mm^{-1})	0.009	0.007	0.009	0.721
Data Collection				
Measured Reflections	1949	2982	2322	2103
Unique Reflections	1949	2982	2322	2103
Reflections with I>2σ(I)	1940	2963	2314	2103
R_{int}	0	0	0	0
h	$-23 \leq h \leq 20$	$-23 \leq h \leq 22$	$-20 \leq h \leq 21$	$-23 \leq h \leq 17$
k	$-22 \leq k \leq 22$	$-23 \leq k \leq 23$	$-22 \leq k \leq 23$	$-23 \leq k \leq 23$
l	$-14 \leq l \leq 23$	$-17 \leq l \leq 21$	$-22 \leq l \leq 23$	$-18 \leq l \leq 22$
Refinement				
Δρmax ($eÅ^{-3}$)/Δρmin ($eÅ^{-3}$)	1.604 / -1.297	1.116 / -1.077	1.297 / -1.35	1.933 / -1.138
GoF	1.084	1.059	1.076	1.031
Extinction coefficient	0.00347(19)	0.0051(2)	0.0058(3)	0.0100(7)
Reflections/Parameters	1949 / 24	2982 / 29	2322 / 24	2103 / 29
R_1 ($F^2 > 2\sigma F^2$) [a]	0.0571	0.0501	0.051	0.0767
wR_2 (F^2) [b]	0.1553	0.1424	0.1398	0.1935

[a] $R_1(F) = \sum ||F_o| - |F_c|| / \sum |F_o|$; [b] $wR_2(F^2) = [\Sigma [w (F_o^2 - F_c^2)^2] / \Sigma [w (F_o^2)^2]]^{1/2}$; $w = 1/[\sigma^2(F_o^2) + (0.105P)^2 + 37.065P]$, $w = 1/[\sigma^2(F_o^2) + (0.1072P)^2 + 9.9351P]$, $w = 1/[\sigma^2(F_o^2) + (0.1032P)^2 + 12.7889P]$, and $w = 1/[\sigma^2(F_o^2) + (0.1557P)^2 + 59.56P]$ for $La(Cu,Al,Ga)_{13-x}$, $Ce(Cu,Al,Ga)_{13-x}$, $Pr(Cu,Al,Ga)_{13-x}$, and $Eu(Cu,Al,Ga)_{13-x}$, respectively.

Table 8.2 Atomic Fractional Coordinates for Ln(Cu,Al,Ga)13-x (Ln = La – Pr, and Eu)

Site	Wyckoff	x	y	z	Occupancy	Ueq ($Å^2$)[a]
La1	8*a*	¼	¼	¼	1	0.0062(2)
Cu1 (M1)	8*b*	0	0	0	0.828(10)	0.0077(3)
Cu2 (M2)	96*i*	0.11918(3)	0.17745(3)	0	0.4585(12)	0.01071(12)
Al2 (M2)	96*i*	0.11918(3)	0.17745(3)	0	0.38(2)	0.01071(12)
Ga2 (M2)	96*i*	0.11918(3)	0.17745(3)	0	0.164(16)	0.01071(12)
Ce1	8*a*	¼	¼	¼	1	0.0061(3)
Cu1 (M1)	8*b*	0	0	0	0.851(9)	0.0086(2)
Cu2 (M2)	96*i*	0.11924(2)	0.17755(2)	0	0.4808(11)	0.01123(9)
Al2 (M2)	96*i*	0.11924(2)	0.17755(2)	0	0.33(2)	0.01123(9)
Ga2 (M2)	96*i*	0.11924(2)	0.17755(2)	0	0.1980(18)	0.01123(9)
Pr1	8*a*	¼	¼	¼	1	0.0059(3)
Cu1 (M1)	8*b*	0	0	0	0.899(11)	0.0086(2)
Cu2 (M2)	96*i*	0.11929(2)	0.17765(2)	0	0.4284(13)	0.01109(10)
Al2 (M2)	96*i*	0.11929(2)	0.17765(2)	0	0.252(18)	0.01109(10)
Ga2 (M2)	96*i*	0.11929(2)	0.17765(2)	0	0.320(19)	0.01109(10)
Eu1	8*a*	¼	¼	¼	1	0.0090(4)
Cu1 (M1)	8*b*	0	0	0	0.767(17)	0.0085(5)
Cu2 (M2)	96*i*	0.11855(5)	0.17745(4)	0	0.4252(16)	0.01180(17)
Al2 (M2)	96*i*	0.11855(5)	0.17745(4)	0	0.37(3)	0.01180(17)
Ga2 (M2)	96*i*	0.11855(5)	0.17745(4)	0	0.21(3)	0.01180(17)

[a]Ueq is defined as one-third of the trace of the orthogonalized Uij tensor.

Table 8.3. Selected Interatomic Distances (Å)

Bonds	$La(Cu,Al,Ga)_{13-x}$	$Ce(Cu,Al,Ga)_{13-x}$	$Pr(Cu,Al,Ga)_{13-x}$	$Eu(Cu,Al,Ga)_{13-x}$
Ln1-M2	3.4659(12)	3.4554(10)	3.4535(11)	3.4765(10)
M1-M2	2.5430(9)	2.5371(8)	2.5375(8)	2.5441(9)
M2-M2	2.5167(10)	2.5079(8)	2.5053(9)	2.5313(11)
M2-M2	2.6358(10)	2.6297(8)	2.6302(9)	2.6393(10)

M1 = Cu1; M2 = Cu2, Al2, and Ga2

8.3 Results and Discussion

$La(Cu,Al,Ga)_{13-x}$ adopts the $NaZn_{13}$ structure type, shown in Figure 8.1, which consists of one La site (8*a*) and two metal sites (8*b* and 96*i*) that are occupied by Al, Cu, and Ga. The M1 site lies at the center of an icosahedron formed by 12 M2 atoms, as shown in Figure 8.2. The La atoms occupy cavities formed by 24 M2 atoms.

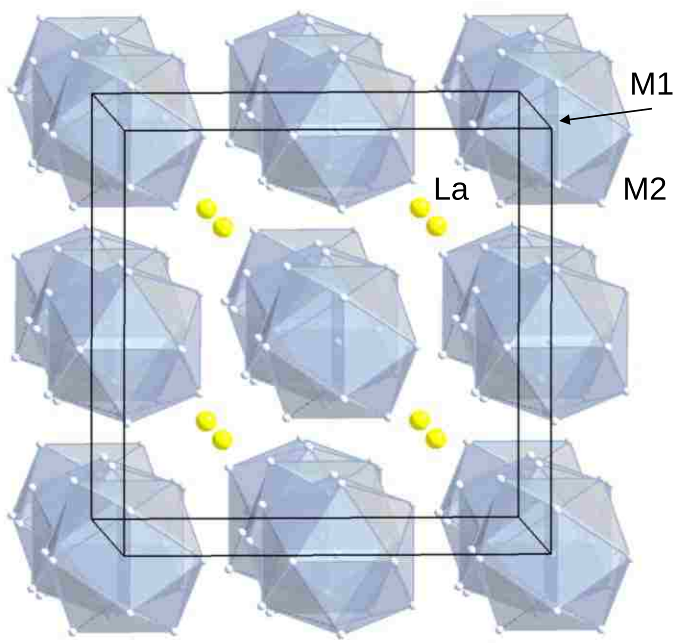

Figure 8.1. M1-centered icosahedra are shown as light blue polyhedra. La atoms occupy voids between the polyhedra and are represented as yellow spheres.

The first model (Model 1 in Table 8.4 and Figure 8.3) of the single-crystal neutron diffraction data for $La(Cu,Al,Ga)_{13-x}$ considered was based on the single crystal X-ray diffraction models with full occupancy and Cu/Al mixing on both the 8*b* and 96*i* sites. While this model does not attempt to model gallium, the final refinement statistics indicate that it is a good fit to the observed data (R_1 = 0.057, wR_2 = 0.156, GOF = 1.08). The refined composition is

$LaCu_{7.95}Al_{5.05}$, and the copper occupancy on the 8*b* and 96*i* sites is 68.9(19) % and 60.6(12) %, respectively. Analysis of a similar model (Model 2 in Table 8.4 and Figure 8.3) with Ga substituted for Cu gives nearly identical statistics and slightly more gallium on each of the two sites 77(2) % (8*b*) and 67.4(13) % (96*i*).

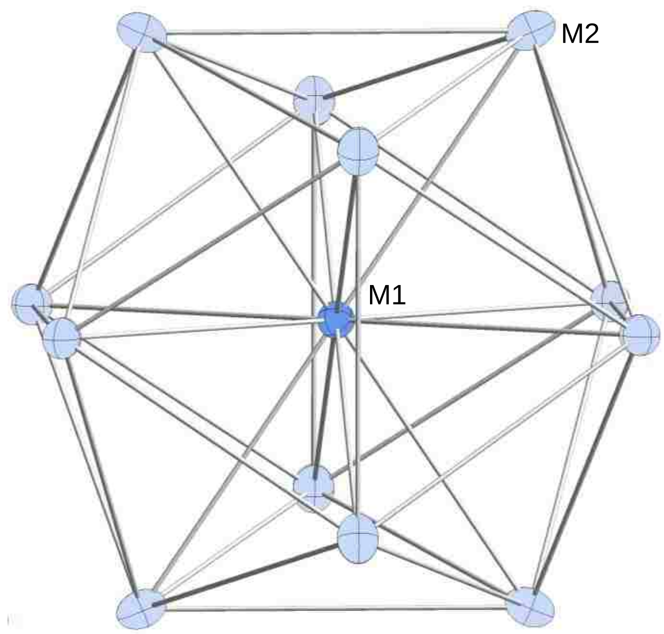

Figure 8.2. The M1 atom (blue) sits at the center of an icosahedron formed by 12 M2 atoms. Both M1 and M2 are illustrated by their respective thermal ellipsoids.

A number of ways to model the Cu, Al, and Ga occupancies can be envisioned, and a model that initially yielded respectable refinement statistics took into account the mixing of Cu, Al, and Ga on both the 8*b* and 96*i* sites (Model 3 in Table 8.4 and Figure 8.3). The copper concentration and the total amount of Al, Cu, and Ga atoms in the asymmetric unit were restrained to EDS values of 6.3 and 12.6, respectively, using the SUMP command in SHELXL. The occupancies of Cu, Al, and Ga on each of the two sites were then refined using 1/3 as the initial free variables for the occupancies. This model yields compositional results comparable to the EDS composition and yields improved refinement statistics (R_1 = 0.056, wR_2 = 0.153, GOF = 1.05). However, analysis of the initial conditions (elemental occupancy values) indicated that the refinement was susceptible to a number of local minima, many of which were unrealistic (site occupancies larger than 100% or less than 0% without additional restraints). Additionally, the data were modeled by taking into account mixing of Cu/Al or Cu/Ga on the 8*b* site, while at the same time mixing Cu, Al, and Ga on 96*i* site. Similar to the model just described, these models gave unrealistic results (site occupancies larger than 100% or less than 0% without additional restraints) depending on the initial parameters used for the occupancy of Cu/Al and Cu/Ga of the 8*b* site.

A literature study revealed a more intricate picture. A number of AM_xT_{13-x} (A = Ba, Sr, La, Eu; M = Cu, Ag; T = Al, Ga, In) compounds showed that the trielide and the transition metal mix on both the 8*b* and 96*i* sites [271]. However, the 8*b* site of the copper analogues was preferentially occupied by copper atoms (91% in $BaCu_5Al_8$ and 72% in $EuCu_{6.5}Al_{6.5}$). Furthermore, a recent reinvestigation of $EuZn_{13-x}$ shows that this structurally related phase is not fully stoichiometric and the true composition is approximately $EuZn_{12.75}$. The Zn at the center of the icosahedron (8*b*) is partially occupied, whereas the Zn atoms (96*i*) at the corners of the icosahedron is fully occupied [279]. It was concluded that the partial occupancy helps the material reach the optimal number of valence electrons as discussed in detail by Nordell and Miller [271].

Taking into consideration the results of these two studies reported for the site occupancy of analogous compounds led us to a model where Cu alone (partially) occupied the 8*b* site, while the 96*i* site is fully occupied with Al, Cu, and Ga substitutionally disordered on this site (Model 4 in Table 8.4 and Figure 8.3).

Table 8.4. Summary of the Neutron Models for La(Cu,Al,Ga)$_{13-x}$

	La(Cu,Al,Ga)$_{13-x}$	La(Cu,Al,Ga)$_{13-x}$	La(Cu,Al,Ga)$_{13-x}$	La(Cu,Al,Ga)$_{13-x}$
	Model 1	**Model 2**	**Model 3**	**Model 4**
Refined Formula	$LaCu_{7.95}Al_{5.05}$	$LaGa_{8.85}Al_{4.15}$	$LaCu_{6.33}Ga_{2.12}Al_{4.17}$	$LaCu_{6.33}Ga_{1.97}Al_{4.53}$
Space group	$Fm\overline{3}c$	$Fm\overline{3}c$	$Fm\overline{3}c$	$Fm\overline{3}c$
Crystal System	Cubic	Cubic	Cubic	Cubic
a (Å)	11.897(4)	11.897(4)	11.897(4)	11.897(4)
V (Å^3)	1683.7(10)	1683.7(10)	1683.7(10)	1683.7(10)
Z	8	8	8	8
S	1.08	1.08	1.05	1.08
$R_1[F^2 > 2\sigma(F^2)]^a$	0.057	0.057	0.056	0.057
$wR_2(F^2)^b$	0.156	0.156	0.153	0.156
$\Delta\rho_{max}$ (fm Å^{-3})	1.60	1.60	1.76	1.60
$\Delta\rho_{min}$ (fm Å^{-3})	-1.30	-1.30	-1.30	-1.30

$^aR_1(F) = \sum ||F_o| - |F_c||/\sum |F_o|$; $^bwR_2(F^2) = [\Sigma [w (F_o^2 - F_c^2)^2]/ \Sigma [w (F_o^2)^2]]^{1/2}$

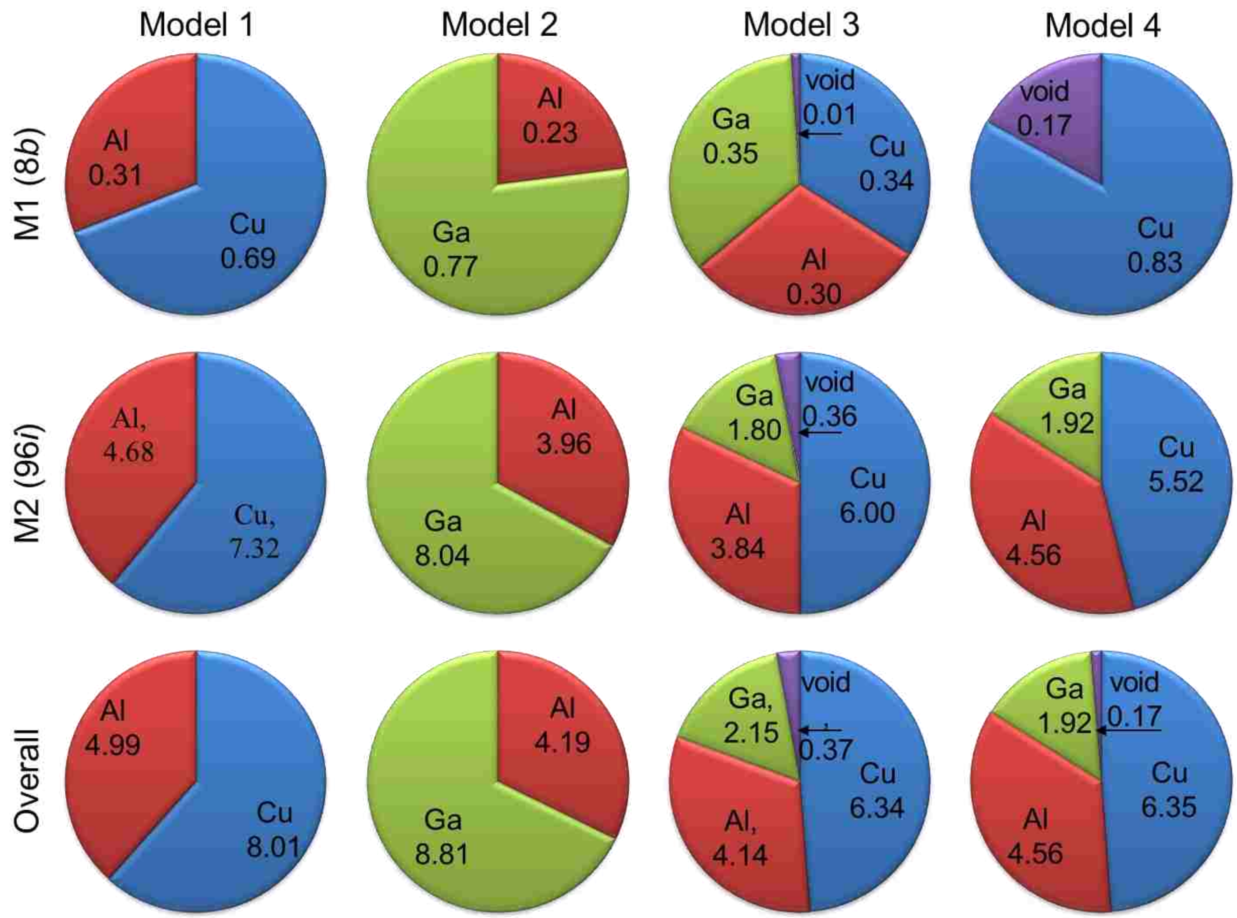

Figure 8.3. The four models for $Ln(Cu,Al,Ga)_{13-x}$ are depicted graphically as a pie chart, where the rows stand for the M1 site, the M2 site, and the total. Al, Ga, and Cu, occupancies are depicted as red, green, and blue, respectively.

We note that a similar approach was effective in modeling the disorder of $Ln(Cu,Ga)_{13-x}$, where Cu partially occupied the 8b site and Cu/Ga were mixed on the 96*i* site [269]. Similar to the model discussed previously, only the overall Cu composition distributed over both sites was restrained to the EDS value. The composition for $La(Cu,Al,Ga)_{13-x}$ resulting from this refinement (R_1 = 0.057, wR_2 = 0.156, GOF = 1.08) is in excellent agreement with the EDS composition (refined formula of $LaCu_{6.33}Al_{4.53}Ga_{1.97}$ compared to normalized EDS formula of $LaCu_{6.3(6)}Al_{4.2(8)}Ga_{2.1(1)}$). The refined composition in Table 8.1 of Ce also matches the EDS values well, while the refined compositions of the Pr and Eu analogues are not as aluminum rich compared to the EDS results. In addition, this model is impervious to the local minimum problem. One final result that lends credence to this particular model is that the M2 (96*i*) atomic displacement parameters (ADPs) are slightly elongated, and the long axis (U_{11}) points toward the center of the icosahedron that limits the partial occupancy of the copper atom at the center of the icosahedron (8*b*) allowing the atoms of the icosahedral framework to relax inward, also observed in $EuZn_{12.75}$ [279].

8.4 Conclusions

Large single crystals of $Ln(Cu, Al, Ga)_{13-x}$ (Ln = La-Pr, Eu) synthesized from a mixed Ga/Al flux [273]. In addition to single crystal X-ray diffraction, single crystal neutron diffraction experiments were conducted to understand the disorder of the Cu, Al, and Ga atoms on the 8*b* and 96*i* sites of the $NaZn_{13-x}$ structure type. Four different neutron models were considered, including Cu and Al mixing only, Ga and Al mixing only, Cu/Al/Ga mixing, and partial occupancy of iron on the 8*b* site and mixing of Cu/Al/Ga on the 96*i* site. All four models gave similar refinement statistics (R_1 ~0.057, wR_2 ~0.156, GOF ~1.08, $\Delta\rho_{min/max}$ -1.30/1.60 fm

Å^{-3}). The fourth model with Cu partially occupying the 8*b* site was selected as the best description of the disorder.

8.5 References

[264] J.A.A. Ketelaar, The crystal structure of alloys of zinc with the alkali and alkaline earth metals and of cadmium with potassium, J. Chem. Phys., 5 (1937) 668.

[265] M.-K. Han, G.J. Miller, An application of the "coloring problem": structure−composition−bonding relationships in the magnetocaloric materials $LaFe_{13-x}Si_x$, Inorg. Chem., 47 (2007) 515-528.

[266] J. Lyubina, R. Schäfer, N. Martin, L. Schultz, O. Gutfleisch, Novel design of $La(Fe,Si)_{13}$ alloys towards high magnetic refrigeration performance, Adv. Mater., 22 (2010) 3735-3739.

[267] Z.S. Wilson, R.T. Macaluso, E.D. Bauer, J.L. Smith, J.D. Thompson, Z. Fisk, G.G. Stanley, J.Y. Chan, Rare beryllium icosahedra in the intermediate valence compound $CeBe_{13}$, J. Am. Chem. Soc., 126 (2004) 13926-13927.

[268] H.R. Ott, H. Rudigier, Z. Fisk, J.L. Smith, UBe_{13}: an unconventional actinide superconductor, Phys. Rev. Lett., 50 (1983) 1595-1598.

[269] J.Y. Cho, E.L. Thomas, Y. Nambu, C. Capan, A.B. Karki, D.P. Young, K. Kuga, S. Nakatsuji, J.Y. Chan, Crystal growth, structure, and physical properties of $Ln(Cu,Ga)_{13-x}$ (Ln = La−Nd, Eu; x ≈ 0.2), Chem. Mater., 21 (2009) 3072-3078.

[270] Y. Shimura, T. Sakakibara, K. Kuga, J.Y. Cho, J.Y. Chan, Low-temperature magnetic properties of $Pr(Cu,Ga)_{12.85}$, J. Phys. Conf. Ser., 273 (2011) 012054.

[271] K.J. Nordell, G.J. Miller, Linking intermetallics and Zintl compounds: An investigation of ternary trielides (Al, Ga, In) forming the $NaZn_{13}$ structure type, Inorg. Chem., 38 (1999) 579-590.

[272] B.L. Drake, C. Capan, J.Y. Cho, Y. Nambu, K. Kuga, Y.M. Xiong, A.B. Karki, S. Nakatsuji, P.W. Adams, D.P. Young, J.Y. Chan, Crystal growth, structure, and physical properties of $Ln(Cu,Al)_{12}$ (Ln = Y, Ce, Pr, Sm, and Yb) and $Ln(Cu,Ga)_{12}$ (Ln = Y, Gd–Er, and Yb), J. Phys.:Condens. Matter, 22 (2010) 066001.

[273] W.A. Phelan, M.J. Kangas, G.T. McCandless, B.L. Drake, N. Haldolaarachchige, L.L. Zhao, J.K. Wang, X.P. Wang, D.P. Young, E. Morosan, C. Hoffmann, J.Y. Chan, Synthesis, structure, and physical properties of $Ln(Cu,Al,Ga)_{13-x}$ (Ln = La – Pr, and Eu) and $Eu(Cu,Al)_{13-x}$ Submitted to Inorg. Chem., (2012).

[274] G. Jogl, X.P. Wang, S.A. Mason, A. Kovalevsky, M. Mustyakimov, Z. Fisher, C. Hoffman, C. Kratky, P. Langan, High-resolution neutron crystallographic studies of the hydration of the coenzyme cob(II)alamin, Acta. Crystallogr. D, 67 (2011) 584-591.

[275] C. Hoffman, X.P. Wang, M. Frost, SNS TOPAZ Single-Crystal Diffractometer. http://neutrons.ornl.gov/instruments/SNS/TOPAZ, (accesed February 2012).

[276] J. Zikovsky, P.F. Peterson, X.P. Wang, M. Frost, C. Hoffmann, CrystalPlan: an experiment-planning tool for crystallography, J. Appl. Crystallogr., 44 (2011) 418-423.

[277] A.J. Schultz, K. Srinivasan, R.G. Teller, J.M. Williams, C.M. Lukehart, Single-crystal time-of-flight neutron-diffraction structureof hydrogen cis-diacetyltetracarbonylrhenate, cis-$(OC)_4Re(CH_3CO)_2H$ - a metallaacetylacetone molecule, J. Am. Chem. Soc., 106 (1984) 999-1003.

[278] G.M. Sheldrick, A short history of SHELX, Acta Crystallogr., A, 64 (2008) 112-122.

[279] B. Saparov, S. Bobev, Zinc-deficiency in intermetallics with the $NaZn_{13}$ type: Re-determination of the crystal structure and physical properties of $EuZn_{13-x}$ (x = 0.25(1)), J. Alloys Comp., 463 (2008) 119-123.

Chapter 9. Conclusions and Future Work

9.1 Conclusions

The growth of large single crystals can be a challenging endeavor, and the challenges of crystal growth have been discussed in the previous chapters and in references [280-285]. However, the growth of single crystals can be well worth the effort due to some key advantages which include single crystal diffraction, anisotropic physical property measurements, and obtaining intrinsic properties [284]. In the research detailed herein, the flux growth technique facilitated a detailed analysis of previously known structure types (LnM_2Al_{20} (Ln = La, Ce, Pr, Yb; M = Ti, V, Cr), $Ln_6M_4Al_{43}$ (Ln = Gd, Yb; M = Cr, Mo), and $Yb_2Pd_3Ga_9$), as well as the synthesis and characterization of new phases ($LnCr_xGa_3$ (Ln = Ho, Er; x ~ 0.15), $YbCr_2Al_{20-x}Fe_x$ (x ~ 0.2), and Ln_2PdGa_{12} (Ln = Pr, Nd, Sm)). Synthesis of large single crystals (up to ~5x5x5 mm^3) of $Ln(CuAlGa)_{13-x}$ allowed the use of single neutron diffraction to investigate the structural disorder.

In the synthesis of $LnCr_2Al_{20}$ and $Ln_6Cr_4Al_{43}$, the reaction ratio governs which of the two competing phases are produced, while the reaction temperature profile influences the size and quality of the crystals. This contrasts with previous systems such as, $CePdGa_6$, Ce_2PdGa_{12}, and Ce_2PdGa_{10} which can be produced with the same reaction ratio by varying the temperature profile to produce the desired phase [283].

Single crystals of $HoCr_{0.15}Ga_3$ and $ErCr_{0.14}Ga_3$ were synthesized with a gallium self-flux. Only the Ho and Er analogues could be grown in sufficient crystal size and quality for physical property measurements [286]. Unexpectedly, the crystal structure is neither the Y_4PdGa_{12} structure-type nor the $AuCu_3$ structure-type which were anticipated based on previous reports [287, 288]. Instead, the crystal structure can be described as a stuffed variant of the $AuCu_3$

structure, which is similar to subunits found in the Y_4PdGa_{12} structure-type. Both analogues exhibit metallic resistivity and positive magnetoresistance. Magnetic susceptibility measurements indicate antiferromagnetic order in $HoCr_{0.15}Ga_3$ at 5.9 K. A downturn in inverse susceptibility at ~7 K may be due to another magnetic transition, such as canted-antiferromagnetism or ferromagnetism, and a similar feature was observed for $ErCr_{0.14}Ga_3$ at ~4 K.

LnM_2Al_{20} (Ln = La, Ce, Pr, Sm, Yb; M = Ti, V, Cr) were synthesized from an aluminum self-flux [289]. All analogues are metallic. The La, Ce, and Yb analogues are temperature independent paramagnets and are consistent with Ce^{4+} and Yb^{2+} and no magnetic moment due to the transition metals. Resistivity and heat capacity measurements for $PrCr_2Al_{20}$ indicate the presence of Kondo interactions. $YbCr_2Al_{20}$ has a slightly enhanced Sommerfeld coefficient of ~74 mJ/K^2-mol, which is very similar to $LaCr_2Al_{20}$ (~63 mJ/K^2-mol) [289] and UCr_2Al_{20} (~80 mJ/K^2-mol) [290].

Single crystals of $YbCr_2Fe_xAl_{20-x}$ (x ~ 0.1, 0.2) were synthesized with the same reaction conditions as $YbCr_2Al_{20}$, except for the addition of Fe. The motivation for the project was to determine if adding iron, which is often magnetic, could affect the physical properties and to gain insight into the stability range of the $CeCr_2Al_{20}$ structure-type. Achieving a higher iron concentration is likely not possible with the flux growth technique as the higher doping level (x~ 0.2) started with a reaction ratio of 1:1:1:50 and produced $YbFe_2Al_{20}$ in addition to the desired product. ^{57}Fe Mössbauer studies indicated that Fe occupies two crystallographic sites. Single crystal X-ray refinements indicated that the Fe atoms occupy the Al1 (Fe site occupancy = 0.013(2), 96*g*) and Al2 (Fe site occupancy = 0.010 (4), 48*f*) sites and not the Cr site (16*d*), and this disorder could not have been determined without the complementary Mössbauer spectroscopy data. The iron site occupancies suggest that the $CeCr_2Al_{20}$ structure-type may not form for the latter transition metals because the transition metal site is unfavorable due to geometrical or electronic factors and other structure types, such as $YbFe_2Al_{10}$ [291], become more stable for the latter transition metals. For both Fe concentrations the $YbCr_2Fe_xAl_{20-x}$ (x ~ 0.1, 0.2) compounds exhibit metallic resistivity. The normalized resistivity and the residual resistivity ratios of $YbCr_2Al_{20}$ and $YbCr_2Fe_{0.1}Al_{19.9}$ are very similar, but the resistivity of $YbCr_2Fe_{0.2}Al_{19.8}$ is higher at low temperatures. Similar to $YbCr_2Al_{20}$, the iron containing compounds are nearly temperature independent paramagnets.

Single crystals of $Ln_6M_4Al_{43}$ (Ln = Gd, Yb; M = Cr, Mo) were also grown with an aluminum flux [292]. All analogues show metallic resistivities of 0.1 to 0.6 mΩ-cm at room temperature. Magnetic measurements indicate that the Yb analogues are non-magnetic, which is consistent with Yb^{2+}. The Gd analogues appear to order antiferromagnetically below 20 K. The magnetic structure, however, is likely complex because the Curie-Weiss fits yield positive θ which is indicative of ferromagnetic interactions. The magnetic structure can potentially be described by one type of exchange within the kagome sheets and another type of exchange between the sheets. A similar explanation was previously provided for the magnetic structure of the layered compounds $NaNiO_2$ and EuSnP [293, 294].

Single crystals of Ln_2PdGa_{12} (Ln = La, Pr, Nd, Sm) were grown with a gallium self-flux [295]. The Pr, Nd, and Sm analogues exhibit antiferromagnetic order at 18, 7.5, and 7.5 K, respectively, and the Pr and Nd analogues also show a metamagnetic transition, at 3 K, between 3 and 4 T. The antiferromagnetic ordering temperatures and metamagnetic transitions are similar to those observed in the previously published Cu and Ni analogues [296-299]. In addition, Pr_2PdGa_{12} has been shown with heat capacity measurements to have an enhanced Sommerfeld coefficient of ~250 mJ/K^2-mol f.u.. This indicates that Pr_2PdGa_{12} can potentially be added to the small but growing group of Pr-containing heavy fermion compounds [300-304].

Single crystals of $Yb_2Pd_3Ga_8$ were also grown with a gallium flux [283]. The crystal structure proved to be difficult to model, and models were constructed in four different space groups. All models indicate the structure is highly disordered. Physical property measurements indicate the sample is metallic and a temperature independent paramagnet. Heat capacity measurements give a Sommerfeld coefficient of ~4 mJ/K^2-mol, which indicates there is no enhancement to the electron's effective mass.

Large single crystals of Ln(Cu, Al, $Ga)_{13-x}$ (Ln = La-Pr, Eu) synthesized from an equimolar Ga/Al flux [305]. In addition to single crystal X-ray diffraction, single crystal neutron diffraction experiments were conducted to understand the disorder of the Cu, Al, and Ga atoms on the 8*b* and 96*i* sites of the $NaZn_{13-x}$ structure-type [306]. Four different neutron models were considered, including Cu and Al mixing, Ga and Al mixing, Cu/Al/Ga mixing on both sites, and partial occupancy of Cu on the 8*b* site and mixing of Cu/Al/Ga on the 96*i* site. All four models gave similar refinement statistics (R_1 ~0.057, wR_2 ~0.156, GOF ~1.08, $\Delta\rho_{min/max}$ -1.30/1.60 fm $Å^{-3}$). The fourth model with Cu partially occupying the 8*b* site was selected as the best description of the disorder. This model is consistent with reports on $NaZn_{13-x}$ where the 8*b* site is partially occupied [307] and calculations on $Ln(CuAl)_{13}$ that showed that Cu occupies the 8*b* site to achieve the correct number of valence and *d* electrons for maximum stability [308].

9.2 Future Work

Future work with the $LnCr_2Fe_xAl_{20-x}$ compounds can include the synthesis and characterization of Gd and Y analogues. The synthesis of the non-magnetic Y analogues will allow a direct observation of any magnetism due to the iron atoms. Characterization of the Gd analogues will show if the addition of iron has any effect on the magnetic Gd sublattice. In the structurally related GdT_2Zn_{20} compounds, the magnetic ordering is very sensitive to the number of valence electrons [309-311]. Additionally, the choice of these two rare earths could allow the synthesis of these materials through arc-melting which may increase the maximum iron content, which may yield a larger effect on the physical properties. In addition, a larger Fe concentration may help to further confirm the observed Fe disorder.

Similarly work with the $LnCr_xGa_3$ (Ln = Ho, Er) compounds could include an explanation as to why the compounds adopt the observed structure, if similar compounds could be prepared for the transition metals Ti and V, and what is the origin of the increase in susceptibility at low temperatures. Calculations may answer the first and second questions, while additional measurements such as heat capacity could answer the third. Additionally, it would be of interest to determine if any ternary or pseudo-binary compounds can be formed for the early lanthanides.

After some success in the synthesis and characterization of Ln-Cr-X (Ln = lanthanides; X = Al, Ga) intermetallics the question can be asked if any analogous phases can be prepared with the other common fluxes (Zn, In, Sn, Sb, Bi). For Sb, the phase $LnCrSb_3$ (Ln = La-Nd, Sm, Gd-Dy, Yb) has been reported and characterized [312-315]. However, no ternary Ln-Cr-X compounds have been reported for Zn, In, Sn, or Bi. Potential Sn and Bi compounds may be difficult to synthesize with the flux growth technique as the Cr-Sn and Cr-Bi binary phase diagrams show no binary phases and limited solubility of the elements even in the liquid phase [316, 317]. Zinc and In, on the other hand, form the binary phases $CrZn_{13}$, $CrZn_{17}$, $CrIn_2$, and $CrIn_3$ with Cr [318, 319]. Therefore Ln-Cr-Zn and Ln-Cr-In may be promising systems for the discovery of new intermetallic phases.

9.3 References

[280] Z. Fisk, J.P. Remeika, Chapter 81 Growth of single crystals from molten metal fluxes, in: Karl A. Gschneidner, Jr., E. LeRoy (Eds.) Handbook on the Physics and Chemistry of Rare Earths, Elsevier, 1989, pp. 53-70.

[281] M.G. Kanatzidis, R. Pöttgen, Wolfgang Jeitschko, The metal flux: A preparative tool for the exploration of intermetallic compounds, Angew. Chem. Int. Ed., 44 (2005) 6996-7023.

[282] Y. Janssen, M. Angst, K.W. Dennis, P.C. Canfield, R.W. McCallum, Small sealed Ta crucible for thermal analysis of volatile metallic samples, Rev. Sci. Instrum., 77 (2006) 056104.

[283] W.A. Phelan, M.C. Menard, M.J. Kangas, G.T. McCandless, B.L. Drake, J.Y. Chan, Adventures in crystal growth: synthesis and characterization of single crystals of complex intermetallic compounds, Chem. Mater., 24 (2012) 409-420.

[284] I.R. Fisher, M.C. Shapiro, J.G. Analytis, Principles of crystal growth of intermetallic and oxide compounds from molten solutions, Philos. Mag., 92 (2012) 2401-2435.

[285] T. Wolf, Flux separation methods for flux-grown single crystals, Philos. Mag., 92 (2012) 2458-2465.

[286] M.J. Kangas, J.D. McAlpin, N. Haldolaarachchige, D.P. Young, J.Y. Chan, Pushing the boundaries of transition metal substitution: Synthesis, structure, magnetic and electrical properties of $LnCr_xGa_3$ (Ln = Ho, Er; x ~ 0.13), To be submitted to J. Alloys Comp., (2012).

[287] F.S. Liu, Y.J. Yu, W.H. Zhang, J.Q. Li, W.Q. Ao, Isothermal section of the Ho-Fe-Ga ternary system at 773 K, J. Alloys Comp., 509 (2011) 1854-1860.

[288] V.Y. Markiv, T.I. Zhunkovskaya, N.N. Belyavina, A.A. Lysenko, Ternary phase diagrams of the systems Y - (Ti, Cr, Zr, Hf) - Ga, Dopov. Akad. Nauk. A, 45 (1983) 84-87.

[289] M.J. Kangas, D.C. Schmitt, A. Sakai, S. Nakatsuji, J.Y. Chan, Structure and physical properties of single crystal $PrCr_2Al_{20}$ and CeM_2Al_{20} (M = V, Cr): A comparison of compounds adopting the $CeCr_2Al_{20}$ structure type, J. Solid State Chem., in press (2012).

[290] K. Okuda, S. Noguchi, Y. Nakazawa, M. Ishikawa, Synthesis and characterization of new ternary uranium compound UCr_2Al_{20}, J. Phys. Soc. Jpn., 58 (1989) 4296-4299.

[291] S. Niemann, W. Jeitschko, The crystal structure of $YbFe_2Al_{10}$, a combined substitution and stacking variant of the $ThMn_{12}$ and $CeMn_4Al_8$ type structures, Z. Kristallogr., 210 (1995) 338-341.

[292] M.J. Kangas, L.J. Treadwell, N. Haldolaarachchige, J.D. McAlpin, D.P. Young, J.Y. Chan, Magnetic and electrical properties of flux grown single crystals of $Ln_6M_4Al_{43}$ (Ln = Gd, Yb; M = Cr, Mo, W) J. Solid State Chem. in press, (2012).

[293] E. Chappel, M.D. Núñez-Regueiro, F. Dupont, G. Chouteau, C. Darie, A. Sulpice, Antiferromagnetic resonance and high magnetic field properties of $NaNiO_2$, Eur. Phys. J. B, 17 (2000) 609-614.

[294] A.C. Payne, A.E. Sprauve, A.P. Holm, M.M. Olmstead, S.M. Kauzlarich, EuSnP: a novel antiferromagnet with two-dimensional, corrugated Sn sheets, J. Magn. Magn. Mater., 338 (2002) 229-234.

[295] M.J. Kangas, B.L. Drake, N. Haldolaarachchige, D.P. Young, J.Y. Chan, Crystal growth, structure, and physical properties of Ln_2PdGa_{12} (Ln = La, Pr, Nd, and Sm), J. Alloys Comp., 514 (2012) 64-70.

[296] X.Z. Chen, P. Small, S. Sportouch, M. Zhuravleva, P. Brazis, C.R. Kannewurf, M.G. Kanatzidis, Molten Ga as a solvent for exploratory synthesis: the new ternary polygallide Sm_2NiGa_{12}, Chem. Mater., 12 (2000) 2520-2522.

[297] R.T. Macaluso, J.N. Millican, S. Nakatsuji, H.-O. Lee, B. Carter, N.O. Moreno, Z. Fisk, J.Y. Chan, A comparison of the structure and localized magnetism in Ce_2PdGa_{12} with the heavy fermion $CePdGa_6$, J. Solid State Chem., 178 (2005) 3547-3553.

[298] J.Y. Cho, J.N. Millican, C. Capan, D.A. Sokolov, M. Moldovan, A.B. Karki, D.P. Young, M.C. Aronson, J.Y. Chan, Crystal growth, structure, and physical properties of Ln_2MGa_{12} (Ln = La, Ce; M = Ni, Cu), Chem. Mater., 20 (2008) 6116-6123.

[299] K.R. Thomas, J.Y. Cho, J.N. Millican, R.D. Hembree, M. Moldovan, A. Karki, D.P. Young, J.Y. Chan, Crystal growth and physical properties of Ln_2MGa_{12} (Ln=Pr, Nd, and Sm; M=Ni, Cu), J. Cryst. Growth, 312 (2010) 1098-1103.

[300] A. Yatskar, W.P. Beyermann, R. Movshovich, P.C. Canfield, Possible correlated-electron behavior from quadrupolar fluctuations in $PrInAg_2$, Phys. Rev. Lett., 77 (1996) 3637.

[301] H. Sugawara, T.D. Matsuda, K. Abe, Y. Aoki, H. Sato, S. Nojiri, Y. Inada, R. Settai, Y. Onuki, Observation of heavy electrons in the filled skutterudite $PrFe_4P_{12}$ via the de Haas-van Alphen effect, J. Magn. Magn. Mater., 226-230 (2001) 48-50.

[302] E.D. Bauer, N.A. Frederick, P.C. Ho, V.S. Zapf, M.B. Maple, Superconductivity and heavy fermion behavior in $PrOs_4Sb_{12}$, Phys. Rev. B, 65 (2002) 100506.

[303] V.K. Anand, Z. Hossain, C. Geibel, Magnetic order in $Pr_2Pd_3Ge_5$ and possible heavy-fermion behavior in $Pr_2Rh_3Ge_5$, Phys. Rev. B, 77 (2008) 184407.

[304] V.K. Anand, Z. Hossain, G. Chen, M. Nicklas, C. Geibel, Heavy fermion behavior in $PrRh_2B_2C$: Excitonic mass enhancement, Phys. Rev. B, 79 (2009) 113107.

[305] W.A. Phelan, M.J. Kangas, G.T. McCandless, B.L. Drake, N. Haldolaarachchige, L.L. Zhao, J.K. Wang, X.P. Wang, D.P. Young, E. Morosan, C. Hoffmann, J.Y. Chan, Synthesis, structure, and physical properties of $Ln(Cu,Al,Ga)_{13-x}$ (Ln = La – Pr, and Eu) and $Eu(Cu,Al)_{13-x}$ Submitted to Inorg. Chem., (2012).

[306] J.A.A. Ketelaar, The crystal structure of alloys of zinc with the alkali and alkaline earth metals and of cadmium with potassium, J. Chem. Phys., 5 (1937) 668.

[307] B. Saparov, S. Bobev, Zinc-deficiency in intermetallics with the $NaZn_{13}$ type: Re-determination of the crystal structure and physical properties of $EuZn_{13-x}$ (x = 0.25(1)), J. Alloys Comp., 463 (2008) 119-123.

[308] K.J. Nordell, G.J. Miller, Linking intermetallics and Zintl compounds: An investigation of ternary trielides (Al, Ga, In) forming the $NaZn_{13}$ structure type, Inorg. Chem., 38 (1999) 579-590.

[309] N. Ni, S. Jia, G.D. Samolyuk, A. Kracher, A.S. Sefat, S.L. Bud'ko, P.C. Canfield, Physical properties of $GdFe_2(Al_xZn_{1-x})_{20}$, Phys. Rev. B, 83 (2011) 054416.

[310] W. Tian, A.D. Christianson, J.L. Zarestky, S. Jia, S.L. Bud'ko, P.C. Canfield, P.M.B. Piccoli, A.J. Schultz, Magnetic order in $TbCo_2Zn_{20}$ and $TbFe_2Zn_{20}$, Phys. Rev. B, 81 (2010) 144409.

[311] S. Jia, N. Ni, G.D. Samolyuk, A. Safa-Sefat, K. Dennis, H. Ko, G.J. Miller, S.L. Bud'ko, P.C. Canfield, Variation of the magnetic ordering in GdT_2Zn_{20} (T=Fe , Ru, Os, Co, Rh and Ir) and its correlation with the electronic structure of isostructural YT_2Zn_{20}, Phys. Rev. B, 77 (2008) 104408.

[312] S.J. Crerar, L. Deakin, A. Mar, Structure and physical properties of ternary antimonide $YbCrSb_3$, Chem. Mater., 17 (2005) 2780-2784.

[313] E. Granado, H. Martinho, M.S. Sercheli, P.G. Pagliuso, D.D. Jackson, M. Torelli, J.W. Lynn, C. Rettori, Z. Fisk, S.B. Oseroff, Unconventional metallic magnetism in $LaCrSb_3$, Phys. Rev. Lett., 89 (2002) 107204.

[314] K. Hartjes, W. Jeitschko, M. Brylak, Magnetic properties of the rare-earth transition metal antimonides $LnVSb_3$ and $LnCrSb_3$ (Ln = La-Nd, Sm), J. Magn. Magn. Mater., 173 (1997) 109-116.

[315] D.D. Jackson, Z. Fisk, Anisotropy in magnetic and transport properties of $GdCrSb_3$, J. Alloys Comp., 377 (2004) 243-247.

[316] M. Venkatraman, J.P. Neumann, The Cr-Sn (chromium-tin) system, Bull. Alloy Phase Diagr., 9 (1988) 159-162.

[317] M. Venkatraman, J.P. Neumann, The Bi-Cr (bismuth-chromium) system, Bull. Alloy Phase Diagr., 9 (1988) 271-273.

[318] G. Reumont, P. Perrot, Thermodynamic assessment of the Zinc-rich part of the Cr-Zn system, J. Phase Equilib., 24 (2003) 50-54.

[319] H. Okamoto, C.E.T. White, Phase diagrams of indium alloys and their engineering applications, in, ASM International, Materials Park, OH, 1992, pp. 338.

Appendix A

Letters of Permission

Copyright Clearance Center RightsLink®

Home | Account Info | Help

Title: Crystal growth, structure, and physical properties of Ln2PdGa12(Ln=La, Pr, Nd, and Sm)

Author: Michael J. Kangas,Brenton L. Drake,Neel Haldolaarachchige,D.P. Young,Julia Y. Chan

Publication: Journal of Alloys and Compounds

Publisher: Elsevier

Date: 15 February 2012

Logged in as:
Michael Kangas
Account #:
3000541262

LOGOUT

Order Completed

Thank you very much for your order.

This is a License Agreement between Michael J Kangas ("You") and Elsevier ("Elsevier"). The license consists of your order details, the terms and conditions provided by Elsevier, and the payment terms and conditions.

Get the printable license.

License Number	2950640657409
License date	Jul 16, 2012
Licensed content publisher	Elsevier
Licensed content publication	Journal of Alloys and Compounds
Licensed content title	Crystal growth, structure, and physical properties of Ln2PdGa12(Ln=La, Pr, Nd, and Sm)
Licensed content author	Michael J. Kangas,Brenton L. Drake,Neel Haldolaarachchige,D.P. Young,Julia Y. Chan
Licensed content date	15 February 2012
Licensed content volume number	514
Number of pages	7
Type of Use	reuse in a thesis/dissertation
Portion	full article
Format	both print and electronic
Are you the author of this Elsevier article?	Yes
Will you be translating?	No
Order reference number	
Title of your thesis/dissertation	On the synthesis, characterization, and magnetism of Ln-M-X (Ln = lanthanide; M = Ti-Cr, Cu, Mo, Pd; X = Group 13 elements) intermetallics
Expected completion date	Sep 2012
Estimated size (number of pages)	200
Elsevier VAT number	GB 494 6272 12
Permissions price	0.00 USD
VAT/Local Sales Tax	0.0 USD / 0.0 GBP
Total	0.00 USD

Copyright Clearance Center RightsLink®

Account Info | Help

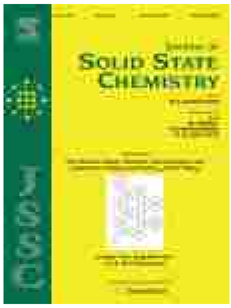

Title:	Structure and physical properties of single crystal PrCr2Al20and CeM2Al20(M=V, Cr): A comparison of compounds adopting the CeCr2Al20structure type
Author:	Michael J. Kangas,Devin C. Schmitt,Akito Sakai,Satoru Nakatsuji,Julia Y. Chan
Publication:	Journal of Solid State Chemistry
Publisher:	Elsevier
Date:	Jun 30, 2012

Logged in as:

Michael Kangas

Account #:

3000541262

LOGOUT

Order Completed

Thank you very much for your order.

This is a License Agreement between Michael J Kangas ("You") and Elsevier ("Elsevier"). The license consists of your order details, the terms and conditions provided by Elsevier, and thepayment terms and conditions.

License number	Reference confirmation email for license number
License date	Jul 16, 2012
Licensed content publisher	Elsevier
Licensed content publication	Journal of Solid State Chemistry
Licensed content title	Structure and physical properties of single crystal PrCr2Al20and CeM2Al20(M=V, Cr): A comparison of compounds adopting the CeCr2Al20structure type
Licensed content author	Michael J. Kangas,Devin C. Schmitt,Akito Sakai,Satoru Nakatsuji,Julia Y. Chan
Licensed content date	30 June 2012
Number of pages	1
Type of Use	reuse in a thesis/dissertation
Portion	full article
Format	both print and electronic
Are you the author of this Elsevier article?	Yes
Will you be translating?	No
Order reference number	
Title of your thesis/dissertation	On the synthesis, characterization, and magnetism of Ln-M-X (Ln = lanthanide; M = Ti-Cr, Cu, Mo, Pd; X = Group 13 elements) intermetallics
Expected completion date	Sep 2012
Estimated size	200

(number of pages)	
Elsevier VAT number	GB 494 6272 12
Billing Type	Invoice
Billing address	LSU
	232 Choppin Hall
	Baton Rouge, LA 70803
	United States
Customer reference info	
Permissions price	0.00 USD
VAT/Local Sales Tax	0.00 USD / GBP
Total	0.00 USD

CLOSE WINDOW

Appendix B

$LnCr_xGa_3$ (Ln = Ho, Er) Crystallographic Information Files

Data $HoCr_{0.14}Ga_3$

_audit_creation_method SHELXL-97
_chemical_name_systematic
;
 ?
;
_chemical_name_common ?
_chemical_melting_point ?
_chemical_formula_moiety 'Cr0.14
Ga3 Ho'
_chemical_formula_sum 'Cr0.14
Ga3 Ho'
_chemical_formula_weight 381.37

loop_
 _atom_type_symbol
 _atom_type_description
 _atom_type_scat_dispersion_real
 _atom_type_scat_dispersion_imag
 _atom_type_scat_source
 'Cr' 'Cr' 0.3209 0.6236
 'International Tables Vol C Tables 4.2.6.8
and 6.1.1.4'
 'Ga' 'Ga' 0.2307 1.6083
 'International Tables Vol C Tables 4.2.6.8
and 6.1.1.4'
 'Ho' 'Ho' -0.2175 4.6783
 'International Tables Vol C Tables 4.2.6.8
and 6.1.1.4'

_symmetry_cell_setting cubic
_symmetry_space_group_name_Hall '-P 4
2 3'
_symmetry_space_group_name_H-M 'P
m -3 m'

loop_
 _symmetry_equiv_pos_as_xyz
 'x, y, z'
'x, -y, -z'
'-x, -y, z'
'-x, y, -z'
'-y, x, z'
'y, x, -z'
'y, -x, z'
'-y, -x, -z'
'y, z, x'
'-y, -z, x'
'y, -z, -x'
'-y, z, -x'
'-z, y, x'
'-z, -y, -x'
'z, -y, x'
'z, y, -x'
'z, x, y'
'-z, x, -y'
'-z, -x, y'
'z, -x, -y'
'-x, -z, -y'
'-x, z, y'
'x, -z, y'
'x, z, -y'
'-x, -y, -z'
'-x, y, z'
'x, y, -z'
'x, -y, z'
'y, -x, -z'
'-y, -x, z'
'-y, x, -z'
'y, x, z'
'-y, -z, -x'
'y, z, -x'
'-y, z, x'
'y, -z, x'
'z, -y, -x'
'z, y, x'
'-z, y, -x'
'-z, -y, x'
'-z, -x, -y'
'z, -x, y'
'z, x, -y'
'-z, x, y'
'x, z, y'
'x, -z, -y'
'-x, z, -y'

'-x, -z, y'

_cell_length_a 4.2508(10)
_cell_length_b 4.2508(10)
_cell_length_c 4.2508(10)
_cell_angle_alpha 90.00
_cell_angle_beta 90.00
_cell_angle_gamma 90.00
_cell_volume 76.81(3)
_cell_formula_units_Z 1
_cell_measurement_temperature 295(1)
_cell_measurement_reflns_used 78
_cell_measurement_theta_min 0.998
_cell_measurement_theta_max 34.972

_exptl_crystal_description cube
_exptl_crystal_colour silver
_exptl_crystal_size_max 0.05
_exptl_crystal_size_mid 0.05
_exptl_crystal_size_min 0.05
_exptl_crystal_density_meas ?
_exptl_crystal_density_diffrn 8.245
_exptl_crystal_density_method 'not
measured'
_exptl_crystal_F_000 163
_exptl_absorpt_coefficient_mu 51.636
_exptl_absorpt_correction_type multi-scan
_exptl_absorpt_correction_T_min 0.1822
_exptl_absorpt_correction_T_max 0.1822
_exptl_absorpt_process_details
'HKL scalepack (Otwinski & Minor, 1997)'

_exptl_special_details
;
?
;

_diffrn_ambient_temperature 295(1)
_diffrn_radiation_wavelength 0.71073
_diffrn_radiation_type MoK\a
_diffrn_radiation_source 'fine-focus
sealed tube'
_diffrn_radiation_monochromator graphite
_diffrn_measurement_device_type 'Nonius
Kappa CCD'
_diffrn_measurement_method '\w and \f
scans'
_diffrn_detector_area_resol_mean ?
_diffrn_standards_number ?
_diffrn_standards_interval_count ?
_diffrn_standards_interval_time ?
_diffrn_standards_decay_% ?
_diffrn_reflns_number 2183
_diffrn_reflns_av_R_equivalents 0.0074
_diffrn_reflns_av_sigmaI/netI 0.0086
_diffrn_reflns_limit_h_min -6
_diffrn_reflns_limit_h_max 6
_diffrn_reflns_limit_k_min -4
_diffrn_reflns_limit_k_max 4
_diffrn_reflns_limit_l_min -4
_diffrn_reflns_limit_l_max 4
_diffrn_reflns_theta_min 4.80
_diffrn_reflns_theta_max 34.54
_reflns_number_total 54
_reflns_number_gt 54
_reflns_threshold_expression >2\s(I)

_computing_data_collection
'Collect (Nonius 1999)'
_computing_cell_refinement
'Denzo and Scalepack (Otwinski & Minor,
1997)'
_computing_data_reduction
'Denzo and Scalepack (Otwinski & Minor,
1997)'
_computing_structure_solution
'Direct methods, SIR97 (Altomare 1999)'
_computing_structure_refinement
'SHELXL-97 (Sheldrick, 2008)'
_computing_molecular_graphics
'Crystal Maker'
_computing_publication_material ?

_refine_special_details
;
Refinement of F^2^ against ALL
reflections. The weighted R-factor wR and
goodness of fit S are based on F^2^,
conventional R-factors R are based
on F, with F set to zero for negative F^2^.
The threshold expression of

F^2^ > 2\s(F^2^) is used only for
calculating R-factors(gt) etc. and is
not relevant to the choice of reflections for
refinement. R-factors based
on F^2^ are statistically about twice as large
as those based on F, and R-
factors based on ALL data will be even
larger.
;

_refine_ls_structure_factor_coef Fsqd
_refine_ls_matrix_type   full
_refine_ls_weighting_scheme   calc
_refine_ls_weighting_details
'calc
w=1/[\s^2^(Fo^2^)+(0.0109P)^2^+0.1800P]
where P=(Fo^2^+2Fc^2^)/3'
_atom_sites_solution_primary   direct
_atom_sites_solution_secondary   difmap
_atom_sites_solution_hydrogens   ?
_refine_ls_hydrogen_treatment   ?
_refine_ls_extinction_method   SHELXL
_refine_ls_extinction_coef   0.132(7)
_refine_ls_extinction_expression

'Fc^*^=kFc[1+0.001xFc^2^\l^3^/sin(2\q)]^-
1/4^'
_refine_ls_number_reflns   54
_refine_ls_number_parameters   7
_refine_ls_number_restraints   0
_refine_ls_R_factor_all   0.0107
_refine_ls_R_factor_gt   0.0107
_refine_ls_wR_factor_ref   0.0272
_refine_ls_wR_factor_gt   0.0272
_refine_ls_goodness_of_fit_ref   1.368
_refine_ls_restrained_S_all   1.368
_refine_ls_shift/su_max   0.000
_refine_ls_shift/su_mean   0.000

loop_
_atom_site_label
_atom_site_type_symbol
_atom_site_fract_x
_atom_site_fract_y
_atom_site_fract_z
_atom_site_U_iso_or_equiv
_atom_site_adp_type
_atom_site_occupancy
_atom_site_symmetry_multiplicity
_atom_site_calc_flag
_atom_site_refinement_flags
_atom_site_disorder_assembly
_atom_site_disorder_group
Ho1 Ho 0.0000 0.0000 0.0000 0.0083(2)
Uani 1 48 d S . .
Cr1 Cr 0.5000 0.5000 0.5000 0.002(3) Uani
0.136(10) 48 d SP . .
Ga1 Ga 0.0000 0.5000 0.5000 0.0215(3)
Uani 1 16 d S . .

loop_
_atom_site_aniso_label
_atom_site_aniso_U_11
_atom_site_aniso_U_22
_atom_site_aniso_U_33
_atom_site_aniso_U_23
_atom_site_aniso_U_13
_atom_site_aniso_U_12
Ho1 0.0083(2) 0.0083(2) 0.0083(2) 0.000
0.000 0.000
Cr1 0.002(3) 0.002(3) 0.002(3) 0.000 0.000
0.000
Ga1 0.0478(6) 0.0083(2) 0.0083(2) 0.000
0.000 0.000

_geom_special_details
;
All s.u.'s (except the s.u. in the dihedral
angle between two l.s. planes)
are estimated using the full covariance
matrix. The cell s.u.'s are taken
into account individually in the estimation
of s.u.'s in distances, angles
and torsion angles; correlations between
s.u.'s in cell parameters are only
used when they are defined by crystal
symmetry. An approximate (isotropic)
treatment of cell s.u.'s is used for estimating
s.u.'s involving l.s. planes.
;

loop_

_geom_bond_atom_site_label_1
_geom_bond_atom_site_label_2
_geom_bond_distance
_geom_bond_site_symmetry_2
_geom_bond_publ_flag
Ho1 Ga1 3.0058(7) 9 ?
Ho1 Ga1 3.0058(7) . ?
Ho1 Ga1 3.0058(7) 1_544 ?
Ho1 Ga1 3.0058(7) 9_445 ?
Ho1 Ga1 3.0058(7) 5_655 ?
Ho1 Ga1 3.0058(7) 5_554 ?
Ho1 Ga1 3.0058(7) 1_554 ?
Ho1 Ga1 3.0058(7) 5 ?
Ho1 Ga1 3.0058(7) 5_654 ?
Ho1 Ga1 3.0058(7) 1_545 ?
Ho1 Ga1 3.0058(7) 9_545 ?
Ho1 Ga1 3.0058(7) 9_455 ?
Cr1 Ga1 2.1254(5) 9_556 ?
Cr1 Ga1 2.1254(5) . ?
Cr1 Ga1 2.1254(5) 1_655 ?
Cr1 Ga1 2.1254(5) 5_655 ?
Cr1 Ga1 2.1254(5) 5_665 ?
Cr1 Ga1 2.1254(5) 9 ?
Ga1 Cr1 2.1254(5) 1_455 ?
Ga1 Ga1 3.0058(7) 9_556 ?
Ga1 Ga1 3.0058(7) 9_455 ?
Ga1 Ga1 3.0058(7) 5_665 ?
Ga1 Ho1 3.0058(7) 1_566 ?
Ga1 Ga1 3.0058(7) 5 ?
Ga1 Ho1 3.0058(7) 1_565 ?
Ga1 Ga1 3.0058(7) 5_565 ?
Ga1 Ga1 3.0058(7) 5_655 ?
Ga1 Ho1 3.0058(7) 1_556 ?

loop_
_geom_angle_atom_site_label_1
_geom_angle_atom_site_label_2
_geom_angle_atom_site_label_3
_geom_angle
_geom_angle_site_symmetry_1
_geom_angle_site_symmetry_3
_geom_angle_publ_flag
Ga1 Ho1 Ga1 60.0 9 . ?
Ga1 Ho1 Ga1 120.0 9 1_544 ?
Ga1 Ho1 Ga1 180.0 . 1_544 ?
Ga1 Ho1 Ga1 180.0 9 9_445 ?
Ga1 Ho1 Ga1 120.0 . 9_445 ?
Ga1 Ho1 Ga1 60.0 1_544 9_445 ?
Ga1 Ho1 Ga1 60.0 9 5_655 ?
Ga1 Ho1 Ga1 60.0 . 5_655 ?
Ga1 Ho1 Ga1 120.0 1_544 5_655 ?
Ga1 Ho1 Ga1 120.0 9_445 5_655 ?
Ga1 Ho1 Ga1 120.0 9 5_554 ?
Ga1 Ho1 Ga1 120.0 . 5_554 ?
Ga1 Ho1 Ga1 60.0 1_544 5_554 ?
Ga1 Ho1 Ga1 60.0 9_445 5_554 ?
Ga1 Ho1 Ga1 180.0 5_655 5_554 ?
Ga1 Ho1 Ga1 60.0 9 1_554 ?
Ga1 Ho1 Ga1 90.0 . 1_554 ?
Ga1 Ho1 Ga1 90.0 1_544 1_554 ?
Ga1 Ho1 Ga1 120.0 9_445 1_554 ?
Ga1 Ho1 Ga1 120.0 5_655 1_554 ?
Ga1 Ho1 Ga1 60.0 5_554 1_554 ?
Ga1 Ho1 Ga1 120.0 9 5 ?
Ga1 Ho1 Ga1 60.0 . 5 ?
Ga1 Ho1 Ga1 120.0 1_544 5 ?
Ga1 Ho1 Ga1 60.0 9_445 5 ?
Ga1 Ho1 Ga1 90.0 5_655 5 ?
Ga1 Ho1 Ga1 90.0 5_554 5 ?
Ga1 Ho1 Ga1 120.0 1_554 5 ?
Ga1 Ho1 Ga1 60.0 9 5_654 ?
Ga1 Ho1 Ga1 120.0 . 5_654 ?
Ga1 Ho1 Ga1 60.0 1_544 5_654 ?
Ga1 Ho1 Ga1 120.0 9_445 5_654 ?
Ga1 Ho1 Ga1 90.0 5_655 5_654 ?
Ga1 Ho1 Ga1 90.0 5_554 5_654 ?
Ga1 Ho1 Ga1 60.0 1_554 5_654 ?
Ga1 Ho1 Ga1 180.0 5 5_654 ?
Ga1 Ho1 Ga1 120.0 9 1_545 ?
Ga1 Ho1 Ga1 90.0 . 1_545 ?
Ga1 Ho1 Ga1 90.0 1_544 1_545 ?
Ga1 Ho1 Ga1 60.0 9_445 1_545 ?
Ga1 Ho1 Ga1 60.0 5_655 1_545 ?
Ga1 Ho1 Ga1 120.0 5_554 1_545 ?
Ga1 Ho1 Ga1 180.0 1_554 1_545 ?
Ga1 Ho1 Ga1 60.0 5 1_545 ?
Ga1 Ho1 Ga1 120.0 5_654 1_545 ?
Ga1 Ho1 Ga1 90.0 9 9_545 ?
Ga1 Ho1 Ga1 120.0 . 9_545 ?
Ga1 Ho1 Ga1 60.0 1_544 9_545 ?
Ga1 Ho1 Ga1 90.0 9_445 9_545 ?
Ga1 Ho1 Ga1 60.0 5_655 9_545 ?

Ga1 Ho1 Ga1 120.0 5_554 9_545 ?
Ga1 Ho1 Ga1 120.0 1_554 9_545 ?
Ga1 Ho1 Ga1 120.0 5 9_545 ?
Ga1 Ho1 Ga1 60.0 5_654 9_545 ?
Ga1 Ho1 Ga1 60.0 1_545 9_545 ?
Ga1 Ho1 Ga1 90.0 9 9_455 ?
Ga1 Ho1 Ga1 60.0 . 9_455 ?
Ga1 Ho1 Ga1 120.0 1_544 9_455 ?
Ga1 Ho1 Ga1 90.0 9_445 9_455 ?
Ga1 Ho1 Ga1 120.0 5_655 9_455 ?
Ga1 Ho1 Ga1 60.0 5_554 9_455 ?
Ga1 Ho1 Ga1 60.0 1_554 9_455 ?
Ga1 Ho1 Ga1 60.0 5 9_455 ?
Ga1 Ho1 Ga1 120.0 5_654 9_455 ?
Ga1 Ho1 Ga1 120.0 1_545 9_455 ?
Ga1 Ho1 Ga1 180.0 9_545 9_455 ?
Ga1 Cr1 Ga1 90.0 9_556 . ?
Ga1 Cr1 Ga1 90.0 9_556 1_655 ?
Ga1 Cr1 Ga1 180.0 . 1_655 ?
Ga1 Cr1 Ga1 90.0 9_556 5_655 ?
Ga1 Cr1 Ga1 90.0 . 5_655 ?
Ga1 Cr1 Ga1 90.0 1_655 5_655 ?
Ga1 Cr1 Ga1 90.0 9_556 5_665 ?
Ga1 Cr1 Ga1 90.0 . 5_665 ?
Ga1 Cr1 Ga1 90.0 1_655 5_665 ?
Ga1 Cr1 Ga1 180.0 5_655 5_665 ?
Ga1 Cr1 Ga1 180.0 9_556 9 ?
Ga1 Cr1 Ga1 90.0 . 9 ?
Ga1 Cr1 Ga1 90.0 1_655 9 ?
Ga1 Cr1 Ga1 90.0 5_655 9 ?
Ga1 Cr1 Ga1 90.0 5_665 9 ?
Cr1 Ga1 Cr1 180.0 1_455 . ?
Cr1 Ga1 Ga1 135.0 1_455 9_556 ?
Cr1 Ga1 Ga1 45.0 . 9_556 ?
Cr1 Ga1 Ga1 45.0 1_455 9_455 ?
Cr1 Ga1 Ga1 135.0 . 9_455 ?
Ga1 Ga1 Ga1 180.0 9_556 9_455 ?
Cr1 Ga1 Ga1 135.0 1_455 5_665 ?
Cr1 Ga1 Ga1 45.0 . 5_665 ?
Ga1 Ga1 Ga1 60.0 9_556 5_665 ?
Ga1 Ga1 Ga1 120.0 9_455 5_665 ?
Cr1 Ga1 Ho1 90.0 1_455 1_566 ?
Cr1 Ga1 Ho1 90.0 . 1_566 ?
Ga1 Ga1 Ho1 60.0 9_556 1_566 ?
Ga1 Ga1 Ho1 120.0 9_455 1_566 ?
Ga1 Ga1 Ho1 60.0 5_665 1_566 ?
Cr1 Ga1 Ho1 90.0 1_455 . ?
Cr1 Ga1 Ho1 90.0 . . ?
Ga1 Ga1 Ho1 120.0 9_556 . ?
Ga1 Ga1 Ho1 60.0 9_455 . ?
Ga1 Ga1 Ho1 120.0 5_665 . ?
Ho1 Ga1 Ho1 180.0 1_566 . ?
Cr1 Ga1 Ga1 45.0 1_455 5 ?
Cr1 Ga1 Ga1 135.0 . 5 ?
Ga1 Ga1 Ga1 120.0 9_556 5 ?
Ga1 Ga1 Ga1 60.0 9_455 5 ?
Ga1 Ga1 Ga1 180.0 5_665 5 ?
Ho1 Ga1 Ga1 120.0 1_566 5 ?
Ho1 Ga1 Ga1 60.0 . 5 ?
Cr1 Ga1 Ho1 90.0 1_455 1_565 ?
Cr1 Ga1 Ho1 90.0 . 1_565 ?
Ga1 Ga1 Ho1 120.0 9_556 1_565 ?
Ga1 Ga1 Ho1 60.0 9_455 1_565 ?
Ga1 Ga1 Ho1 60.0 5_665 1_565 ?
Ho1 Ga1 Ho1 90.0 1_566 1_565 ?
Ho1 Ga1 Ho1 90.0 . 1_565 ?
Ga1 Ga1 Ho1 120.0 5 1_565 ?
Cr1 Ga1 Ga1 45.0 1_455 5_565 ?
Cr1 Ga1 Ga1 135.0 . 5_565 ?
Ga1 Ga1 Ga1 120.0 9_556 5_565 ?
Ga1 Ga1 Ga1 60.0 9_455 5_565 ?
Ga1 Ga1 Ga1 90.0 5_665 5_565 ?
Ho1 Ga1 Ga1 60.0 1_566 5_565 ?
Ho1 Ga1 Ga1 120.0 . 5_565 ?
Ga1 Ga1 Ga1 90.0 5 5_565 ?
Ho1 Ga1 Ga1 60.0 1_565 5_565 ?
Cr1 Ga1 Ga1 135.0 1_455 5_655 ?
Cr1 Ga1 Ga1 45.0 . 5_655 ?
Ga1 Ga1 Ga1 60.0 9_556 5_655 ?
Ga1 Ga1 Ga1 120.0 9_455 5_655 ?
Ga1 Ga1 Ga1 90.0 5_665 5_655 ?
Ho1 Ga1 Ga1 120.0 1_566 5_655 ?
Ho1 Ga1 Ga1 60.0 . 5_655 ?
Ga1 Ga1 Ga1 90.0 5 5_655 ?
Ho1 Ga1 Ga1 120.0 1_565 5_655 ?
Ga1 Ga1 Ga1 180.0 5_565 5_655 ?
Cr1 Ga1 Ho1 90.0 1_455 1_556 ?
Cr1 Ga1 Ho1 90.0 . 1_556 ?
Ga1 Ga1 Ho1 60.0 9_556 1_556 ?
Ga1 Ga1 Ho1 120.0 9_455 1_556 ?
Ga1 Ga1 Ho1 120.0 5_665 1_556 ?
Ho1 Ga1 Ho1 90.0 1_566 1_556 ?

Ho1 Ga1 Ho1 90.0 . 1_556 ?
Ga1 Ga1 Ho1 60.0 5 1_556 ?
Ho1 Ga1 Ho1 180.0 1_565 1_556 ?
Ga1 Ga1 Ho1 120.0 5_565 1_556 ?
Ga1 Ga1 Ho1 60.0 5_655 1_556 ?

_diffrn_measured_fraction_theta_max
1.000
_diffrn_reflns_theta_full 34.54
_diffrn_measured_fraction_theta_full
1.000
_refine_diff_density_max 0.420
_refine_diff_density_min -0.708
_refine_diff_density_rms 0.172

##END

data_ErCr$_{0.12}$Ga$_3$

_audit_creation_method SHELXL-97
_chemical_name_systematic
;
 ?
;
_chemical_name_common ?
_chemical_melting_point ?
_chemical_formula_moiety 'Cr0.12 Er
Ga3'
_chemical_formula_sum 'Cr0.12 Er
Ga3'

_chemical_formula_weight 382.66

loop_
 _atom_type_symbol
 _atom_type_description
 _atom_type_scat_dispersion_real
 _atom_type_scat_dispersion_imag
 _atom_type_scat_source
 'Er' 'Er' -0.2586 4.9576
 'International Tables Vol C Tables 4.2.6.8
and 6.1.1.4'
 'Cr' 'Cr' 0.3209 0.6236
 'International Tables Vol C Tables 4.2.6.8
and 6.1.1.4'
 'Ga' 'Ga' 0.2307 1.6083
 'International Tables Vol C Tables 4.2.6.8
and 6.1.1.4'

_symmetry_cell_setting cubic
_symmetry_space_group_name_H-M 'P m
-3 m'
_symmetry_space_group_name_Hall '-P 4
2 3'

loop_
 _symmetry_equiv_pos_as_xyz
 'x, y, z'
 'x, z, y'
 'y, -z, x'
 'y, x, -z'
 'x, -z, y'
 '-z, y, x'
 'z, x, -y'
 'y, z, -x'
 'z, y, -x'
 '-z, x, -y'
 'x, z, -y'
 'y, -z, -x'
 'x, -z, -y'
 '-z, y, -x'
 'x, -y, z'
 'y, -x, z'
 'x, -y, -z'
 'y, -x, -z'
 '-y, -z, -x'
 '-x, -y, z'
 '-y, -x, -z'
 '-z, -x, -y'
 '-z, -y, -x'
 'z, -x, -y'
 '-x, -y, -z'
 '-x, -z, -y'
 '-y, z, -x'
 '-y, -x, z'
 '-x, z, -y'
 'z, -y, -x'
 '-z, -x, y'
 '-y, -z, x'
 '-z, -y, x'
 'z, -x, y'

```
 '-x, -z, y'
 '-y, z, x'
 '-x, z, y'
 'z, -y, x'
 '-x, y, -z'
 '-y, x, -z'
 '-x, y, z'
 '-y, x, z'
 'y, z, x'
 'x, y, -z'
 'y, x, z'
 'z, x, y'
 'z, y, x'
 '-z, x, y'

_cell_length_a                    4.2383(10)
_cell_length_b                    4.2383(10)
_cell_length_c                    4.2383(10)
_cell_angle_alpha                 90.00
_cell_angle_beta                  90.00
_cell_angle_gamma                 90.00
_cell_volume                      76.13(3)
_cell_formula_units_Z             1
_cell_measurement_temperature     296(1)
_cell_measurement_reflns_used     192
_cell_measurement_theta_min       0.998
_cell_measurement_theta_max       34.972

_exptl_crystal_description        cube
_exptl_crystal_colour             silver
_exptl_crystal_size_max           0.08
_exptl_crystal_size_mid           0.08
_exptl_crystal_size_min           0.08
_exptl_crystal_density_meas       ?
_exptl_crystal_density_diffrn     8.346
_exptl_crystal_density_method     'not
measured'
_exptl_crystal_F_000              164
_exptl_absorpt_coefficient_mu     53.603
_exptl_absorpt_correction_type    multi-scan
_exptl_absorpt_correction_T_min   0.0994
_exptl_absorpt_correction_T_max   0.0994
_exptl_absorpt_process_details
'HKL scalepack (Otwinski & Minor, 1997)'

_exptl_special_details
;
 ?
;

_diffrn_ambient_temperature       296(1)
_diffrn_radiation_wavelength      0.71073
_diffrn_radiation_type            MoK\a
_diffrn_radiation_source          'fine-focus
sealed tube'
_diffrn_radiation_monochromator   graphite
_diffrn_measurement_device_type   'Nonius
Kappa CCD'
_diffrn_measurement_method        '\w adn \f
scans'
_diffrn_detector_area_resol_mean  ?
_diffrn_standards_number          ?
_diffrn_standards_interval_count  ?
_diffrn_standards_interval_time   ?
_diffrn_standards_decay_%         ?
_diffrn_reflns_number             2979
_diffrn_reflns_av_R_equivalents   0.0466
_diffrn_reflns_av_sigmaI/netI     0.0260
_diffrn_reflns_limit_h_min        -6
_diffrn_reflns_limit_h_max        6
_diffrn_reflns_limit_k_min        -4
_diffrn_reflns_limit_k_max        4
_diffrn_reflns_limit_l_min        -6
_diffrn_reflns_limit_l_max        6
_diffrn_reflns_theta_min          4.81
_diffrn_reflns_theta_max          34.66
_reflns_number_total              54
_reflns_number_gt                 54
_reflns_threshold_expression      >2\s(I)

_computing_data_collection
'Collect (Nonius 1999)'
_computing_cell_refinement
'Denzo and scalepack (Otwinski & Minor
1997)'
_computing_data_reduction
'Denzo and scalepack (Otwinski & Minor
1997)'
_computing_structure_solution
'Direct methods, SIR 97 (Altomare 1999)'
_computing_structure_refinement
'SHELXL-97 (Sheldrick, 2008)'
```

_computing_molecular_graphics
'Crystal Maker'
_computing_publication_material ?

_refine_special_details
;
Refinement of F^2^ against ALL reflections. The weighted R-factor wR and goodness of fit S are based on F^2^, conventional R-factors R are based on F, with F set to zero for negative F^2^. The threshold expression of F^2^ > 2\s(F^2^) is used only for calculating R-factors(gt) etc. and is not relevant to the choice of reflections for refinement. R-factors based on F^2^ are statistically about twice as large as those based on F, and R-factors based on ALL data will be even larger.
;

_refine_ls_structure_factor_coef Fsqd
_refine_ls_matrix_type full
_refine_ls_weighting_scheme calc
_refine_ls_weighting_details
'calc w=1/[\s^2^(Fo^2^)+(0.0000P)^2^+0.3040P] where P=(Fo^2^+2Fc^2^)/3'
_atom_sites_solution_primary direct
_atom_sites_solution_secondary difmap
_atom_sites_solution_hydrogens ?
_refine_ls_hydrogen_treatment ?
_refine_ls_extinction_method SHELXL
_refine_ls_extinction_coef 0.131(10)
_refine_ls_extinction_expression

'Fc^*^=kFc[1+0.001xFc^2^\l^3^/sin(2\q)]^-1/4^'
_refine_ls_number_reflns 54
_refine_ls_number_parameters 7
_refine_ls_number_restraints 0
_refine_ls_R_factor_all 0.0159
_refine_ls_R_factor_gt 0.0159
_refine_ls_wR_factor_ref 0.0360
_refine_ls_wR_factor_gt 0.0360
_refine_ls_goodness_of_fit_ref 1.340
_refine_ls_restrained_S_all 1.340
_refine_ls_shift/su_max 0.000
_refine_ls_shift/su_mean 0.000

loop_
_atom_site_label
_atom_site_type_symbol
_atom_site_fract_x
_atom_site_fract_y
_atom_site_fract_z
_atom_site_U_iso_or_equiv
_atom_site_adp_type
_atom_site_occupancy
_atom_site_symmetry_multiplicity
_atom_site_calc_flag
_atom_site_refinement_flags
_atom_site_disorder_assembly
_atom_site_disorder_group
Er1 Er 0.0000 0.0000 0.0000 0.0091(3) Uani 1 48 d S . .
Cr1 Cr 0.5000 0.5000 0.5000 0.003(5) Uani 0.122(13) 48 d SP . .
Ga1 Ga 0.0000 0.5000 0.5000 0.0203(4) Uani 1 16 d S . .

loop_
_atom_site_aniso_label
_atom_site_aniso_U_11
_atom_site_aniso_U_22
_atom_site_aniso_U_33
_atom_site_aniso_U_23
_atom_site_aniso_U_13
_atom_site_aniso_U_12
Er1 0.0091(3) 0.0091(3) 0.0091(3) 0.000 0.000 0.000
Cr1 0.003(5) 0.003(5) 0.003(5) 0.000 0.000 0.000
Ga1 0.0435(8) 0.0086(3) 0.0086(3) 0.000 0.000 0.000

_geom_special_details
;
All s.u.'s (except the s.u. in the dihedral angle between two l.s. planes)

are estimated using the full covariance
matrix. The cell s.u.'s are taken
into account individually in the estimation
of s.u.'s in distances, angles
and torsion angles; correlations between
s.u.'s in cell parameters are only
used when they are defined by crystal
symmetry. An approximate (isotropic)
treatment of cell s.u.'s is used for estimating
s.u.'s involving l.s. planes.
;

loop_
_geom_bond_atom_site_label_1
_geom_bond_atom_site_label_2
_geom_bond_distance
_geom_bond_site_symmetry_2
_geom_bond_publ_flag
Er1 Ga1 2.9969(7) 4_556 ?
Er1 Ga1 2.9969(7) . ?
Er1 Ga1 2.9969(7) 1_544 ?
Er1 Ga1 2.9969(7) 4_455 ?
Er1 Ga1 2.9969(7) 3_565 ?
Er1 Ga1 2.9969(7) 3_455 ?
Er1 Ga1 2.9969(7) 1_554 ?
Er1 Ga1 2.9969(7) 3_465 ?
Er1 Ga1 2.9969(7) 3 ?
Er1 Ga1 2.9969(7) 1_545 ?
Er1 Ga1 2.9969(7) 4 ?
Er1 Ga1 2.9969(7) 4_456 ?
Cr1 Ga1 2.1191(5) 4_566 ?
Cr1 Ga1 2.1191(5) . ?
Cr1 Ga1 2.1192(5) 1_655 ?
Cr1 Ga1 2.1191(5) 3_565 ?
Cr1 Ga1 2.1191(5) 3_566 ?
Cr1 Ga1 2.1191(5) 4_556 ?
Ga1 Cr1 2.1191(5) 1_455 ?
Ga1 Ga1 2.9969(7) 4_566 ?
Ga1 Ga1 2.9969(7) 4_456 ?
Ga1 Ga1 2.9969(7) 3_566 ?
Ga1 Er1 2.9969(7) 1_566 ?
Ga1 Ga1 2.9969(7) 3_465 ?
Ga1 Er1 2.9969(7) 1_565 ?
Ga1 Ga1 2.9969(7) 3_466 ?
Ga1 Ga1 2.9969(7) 3_565 ?
Ga1 Er1 2.9969(7) 1_556 ?

loop_
_geom_angle_atom_site_label_1
_geom_angle_atom_site_label_2
_geom_angle_atom_site_label_3
_geom_angle
_geom_angle_site_symmetry_1
_geom_angle_site_symmetry_3
_geom_angle_publ_flag
Ga1 Er1 Ga1 60.0 4_556 . ?
Ga1 Er1 Ga1 120.0 4_556 1_544 ?
Ga1 Er1 Ga1 180.0 . 1_544 ?
Ga1 Er1 Ga1 180.0 4_556 4_455 ?
Ga1 Er1 Ga1 120.0 . 4_455 ?
Ga1 Er1 Ga1 60.0 1_544 4_455 ?
Ga1 Er1 Ga1 60.0 4_556 3_565 ?
Ga1 Er1 Ga1 60.0 . 3_565 ?
Ga1 Er1 Ga1 120.0 1_544 3_565 ?
Ga1 Er1 Ga1 120.0 4_455 3_565 ?
Ga1 Er1 Ga1 120.0 4_556 3_455 ?
Ga1 Er1 Ga1 120.0 . 3_455 ?
Ga1 Er1 Ga1 60.0 1_544 3_455 ?
Ga1 Er1 Ga1 60.0 4_455 3_455 ?
Ga1 Er1 Ga1 180.0 3_565 3_455 ?
Ga1 Er1 Ga1 120.0 4_556 1_554 ?
Ga1 Er1 Ga1 90.0 . 1_554 ?
Ga1 Er1 Ga1 90.0 1_544 1_554 ?
Ga1 Er1 Ga1 60.0 4_455 1_554 ?
Ga1 Er1 Ga1 60.0 3_565 1_554 ?
Ga1 Er1 Ga1 120.0 3_455 1_554 ?
Ga1 Er1 Ga1 120.0 4_556 3_465 ?
Ga1 Er1 Ga1 60.0 . 3_465 ?
Ga1 Er1 Ga1 120.0 1_544 3_465 ?
Ga1 Er1 Ga1 60.0 4_455 3_465 ?
Ga1 Er1 Ga1 90.0 3_565 3_465 ?
Ga1 Er1 Ga1 90.0 3_455 3_465 ?
Ga1 Er1 Ga1 60.0 1_554 3_465 ?
Ga1 Er1 Ga1 60.0 4_556 3 ?
Ga1 Er1 Ga1 120.0 . 3 ?
Ga1 Er1 Ga1 60.0 1_544 3 ?
Ga1 Er1 Ga1 120.0 4_455 3 ?
Ga1 Er1 Ga1 90.0 3_565 3 ?
Ga1 Er1 Ga1 90.0 3_455 3 ?
Ga1 Er1 Ga1 120.0 1_554 3 ?
Ga1 Er1 Ga1 180.0 3_465 3 ?
Ga1 Er1 Ga1 60.0 4_556 1_545 ?

Ga1 Er1 Ga1 90.0 . 1_545 ?
Ga1 Er1 Ga1 90.0 1_544 1_545 ?
Ga1 Er1 Ga1 120.0 4_455 1_545 ?
Ga1 Er1 Ga1 120.0 3_565 1_545 ?
Ga1 Er1 Ga1 60.0 3_455 1_545 ?
Ga1 Er1 Ga1 180.0 1_554 1_545 ?
Ga1 Er1 Ga1 120.0 3_465 1_545 ?
Ga1 Er1 Ga1 60.0 3 1_545 ?
Ga1 Er1 Ga1 90.0 4_556 4 ?
Ga1 Er1 Ga1 120.0 . 4 ?
Ga1 Er1 Ga1 60.0 1_544 4 ?
Ga1 Er1 Ga1 90.0 4_455 4 ?
Ga1 Er1 Ga1 60.0 3_565 4 ?
Ga1 Er1 Ga1 120.0 3_455 4 ?
Ga1 Er1 Ga1 60.0 1_554 4 ?
Ga1 Er1 Ga1 120.0 3_465 4 ?
Ga1 Er1 Ga1 60.0 3 4 ?
Ga1 Er1 Ga1 120.0 1_545 4 ?
Ga1 Er1 Ga1 90.0 4_556 4_456 ?
Ga1 Er1 Ga1 60.0 . 4_456 ?
Ga1 Er1 Ga1 120.0 1_544 4_456 ?
Ga1 Er1 Ga1 90.0 4_455 4_456 ?
Ga1 Er1 Ga1 120.0 3_565 4_456 ?
Ga1 Er1 Ga1 60.0 3_455 4_456 ?
Ga1 Er1 Ga1 120.0 1_554 4_456 ?
Ga1 Er1 Ga1 60.0 3_465 4_456 ?
Ga1 Er1 Ga1 120.0 3 4_456 ?
Ga1 Er1 Ga1 60.0 1_545 4_456 ?
Ga1 Er1 Ga1 180.0 4 4_456 ?
Ga1 Cr1 Ga1 90.0 4_566 . ?
Ga1 Cr1 Ga1 90.0 4_566 1_655 ?
Ga1 Cr1 Ga1 180.0 . 1_655 ?
Ga1 Cr1 Ga1 90.0 4_566 3_565 ?
Ga1 Cr1 Ga1 90.0 . 3_565 ?
Ga1 Cr1 Ga1 90.0 1_655 3_565 ?
Ga1 Cr1 Ga1 90.0 4_566 3_566 ?
Ga1 Cr1 Ga1 90.0 . 3_566 ?
Ga1 Cr1 Ga1 90.0 1_655 3_566 ?
Ga1 Cr1 Ga1 180.0 3_565 3_566 ?
Ga1 Cr1 Ga1 180.0 4_566 4_556 ?
Ga1 Cr1 Ga1 90.0 . 4_556 ?
Ga1 Cr1 Ga1 90.0 1_655 4_556 ?
Ga1 Cr1 Ga1 90.0 3_565 4_556 ?
Ga1 Cr1 Ga1 90.0 3_566 4_556 ?
Cr1 Ga1 Cr1 180.0 1_455 . ?
Cr1 Ga1 Ga1 135.0 1_455 4_566 ?
Cr1 Ga1 Ga1 45.0 . 4_566 ?
Cr1 Ga1 Ga1 45.0 1_455 4_456 ?
Cr1 Ga1 Ga1 135.0 . 4_456 ?
Ga1 Ga1 Ga1 180.0 4_566 4_456 ?
Cr1 Ga1 Ga1 135.0 1_455 3_566 ?
Cr1 Ga1 Ga1 45.0 . 3_566 ?
Ga1 Ga1 Ga1 60.0 4_566 3_566 ?
Ga1 Ga1 Ga1 120.0 4_456 3_566 ?
Cr1 Ga1 Er1 90.0 1_455 1_566 ?
Cr1 Ga1 Er1 90.0 . 1_566 ?
Ga1 Ga1 Er1 60.0 4_566 1_566 ?
Ga1 Ga1 Er1 120.0 4_456 1_566 ?
Ga1 Ga1 Er1 60.0 3_566 1_566 ?
Cr1 Ga1 Er1 90.0 1_455 . ?
Cr1 Ga1 Er1 90.0 . . ?
Ga1 Ga1 Er1 120.0 4_566 . ?
Ga1 Ga1 Er1 60.0 4_456 . ?
Ga1 Ga1 Er1 120.0 3_566 . ?
Er1 Ga1 Er1 180.0 1_566 . ?
Cr1 Ga1 Ga1 45.0 1_455 3_465 ?
Cr1 Ga1 Ga1 135.0 . 3_465 ?
Ga1 Ga1 Ga1 120.0 4_566 3_465 ?
Ga1 Ga1 Ga1 60.0 4_456 3_465 ?
Ga1 Ga1 Ga1 180.0 3_566 3_465 ?
Er1 Ga1 Ga1 120.0 1_566 3_465 ?
Er1 Ga1 Ga1 60.0 . 3_465 ?
Cr1 Ga1 Er1 90.0 1_455 1_565 ?
Cr1 Ga1 Er1 90.0 . 1_565 ?
Ga1 Ga1 Er1 60.0 4_566 1_565 ?
Ga1 Ga1 Er1 120.0 4_456 1_565 ?
Ga1 Ga1 Er1 120.0 3_566 1_565 ?
Er1 Ga1 Er1 90.0 1_566 1_565 ?
Er1 Ga1 Er1 90.0 . 1_565 ?
Ga1 Ga1 Er1 60.0 3_465 1_565 ?
Cr1 Ga1 Ga1 45.0 1_455 3_466 ?
Cr1 Ga1 Ga1 135.0 . 3_466 ?
Ga1 Ga1 Ga1 120.0 4_566 3_466 ?
Ga1 Ga1 Ga1 60.0 4_456 3_466 ?
Ga1 Ga1 Ga1 90.0 3_566 3_466 ?
Er1 Ga1 Ga1 60.0 1_566 3_466 ?
Er1 Ga1 Ga1 120.0 . 3_466 ?
Ga1 Ga1 Ga1 90.0 3_465 3_466 ?
Er1 Ga1 Ga1 120.0 1_565 3_466 ?
Cr1 Ga1 Ga1 135.0 1_455 3_565 ?
Cr1 Ga1 Ga1 45.0 . 3_565 ?
Ga1 Ga1 Ga1 60.0 4_566 3_565 ?

Ga1 Ga1 Ga1 120.0 4_456 3_565 ?
Ga1 Ga1 Ga1 90.0 3_566 3_565 ?
Er1 Ga1 Ga1 120.0 1_566 3_565 ?
Er1 Ga1 Ga1 60.0 . 3_565 ?
Ga1 Ga1 Ga1 90.0 3_465 3_565 ?
Er1 Ga1 Ga1 60.0 1_565 3_565 ?
Ga1 Ga1 Ga1 180.0 3_466 3_565 ?
Cr1 Ga1 Er1 90.0 1_455 1_556 ?
Cr1 Ga1 Er1 90.0 . 1_556 ?
Ga1 Ga1 Er1 120.0 4_566 1_556 ?
Ga1 Ga1 Er1 60.0 4_456 1_556 ?
Ga1 Ga1 Er1 60.0 3_566 1_556 ?
Er1 Ga1 Er1 90.0 1_566 1_556 ?
Er1 Ga1 Er1 90.0 . 1_556 ?
Ga1 Ga1 Er1 120.0 3_465 1_556 ?
Er1 Ga1 Er1 180.0 1_565 1_556 ?
Ga1 Ga1 Er1 60.0 3_466 1_556 ?
Ga1 Ga1 Er1 120.0 3_565 1_556 ?

_diffrn_measured_fraction_theta_max
1.000
_diffrn_reflns_theta_full 34.66
_diffrn_measured_fraction_theta_full
1.000
_refine_diff_density_max 1.200
_refine_diff_density_min -0.866
_refine_diff_density_rms 0.229

##END

Appendix C

$YbCr_2Fe_xAl_{20-x}$ Crystallographic Information Files

data_$YbCr_2Fe_{0.1}Al_{19.9}$

_audit_update_record
;
2012-03-23 # Formatted by publCIF
;

_audit_creation_method SHELXL-97
_chemical_name_systematic
;
?
;
_chemical_name_common ?
_chemical_melting_point ?
_chemical_formula_moiety 'Al19.90 Cr2 Fe0.10 Yb'
_chemical_formula_sum
'Al19.90 Cr2 Fe0.10 Yb'
_chemical_formula_weight 819.53

loop_
_atom_type_symbol
_atom_type_description
_atom_type_scat_dispersion_real
_atom_type_scat_dispersion_imag
_atom_type_scat_source
'Yb' 'Yb' -0.3850 5.5486
'International Tables Vol C Tables 4.2.6.8 and 6.1.1.4'
'Cr' 'Cr' 0.3209 0.6236
'International Tables Vol C Tables 4.2.6.8 and 6.1.1.4'
'Fe' 'Fe' 0.3463 0.8444
'International Tables Vol C Tables 4.2.6.8 and 6.1.1.4'
'Al' 'Al' 0.0645 0.0514
'International Tables Vol C Tables 4.2.6.8 and 6.1.1.4'

_symmetry_cell_setting cubic
_symmetry_space_group_name_H-M 'F d -3 m'
_symmetry_space_group_name_Hall '-F 4vw 2vw'

loop_
_symmetry_equiv_pos_as_xyz
'x, y, z'
'x, z, y'
'y+1/4, -z, x+1/4'
'y+1/4, x+1/4, -z'
'x+1/4, -z, y+1/4'
'-z, y+1/4, x+1/4'
'z+1/4, x+1/4, -y'
'y+1/4, z+1/4, -x'
'z+1/4, y+1/4, -x'
'-z+1/4, x, -y+1/4'
'x+1/4, z+1/4, -y'
'y, -z+1/4, -x+1/4'
'x, -z+1/4, -y+1/4'
'-z+1/4, y, -x+1/4'
'x+1/4, -y, z+1/4'
'y+1/4, -x, z+1/4'
'x, -y+1/4, -z+1/4'
'y, -x+1/4, -z+1/4'
'-y, -z, -x'
'-x+1/4, -y+1/4, z'
'-y, -x, -z'
'-z, -x, -y'
'-z, -y, -x'
'z, -x+1/4, -y+1/4'
'x, y+1/2, z+1/2'
'x, z+1/2, y+1/2'
'y+1/4, -z+1/2, x+3/4'
'y+1/4, x+3/4, -z+1/2'
'x+1/4, -z+1/2, y+3/4'
'-z, y+3/4, x+3/4'
'z+1/4, x+3/4, -y+1/2'
'y+1/4, z+3/4, -x+1/2'
'z+1/4, y+3/4, -x+1/2'
'-z+1/4, x+1/2, -y+3/4'
'x+1/4, z+3/4, -y+1/2'
'y, -z+3/4, -x+3/4'
'x, -z+3/4, -y+3/4'
'-z+1/4, y+1/2, -x+3/4'
'x+1/4, -y+1/2, z+3/4'

'y+1/4, -x+1/2, z+3/4'
'x, -y+3/4, -z+3/4'
'y, -x+3/4, -z+3/4'
'-y, -z+1/2, -x+1/2'
'-x+1/4, -y+3/4, z+1/2'
'-y, -x+1/2, -z+1/2'
'-z, -x+1/2, -y+1/2'
'-z, -y+1/2, -x+1/2'
'z, -x+3/4, -y+3/4'
'x+1/2, y, z+1/2'
'x+1/2, z, y+1/2'
'y+3/4, -z, x+3/4'
'y+3/4, x+1/4, -z+1/2'
'x+3/4, -z, y+3/4'
'-z+1/2, y+1/4, x+3/4'
'z+3/4, x+1/4, -y+1/2'
'y+3/4, z+1/4, -x+1/2'
'z+3/4, y+1/4, -x+1/2'
'-z+3/4, x, -y+3/4'
'x+3/4, z+1/4, -y+1/2'
'y+1/2, -z+1/4, -x+3/4'
'x+1/2, -z+1/4, -y+3/4'
'-z+3/4, y, -x+3/4'
'x+3/4, -y, z+3/4'
'y+3/4, -x, z+3/4'
'x+1/2, -y+1/4, -z+3/4'
'y+1/2, -x+1/4, -z+3/4'
'-y+1/2, -z, -x+1/2'
'-x+3/4, -y+1/4, z+1/2'
'-y+1/2, -x, -z+1/2'
'-z+1/2, -x, -y+1/2'
'-z+1/2, -y, -x+1/2'
'z+1/2, -x+1/4, -y+3/4'
'x+1/2, y+1/2, z'
'x+1/2, z+1/2, y'
'y+3/4, -z+1/2, x+1/4'
'y+3/4, x+3/4, -z'
'x+3/4, -z+1/2, y+1/4'
'-z+1/2, y+3/4, x+1/4'
'z+3/4, x+3/4, -y'
'y+3/4, z+3/4, -x'
'z+3/4, y+3/4, -x'
'-z+3/4, x+1/2, -y+1/4'
'x+3/4, z+3/4, -y'
'y+1/2, -z+3/4, -x+1/4'
'x+1/2, -z+3/4, -y+1/4'
'-z+3/4, y+1/2, -x+1/4'
'x+3/4, -y+1/2, z+1/4'
'y+3/4, -x+1/2, z+1/4'
'x+1/2, -y+3/4, -z+1/4'
'y+1/2, -x+3/4, -z+1/4'
'-y+1/2, -z+1/2, -x'
'-x+3/4, -y+3/4, z'
'-y+1/2, -x+1/2, -z'
'-z+1/2, -x+1/2, -y'
'-z+1/2, -y+1/2, -x'
'z+1/2, -x+3/4, -y+1/4'
'-x, -y, -z'
'-x, -z, -y'
'-y-1/4, z, -x-1/4'
'-y-1/4, -x-1/4, z'
'-x-1/4, z, -y-1/4'
'z, -y-1/4, -x-1/4'
'-z-1/4, -x-1/4, y'
'-y-1/4, -z-1/4, x'
'-z-1/4, -y-1/4, x'
'z-1/4, -x, y-1/4'
'-x-1/4, -z-1/4, y'
'-y, z-1/4, x-1/4'
'-x, z-1/4, y-1/4'
'z-1/4, -y, x-1/4'
'-x-1/4, y, -z-1/4'
'-y-1/4, x, -z-1/4'
'-x, y-1/4, z-1/4'
'-y, x-1/4, z-1/4'
'y, z, x'
'x-1/4, y-1/4, -z'
'y, x, z'
'z, x, y'
'z, y, x'
'-z, x-1/4, y-1/4'
'-x, -y+1/2, -z+1/2'
'-x, -z+1/2, -y+1/2'
'-y-1/4, z+1/2, -x+1/4'
'-y-1/4, -x+1/4, z+1/2'
'-x-1/4, z+1/2, -y+1/4'
'z, -y+1/4, -x+1/4'
'-z-1/4, -x+1/4, y+1/2'
'-y-1/4, -z+1/4, x+1/2'
'-z-1/4, -y+1/4, x+1/2'
'z-1/4, -x+1/2, y+1/4'
'-x-1/4, -z+1/4, y+1/2'

'-y, z+1/4, x+1/4'
'-x, z+1/4, y+1/4'
'z-1/4, -y+1/2, x+1/4'
'-x-1/4, y+1/2, -z+1/4'
'-y-1/4, x+1/2, -z+1/4'
'-x, y+1/4, z+1/4'
'-y, x+1/4, z+1/4'
'y, z+1/2, x+1/2'
'x-1/4, y+1/4, -z+1/2'
'y, x+1/2, z+1/2'
'z, x+1/2, y+1/2'
'z, y+1/2, x+1/2'
'-z, x+1/4, y+1/4'
'-x+1/2, -y, -z+1/2'
'-x+1/2, -z, -y+1/2'
'-y+1/4, z, -x+1/4'
'-y+1/4, -x-1/4, z+1/2'
'-x+1/4, z, -y+1/4'
'z+1/2, -y-1/4, -x+1/4'
'-z+1/4, -x-1/4, y+1/2'
'-y+1/4, -z-1/4, x+1/2'
'-z+1/4, -y-1/4, x+1/2'
'z+1/4, -x, y+1/4'
'-x+1/4, -z-1/4, y+1/2'
'-y+1/2, z-1/4, x+1/4'
'-x+1/2, z-1/4, y+1/4'
'z+1/4, -y, x+1/4'
'-x+1/4, y, -z+1/4'
'-y+1/4, x, -z+1/4'
'-x+1/2, y-1/4, z+1/4'
'-y+1/2, x-1/4, z+1/4'
'y+1/2, z, x+1/2'
'x+1/4, y-1/4, -z+1/2'
'y+1/2, x, z+1/2'
'z+1/2, x, y+1/2'
'z+1/2, y, x+1/2'
'-z+1/2, x-1/4, y+1/4'
'-x+1/2, -y+1/2, -z'
'-x+1/2, -z+1/2, -y'
'-y+1/4, z+1/2, -x-1/4'
'-y+1/4, -x+1/4, z'
'-x+1/4, z+1/2, -y-1/4'
'z+1/2, -y+1/4, -x-1/4'
'-z+1/4, -x+1/4, y'
'-y+1/4, -z+1/4, x'
'-z+1/4, -y+1/4, x'
'z+1/4, -x+1/2, y-1/4'
'-x+1/4, -z+1/4, y'
'-y+1/2, z+1/4, x-1/4'
'-x+1/2, z+1/4, y-1/4'
'z+1/4, -y+1/2, x-1/4'
'-x+1/4, y+1/2, -z-1/4'
'-y+1/4, x+1/2, -z-1/4'
'-x+1/2, y+1/4, z-1/4'
'-y+1/2, x+1/4, z-1/4'
'y+1/2, z+1/2, x'
'x+1/4, y+1/4, -z'
'y+1/2, x+1/2, z'
'z+1/2, x+1/2, y'
'z+1/2, y+1/2, x'
'-z+1/2, x+1/4, y-1/4'

_cell_length_a 14.450(4)
_cell_length_b 14.450(4)
_cell_length_c 14.450(4)
_cell_angle_alpha 90.00
_cell_angle_beta 90.00
_cell_angle_gamma 90.00
_cell_volume 3017.2(14)
_cell_formula_units_Z 8
_cell_measurement_temperature 296(1)
_cell_measurement_reflns_used 392
_cell_measurement_theta_min 0.998
_cell_measurement_theta_max 30.034

_exptl_crystal_description fragment
_exptl_crystal_colour 'silver'
_exptl_crystal_size_max 0.10
_exptl_crystal_size_mid 0.08
_exptl_crystal_size_min 0.05
_exptl_crystal_density_meas ?
_exptl_crystal_density_diffrn 3.608
_exptl_crystal_density_method 'not measured'
_exptl_crystal_F_000 3034
_exptl_absorpt_coefficient_mu 8.794
_exptl_absorpt_correction_type 'Multi-scan'
_exptl_absorpt_correction_T_min 0.4734
_exptl_absorpt_correction_T_max 0.6675
_exptl_absorpt_process_details 'HKL scalepack (Otwinski & Minor, 1997)'

_exptl_special_details
;
 ?
;

_diffrn_ambient_temperature 296(1)
_diffrn_radiation_wavelength 0.71073
_diffrn_radiation_type MoK\a
_diffrn_radiation_source 'fine-focus sealed tube'
_diffrn_radiation_monochromator graphite
_diffrn_measurement_device_type 'Nonius Kappa CCD'
_diffrn_measurement_method '\f and \w scans'
_diffrn_detector_area_resol_mean ?
_diffrn_standards_number ?
_diffrn_standards_interval_count ?
_diffrn_standards_interval_time ?
_diffrn_standards_decay_% ?
_diffrn_reflns_number 1785
_diffrn_reflns_av_R_equivalents 0.0384
_diffrn_reflns_av_sigmaI/netI 0.0336
_diffrn_reflns_limit_h_min -20
_diffrn_reflns_limit_h_max 20
_diffrn_reflns_limit_k_min -14
_diffrn_reflns_limit_k_max 14
_diffrn_reflns_limit_l_min -13
_diffrn_reflns_limit_l_max 13
_diffrn_reflns_theta_min 3.99
_diffrn_reflns_theta_max 29.91
_reflns_number_total 247
_reflns_number_gt 223
_reflns_threshold_expression >2\s(I)

_computing_data_collection 'Collect (Nonius 1999)'
_computing_cell_refinement 'Denzo and Scalepack (Otwinski & Minor 1997)'
_computing_data_reduction 'Denzo and Scalepack (Otwinski & Minor 1997)'
_computing_structure_solution 'Direct Methods, SIR 97'
_computing_structure_refinement 'SHELXL-97 (Sheldrick, 2008)'
_computing_molecular_graphics 'Crystal Maker'
_computing_publication_material 'Publcif'

_refine_special_details
;
 Refinement of F^2^ against ALL reflections. The weighted R-factor wR and goodness of fit S are based on F^2^, conventional R-factors R are based on F, with F set to zero for negative F^2^. The threshold expression of F^2^ > 2\s(F^2^) is used only for calculating R-factors(gt) etc. and is not relevant to the choice of reflections for refinement. R-factors based on F^2^ are statistically about twice as large as those based on F, and R-factors based on ALL data will be even larger.
;

_refine_ls_structure_factor_coef Fsqd
_refine_ls_matrix_type full
_refine_ls_weighting_scheme calc
_refine_ls_weighting_details
 'calc w=1/[\s^2^(Fo^2^)+(0.0188P)^2^+14.4800P] where P=(Fo^2^+2Fc^2^)/3'
_atom_sites_solution_primary direct
_atom_sites_solution_secondary difmap
_atom_sites_solution_hydrogens ?
_refine_ls_hydrogen_treatment ?
_refine_ls_extinction_method SHELXL
_refine_ls_extinction_coef 0.00035(5)
_refine_ls_extinction_expression

'Fc^*^=kFc[1+0.001xFc^2^\l^3^/sin(2\q)]^-1/4^'
_refine_ls_number_reflns 247
_refine_ls_number_parameters 21
_refine_ls_number_restraints 3
_refine_ls_R_factor_all 0.0252
_refine_ls_R_factor_gt 0.0215
_refine_ls_wR_factor_ref 0.0466
_refine_ls_wR_factor_gt 0.0456

_refine_ls_goodness_of_fit_ref 1.062
_refine_ls_restrained_S_all 1.055
_refine_ls_shift/su_max 0.000
_refine_ls_shift/su_mean 0.000

loop_
 _atom_site_label
 _atom_site_type_symbol
 _atom_site_fract_x
 _atom_site_fract_y
 _atom_site_fract_z
 _atom_site_U_iso_or_equiv
 _atom_site_adp_type
 _atom_site_occupancy
 _atom_site_symmetry_multiplicity
 _atom_site_calc_flag
 _atom_site_refinement_flags
 _atom_site_disorder_assembly
 _atom_site_disorder_group
Yb1 Yb 0.1250 0.1250 0.1250 0.0113(2)
Uani 1 24 d S . .
Cr1 Cr 0.5000 0.5000 0.5000 0.0091(3)
Uani 1 12 d S . .
Al1 Al 0.05899(5) 0.05899(5) 0.32525(8)
0.0121(3) Uani 0.996(3) 2 d SP . .
Fe1 Fe 0.05899(5) 0.05899(5) 0.32525(8)
0.0121(3) Uani 0.004(3) 2 d SP . .
Al2 Al 0.48670(11) 0.1250 0.1250
0.0099(4) Uani 0.992(5) 4 d SP . .
Fe2 Fe 0.48670(11) 0.1250 0.1250
0.0099(4) Uani 0.008(5) 4 d SP . .
Al3 Al 0.0000 0.0000 0.0000 0.0204(7)
Uani 1 12 d S . .

loop_
 _atom_site_aniso_label
 _atom_site_aniso_U_11
 _atom_site_aniso_U_22
 _atom_site_aniso_U_33
 _atom_site_aniso_U_23
 _atom_site_aniso_U_13
 _atom_site_aniso_U_12
Yb1 0.0113(2) 0.0113(2) 0.0113(2) 0.000
0.000 0.000
Cr1 0.0091(3) 0.0091(3) 0.0091(3) -
0.0007(3) -0.0007(3) -0.0007(3)
Al1 0.0130(4) 0.0130(4) 0.0103(6) -
0.0005(3) -0.0005(3) -0.0040(4)
Fe1 0.0130(4) 0.0130(4) 0.0103(6) -
0.0005(3) -0.0005(3) -0.0040(4)
Al2 0.0105(8) 0.0096(5) 0.0096(5) -
0.0020(6) 0.000 0.000
Fe2 0.0105(8) 0.0096(5) 0.0096(5) -
0.0020(6) 0.000 0.000
Al3 0.0204(7) 0.0204(7) 0.0204(7) -
0.0037(7) -0.0037(7) -0.0037(7)

_geom_special_details
;
 All s.u.'s (except the s.u. in the dihedral
angle between two l.s. planes)
 are estimated using the full covariance
matrix. The cell s.u.'s are taken
 into account individually in the estimation
of s.u.'s in distances, angles
 and torsion angles; correlations between
s.u.'s in cell parameters are only
 used when they are defined by crystal
symmetry. An approximate (isotropic)
 treatment of cell s.u.'s is used for estimating
s.u.'s involving l.s. planes.
;

loop_
 _geom_bond_atom_site_label_1
 _geom_bond_atom_site_label_2
 _geom_bond_distance
 _geom_bond_site_symmetry_2
 _geom_bond_publ_flag
Yb1 Al3 3.1284(9) 6 ?
Yb1 Al3 3.1284(9) 4 ?
Yb1 Al3 3.1284(9) 3 ?
Yb1 Al3 3.1288(9) . ?
Yb1 Fe1 3.1924(15) 126 ?
Yb1 Al1 3.1924(15) 147 ?
Yb1 Al1 3.1924(15) 172 ?
Yb1 Al1 3.1924(15) 126 ?
Yb1 Fe1 3.1924(15) 172 ?
Yb1 Fe1 3.1924(15) 147 ?
Yb1 Al1 3.1925(15) 2 ?
Yb1 Fe1 3.1925(15) 118 ?
Cr1 Fe2 2.5614(7) 58 ?

Cr1 Fe2 2.5614(7) 104_665 ?
Cr1 Al2 2.5614(7) 58 ?
Cr1 Al2 2.5614(7) 104_665 ?
Cr1 Fe2 2.5614(7) 154_565 ?
Cr1 Fe2 2.5614(7) 8_556 ?
Cr1 Al2 2.5614(7) 154_565 ?
Cr1 Al2 2.5614(7) 8_556 ?
Cr1 Fe2 2.5619(7) 25 ?
Cr1 Al2 2.5619(7) 25 ?
Cr1 Fe2 2.5619(7) 121_655 ?
Cr1 Al2 2.5619(7) 121_655 ?
Al1 Fe2 2.6947(19) 176 ?
Al1 Al2 2.6947(19) 176 ?
Al1 Fe1 2.698(2) 172 ?
Al1 Al1 2.698(2) 172 ?
Al1 Fe1 2.743(2) 12 ?
Al1 Al1 2.743(2) 10 ?
Al1 Al1 2.743(2) 12 ?
Al1 Fe1 2.743(2) 10 ?
Al1 Cr1 2.7981(14) 73_445 ?
Al1 Fe2 2.8321(13) 130 ?
Al1 Al2 2.8321(13) 130 ?
Al1 Fe2 2.8323(13) 145 ?
Al2 Cr1 2.5614(7) 30_644 ?
Al2 Cr1 2.5619(7) 25_544 ?
Al2 Fe1 2.6947(19) 126 ?
Al2 Al1 2.6947(19) 126 ?
Al2 Fe1 2.6949(19) 118 ?
Al2 Al1 2.6949(19) 118 ?
Al2 Fe2 2.826(2) 100_665 ?
Al2 Fe2 2.826(2) 99_656 ?
Al2 Al2 2.826(2) 100_665 ?
Al2 Al2 2.826(2) 99_656 ?
Al2 Fe2 2.826(2) 82_545 ?
Al2 Fe2 2.826(2) 128_654 ?
Al3 Yb1 3.1288(9) 97 ?

loop_
 _geom_angle_atom_site_label_1
 _geom_angle_atom_site_label_2
 _geom_angle_atom_site_label_3
 _geom_angle
 _geom_angle_site_symmetry_1
 _geom_angle_site_symmetry_3
 _geom_angle_publ_flag
Al3 Yb1 Al3 109.5 6 4 ?
Al3 Yb1 Al3 109.5 6 3 ?
Al3 Yb1 Al3 109.5 4 3 ?
Al3 Yb1 Al3 109.5 6 . ?
Al3 Yb1 Al3 109.5 4 . ?
Al3 Yb1 Al3 109.5 3 . ?
Al3 Yb1 Fe1 100.278(19) 6 126 ?
Al3 Yb1 Fe1 58.450(5) 4 126 ?
Al3 Yb1 Fe1 58.450(5) 3 126 ?
Al3 Yb1 Fe1 150.255(19) . 126 ?
Al3 Yb1 Al1 58.450(5) 6 147 ?
Al3 Yb1 Al1 58.450(5) 4 147 ?
Al3 Yb1 Al1 100.278(19) 3 147 ?
Al3 Yb1 Al1 150.255(19) . 147 ?
Fe1 Yb1 Al1 50.89(3) 126 147 ?
Al3 Yb1 Al1 58.450(5) 6 172 ?
Al3 Yb1 Al1 100.278(19) 4 172 ?
Al3 Yb1 Al1 58.450(5) 3 172 ?
Al3 Yb1 Al1 150.255(19) . 172 ?
Fe1 Yb1 Al1 50.89(3) 126 172 ?
Al1 Yb1 Al1 50.89(3) 147 172 ?
Al3 Yb1 Al1 100.278(19) 6 126 ?
Al3 Yb1 Al1 58.450(5) 4 126 ?
Al3 Yb1 Al1 58.450(5) 3 126 ?
Al3 Yb1 Al1 150.255(19) . 126 ?
Fe1 Yb1 Al1 0.00(6) 126 126 ?
Al1 Yb1 Al1 50.89(3) 147 126 ?
Al1 Yb1 Al1 50.89(3) 172 126 ?
Al3 Yb1 Fe1 58.450(5) 6 172 ?
Al3 Yb1 Fe1 100.278(19) 4 172 ?
Al3 Yb1 Fe1 58.450(5) 3 172 ?
Al3 Yb1 Fe1 150.255(19) . 172 ?
Fe1 Yb1 Fe1 50.89(3) 126 172 ?
Al1 Yb1 Fe1 50.89(3) 147 172 ?
Al1 Yb1 Fe1 0.000(17) 172 172 ?
Al1 Yb1 Fe1 50.89(3) 126 172 ?
Al3 Yb1 Fe1 58.450(5) 6 147 ?
Al3 Yb1 Fe1 58.450(5) 4 147 ?
Al3 Yb1 Fe1 100.278(19) 3 147 ?
Al3 Yb1 Fe1 150.255(19) . 147 ?
Fe1 Yb1 Fe1 50.89(3) 126 147 ?
Al1 Yb1 Fe1 0.00(3) 147 147 ?
Al1 Yb1 Fe1 50.89(3) 172 147 ?
Al1 Yb1 Fe1 50.89(3) 126 147 ?
Fe1 Yb1 Fe1 50.89(3) 172 147 ?
Al3 Yb1 Al1 58.448(5) 6 2 ?
Al3 Yb1 Al1 58.448(5) 4 2 ?

Al3 Yb1 Al1 150.267(19) 3 2 ?
Al3 Yb1 Al1 100.266(19) . 2 ?
Fe1 Yb1 Al1 95.126(7) 126 2 ?
Al1 Yb1 Al1 49.99(4) 147 2 ?
Al1 Yb1 Al1 95.126(7) 172 2 ?
Al1 Yb1 Al1 95.126(7) 126 2 ?
Fe1 Yb1 Al1 95.126(7) 172 2 ?
Fe1 Yb1 Al1 49.99(4) 147 2 ?
Al3 Yb1 Fe1 150.267(19) 6 118 ?
Al3 Yb1 Fe1 58.448(5) 4 118 ?
Al3 Yb1 Fe1 58.448(5) 3 118 ?
Al3 Yb1 Fe1 100.266(19) . 118 ?
Fe1 Yb1 Fe1 49.99(4) 126 118 ?
Al1 Yb1 Fe1 95.126(7) 147 118 ?
Al1 Yb1 Fe1 95.126(7) 172 118 ?
Al1 Yb1 Fe1 49.99(4) 126 118 ?
Fe1 Yb1 Fe1 95.126(7) 172 118 ?
Fe1 Yb1 Fe1 95.126(7) 147 118 ?
Al1 Yb1 Fe1 116.895(11) 2 118 ?
Fe2 Cr1 Fe2 66.96(6) 58 104_665 ?
Fe2 Cr1 Al2 0.00(7) 58 58 ?
Fe2 Cr1 Al2 66.96(6) 104_665 58 ?
Fe2 Cr1 Al2 66.96(6) 58 104_665 ?
Fe2 Cr1 Al2 0.00(7) 104_665 104_665 ?
Al2 Cr1 Al2 66.96(6) 58 104_665 ?
Fe2 Cr1 Fe2 180.0 58 154_565 ?
Fe2 Cr1 Fe2 113.04(6) 104_665 154_565 ?
Al2 Cr1 Fe2 180.0 58 154_565 ?
Al2 Cr1 Fe2 113.04(6) 104_665 154_565 ?
Fe2 Cr1 Fe2 113.04(6) 58 8_556 ?
Fe2 Cr1 Fe2 180.0 104_665 8_556 ?
Al2 Cr1 Fe2 113.04(6) 58 8_556 ?
Al2 Cr1 Fe2 180.0 104_665 8_556 ?
Fe2 Cr1 Fe2 66.96(6) 154_565 8_556 ?
Fe2 Cr1 Al2 180.0 58 154_565 ?
Fe2 Cr1 Al2 113.04(6) 104_665 154_565 ?
Al2 Cr1 Al2 180.0 58 154_565 ?
Al2 Cr1 Al2 113.04(6) 104_665 154_565 ?
Fe2 Cr1 Al2 0.0 154_565 154_565 ?
Fe2 Cr1 Al2 66.96(6) 8_556 154_565 ?
Fe2 Cr1 Al2 113.04(6) 58 8_556 ?
Fe2 Cr1 Al2 180.0 104_665 8_556 ?
Al2 Cr1 Al2 113.04(6) 58 8_556 ?
Al2 Cr1 Al2 180.0 104_665 8_556 ?
Fe2 Cr1 Al2 66.96(6) 154_565 8_556 ?
Fe2 Cr1 Al2 0.0 8_556 8_556 ?
Al2 Cr1 Al2 66.96(6) 154_565 8_556 ?
Fe2 Cr1 Fe2 66.96(6) 58 25 ?
Fe2 Cr1 Fe2 66.96(6) 104_665 25 ?
Al2 Cr1 Fe2 66.96(6) 58 25 ?
Al2 Cr1 Fe2 66.96(6) 104_665 25 ?
Fe2 Cr1 Fe2 113.04(6) 154_565 25 ?
Fe2 Cr1 Fe2 113.04(6) 8_556 25 ?
Al2 Cr1 Fe2 113.04(6) 154_565 25 ?
Al2 Cr1 Fe2 113.04(6) 8_556 25 ?
Fe2 Cr1 Al2 66.96(6) 58 25 ?
Fe2 Cr1 Al2 66.96(6) 104_665 25 ?
Al2 Cr1 Al2 66.96(6) 58 25 ?
Al2 Cr1 Al2 66.96(6) 104_665 25 ?
Fe2 Cr1 Al2 113.04(6) 154_565 25 ?
Fe2 Cr1 Al2 113.04(6) 8_556 25 ?
Al2 Cr1 Al2 113.04(6) 154_565 25 ?
Al2 Cr1 Al2 113.04(6) 8_556 25 ?
Fe2 Cr1 Al2 0.00(7) 25 25 ?
Fe2 Cr1 Fe2 113.04(6) 58 121_655 ?
Fe2 Cr1 Fe2 113.04(6) 104_665 121_655 ?
Al2 Cr1 Fe2 113.04(6) 58 121_655 ?
Al2 Cr1 Fe2 113.04(6) 104_665 121_655 ?
Fe2 Cr1 Fe2 66.96(6) 154_565 121_655 ?
Fe2 Cr1 Fe2 66.96(6) 8_556 121_655 ?
Al2 Cr1 Fe2 66.96(6) 154_565 121_655 ?
Al2 Cr1 Fe2 66.96(6) 8_556 121_655 ?
Fe2 Cr1 Fe2 180.0 25 121_655 ?
Al2 Cr1 Fe2 180.0 25 121_655 ?
Fe2 Cr1 Al2 113.04(6) 58 121_655 ?
Fe2 Cr1 Al2 113.04(6) 104_665 121_655 ?
Al2 Cr1 Al2 113.04(6) 58 121_655 ?
Al2 Cr1 Al2 113.04(6) 104_665 121_655 ?
Fe2 Cr1 Al2 66.96(6) 154_565 121_655 ?
Fe2 Cr1 Al2 66.96(6) 8_556 121_655 ?
Al2 Cr1 Al2 66.96(6) 154_565 121_655 ?
Al2 Cr1 Al2 66.96(6) 8_556 121_655 ?
Fe2 Cr1 Al2 180.0 25 121_655 ?
Al2 Cr1 Al2 180.0 25 121_655 ?
Fe2 Cr1 Al2 0.0 121_655 121_655 ?
Fe2 Al1 Al2 0.00(3) 176 176 ?
Fe2 Al1 Fe1 59.97(3) 176 172 ?
Al2 Al1 Fe1 59.97(3) 176 172 ?
Fe2 Al1 Al1 59.97(3) 176 172 ?
Al2 Al1 Al1 59.97(3) 176 172 ?
Fe1 Al1 Al1 0.00(6) 172 172 ?
Fe2 Al1 Fe1 149.589(5) 176 12 ?

Al2 Al1 Fe1 149.589(5) 176 12 ?
Fe1 Al1 Fe1 120.0 172 12 ?
Al1 Al1 Fe1 120.0 172 12 ?
Fe2 Al1 Al1 149.589(5) 176 10 ?
Al2 Al1 Al1 149.589(5) 176 10 ?
Fe1 Al1 Al1 120.0 172 10 ?
Al1 Al1 Al1 120.0 172 10 ?
Fe1 Al1 Al1 60.0 12 10 ?
Fe2 Al1 Al1 149.589(5) 176 12 ?
Al2 Al1 Al1 149.589(5) 176 12 ?
Fe1 Al1 Al1 120.0 172 12 ?
Al1 Al1 Al1 120.0 172 12 ?
Fe1 Al1 Al1 0.00(4) 12 12 ?
Al1 Al1 Al1 60.0 10 12 ?
Fe2 Al1 Fe1 149.589(5) 176 10 ?
Al2 Al1 Fe1 149.589(5) 176 10 ?
Fe1 Al1 Fe1 120.0 172 10 ?
Al1 Al1 Fe1 120.0 172 10 ?
Fe1 Al1 Fe1 60.0 12 10 ?
Al1 Al1 Fe1 0.00(4) 10 10 ?
Al1 Al1 Fe1 60.0 12 10 ?
Fe2 Al1 Cr1 55.55(3) 176 73_445 ?
Al2 Al1 Cr1 55.55(3) 176 73_445 ?
Fe1 Al1 Cr1 115.52(2) 172 73_445 ?
Al1 Al1 Cr1 115.52(2) 172 73_445 ?
Fe1 Al1 Cr1 115.005(18) 12 73_445 ?
Al1 Al1 Cr1 115.005(18) 10 73_445 ?
Al1 Al1 Cr1 115.005(18) 12 73_445 ?
Fe1 Al1 Cr1 115.005(18) 10 73_445 ?
Fe2 Al1 Fe2 101.24(3) 176 130 ?
Al2 Al1 Fe2 101.24(3) 176 130 ?
Fe1 Al1 Fe2 145.96(3) 172 130 ?
Al1 Al1 Fe2 145.96(3) 172 130 ?
Fe1 Al1 Fe2 90.84(3) 12 130 ?
Al1 Al1 Fe2 61.04(2) 10 130 ?
Al1 Al1 Fe2 90.84(3) 12 130 ?
Fe1 Al1 Fe2 61.04(2) 10 130 ?
Cr1 Al1 Fe2 54.12(2) 73_445 130 ?
Fe2 Al1 Al2 101.24(3) 176 130 ?
Al2 Al1 Al2 101.24(3) 176 130 ?
Fe1 Al1 Al2 145.96(3) 172 130 ?
Al1 Al1 Al2 145.96(3) 172 130 ?
Fe1 Al1 Al2 90.84(3) 12 130 ?
Al1 Al1 Al2 61.04(2) 10 130 ?
Al1 Al1 Al2 90.84(3) 12 130 ?
Fe1 Al1 Al2 61.04(2) 10 130 ?
Cr1 Al1 Al2 54.12(2) 73_445 130 ?
Fe2 Al1 Al2 0.00(6) 130 130 ?
Fe2 Al1 Fe2 101.25(3) 176 145 ?
Al2 Al1 Fe2 101.25(3) 176 145 ?
Fe1 Al1 Fe2 145.96(3) 172 145 ?
Al1 Al1 Fe2 145.96(3) 172 145 ?
Fe1 Al1 Fe2 61.03(2) 12 145 ?
Al1 Al1 Fe2 90.84(3) 10 145 ?
Al1 Al1 Fe2 61.03(2) 12 145 ?
Fe1 Al1 Fe2 90.84(3) 10 145 ?
Cr1 Al1 Fe2 54.13(2) 73_445 145 ?
Fe2 Al1 Fe2 59.86(7) 130 145 ?
Al2 Al1 Fe2 59.86(7) 130 145 ?
Cr1 Al2 Cr1 171.39(7) 30_644 25_544 ?
Cr1 Al2 Fe1 64.27(3) 30_644 126 ?
Cr1 Al2 Fe1 124.34(6) 25_544 126 ?
Cr1 Al2 Al1 64.27(3) 30_644 126 ?
Cr1 Al2 Al1 124.34(6) 25_544 126 ?
Fe1 Al2 Al1 0.00(4) 126 126 ?
Cr1 Al2 Fe1 124.35(6) 30_644 118 ?
Cr1 Al2 Fe1 64.26(3) 25_544 118 ?
Fe1 Al2 Fe1 60.07(6) 126 118 ?
Al1 Al2 Fe1 60.07(6) 126 118 ?
Cr1 Al2 Al1 124.35(6) 30_644 118 ?
Cr1 Al2 Al1 64.26(3) 25_544 118 ?
Fe1 Al2 Al1 60.07(6) 126 118 ?
Al1 Al2 Al1 60.07(6) 126 118 ?
Fe1 Al2 Al1 0.00(6) 118 118 ?
Cr1 Al2 Fe2 56.52(3) 30_644 100_665 ?
Cr1 Al2 Fe2 116.46(3) 25_544 100_665 ?
Fe1 Al2 Fe2 111.22(2) 126 100_665 ?
Al1 Al2 Fe2 111.22(2) 126 100_665 ?
Fe1 Al2 Fe2 149.590(5) 118 100_665 ?
Al1 Al2 Fe2 149.590(5) 118 100_665 ?
Cr1 Al2 Fe2 56.52(3) 30_644 99_656 ?
Cr1 Al2 Fe2 116.46(3) 25_544 99_656 ?
Fe1 Al2 Fe2 111.22(2) 126 99_656 ?
Al1 Al2 Fe2 111.22(2) 126 99_656 ?
Fe1 Al2 Fe2 149.590(5) 118 99_656 ?
Al1 Al2 Fe2 149.590(5) 118 99_656 ?
Fe2 Al2 Fe2 60.0 100_665 99_656 ?
Cr1 Al2 Al2 56.52(3) 30_644 100_665 ?
Cr1 Al2 Al2 116.46(3) 25_544 100_665 ?
Fe1 Al2 Al2 111.22(2) 126 100_665 ?
Al1 Al2 Al2 111.22(2) 126 100_665 ?
Fe1 Al2 Al2 149.590(5) 118 100_665 ?

Al1 Al2 Al2 149.590(5) 118 100_665 ?
Fe2 Al2 Al2 0.00(5) 100_665 100_665 ?
Fe2 Al2 Al2 60.0 99_656 100_665 ?
Cr1 Al2 Al2 56.52(3) 30_644 99_656 ?
Cr1 Al2 Al2 116.46(3) 25_544 99_656 ?
Fe1 Al2 Al2 111.22(2) 126 99_656 ?
Al1 Al2 Al2 111.22(2) 126 99_656 ?
Fe1 Al2 Al2 149.590(5) 118 99_656 ?
Al1 Al2 Al2 149.590(5) 118 99_656 ?
Fe2 Al2 Al2 60.0 100_665 99_656 ?
Fe2 Al2 Al2 0.00(5) 99_656 99_656 ?
Al2 Al2 Al2 60.0 100_665 99_656 ?
Cr1 Al2 Fe2 116.46(3) 30_644 82_545 ?
Cr1 Al2 Fe2 56.51(3) 25_544 82_545 ?
Fe1 Al2 Fe2 149.590(5) 126 82_545 ?
Al1 Al2 Fe2 149.590(5) 126 82_545 ?
Fe1 Al2 Fe2 111.21(2) 118 82_545 ?
Al1 Al2 Fe2 111.21(2) 118 82_545 ?
Fe2 Al2 Fe2 90.0 100_665 82_545 ?
Fe2 Al2 Fe2 60.0 99_656 82_545 ?
Al2 Al2 Fe2 90.0 100_665 82_545 ?
Al2 Al2 Fe2 60.0 99_656 82_545 ?
Cr1 Al2 Fe2 116.46(3) 30_644 128_654 ?
Cr1 Al2 Fe2 56.51(3) 25_544 128_654 ?
Fe1 Al2 Fe2 149.590(5) 126 128_654 ?
Al1 Al2 Fe2 149.590(5) 126 128_654 ?
Fe1 Al2 Fe2 111.21(2) 118 128_654 ?
Al1 Al2 Fe2 111.21(2) 118 128_654 ?
Fe2 Al2 Fe2 60.0 100_665 128_654 ?
Fe2 Al2 Fe2 90.0 99_656 128_654 ?
Al2 Al2 Fe2 60.0 100_665 128_654 ?
Al2 Al2 Fe2 90.0 99_656 128_654 ?
Fe2 Al2 Fe2 60.0 82_545 128_654 ?
Yb1 Al3 Yb1 180.0 97 . ?

_diffrn_measured_fraction_theta_max
0.996
_diffrn_reflns_theta_full 29.91
_diffrn_measured_fraction_theta_full
0.996
_refine_diff_density_max 0.862
_refine_diff_density_min -0.744
_refine_diff_density_rms 0.137

##END

data_Yb$Cr_2Fe_{0.2}Al_{19.8}$

_audit_update_record
;
2012-03-23 # Formatted by publCIF
;

_audit_creation_method SHELXL-97
_chemical_name_systematic
;
?
;
_chemical_name_common ?
_chemical_melting_point ?
_chemical_formula_moiety 'Al19.78
Cr2 Fe0.22 Yb'
_chemical_formula_sum
'Al19.78 Cr2 Fe0.22 Yb'
_chemical_formula_weight 822.99

loop_
_atom_type_symbol
_atom_type_description
_atom_type_scat_dispersion_real
_atom_type_scat_dispersion_imag
_atom_type_scat_source
'Yb' 'Yb' -0.3850 5.5486
'International Tables Vol C Tables 4.2.6.8
and 6.1.1.4'
'Cr' 'Cr' 0.3209 0.6236
'International Tables Vol C Tables 4.2.6.8
and 6.1.1.4'
'Fe' 'Fe' 0.3463 0.8444
'International Tables Vol C Tables 4.2.6.8
and 6.1.1.4'
'Al' 'Al' 0.0645 0.0514
'International Tables Vol C Tables 4.2.6.8
and 6.1.1.4'

_symmetry_cell_setting cubic
_symmetry_space_group_name_H-M 'F d
-3 m'
_symmetry_space_group_name_Hall '-F
4vw 2vw'

loop_

```
_symmetry_equiv_pos_as_xyz
'x, y, z'
'x, z, y'
'y+1/4, -z, x+1/4'
'y+1/4, x+1/4, -z'
'x+1/4, -z, y+1/4'
'-z, y+1/4, x+1/4'
'z+1/4, x+1/4, -y'
'y+1/4, z+1/4, -x'
'z+1/4, y+1/4, -x'
'-z+1/4, x, -y+1/4'
'x+1/4, z+1/4, -y'
'y, -z+1/4, -x+1/4'
'x, -z+1/4, -y+1/4'
'-z+1/4, y, -x+1/4'
'x+1/4, -y, z+1/4'
'y+1/4, -x, z+1/4'
'x, -y+1/4, -z+1/4'
'y, -x+1/4, -z+1/4'
'-y, -z, -x'
'-x+1/4, -y+1/4, z'
'-y, -x, -z'
'-z, -x, -y'
'-z, -y, -x'
'z, -x+1/4, -y+1/4'
'x, y+1/2, z+1/2'
'x, z+1/2, y+1/2'
'y+1/4, -z+1/2, x+3/4'
'y+1/4, x+3/4, -z+1/2'
'x+1/4, -z+1/2, y+3/4'
'-z, y+3/4, x+3/4'
'z+1/4, x+3/4, -y+1/2'
'y+1/4, z+3/4, -x+1/2'
'z+1/4, y+3/4, -x+1/2'
'-z+1/4, x+1/2, -y+3/4'
'x+1/4, z+3/4, -y+1/2'
'y, -z+3/4, -x+3/4'
'x, -z+3/4, -y+3/4'
'-z+1/4, y+1/2, -x+3/4'
'x+1/4, -y+1/2, z+3/4'
'y+1/4, -x+1/2, z+3/4'
'x, -y+3/4, -z+3/4'
'y, -x+3/4, -z+3/4'
'-y, -z+1/2, -x+1/2'
'-x+1/4, -y+3/4, z+1/2'
'-y, -x+1/2, -z+1/2'
'-z, -x+1/2, -y+1/2'
'-z, -y+1/2, -x+1/2'
'z, -x+3/4, -y+3/4'
'x+1/2, y, z+1/2'
'x+1/2, z, y+1/2'
'y+3/4, -z, x+3/4'
'y+3/4, x+1/4, -z+1/2'
'x+3/4, -z, y+3/4'
'-z+1/2, y+1/4, x+3/4'
'z+3/4, x+1/4, -y+1/2'
'y+3/4, z+1/4, -x+1/2'
'z+3/4, y+1/4, -x+1/2'
'-z+3/4, x, -y+3/4'
'x+3/4, z+1/4, -y+1/2'
'y+1/2, -z+1/4, -x+3/4'
'x+1/2, -z+1/4, -y+3/4'
'-z+3/4, y, -x+3/4'
'x+3/4, -y, z+3/4'
'y+3/4, -x, z+3/4'
'x+1/2, -y+1/4, -z+3/4'
'y+1/2, -x+1/4, -z+3/4'
'-y+1/2, -z, -x+1/2'
'-x+3/4, -y+1/4, z+1/2'
'-y+1/2, -x, -z+1/2'
'-z+1/2, -x, -y+1/2'
'-z+1/2, -y, -x+1/2'
'z+1/2, -x+1/4, -y+3/4'
'x+1/2, y+1/2, z'
'x+1/2, z+1/2, y'
'y+3/4, -z+1/2, x+1/4'
'y+3/4, x+3/4, -z'
'x+3/4, -z+1/2, y+1/4'
'-z+1/2, y+3/4, x+1/4'
'z+3/4, x+3/4, -y'
'y+3/4, z+3/4, -x'
'z+3/4, y+3/4, -x'
'-z+3/4, x+1/2, -y+1/4'
'x+3/4, z+3/4, -y'
'y+1/2, -z+3/4, -x+1/4'
'x+1/2, -z+3/4, -y+1/4'
'-z+3/4, y+1/2, -x+1/4'
'x+3/4, -y+1/2, z+1/4'
'y+3/4, -x+1/2, z+1/4'
'x+1/2, -y+3/4, -z+1/4'
'y+1/2, -x+3/4, -z+1/4'
'-y+1/2, -z+1/2, -x'
```

'-x+3/4, -y+3/4, z'
'-y+1/2, -x+1/2, -z'
'-z+1/2, -x+1/2, -y'
'-z+1/2, -y+1/2, -x'
'z+1/2, -x+3/4, -y+1/4'
'-x, -y, -z'
'-x, -z, -y'
'-y-1/4, z, -x-1/4'
'-y-1/4, -x-1/4, z'
'-x-1/4, z, -y-1/4'
'z, -y-1/4, -x-1/4'
'-z-1/4, -x-1/4, y'
'-y-1/4, -z-1/4, x'
'-z-1/4, -y-1/4, x'
'z-1/4, -x, y-1/4'
'-x-1/4, -z-1/4, y'
'-y, z-1/4, x-1/4'
'-x, z-1/4, y-1/4'
'z-1/4, -y, x-1/4'
'-x-1/4, y, -z-1/4'
'-y-1/4, x, -z-1/4'
'-x, y-1/4, z-1/4'
'-y, x-1/4, z-1/4'
'y, z, x'
'x-1/4, y-1/4, -z'
'y, x, z'
'z, x, y'
'z, y, x'
'-z, x-1/4, y-1/4'
'-x, -y+1/2, -z+1/2'
'-x, -z+1/2, -y+1/2'
'-y-1/4, z+1/2, -x+1/4'
'-y-1/4, -x+1/4, z+1/2'
'-x-1/4, z+1/2, -y+1/4'
'z, -y+1/4, -x+1/4'
'-z-1/4, -x+1/4, y+1/2'
'-y-1/4, -z+1/4, x+1/2'
'-z-1/4, -y+1/4, x+1/2'
'z-1/4, -x+1/2, y+1/4'
'-x-1/4, -z+1/4, y+1/2'
'-y, z+1/4, x+1/4'
'-x, z+1/4, y+1/4'
'z-1/4, -y+1/2, x+1/4'
'-x-1/4, y+1/2, -z+1/4'
'-y-1/4, x+1/2, -z+1/4'
'-x, y+1/4, z+1/4'
'-y, x+1/4, z+1/4'
'y, z+1/2, x+1/2'
'x-1/4, y+1/4, -z+1/2'
'y, x+1/2, z+1/2'
'z, x+1/2, y+1/2'
'z, y+1/2, x+1/2'
'-z, x+1/4, y+1/4'
'-x+1/2, -y, -z+1/2'
'-x+1/2, -z, -y+1/2'
'-y+1/4, z, -x+1/4'
'-y+1/4, -x-1/4, z+1/2'
'-x+1/4, z, -y+1/4'
'z+1/2, -y-1/4, -x+1/4'
'-z+1/4, -x-1/4, y+1/2'
'-y+1/4, -z-1/4, x+1/2'
'-z+1/4, -y-1/4, x+1/2'
'z+1/4, -x, y+1/4'
'-x+1/4, -z-1/4, y+1/2'
'-y+1/2, z-1/4, x+1/4'
'-x+1/2, z-1/4, y+1/4'
'z+1/4, -y, x+1/4'
'-x+1/4, y, -z+1/4'
'-y+1/4, x, -z+1/4'
'-x+1/2, y-1/4, z+1/4'
'-y+1/2, x-1/4, z+1/4'
'y+1/2, z, x+1/2'
'x+1/4, y-1/4, -z+1/2'
'y+1/2, x, z+1/2'
'z+1/2, x, y+1/2'
'z+1/2, y, x+1/2'
'-z+1/2, x-1/4, y+1/4'
'-x+1/2, -y+1/2, -z'
'-x+1/2, -z+1/2, -y'
'-y+1/4, z+1/2, -x-1/4'
'-y+1/4, -x+1/4, z'
'-x+1/4, z+1/2, -y-1/4'
'z+1/2, -y+1/4, -x-1/4'
'-z+1/4, -x+1/4, y'
'-y+1/4, -z+1/4, x'
'-z+1/4, -y+1/4, x'
'z+1/4, -x+1/2, y-1/4'
'-x+1/4, -z+1/4, y'
'-y+1/2, z+1/4, x-1/4'
'-x+1/2, z+1/4, y-1/4'
'z+1/4, -y+1/2, x-1/4'
'-x+1/4, y+1/2, -z-1/4'

'-y+1/4, x+1/2, -z-1/4'
'-x+1/2, y+1/4, z-1/4'
'-y+1/2, x+1/4, z-1/4'
'y+1/2, z+1/2, x'
'x+1/4, y+1/4, -z'
'y+1/2, x+1/2, z'
'z+1/2, x+1/2, y'
'z+1/2, y+1/2, x'
'-z+1/2, x+1/4, y-1/4'

_cell_length_a 14.443(4)
_cell_length_b 14.443(4)
_cell_length_c 14.443(4)
_cell_angle_alpha 90.00
_cell_angle_beta 90.00
_cell_angle_gamma 90.00
_cell_volume 3012.8(14)
_cell_formula_units_Z 8
_cell_measurement_temperature 296(2)
_cell_measurement_reflns_used 384
_cell_measurement_theta_min 0.998
_cell_measurement_theta_max 30.034

_exptl_crystal_description fragment
_exptl_crystal_colour silver
_exptl_crystal_size_max 0.10
_exptl_crystal_size_mid 0.05
_exptl_crystal_size_min 0.05
_exptl_crystal_density_meas ?
_exptl_crystal_density_diffrn 3.629
_exptl_crystal_density_method 'not measured'
_exptl_crystal_F_000 3047
_exptl_absorpt_coefficient_mu 8.911
_exptl_absorpt_correction_type 'Multi-scan'
_exptl_absorpt_correction_T_min 0.4694
_exptl_absorpt_correction_T_max 0.6643
_exptl_absorpt_process_details 'HKL scalepack (Otwinski & Minor, 1997)'

_exptl_special_details
;
?
;

_diffrn_ambient_temperature 296(1)
_diffrn_radiation_wavelength 0.71073
_diffrn_radiation_type MoK\a
_diffrn_radiation_source 'fine-focus sealed tube'
_diffrn_radiation_monochromator graphite
_diffrn_measurement_device_type 'Nonius Kappa CCD'
_diffrn_measurement_method '\w and \f scans'
_diffrn_detector_area_resol_mean ?
_diffrn_standards_number ?
_diffrn_standards_interval_count ?
_diffrn_standards_interval_time ?
_diffrn_standards_decay_% ?
_diffrn_reflns_number 1582
_diffrn_reflns_av_R_equivalents 0.0182
_diffrn_reflns_av_sigmaI/netI 0.0280
_diffrn_reflns_limit_h_min 2
_diffrn_reflns_limit_h_max 20
_diffrn_reflns_limit_k_min 0
_diffrn_reflns_limit_k_max 14
_diffrn_reflns_limit_l_min 0
_diffrn_reflns_limit_l_max 13
_diffrn_reflns_theta_min 3.99
_diffrn_reflns_theta_max 30.44
_reflns_number_total 258
_reflns_number_gt 240
_reflns_threshold_expression >2\s(I)

_computing_data_collection 'Collect (Nonius 1999)'
_computing_cell_refinement 'Denzo and Scalepack (Otwinski & Minor, 1997)'
_computing_data_reduction 'Denzo and Scalepack (Otwinski & Minor, 1997)'
_computing_structure_solution 'Dirct Methods, SIR97'
_computing_structure_refinement 'SHELXL-97 (Sheldrick, 2008)'
_computing_molecular_graphics 'Crystal Maker'
_computing_publication_material 'Publcif'

_refine_special_details
;

Refinement of F^2^ against ALL reflections. The weighted R-factor wR and goodness of fit S are based on F^2^, conventional R-factors R are based on F, with F set to zero for negative F^2^. The threshold expression of F^2^ > 2\s(F^2^) is used only for calculating R-factors(gt) etc. and is not relevant to the choice of reflections for refinement. R-factors based on F^2^ are statistically about twice as large as those based on F, and R-factors based on ALL data will be even larger.
;

_refine_ls_structure_factor_coef Fsqd
_refine_ls_matrix_type   full
_refine_ls_weighting_scheme   calc
_refine_ls_weighting_details
 'calc
w=1/[\s^2^(Fo^2^)+(0.0138P)^2^+6.4100P]
where P=(Fo^2^+2Fc^2^)/3'
_atom_sites_solution_primary   direct
_atom_sites_solution_secondary   difmap
_atom_sites_solution_hydrogens   ?
_refine_ls_hydrogen_treatment   ?
_refine_ls_extinction_method   SHELXL
_refine_ls_extinction_coef   0.00023(4)
_refine_ls_extinction_expression

'Fc^*^=kFc[1+0.001xFc^2^\l^3^/sin(2\q)]^-1/4^'
_refine_ls_number_reflns   258
_refine_ls_number_parameters   21
_refine_ls_number_restraints   3
_refine_ls_R_factor_all   0.0230
_refine_ls_R_factor_gt   0.0198
_refine_ls_wR_factor_ref   0.0386
_refine_ls_wR_factor_gt   0.0381
_refine_ls_goodness_of_fit_ref   1.123
_refine_ls_restrained_S_all   1.116
_refine_ls_shift/su_max   0.000
_refine_ls_shift/su_mean   0.000

loop_
 _atom_site_label
 _atom_site_type_symbol
 _atom_site_fract_x
 _atom_site_fract_y
 _atom_site_fract_z
 _atom_site_U_iso_or_equiv
 _atom_site_adp_type
 _atom_site_occupancy
 _atom_site_symmetry_multiplicity
 _atom_site_calc_flag
 _atom_site_refinement_flags
 _atom_site_disorder_assembly
 _atom_site_disorder_group
Yb1 Yb 0.1250 0.1250 0.1250 0.00861(15) Uani 1 24 d S . .
Cr1 Cr 0.5000 0.5000 0.5000 0.0066(2) Uani 1 12 d S . .
Al1 Al 0.05897(4) 0.05897(4) 0.32525(6) 0.0109(3) Uani 0.987(2) 2 d SP . .
Fe1 Fe 0.05897(4) 0.05897(4) 0.32525(6) 0.0086(2) Uani 0.013(2) 2 d SP . .
Al2 Al 0.48676(9) 0.1250 0.1250 0.0080(4) Uani 0.990(4) 4 d SP . .
Fe2 Fe 0.48676(9) 0.1250 0.1250 0.0064(4) Uani 0.010(4) 4 d SP . .
Al3 Al 0.0000 0.0000 0.0000 0.0185(5) Uani 1 12 d S . .

loop_
 _atom_site_aniso_label
 _atom_site_aniso_U_11
 _atom_site_aniso_U_22
 _atom_site_aniso_U_33
 _atom_site_aniso_U_23
 _atom_site_aniso_U_13
 _atom_site_aniso_U_12
Yb1 0.00861(15) 0.00861(15) 0.00861(15) 0.000 0.000 0.000
Cr1 0.0066(2) 0.0066(2) 0.0066(2) -0.0012(2) -0.0012(2) -0.0012(2)
Al1 0.0121(3) 0.0121(3) 0.0084(5) -0.0006(3) -0.0006(3) -0.0039(4)
Fe1 0.00959(9) 0.00959(9) 0.0066(6) -0.0004(4) -0.0004(4) -0.0037(5)
Al2 0.0083(6) 0.0079(4) 0.0079(4) -0.0031(5) 0.000 0.000

Fe2 0.0062(5) 0.0065(6) 0.0065(6) 0.0(3) 0.000 0.000
Al3 0.0185(5) 0.0185(5) 0.0185(5) -0.0043(6) -0.0043(6) -0.0043(6)

_geom_special_details
;
All s.u.'s (except the s.u. in the dihedral angle between two l.s. planes) are estimated using the full covariance matrix. The cell s.u.'s are taken into account individually in the estimation of s.u.'s in distances, angles and torsion angles; correlations between s.u.'s in cell parameters are only used when they are defined by crystal symmetry. An approximate (isotropic) treatment of cell s.u.'s is used for estimating s.u.'s involving l.s. planes.
;

loop_
_geom_bond_atom_site_label_1
_geom_bond_atom_site_label_2
_geom_bond_distance
_geom_bond_site_symmetry_2
_geom_bond_publ_flag
Yb1 Al3 3.1269(9) 6 ?
Yb1 Al3 3.1269(9) 4 ?
Yb1 Al3 3.1269(9) 3 ?
Yb1 Al3 3.1273(9) . ?
Yb1 Fe1 3.1910(13) 126 ?
Yb1 Al1 3.1910(13) 147 ?
Yb1 Fe1 3.1910(13) 147 ?
Yb1 Al1 3.1910(13) 126 ?
Yb1 Al1 3.1910(13) 172 ?
Yb1 Fe1 3.1910(13) 172 ?
Yb1 Al1 3.1912(13) 2 ?
Yb1 Fe1 3.1912(13) 118 ?
Cr1 Fe2 2.5601(7) 8_556 ?
Cr1 Al2 2.5601(7) 8_556 ?
Cr1 Fe2 2.5601(7) 154_565 ?
Cr1 Al2 2.5601(7) 154_565 ?
Cr1 Fe2 2.5601(7) 58 ?
Cr1 Fe2 2.5601(7) 104_665 ?
Cr1 Al2 2.5601(7) 58 ?
Cr1 Al2 2.5601(7) 104_665 ?
Cr1 Fe2 2.5605(7) 121_655 ?
Cr1 Al2 2.5605(7) 121_655 ?
Cr1 Fe2 2.5605(7) 25 ?
Cr1 Al2 2.5605(7) 25 ?
Al1 Fe2 2.6944(15) 176 ?
Al1 Al2 2.6944(15) 176 ?
Al1 Fe1 2.6972(19) 172 ?
Al1 Al1 2.6972(19) 172 ?
Al1 Fe1 2.7416(16) 12 ?
Al1 Al1 2.7416(16) 10 ?
Al1 Al1 2.7416(16) 12 ?
Al1 Fe1 2.7416(16) 10 ?
Al1 Cr1 2.7966(12) 73_445 ?
Al1 Fe2 2.8306(11) 130 ?
Al1 Al2 2.8306(11) 130 ?
Al1 Fe2 2.8308(11) 145 ?
Al2 Cr1 2.5601(7) 30_644 ?
Al2 Cr1 2.5605(7) 25_544 ?
Al2 Fe1 2.6944(15) 126 ?
Al2 Al1 2.6944(15) 126 ?
Al2 Fe1 2.6946(15) 118 ?
Al2 Al1 2.6946(15) 118 ?
Al2 Fe2 2.8234(19) 100_665 ?
Al2 Fe2 2.8234(19) 99_656 ?
Al2 Al2 2.8234(19) 100_665 ?
Al2 Al2 2.8234(19) 99_656 ?
Al2 Fe2 2.8236(19) 82_545 ?
Al2 Fe2 2.8236(19) 128_654 ?
Al3 Yb1 3.1273(9) 97 ?

loop_
_geom_angle_atom_site_label_1
_geom_angle_atom_site_label_2
_geom_angle_atom_site_label_3
_geom_angle
_geom_angle_site_symmetry_1
_geom_angle_site_symmetry_3
_geom_angle_publ_flag
Al3 Yb1 Al3 109.5 6 4 ?
Al3 Yb1 Al3 109.5 6 3 ?
Al3 Yb1 Al3 109.5 4 3 ?
Al3 Yb1 Al3 109.5 6 . ?
Al3 Yb1 Al3 109.5 4 . ?
Al3 Yb1 Al3 109.5 3 . ?
Al3 Yb1 Fe1 100.272(15) 6 126 ?

Al3 Yb1 Fe1 58.452(4) 4 126 ?
Al3 Yb1 Fe1 58.452(4) 3 126 ?
Al3 Yb1 Fe1 150.261(15) . 126 ?
Al3 Yb1 Al1 58.452(4) 6 147 ?
Al3 Yb1 Al1 58.452(4) 4 147 ?
Al3 Yb1 Al1 100.272(15) 3 147 ?
Al3 Yb1 Al1 150.261(15) . 147 ?
Fe1 Yb1 Al1 50.88(2) 126 147 ?
Al3 Yb1 Fe1 58.452(4) 6 147 ?
Al3 Yb1 Fe1 58.452(4) 4 147 ?
Al3 Yb1 Fe1 100.272(15) 3 147 ?
Al3 Yb1 Fe1 150.261(15) . 147 ?
Fe1 Yb1 Fe1 50.88(2) 126 147 ?
Al1 Yb1 Fe1 0.00(3) 147 147 ?
Al3 Yb1 Al1 100.272(15) 6 126 ?
Al3 Yb1 Al1 58.452(4) 4 126 ?
Al3 Yb1 Al1 58.452(4) 3 126 ?
Al3 Yb1 Al1 150.261(15) . 126 ?
Fe1 Yb1 Al1 0.00(5) 126 126 ?
Al1 Yb1 Al1 50.88(2) 147 126 ?
Fe1 Yb1 Al1 50.88(2) 147 126 ?
Al3 Yb1 Al1 58.452(4) 6 172 ?
Al3 Yb1 Al1 100.272(15) 4 172 ?
Al3 Yb1 Al1 58.452(4) 3 172 ?
Al3 Yb1 Al1 150.261(15) . 172 ?
Fe1 Yb1 Al1 50.88(2) 126 172 ?
Al1 Yb1 Al1 50.88(2) 147 172 ?
Fe1 Yb1 Al1 50.88(2) 147 172 ?
Al1 Yb1 Al1 50.88(2) 126 172 ?
Al3 Yb1 Fe1 58.452(4) 6 172 ?
Al3 Yb1 Fe1 100.272(15) 4 172 ?
Al3 Yb1 Fe1 58.452(4) 3 172 ?
Al3 Yb1 Fe1 150.261(15) . 172 ?
Fe1 Yb1 Fe1 50.88(2) 126 172 ?
Al1 Yb1 Fe1 50.88(2) 147 172 ?
Fe1 Yb1 Fe1 50.88(2) 147 172 ?
Al1 Yb1 Fe1 50.88(2) 126 172 ?
Al1 Yb1 Fe1 0.000(13) 172 172 ?
Al3 Yb1 Al1 58.450(4) 6 2 ?
Al3 Yb1 Al1 58.450(4) 4 2 ?
Al3 Yb1 Al1 150.273(15) 3 2 ?
Al3 Yb1 Al1 100.261(15) . 2 ?
Fe1 Yb1 Al1 95.129(6) 126 2 ?
Al1 Yb1 Al1 50.00(3) 147 2 ?
Fe1 Yb1 Al1 50.00(3) 147 2 ?
Al1 Yb1 Al1 95.129(6) 126 2 ?
Al1 Yb1 Al1 95.129(6) 172 2 ?
Fe1 Yb1 Al1 95.129(6) 172 2 ?
Al3 Yb1 Fe1 150.273(15) 6 118 ?
Al3 Yb1 Fe1 58.450(4) 4 118 ?
Al3 Yb1 Fe1 58.450(4) 3 118 ?
Al3 Yb1 Fe1 100.261(15) . 118 ?
Fe1 Yb1 Fe1 50.00(3) 126 118 ?
Al1 Yb1 Fe1 95.129(6) 147 118 ?
Fe1 Yb1 Fe1 95.129(6) 147 118 ?
Al1 Yb1 Fe1 50.00(3) 126 118 ?
Al1 Yb1 Fe1 95.129(6) 172 118 ?
Fe1 Yb1 Fe1 95.129(6) 172 118 ?
Al1 Yb1 Fe1 116.898(9) 2 118 ?
Fe2 Cr1 Al2 0.0 8_556 8_556 ?
Fe2 Cr1 Fe2 66.93(4) 8_556 154_565 ?
Al2 Cr1 Fe2 66.93(4) 8_556 154_565 ?
Fe2 Cr1 Al2 66.93(4) 8_556 154_565 ?
Al2 Cr1 Al2 66.93(4) 8_556 154_565 ?
Fe2 Cr1 Al2 0.0 154_565 154_565 ?
Fe2 Cr1 Fe2 113.07(4) 8_556 58 ?
Al2 Cr1 Fe2 113.07(4) 8_556 58 ?
Fe2 Cr1 Fe2 180.0 154_565 58 ?
Al2 Cr1 Fe2 180.0 154_565 58 ?
Fe2 Cr1 Fe2 180.00(6) 8_556 104_665 ?
Al2 Cr1 Fe2 180.00(6) 8_556 104_665 ?
Fe2 Cr1 Fe2 113.07(4) 154_565 104_665 ?
Al2 Cr1 Fe2 113.07(4) 154_565 104_665 ?
Fe2 Cr1 Fe2 66.93(4) 58 104_665 ?
Fe2 Cr1 Al2 113.07(4) 8_556 58 ?
Al2 Cr1 Al2 113.07(4) 8_556 58 ?
Fe2 Cr1 Al2 180.0 154_565 58 ?
Al2 Cr1 Al2 180.0 154_565 58 ?
Fe2 Cr1 Al2 0.00(6) 58 58 ?
Fe2 Cr1 Al2 66.93(4) 104_665 58 ?
Fe2 Cr1 Al2 180.00(6) 8_556 104_665 ?
Al2 Cr1 Al2 180.00(6) 8_556 104_665 ?
Fe2 Cr1 Al2 113.07(4) 154_565 104_665 ?
Al2 Cr1 Al2 113.07(4) 154_565 104_665 ?
Fe2 Cr1 Al2 66.93(4) 58 104_665 ?
Fe2 Cr1 Al2 0.00(6) 104_665 104_665 ?
Al2 Cr1 Al2 66.93(4) 58 104_665 ?
Fe2 Cr1 Fe2 66.93(4) 8_556 121_655 ?
Al2 Cr1 Fe2 66.93(4) 8_556 121_655 ?
Fe2 Cr1 Fe2 66.93(4) 154_565 121_655 ?
Al2 Cr1 Fe2 66.93(4) 154_565 121_655 ?
Fe2 Cr1 Fe2 113.07(4) 58 121_655 ?

Fe2 Cr1 Fe2 113.07(4) 104_665 121_655 ?
Al2 Cr1 Fe2 113.07(4) 58 121_655 ?
Al2 Cr1 Fe2 113.07(4) 104_665 121_655 ?
Fe2 Cr1 Al2 66.93(4) 8_556 121_655 ?
Al2 Cr1 Al2 66.93(4) 8_556 121_655 ?
Fe2 Cr1 Al2 66.93(4) 154_565 121_655 ?
Al2 Cr1 Al2 66.93(4) 154_565 121_655 ?
Fe2 Cr1 Al2 113.07(4) 58 121_655 ?
Fe2 Cr1 Al2 113.07(4) 104_665 121_655 ?
Al2 Cr1 Al2 113.07(4) 58 121_655 ?
Al2 Cr1 Al2 113.07(4) 104_665 121_655 ?
Fe2 Cr1 Al2 0.0 121_655 121_655 ?
Fe2 Cr1 Fe2 113.07(4) 8_556 25 ?
Al2 Cr1 Fe2 113.07(4) 8_556 25 ?
Fe2 Cr1 Fe2 113.07(4) 154_565 25 ?
Al2 Cr1 Fe2 113.07(4) 154_565 25 ?
Fe2 Cr1 Fe2 66.93(4) 58 25 ?
Fe2 Cr1 Fe2 66.93(4) 104_665 25 ?
Al2 Cr1 Fe2 66.93(4) 58 25 ?
Al2 Cr1 Fe2 66.93(4) 104_665 25 ?
Fe2 Cr1 Fe2 180.0 121_655 25 ?
Al2 Cr1 Fe2 180.0 121_655 25 ?
Fe2 Cr1 Al2 113.07(4) 8_556 25 ?
Al2 Cr1 Al2 113.07(4) 8_556 25 ?
Fe2 Cr1 Al2 113.07(4) 154_565 25 ?
Al2 Cr1 Al2 113.07(4) 154_565 25 ?
Fe2 Cr1 Al2 66.93(4) 58 25 ?
Fe2 Cr1 Al2 66.93(4) 104_665 25 ?
Al2 Cr1 Al2 66.93(4) 58 25 ?
Al2 Cr1 Al2 66.93(4) 104_665 25 ?
Fe2 Cr1 Al2 180.0 121_655 25 ?
Al2 Cr1 Al2 180.0 121_655 25 ?
Fe2 Cr1 Al2 0.00(6) 25 25 ?
Fe2 Al1 Al2 0.00(3) 176 176 ?
Fe2 Al1 Fe1 59.97(2) 176 172 ?
Al2 Al1 Fe1 59.97(2) 176 172 ?
Fe2 Al1 Al1 59.97(2) 176 172 ?
Al2 Al1 Al1 59.97(2) 176 172 ?
Fe1 Al1 Al1 0.00(5) 172 172 ?
Fe2 Al1 Fe1 149.589(4) 176 12 ?
Al2 Al1 Fe1 149.589(4) 176 12 ?
Fe1 Al1 Fe1 120.0 172 12 ?
Al1 Al1 Fe1 120.0 172 12 ?
Fe2 Al1 Al1 149.589(4) 176 10 ?
Al2 Al1 Al1 149.589(4) 176 10 ?
Fe1 Al1 Al1 120.0 172 10 ?
Al1 Al1 Al1 120.0 172 10 ?
Fe1 Al1 Al1 60.0 12 10 ?
Fe2 Al1 Al1 149.589(4) 176 12 ?
Al2 Al1 Al1 149.589(4) 176 12 ?
Fe1 Al1 Al1 120.0 172 12 ?
Al1 Al1 Al1 120.0 172 12 ?
Fe1 Al1 Al1 0.00(3) 12 12 ?
Al1 Al1 Al1 60.0 10 12 ?
Fe2 Al1 Fe1 149.589(4) 176 10 ?
Al2 Al1 Fe1 149.589(4) 176 10 ?
Fe1 Al1 Fe1 120.0 172 10 ?
Al1 Al1 Fe1 120.0 172 10 ?
Fe1 Al1 Fe1 60.0 12 10 ?
Al1 Al1 Fe1 0.00(3) 10 10 ?
Al1 Al1 Fe1 60.0 12 10 ?
Fe2 Al1 Cr1 55.54(2) 176 73_445 ?
Al2 Al1 Cr1 55.54(2) 176 73_445 ?
Fe1 Al1 Cr1 115.514(17) 172 73_445 ?
Al1 Al1 Cr1 115.514(17) 172 73_445 ?
Fe1 Al1 Cr1 115.011(14) 12 73_445 ?
Al1 Al1 Cr1 115.011(14) 10 73_445 ?
Al1 Al1 Cr1 115.011(14) 12 73_445 ?
Fe1 Al1 Cr1 115.011(14) 10 73_445 ?
Fe2 Al1 Fe2 101.24(3) 176 130 ?
Al2 Al1 Fe2 101.24(3) 176 130 ?
Fe1 Al1 Fe2 145.97(3) 172 130 ?
Al1 Al1 Fe2 145.97(3) 172 130 ?
Fe1 Al1 Fe2 90.83(2) 12 130 ?
Al1 Al1 Fe2 61.040(17) 10 130 ?
Al1 Al1 Fe2 90.83(2) 12 130 ?
Fe1 Al1 Fe2 61.040(17) 10 130 ?
Cr1 Al1 Fe2 54.120(17) 73_445 130 ?
Fe2 Al1 Al2 101.24(3) 176 130 ?
Al2 Al1 Al2 101.24(3) 176 130 ?
Fe1 Al1 Al2 145.97(3) 172 130 ?
Al1 Al1 Al2 145.97(3) 172 130 ?
Fe1 Al1 Al2 90.83(2) 12 130 ?
Al1 Al1 Al2 61.040(17) 10 130 ?
Al1 Al1 Al2 90.83(2) 12 130 ?
Fe1 Al1 Al2 61.040(17) 10 130 ?
Cr1 Al1 Al2 54.120(17) 73_445 130 ?
Fe2 Al1 Al2 0.00(5) 130 130 ?
Fe2 Al1 Fe2 101.25(3) 176 145 ?
Al2 Al1 Fe2 101.25(3) 176 145 ?
Fe1 Al1 Fe2 145.97(3) 172 145 ?
Al1 Al1 Fe2 145.97(3) 172 145 ?

Fe1 Al1 Fe2 61.032(17) 12 145 ?
Al1 Al1 Fe2 90.83(2) 10 145 ?
Al1 Al1 Fe2 61.032(17) 12 145 ?
Fe1 Al1 Fe2 90.83(2) 10 145 ?
Cr1 Al1 Fe2 54.127(17) 73_445 145 ?
Fe2 Al1 Fe2 59.83(5) 130 145 ?
Al2 Al1 Fe2 59.83(5) 130 145 ?
Cr1 Al2 Cr1 171.43(6) 30_644 25_544 ?
Cr1 Al2 Fe1 64.25(2) 30_644 126 ?
Cr1 Al2 Fe1 124.31(4) 25_544 126 ?
Cr1 Al2 Al1 64.25(2) 30_644 126 ?
Cr1 Al2 Al1 124.31(4) 25_544 126 ?
Fe1 Al2 Al1 0.00(3) 126 126 ?
Cr1 Al2 Fe1 124.32(4) 30_644 118 ?
Cr1 Al2 Fe1 64.24(2) 25_544 118 ?
Fe1 Al2 Fe1 60.07(5) 126 118 ?
Al1 Al2 Fe1 60.07(5) 126 118 ?
Cr1 Al2 Al1 124.32(4) 30_644 118 ?
Cr1 Al2 Al1 64.24(2) 25_544 118 ?
Fe1 Al2 Al1 60.07(5) 126 118 ?
Al1 Al2 Al1 60.07(5) 126 118 ?
Fe1 Al2 Al1 0.00(5) 118 118 ?
Cr1 Al2 Fe2 56.54(2) 30_644 100_665 ?
Cr1 Al2 Fe2 116.47(2) 25_544 100_665 ?
Fe1 Al2 Fe2 111.22(2) 126 100_665 ?
Al1 Al2 Fe2 111.22(2) 126 100_665 ?
Fe1 Al2 Fe2 149.590(4) 118 100_665 ?
Al1 Al2 Fe2 149.590(4) 118 100_665 ?
Cr1 Al2 Fe2 56.54(2) 30_644 99_656 ?
Cr1 Al2 Fe2 116.47(2) 25_544 99_656 ?
Fe1 Al2 Fe2 111.221(19) 126 99_656 ?
Al1 Al2 Fe2 111.221(19) 126 99_656 ?
Fe1 Al2 Fe2 149.590(4) 118 99_656 ?
Al1 Al2 Fe2 149.590(4) 118 99_656 ?
Fe2 Al2 Fe2 60.0 100_665 99_656 ?
Cr1 Al2 Al2 56.54(2) 30_644 100_665 ?
Cr1 Al2 Al2 116.47(2) 25_544 100_665 ?
Fe1 Al2 Al2 111.22(2) 126 100_665 ?
Al1 Al2 Al2 111.22(2) 126 100_665 ?
Fe1 Al2 Al2 149.590(4) 118 100_665 ?
Al1 Al2 Al2 149.590(4) 118 100_665 ?
Fe2 Al2 Al2 0.00(4) 100_665 100_665 ?
Fe2 Al2 Al2 60.0 99_656 100_665 ?
Cr1 Al2 Al2 56.54(2) 30_644 99_656 ?
Cr1 Al2 Al2 116.47(2) 25_544 99_656 ?
Fe1 Al2 Al2 111.221(19) 126 99_656 ?
Al1 Al2 Al2 111.221(19) 126 99_656 ?
Fe1 Al2 Al2 149.590(4) 118 99_656 ?
Al1 Al2 Al2 149.590(4) 118 99_656 ?
Fe2 Al2 Al2 60.0 100_665 99_656 ?
Fe2 Al2 Al2 0.00(4) 99_656 99_656 ?
Al2 Al2 Al2 60.0 100_665 99_656 ?
Cr1 Al2 Fe2 116.48(2) 30_644 82_545 ?
Cr1 Al2 Fe2 56.53(2) 25_544 82_545 ?
Fe1 Al2 Fe2 149.590(4) 126 82_545 ?
Al1 Al2 Fe2 149.590(4) 126 82_545 ?
Fe1 Al2 Fe2 111.208(19) 118 82_545 ?
Al1 Al2 Fe2 111.208(19) 118 82_545 ?
Fe2 Al2 Fe2 90.0 100_665 82_545 ?
Fe2 Al2 Fe2 60.0 99_656 82_545 ?
Al2 Al2 Fe2 90.0 100_665 82_545 ?
Al2 Al2 Fe2 60.0 99_656 82_545 ?
Cr1 Al2 Fe2 116.48(2) 30_644 128_654 ?
Cr1 Al2 Fe2 56.53(2) 25_544 128_654 ?
Fe1 Al2 Fe2 149.590(4) 126 128_654 ?
Al1 Al2 Fe2 149.590(4) 126 128_654 ?
Fe1 Al2 Fe2 111.208(19) 118 128_654 ?
Al1 Al2 Fe2 111.208(19) 118 128_654 ?
Fe2 Al2 Fe2 60.0 100_665 128_654 ?
Fe2 Al2 Fe2 90.0 99_656 128_654 ?
Al2 Al2 Fe2 60.0 100_665 128_654 ?
Al2 Al2 Fe2 90.0 99_656 128_654 ?
Fe2 Al2 Fe2 60.0 82_545 128_654 ?
Yb1 Al3 Yb1 180.0 97 . ?

_diffrn_measured_fraction_theta_max
0.996
_diffrn_reflns_theta_full 30.44
_diffrn_measured_fraction_theta_full
0.996
_refine_diff_density_max 0.681
_refine_diff_density_min -0.701
_refine_diff_density_rms 0.126

##END

Appendix D

$YbCr_2Fe_xAl_{20-x}$ Fe Site Occupancy Data

YbCr2Fe0.1Al19.9	Fe site occupancies					Composition (occupancy * multiplicity / Z)						Ratios	Comments
Sites	Yb	Cr	Al1	Al2	Al3	Yb	Cr	Al1	Al2	Al3	SUM	Order/ Disorder	
Cr-Yb	0.0062	0.04635				0.00616	0.0927				0.09886	0.07	
Cr-Al1		0.00489	0.00752				0.00978	0.09024			0.10002	0.11	
Cr-Al2		0.01602		0.01132			0.03204		0.06792		0.09996	0.47	
Cr-Al3													unstable
Yb-Al1	0.005		0.0078			0.00495		0.0936			0.09855	0.05	
Yb-Al2	0.005			0.0154		0.00496			0.0924		0.09736	0.05	
Yb-Al3	0.0147				0.03432	0.01474				0.06864	0.08338	0.21	
Al1-Al2			0.00424	0.00838				0.05088	0.05028		0.10116	0.99	
Al1-Al3			0.00821		0.00015			0.09852		0.0003	0.09882	0.00	
Al2-Al3													unstable
Mossbauer												1.33	
YbCr2Fe0.2Al19.8	Fe site occupancies					Composition (occupancy * multiplicity / Z)						Ratios	comments
Sites	Yb	Cr	Al1	Al2	Al3	Yb	Cr	Al1	Al2	Al3	SUM	Order/ Disorder	
Cr-Yb	0	0.10805					0.2161				0.2161	0.00	
Cr-Al1		0.02209	0.01448				0.04418	0.17376			0.21794	0.25	
Cr-Al2		0.07407		0.01142			0.14814		0.06852		0.21666	2.16	
Cr-Al3													unstable
Yb-Al1													negative
Yb-Al2	0.0025			0.03418		0.0025			0.20508		0.20758	0.01	
Yb-Al3	0.0154				0.08478	0.01537				0.16956	0.18493	0.09	
Al1-Al2			0.01226	0.0119				0.14712	0.0714		0.21852	0.49	
Al1-Al3			0.01684		0.00781			0.20208		0.01562	0.2177	0.08	
Al2-Al3				0.03142	0.00986				0.18852	0.01972	0.20824	0.10	
Mossbauer												0.67	

Appendix E

Temperature Dependent Studies of $Ni_{50}Mn_{35}(In,Si)_{15}$ for Magnetocaloric Applications

E.1 Introduction

Heusler alloys, which are compounds with a X_2YZ stoichiometry where X and Y are typically transition metals and Z is a main group element. The high temperature crystal structure is based on 4 interpenetrating FCC lattices, as shown in Figure E.1. At lower temperatures Heusler alloys have been shown to exhibit Martensitic transitions to tetragonal or monoclinic phases [320]. Heusler alloys as a class encompass many topics of interest, including superconductivity, magnetism, semiconductors, thermoelectrics and structural transitions. The Ni_2MnGa-based Heusler alloys have been investigated for the magnetocaloric effect. However, the lack of high quality single crystals and variability in sample composition add complications to understanding these materials [321].

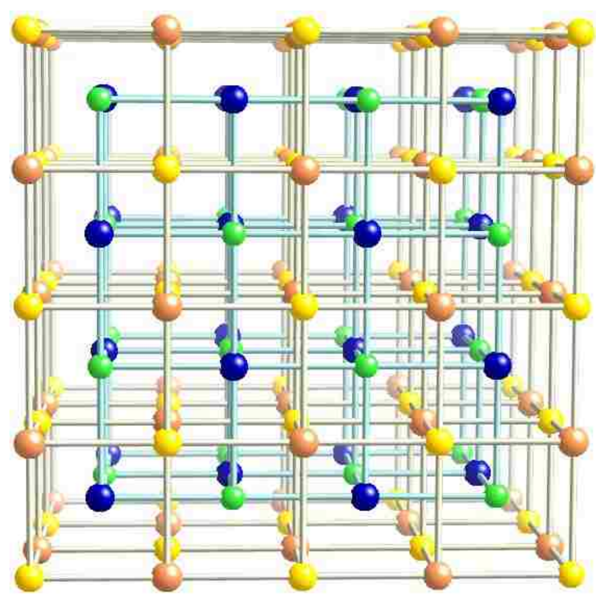

Figure E.1. Four interpenetrating FCC lattices in the Heusler alloy structure. Unit cell length is ½ of the picture. In the traditional Heusler alloy two colors (ex. Blue and green) are the same element.

E.2 Experimental

In collaboration, we have recently characterized polycrystalline $Ni_{50}Mn_{35}In_{15-x}Si_x$ (x = 0-5) as prepared by arc melting. $Ni_{50}Mn_{35}In_{15-x}Si_x$ (x = 0 – 5) is of particular interest as this system exhibits a magnetic and structural transition near room temperature, ideal for room temperature magnetic refrigeration [322]. Doping with small amounts of silicon (x = 3) increases the efficiency 300% over $Ni_{50}Mn_{35}In_{15}$, resulting in one of the largest magnetocaloric effects for any compound near room temperature.

To investigate the occurrence of a Martensitic transition, samples of $Ni_{50}Mn_{35}In_{15-x}Si_x$ (x = 0-5) were characterized by X-ray diffraction at various temperatures via the capillary method [323, 324]. A small portion each alloy ingot was cut off and ground in ethanol to prevent oxidation. The sample was mounted on a Mitigen holder by dipping the tip into Paratone oil and the excess oil was wiped off leaving a thin film. The fiber was then gently rolled in the powdered sample to coat the tip [323]. The resulting sample is shown in Figure E.2.

Figure E.2. The sample holder used for temperature-dependent X-ray diffraction experiments.

X-ray diffraction data was collected on a Bruker Kappa Apex II single crystal X-ray diffractometer using the parameters as shown in Table E.1. Integration time was also evaluated and diffraction patterns were collected with 120 seconds per frame. Other detector distances and integration times were tested and the conditions in Table E.1 were suitable in terms of collection time, signal intensity and resolution. Integration of the diffraction patterns was done using the **XRD^2 Eval** feature of the APEX2 program. Baseline correction was done with the EVA program. Temperatures were selected based on features in the magnetization data.

Table E.1 Instrumental Parameters

Parameter	Setting
Voltage	50 kV
Current	24 mΩ
Direction	Negative
Sweep	180 degrees
Ω	-5, -12.5, -20, -27.5, -35, -42.5
χ	54.818
Time	120 seconds
Width	180 degrees
2 θ	10, 25, 40, 55, 70 85

To determine how long it would take to equilibrate at the new temperatures a scan was collected shortly after reaching each new temperature and a second scan was taken 10 minutes after the first was completed (approx. 30 minutes after reaching the temperature). Initial and final diffraction patterns showed minimal differences. Two diffraction patterns were collected for each compound in this manner and the second data set was used for analysis.

E.3. Results

X-ray powder diffraction patterns were collected on all 6 materials, $Ni_{50}Mn_{35}In_{15-x}Si_x$ (x=0-5), and the room temperature diffraction patterns are shown in Figure E.3. All patterns are consistent with the Heuser alloy structure, with a few impurity peaks in pattern of $Ni_{50}Mn_{35}In_{10}Si_5$. The shoulder observed at ~43° and ~80° 2-θ in the pattern of $Ni_{50}Mn_{35}In_{15}$

indicates that this material is in the Martensitic phase at room temperature. This structure has been tentatively assigned to the tetragonal model. However the resolution does not appear to be sufficient to determine if any material remains in the cubic phase. Further discussion of the temperature will be done using only the $Ni_{50}Mn_{35}In_{12}Si_3$ composition due to similarities in the diffraction patterns.

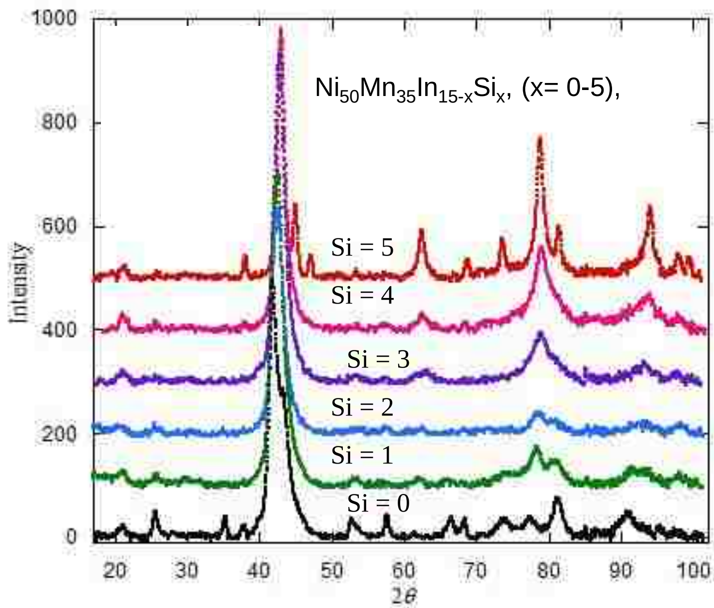

Figure E.3. The diffraction patterns for $Ni_{50}Mn_{35}In_{15-x}Si_x$ (x = 0-5) at room temperature. Extra peaks in $Ni_{50}Mn_{35}In_{10}Si_5$ are due to an impurity phase. The shoulder on the peak at 43° 2-θ indicates that the Martensitic transition has occurred in Si = 0.

Figure E.4 shows the diffraction pattern as a function of temperature for $Ni_{50}Mn_{35}In_{12}Si_3$. The measurements were conducted at 298K, 200 K, 150K and 100K in both warming and cooling directions, shown as red and blue respectively. The similarities in heating and cooling show the measurement is reproducible and the structural transition is reversible. The peak splitting in the 200 K diffraction pattern shows that the Martensitic transition occurs between 298 and 200K consistent with the temperature of 276K determined by magnetic measurements [325].

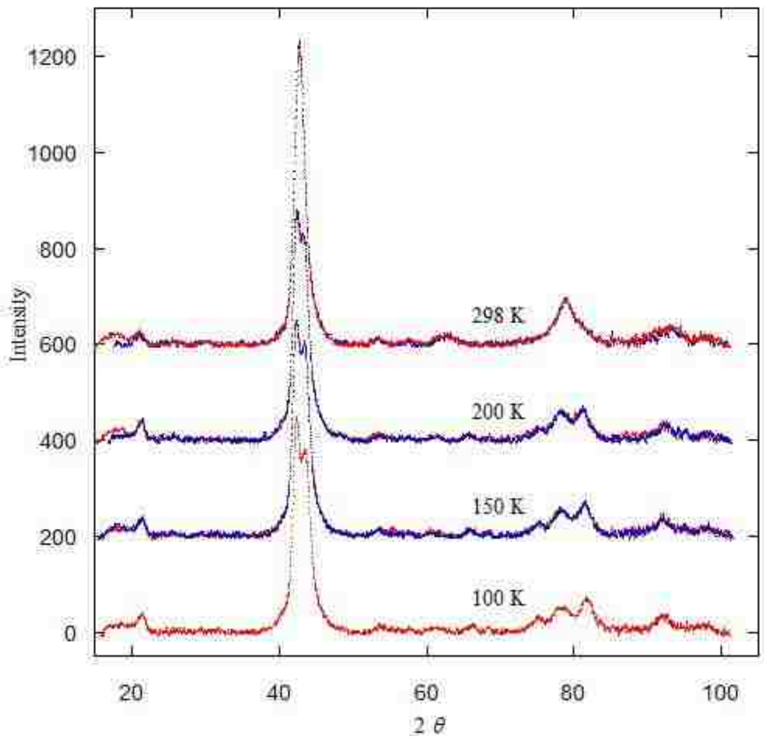

Figure E.4. The diffraction pattern of Ni50Mn35In12Si3 as a function of temperature. Blue diffraction patterns were collected during cooling and red patterns were collected upon warming. The peak splitting shows the structural transition occurs between 200 and 298 K.

E.4 References

[320] B. Wedel, M. Suzuki, Y. Murakami, C. Wedel, T. Suzuki, D. Shindo, K. Itagaki, Low temperature crystal structure of Ni-Mn-Ga alloys, J. Alloys Comp., 290 (1999) 137-143.

[321] M. Pasquale, C.P. Sasso, L.H. Lewis, Magnetic entropy in Ni_2MnGa single crystals, J. Appl. Phys., 95 (2004) 6918-6920.

[322] A.K. Pathak, I. Dubenko, S. Stadler, N. Ali, The effect of partial substitution of In by Si on the phase transitions and respective magnetic entropy changes of $Ni_{50}Mn_{35}In_{15}$ Heusler alloy, J. Phys. D: Appl. Phys. , 41 (2008) 202004.

[323] N.S.P. Bhuvanesh, J.H. Reibenspies, A novel approach to micro-sample X-ray powder diffraction using nylon loops, J. Appl. Crystallogr., 36 (2003) 1480-1481.

[324] J.H. Reibenspies, N. Bhuvanesh, Capillaries prepared from thin-walled heat-shrink poly(ethylene terephthalate) (PET) tubing for X-ray powder diffraction analysis, Powder Diffr., 21 (2006) 323-325.

[325] A.K. Pathak, et al., The effect of partial substitution of In by Si on the phase transitions and respective magnetic entropy changes of $Ni_{50}Mn_{35}In_{15}$ Heusler alloy, J. Phys. D: Appl. Phys., 41 (2008) 202004.

Appendix F

Temperature Dependent X-ray Diffraction Studies of NiMn(Ge,Al)

F.1 Introduction

Similar to the Ni_2MnGa based Heusler alloys, NiMnGe based compounds show magnetic ordering near or above room temperature making them potentially useful magnetocaloric materials. These materials can also exhibit Martensitic transitions [326] which can lead to an enhancement of the magnetocaloric effect. Herein the temperature-dependent structural transformation of $NiMnGe_{0.91}Al_{0.9}$ is studied with single crystal X-ray diffraction.

F.2 Experimental

A single crystal was selected from a crushed polycrystalline ingot and cut to ~0.05 x 0.05 x 0.1 mm for X-ray diffraction measurements. The crystal was mounted on a glass fiber with epoxy, coated in vacuum grease (as the adhesive for low temperature collections), and mounted on the goniometer of a Nonius Kappa CCD X-ray diffractometer with Mo Kα radiation (λ = 0.71073 Å). Crystallographic data was collected at 100, 200, 296, and 370 K to investigate features in the temperature-dependent magnetism. All temperature ramp rates were 60 K/h to minimize stress on the crystal, and the crystal was equilibrated at the targeted temperature for a minimum of 20 minutes. At room temperature, the diffraction pattern was indexed to a hexagonal unit cell with lattice parameters a = 4.106(4) Å and c = 5.426(4) Å. Systematic absences indicated the spacegroup $P6_3/mmc$, and the crystal structures were solved by direct methods with SIR97 [327] and refined with SHELXL97 [328]. The final models were corrected for extinction and the atomic displacement parameters were treated anisotropically. The crystal structure was found to be isostructural with the previously reported high-temperature polymorph of NiMnGe [326]. The aluminum atoms were initially mixed with the germanium (2*c*) based on the nominal composition. The refined occupancy of aluminum (8%) was in agreement with the nominal composition (9%), so the aluminum was kept on the germanium site (2*c*) and fixed to the nominal value. The structure determinations at 200 and 370 K were also consistent with the room temperature polymorph. However, at 100 K $NiMnGe_{0.91}Al_{0.09}$ adopts the previously reported low-temperature polymorph of NiMnGe (*Pnma*, a = 6.015(1) Å, b = 3.734(2) Å, c = 7.189(2) Å) [326]. Details of the data collections and refinements at 100 and 297 K, are provided in Table F.1, and atomic positions and displacement parameters for both polymorphs are provided in Table F.2.

To further investigate the phase transformation, lattice parameters were determined between 100 and 300 K. To be consistent with the heat treatment in the magnetic measurements, the crystal was first heated to 370 K and then cooled to 100 K. Unit cell determinations were then conducted at 15 K intervals upon warming, and consisted of 20° phi scans below 200 K and 30° phi scans above 300 K. The longer scans at higher temperature were to compensate for the smaller unit cell which resulted in fewer diffraction peaks. The orthorhombic and hexagonal polymorphs were observed at temperatures ≤ 195 K and ≥ 210 K, respectively.

Good crystal quality was evident from low mosaicity values (<1°) even after a number of thermal cycles, which is consistent with previous reports where single crystals exhibiting martensitic transitions can be repeatedly cycled. This behavior contrasts with polycrystalline samples that degrade upon cycling [329].

Table F.1 Crystallographic Paramters

Compound	$NiMnGe_{0.91}Al_{0.09}$	$NiMnGe_{0.91}Al_{0.09}$
Crystal System	hexagonal	orthorhombic
T (K)	297(1)	100(1)
Space Group	$P6_3/mmc$	*Pnma*
a (Å)	4.102(2)	6.0150(10)
b (Å)	4.102(2)	3.734(2)
c (Å)	5.416(3)	7.089(2)
V (Å^3)	78.92(7)	159.22(10)
Z	2	4
Crystal dimensions (mm)	0.05 x 0.05 x 0.10	0.05 x 0.05 x 0.10
θ range (°)	5.74 - 34.39	4.44 – 31.00
μ (mm^{-1})	36.305	35.992
Data Collection		
Measured Reflections	2079	1934
Independent Reflections	77	287
Reflections with I>2σ(I)	58	278
R_{int}	0.0343	0.0169
h	$0 \leq h \leq 6$	$-8 \leq h \leq 8$
k	$-4 \leq k \leq 0$	$-5 \leq k \leq 5$
l	$-8 \leq l \leq 8$	$-10 \leq l \leq 10$
Refinement		
$R_1{}^a$	0.0275	0.0227
$wR_2{}^b$	0.0721	0.0548
Reflections	77	287
Parameters	8	20
$\Delta\rho_{max}$	1.808	1.253
$\Delta\rho_{min}$	-1.368	-1.174
Extinction coefficient	0.071(16)	0.019(3)
GoF	1.085	1.178

$^a R_1 = \Sigma||F_o| - |F_c||/\Sigma|F_o|$
$^b R_w = [\Sigma [w (F_o^2 - F_c^2)^2]/ \Sigma [w (F_o^2)^2]]^{1/2}$; $w = 1/[\sigma^2(F_o^2) + (0.0488 P)^2]$, $w = 1/[\sigma^2(F_o^2) + (0.0282 P)^2 + 0.5362 P]$; $P = (F_o^2 + 2 Fc^2)/3$ for297 K and 100 K, respectively.

Table F.2 Atomic Positions and Displacement Parameters

T (K)	Site	Position	*x*	*y*	*z*	Occ.[a]	U_{eq}[b]
297							
	Ni1	2*d*	1/3	2/3	3/4	1	0.0128(4)
	Ge1	2*c*	1/3	2/3	1/4	0.91	0.0104(5)
	Al1	2*c*	1/3	2/3	1/4	0.09	0.0104(5)
	Mn1	2*a*	0	0	1/2	1	0.0087(4)
100							
	Ni1	4*c*	0.14667(9)	1/4	0.05818(8)	1	0.0053(2)
	Mn1	4*c*	0.03014(11)	1/4	0.68047(9)	1	0.0051(2)
	Ge1	4*c*	0.25894(7)	1/4	0.37440(6)	0.91	0.0042(2)
	Al1	4*c*	0.25894(7)	1/4	0.37440(6)	0.09	0.0042(2)

[a] Site occupancy
[b] U_{eq} is defined as one-third of the trace of the orthogonalized U_{ij} tensor

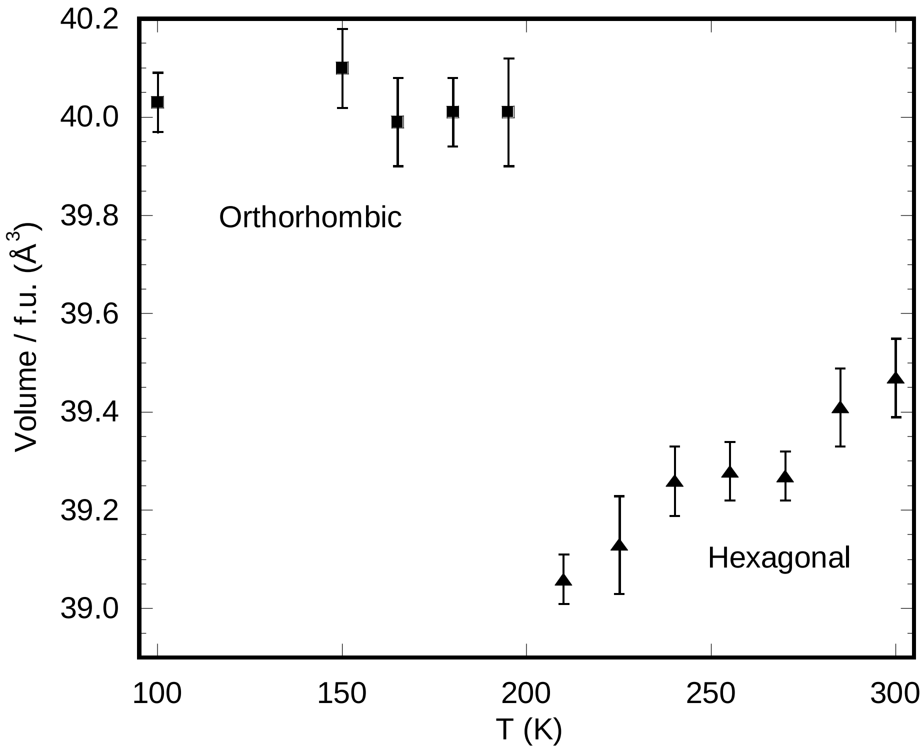

Figure F.1 Volume per formula unit as a function of temperature for $NiMnGe_{0.91}Al_{0.9}$. The triangles indicate the hexagonal polymorph and the squares indicate the orthorhombic polymorph.

F.3 References

[326] W. Bazela, A. Szytuła, J. Todorović, Z. Tomkowicz, A. Zięba, Crystal and magnetic structure of NiMnGe, Phys. Status Solidi A, 38 (1976) 721-729.

[327] A. Altomare, M.C. Burla, M. Camalli, G.L. Cascarano, C. Giacovazzo, A. Guagliardi, A.G.G. Moliterni, G. Polidori, R. Spagna, SIR97: a new tool for crystal structure determination and refinement, J. Appl. Crystallogr., 32 (1999) 115-119.

[328] G. Sheldrick, A short history of SHELX, Acta Crystallogr. A, 64 (2008) 112-122.

[329] C.P. Sasso, P. Zheng, V. Basso, P. Müllner, D.C. Dunand, Enhanced field induced martensitic phase transition and magnetocaloric effect in $Ni_{55}Mn_{20}Ga_{25}$ metallic foams, Intermetallics, 19 (2011) 952-956.

Vita

Michael J. Kangas was born and raised in Iron River, Michigan where he spent most of his childhood playing hockey. At West Iron County High School he developed an interest in chemistry. After high school he attended Carthage College in Kenosha, Wisconsin where he majored in chemistry and earned a bachelor of arts degree in 2004. After a journey that included stops at Michigan State University and Dow Chemical he made his way to Louisiana State University in 2008. He joined professor Julia Chan's research group and studied the synthesis and characterization of rare earth intermetallics. He will graduate with a doctorate in chemistry in December 2012.